DESIGN AND ADVANCED CONTROL OF

ACTIVE SUSPENSION SYSTEM WITH

LINEAR ACTUATOR

LIN JIONGKANG

Ph.D

The Hong Kong Polytechnic University

2014

The Hong Kong Polytechnic University

Department of Electrical Engineering

Design and Advanced Control of Active Suspension System with Linear Actuator

LIN Jiongkang

A thesis submitted in partial fulfilment of the requirements

for the degree of Doctor of Philosophy

September 2013

CERTIFICATE OF ORIGINALITY

I hereby declare that this thesis is my own work and that, to the best of my knowledge and belief, it reproduces no material previously published or written, nor material that has been accepted for the award of any other degree or diploma, except where due acknowledgement has been made in the text.

_____(Signed)

_____LIN Jiongkang_____(Name of student)

To my parents, Han Lun Lin and Xiu Ling Hu.

Abstract

Active suspension system (ASS) has been growing its popularity in industrial development and academic research since 1980s. The main advantage of electromagnetic ASS is its high performance in automotive applications. The ASS shows a high flexibility in control and provides enhanced comfort and safety to drivers and passengers when it is compared with the passive suspension. While compared to the pneumatic and hydraulic types, the ASS with electrical actuators can eliminate many mechanical components and perform faster response which in turn reduces the maintenance cost. Investigations into the electromagnetic ASS have been actively performed by worldwide researchers.

Switched reluctance actuator (SRA) is a type of synchronous motors that has simple structure, low cost, robustness, and reliability characteristics. The linear motion type of SRA, linear switched reluctance actuator (LSRA), has inherent distinct advantages of high force and fault tolerance features, which align with the ASS operations to maintain equilibrium.

The ASS with LSRA involves complex control. Variable reluctance and inherent nonlinear force characteristics are two major uncertainties that lead to implementation difficulty of LSRA control. Hence, an accurate position sensor is installed to the system for phase commutation and force control. A noise-free tracking mechanism is developed to acquire high precision position control.

The ultimate objective of this project is to investigate and propose an effective nonlinear controller and position-tracking scheme for the quarter-car and full-car ASS equipped with LSRA. To achieve this target, the whole research work frame is divided into three phases. The first phase of research work is to investigate the linear actuator and develop the prototype of LSRA for the ASS. The magnetic path of the LSRA and its operation principle are reviewed. Based on the dimension and force requirement of the ASS, the specified magnetic circuit is modelled and analysed through finite element analysis (FEA). Moreover, the prototype model is developed and verified by experimental implementation through direct drive converter.

Following the fabrication of the proposed LSRA, the experimental platform of the quarter-car ASS is built. The models of the quarter-car ASS and full-car ASS are developed for both force control of LSRA and nonlinear advanced control of ASS. The open-loop instability exists due to the external road disturbances which compensation algorithms are used to meet the standstill requirement; moreover, the coupling behaviour of the full-car ASS deteriorates the performance of the controller. To simplify the control scheme of the overall system, the ASS is divided into two subsystems, sprung part and unsprung part. The control issue focuses on the sprung part to improve the performance of the ASS.

High accuracy position feedback is critical in this application. A novel tracking mechanism without the requirement of the system state equation, the so-called tracking differentiator (TD), is introduced to track the feedback displacement signal and to calculate its velocity directly through numerical method based on optimal control theory. The effectiveness of the TD is verified through position tracking of the sinusoidal road profile.

A nonlinear proportional-derivative (PD) controller is developed for the quarter-car ASS. Both the simulation and experimental results illustrate that the electromagnetic active suspension control system can achieve a high motion performance and keep the system stable consistently with the proposed nonlinear PD controller. The developed nonlinear control method is more robust than that of linear PD controller under the variations of system parameters and road disturbances.

The second phase of the research work is to improve the robustness of the whole suspension system by implementing the nonlinear controllers into the ASS. An integral sliding mode controller is examined. The integral item of integral sliding surface guarantees the stability of the nominal system at the initial time instant. In addition, adaptive mechanism is applied to the quarter-car ASS. An adaptive model following control method is used to determine the dynamic behaviour of the suspension system by predefining a reference model. The control input is generated through adaptive regulator based on partially known parameters and disturbances. Furthermore, combination of sliding mode technique and adaptation mechanism is attempted in this research to obtain the advantages of simplicity and robustness.

The final phase of the research work is to propose both linear and nonlinear control algorithms for the full-car ASS. The full-car sprung mass subsystem is decoupled into three individual single-input single-output subsystems using decoupling transformation matrix. This results that the control complexity of the full-car active suspension is significantly simplified. The proposed control algorithms are categorised by two types of suspension models such that one is linear and the other is nonlinear. For the linear model, a Linear Model Following Control method is used to suppress the vertical vibration due to road profile. A proportional-derivative regulator is added to compensate the parameters variation and external disturbance. For the other one, a nonlinear sliding mode controller is applied. The discontinuous control laws of the sliding mode controller compensate the system uncertainties and unmodelled dynamics.

The thesis presents a number of advanced control methods to successfully suppress the vertical oscillation of the ASS and it thus enhance the safety and comfort. It is confident that the new development will be applied to a vehicle for the next generation of mobility.

List of Publications

Technical Papers in Refereed Journals

[1] **Jiongkang Lin**, Ka Wai Eric Cheng, Zhu Zhang, Norbert C. Cheung, and Xiangdang Xue, "Adaptive sliding mode technique-based electromagnetic suspension system with linear switched reluctance actuator", *IET Electric Power Applications*, vol. 9, no. 1, pp. 50-59, 2015.

[2] **Jiongkang Lin**, Ka Wai Eric Cheng, Xiangdang Xue, Norbert C. Cheung, and Zhu Zhang, "Estimation of inductance derivative for force control of linear switched reluctance actuator", *IEEE Transactions on Magnetics*, vol. 50, no. 11, 2014.

[3] **Jiongkang Lin**, Ka Wai Eric Cheng, Zhu Zhang, Norbert C. Cheung, Xiangdang Xue, and Tsz Wang Ng, "Active suspension system based on linear switched reluctance actuator and control schemes", *IEEE Transactions on Vehicular Technology*, vol. 62, no. 2, pp. 562-572, 2013.

[4] **J. K. Lin**, K.W.E. Cheng, N.C. Cheung, Z. Zhang, X. Xue and S.W. Zhao, "Active damper control system based on LMFC", *World Electric Vehicle Journal*, vol. 4, pp.517-524, 2010.

Conference Papers in Refereed Proceedings

[5] **J. K. Lin**, K. W. E. Cheng, et al., "Integral sliding mode control and its application on active suspension system", *The 4th International conference on power electronics systems and applications (PESA 2011)*, Hong Kong, 2011.

Acknowledgements

Firstly and foremost, I would like to express my sincere gratitude and appreciation to my chief supervisor, Prof. K. W. Eric Cheng. He has always been supportive and encouraging throughout my research period. His academic guidance is extremely useful and beneficial. Without him, it would be impossible for me to fulfil my goal of pursuing for a PhD degree.

Secondly, I would like to thank Prof. Jie Wu, a senior professor from South China University of Technology. He was my supervisor during my master study in Guangzhou, China. His spirit and attitude encourages me to take up the research work.

I greatly appreciate helps and support from my co-supervisor Dr. Norbert C. Cheung, who has made available his support in a number of ways.

I would like to thank Dr. Shiwei Zhao, Dr. Zhengang Sun, Dr. Zhanghai Shi, Dr. Sizhe Chen, Dr. Ping Dong, Dr. Nelson Chan, Dr. Kai Ding, and Dr. Benny Yeung for their helpful discussion and suggestions on my research topic.

Special thanks go to my colleagues and friends, Dr. Xiangdang Xue, Dr. Zhu Zhang, Mr. Daohong Wang, Mr. Yanjie Bao, Mr. Jones Chan, and Mr. John Lam for all their technical support in this research.

I have to thank all my friends and colleagues in the Power Electronics Research Centre for all their helps, supports, and valuable hints: Mr. Tsz Wang Ng, Mr. Man Keung Wong, Mr. Ka Yin Tse, Mr. Ricky Chang, Mr. K. F. Kwok, Dr. Junfeng Liu, Dr. Lichan Meng, Ms. Cuidong Xu, Dr. Shuxiao Wang, Mr. Dickson Chau, and Mr. Yuanmao Ye.

Lastly, I would like to deeply thank my parents, my brother, my girl friend, and my family for their endless love, patience, care, and devotion.

Table of Contents

List of Figures

List of Tables

List of Acronyms

AMFC	Adaptive Model Following Control
ASS	Active Suspension System
C.G.	Centre of Gravity
DC	Direct Current
DOF	Degree-Of-Freedom
DSP	Digital Signal Processor
DTM	Decoupling Transformation Matrix
EH	Electrohydraulic
EMI	Electromagnetic Interference
ER	Electrorheological
FEA	Finite Element Analysis
FDF	Force Distribution Function
GUUB	Globally Uniformly Ultimately Bounded
IGBT	Insulated-Gate Bipolar Transistor
ISMC	Integral Sliding Mode Control
LMFC	Linear Model Following Control
LMI	Linear Matrix Inequality
LQR	Linear Quadratic Regulation
LSRA	Linear Switched Reluctance Actuator
LVDT	Linear Variable Differential Transducer
MCA	Magnetic Circuit Analysis
MFC	Model Following Control
MIMO	Multiple-Input Multiple-Output
MMF	Magnetomotive Force

MR	Magnetorheological
PD	Proportional-Derivative
PI	Proportional-Integral
PID	Proportional-Integral-Derivative
PM	Permanent Magnet
PMF	Perfect Model Following
PSD	Power Spectral Density
PWM	Pulse Width Modulation
RSRA	Rotary Switched Reluctance Actuator
SISO	Single-Input Single-Out
SMC	Sliding Mode Control
SRA	Switched Reluctance Actuator
TD	Tracking Differentiator
VSC	Variable Structure Control
ZVS	Zero Voltage Switching

List of Symbols

A	effective area
A_c	winding area
B	flux density
C_s	equivalent damper ratio of quarter-car ASS
D	width of LSRA
e	error
e_a	back EMF
F	linear active force of quarter-car ASS
F_e	electromagnetic force
F_m	magnetomotive force
F_{fl}	active force generated by front left electromagnetic actuator
F_{fr}	active force generated by front right electromagnetic actuator
F_{rl}	active force generated by rear left electromagnetic actuator
F_{rr}	active force generated by rear right electromagnetic actuator
g	gravitational constant
g_a	air gap
H	magnetic field intensity, in Chapter 3
H	mass and inertia matrix, in Chapter 6
h_c	winding height
h_s	stator pole height
h_t	translator pole height
i	current

I_p	pitch axle moment of inertia
I_r	roll axle moment of inertia
k_d	derivative gain
k_i	integral gain
k_p	proportional gain
K_s	spring stiffness of quarter-car ASS
K_{sf}	stiffness of front springs of full-car ASS
K_{sr}	stiffness of rear springs of full-car ASS
K_u	tire stiffness of quarter-car ASS
K_{uf}	stiffness of front tires of full-car ASS
K_{ur}	stiffness of rear tires of full-car ASS
l	effective length
l	length of stator
l_s	stator back iron thickness
L	inductance
$L_{\min}$	minimum inductance
$L_{\max}$	maximum inductance
L_{nom}	nominal inductance
L_f	distance from centre of gravity to front axle
L_r	distance from centre of gravity to rear axle
M_s	sprung mass of quarter-car ASS
M_u	unsprung mass of quarter-car ASS

N_{ph}	number of phases
N_{sp}	number of stator poles
N_{tp}	number of translator poles
P	power
q_e	error vector
q_s	sprung variable vector
q_s^*	required sprung variable vector
q_u	unsprung variable vector
r	reference input
R	resistance
$R(\Omega)$	roughness of the road profile
T	sampling time
T_f	half track width of front car body
T_r	half track width of rear car body
T_s	settling time
u	system input
v_a	movement speed
V	voltage
w	double-sided module width
w_c	winding width
w_{sp}	stator pole width
w_{ss}	stator pole slot
w_{tp}	translator pole width

w_{ts}	translator pole slot
W_c	co-energy
W_e	electrical energy
W_f	magnetic field energy
W_m	mechanical work
x	state variable
x_a	translator position
X	state vector
y	system output
z	heave position of full-car ASS
z_r	road disturbance of quarter-car ASS
z_s	sprung displacement of quarter-car ASS
z_u	unsprung displacement of quarter-car ASS
z_{rfl}	vertical road disturbance of front left wheel
z_{rfr}	vertical road disturbance of front right wheel
z_{rrl}	vertical road disturbance of rear left wheel
z_{rrr}	vertical road disturbance of rear right wheel
z_{ufl}	unsprung displacement of front left corner of full-car ASS
z_{ufr}	unsprung displacement of front right corner of full-car ASS
z_{url}	unsprung displacement of rear left corner of full-car ASS
z_{urr}	unsprung displacement of rear right corner of full-car ASS
φ	flux
φ	roll angle of full-car ASS

σ	stroke
λ	flux linkage
θ	pitch angle of full-car ASS
τ_t	stator pole pitch
τ_t	translator pole pitch
μ	permeability
Ω	angular spatial frequency

Chapter 1   Introduction

Suspension system is a device widely equipped in vehicles to provide riding comfort and handling safety in a reasonable way. The purposes of installing suspension system into vehicle are: i) keeping in contact with the road surfaces for good active safety and driving pleasure with excellent steering performance; ii) suppressing the vibration of vehicle body and isolating from road noise for passenger comfort [1]-[3], respectively. These two goals are controversial generally, thus developing of suspensions involves finding the right compromise of driving comfort and safety. In recent decades, active suspension systems and its control strategies have become a new technology to improve the dynamic performance. Research interest has been risen in automotive industry [4]-[8] and academy institutions [9]-[11].

This thesis investigates the applicability of ASS equipped with linear switched reluctance actuator (LSRA). The linear motion between the stator and translator of a LSRA is driven by attraction force, which is used to compensate the vertical vibration of the automotive suspension and stabilise the chassis.

The construction and performance analysis of the electro-mechanical system is investigated, including the magnetic characteristics and standstill performance. Modelling and controllers design of quarter-car system and full-car system are developed to achieve excellent performance based on the analysis of the electro mechanical system.

In this chapter, an ASS with LSRA is proposed. Background and history of the suspension system will be introduced in the beginning. The development progress is reviewed over both industry manufacturing and academic research. Then the significance of ASS and project objectives will be presented and finally the organization of the thesis is outlined.

1.1 Background

In modern automotive industry, the vehicle dynamics are composed of kinematics, mechanics, dynamics, and vibrations [12]. The development of vehicle involves the improvement of ride quality, handling, and traction [13]. It is still a challenge to solve the conflicting requirements of safety and comfort. Since the first appearance of leaf springs, the suspension system plays a vital role in improving the dynamic performance of grounded vehicle. The development of vehicle suspension is the continuously compromising of driving safety and passenger comfort.

The development of suspension system of ground vehicle involves into three types: passive type, semi-active type and fully active type [10], [14], [15]. Generally, the design of suspension is limited by the compromise between riding comfort and handling safety. Thus, there are different structures and detailed functions in each type. For example, a racing car driver are concerned for handling safety of high speed driving and cornering rather than driving comfort, vice versa for the passengers in a sedan.

Passive suspensions are composed of fixed coefficients components, such as springs, dampers, and absorbers. Energy can only be stored or dissipated in these passive elements. Since only mechanical components exist, the passive suspension has advantages of simple structure, high reliability, and low cost, which are at the expense of performance limitations [16]. In conventional passive suspension, the vehicle is supported by a spring in parallel with a damper placed at four corners, which are referred to strut. Along with the increasing performance requirement, the passive suspension system has been developed from dependent type to independent type. However, the instinct drawback of passive components with fixed coefficients limits the performance of ride quality [17].

Semi-active suspension systems are equipped with passive springs and varying dampers with changeable damping ratio. The damping ratio can be controlled through variable means. It provides flexibility for suspensions according to different situations [2]. Meanwhile, optimization of the damping ratio becomes a design problem in the closed-loop control algorithm. Once the controls of the damping ratio are well tuned, the semi-active suspensions can ensure good filtering performance and guarantee

good damping of the body resonance together [18]. There are three main types of semi-active suspension system: solenoid-valve electrohydraulic damper [19], magnetorheological damper [20]-[22] and electrorheological damper [23], [24]. Though the filtering function and response of the semi-active suspension is better than that of passive suspension, the performance of the semi-active suspension is also limited because only energy dissipation exists in the system and no external force is injected [25].

The fully active suspension system provides further flexibility by replacing the damper with actuators, which can generate active force. The ASS can satisfy the requirement of handling safety and riding comfort simultaneously, i.e. achieving excellent driving experience without compromise [13], [26]. The structure of active suspension is a spring in parallel with active actuator. The types of active actuator are pneumatic, hydraulic and electromagnetic. ASS achieves faster time response and wider frequency range than the passive and semi-active type. The application of active suspension in commercial vehicle is mainly for luxury cars because the cost and energy consumption are relatively high. Bose has demonstrated the capability of electromagnetic ASS with linear electromagnetic motors [8]. Along with the appearance of new materials and development in power electronics technologies and control methodologies, the ASS will be more compact, cheaper, and lighter with better performance, which will prevail on future automotive suspension industry.

1.2 Literature review

1.2.1 Control of active suspension system

The most remarkable advantage of ASS is the establishment of active actuator to provide external force and eliminate trade-off between handling safety and driving comfort [13], [27]. Therefore, the performance of ASS is determined by the control methods and their implementation. The control schemes of ASS are described as below, including the pneumatic type, hydraulic type and electromagnetic type. Though the implementation actuators are different in each type, the ASSs are controlled by the control unit based on the sensed signals, as shown in Fig. 1-1. Based on different implementation unit and system model, the control methods for active suspension vary from the conventional linear control schemes to advanced intelligent control schemes. In this section, some published control methods will be reviewed.
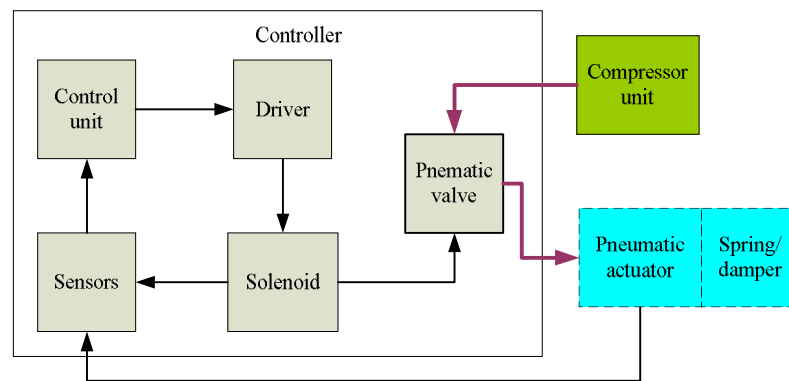
(a) Pneumatic type
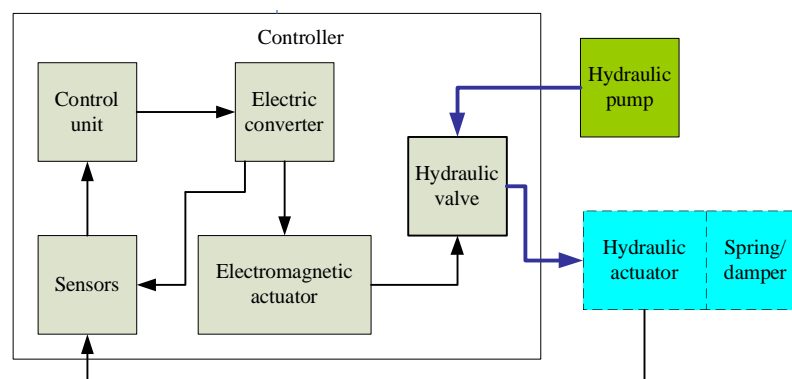
(b) Hydraulic type
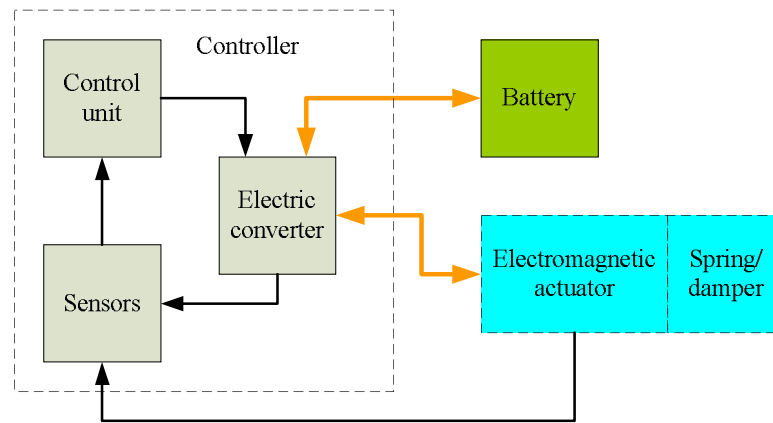
(c) Electromagnetic type

Fig. 1-1 Block diagram of ASSs

Among classical control methods, proportional-integral-derivative (PID) control is widely used in industry application because it is simple and reliable [28], [29]. In automotive active suspension, the variables are fed back to the PID controller combined with the referenced input and generate the desired force, thus the car body can be stabilised under the occurrence of external disturbance [30], [31]. The parameters of PID controller can be tuned in many ways according to different road profiles, such as [32]. Furthermore, the robustness of the PID controller can be improved by adding fuzzy logic [33].

The suspension model should be linearised for simplicity. Thus, various linear optimal control methods can be used for the ASS, such as linear quadratic regulation (LQR) optimal control [11]. LQR deals with a set of linear differential equations based on optimal control and develops a state feedback control law to minimise the quadratic function of the system [34], [35] . In [36] the suspension system is described as a continuous time linear optimal problem and is solved in deterministic and stochastic environments. With the property of model prediction, LQR can estimate the road profile and system states to construct a simple and effective feedback control law [11], [14], [36], [37]. The examination of LQR method had been carried out in a laboratory-scale model with a pneumatic actuator, and the experimental results show the linear feedback law can minimise the pre-specified performance index [38], [39].

For a nonlinear physical model of full-car ASS, the performance of the aforementioned linear control methods is affected by the nonlinear characteristics of

the system model. Thus, nonlinear control methods and intelligent control methods will be more appropriate for the sophisticated ASS. Nonlinear control methods including sliding mode control and adaptive control have been investigated for decades to deal with nonlinear time varying system [40], [41]. Sliding mode control [42]-[44] is widely used to solve the practical nonlinear system control problems, such as robot manipulators [45]-[47], unmanned vehicle [48], [49], aircraft [50], [51], electric drive [52], [53] and suspension system [54]-[57]. The sliding mode control originates from variable structure control [58], [59] by using on/off relay to implement discontinuous control and force the system state trajectories to track the designed sliding surfaces. The most attractive properties of sliding mode control are simplicity, robustness, stability, rejection of disturbance and order reduction [44], [52]. The design issue of sliding mode controller has been extensively investigated for ASS [55], [57], [60], [61]. A quarter-car nonlinear active suspension model is studied in [57] with the consideration of suspension nonlinearities including hardening spring, quadratic damping force and tyre lift-off phenomenon. A sliding mode controller utilizing a variant of sky-hook damper system is developed to achieve the desired performance for a wide range of operating conditions. The robustness of the proposed scheme is verified both in time and frequency domain by varying sprung mass load. The linear and nonlinear seven degrees of freedom full-car suspension models have been studied in [60] and [55] respectively. Sliding mode control is designed to improve the ride comfort by decreasing the vehicle vibration amplitudes. The simulation results show the improved vehicle body motion when running on a ramp. Furthermore, robustness of the sliding mode controller is examined by varying vehicle mass and damper ratio. A nonlinear pneumatic ASS has been investigated in [61]; a fourth-order polynomial function nonlinear air-spring model for railway and road vehicles is developed based on the measured and experimental data with the consideration of nonlinear force-deflection relationship and preload characteristics. A reference model feedback control is developed to improve the ride quality of a nonlinear suspension; the sliding mode controller is designed to address the model nonlinearities and parameter variation, such as load conditions and road profiles.

  Adaptive mechanism is developed to deal with slowly time-varying nonlinear system without a prior knowledge of the model [40], [62], which is extremely suitable for the suspension system when the vehicle is exposed to road disturbances and load

variation from time to time [63]-[67]. In [63], a quarter-car hydraulic active suspension model is investigated. Sliding mode control is developed to an accurate electro-hydraulic suspension system. While the parameters vary, the predefined model is implicit and higher control gains are needed to ensure the effectiveness of the controller. However, large gains cause chattering problem in practical implementation. An adaptation scheme is used to identify the system uncertainty and slowly varying parameters, and ensure the accuracy of the system model. Thus, the adaptive control scheme maintains high performance ASS in which the control gains vary with the tracking errors. Besides, adaptive scheme can be used for parameter identification in active suspension. In [64], a dedicated adaptive observer is developed to estimate the time varying sprung mass online that depends on the number of passengers and the load. The convergence of adaptation mechanism is ensured by the measurement of two accelerometers and an linear variable differential transformer (LVDT). The proposed adaptive observer is applied to a realistic half-car suspension model and the performance is examined experimentally. The attenuation of time varying unknown narrow band disturbances for a quarter-car active vibration system is achieved by utilizing feedback adaptive control in [66]. Based on the internal model principle and the Youla-Kucera parametrization, the unknown disturbances can be incorporated into the system model. Thus, a direct adaptive control scheme is applied directly to adjust the internal model without recomputing the controller, and the size of the adaptive scheme depends on the complexity of the disturbance model. Both direct and indirect adaptation mechanisms have been developed and tested comparatively. The real time results indicate that the direct adaptive scheme outperforms the indirect adaptive scheme. In [67], a model-free adaptive sliding mode controller is proposed. System uncertainties and vibration are lumped into two unknown time-varying functions, and these unknown functions are represented as a finite set of basic functions utilizing function approximation technique. Based on Lyapunov direct method, the adaptive laws are obtained to suppress the vertical vibration and improve ride quality.

Recently intelligent control methods have been applied to ASS extensively [68], such as fuzzy logic [69], [70] and combination with nonlinear control methods [71]-[75]. Fuzzy logic is founded by Zadah [76], which can be viewed as an extension of multi-valued logic [77]. Fuzzy logic describes the object in an approximate way and establishes the fuzzy rule to solve problems [78]. In [70], a fuzzy logic controller is

developed with look-up table rule to reduce the vertical acceleration amplitude. The parameters of the membership functions are tuned by trial and error method. A detailed design of fuzzy logic for ASS is presented in [69]. Two-loop control is constructed for quarter-car hydraulic suspension system to avoid hitting the rattle-space limits and minimise the car body acceleration. The outer loop employs fuzzy logic rule to generate the desired active force, in which the parameters of fuzzy logic are fine-tuned via genetic algorithm. Furthermore, the combined control methods with fuzzy logic, sliding mode control, adaptation mechanism and genetic algorithm are investigated to take the advantages of these controllers. The sliding mode slope is tuned by the fuzzy logic continuously to avoid the chattering problem and maintain the robustness of the fuzzy sliding mode controller proposed by [73]; while the performance of improving riding quality using adaptive fuzzy logic control is superior with respect to optimal method in [79]. Adaptive fuzzy sliding mode controllers for ASS are proposed in [71], [74]. The equivalent control of the sliding mode controller is obtained by fuzzy logic and the vertical oscillation is suppressed significantly. Besides, combination of neural network, fuzzy logic, and sliding mode methodologies has been proved an effective technique to minimise the body acceleration and suspension deflection of the nonlinear suspension model [72].

Robustness is the essential requirement to the controller of ASS arises from the parameter nonlinearities and road disturbances. Therefore, robust control is an important control method for ASS. To date, linear matrix inequality (LMI) based H_∞ control technique [80]-[83] has been investigated extensively and successfully applied in a class of delay [84], [85] and uncertain [86]-[88] system with feedback scheme [89] and network-based [90], [91]. H_∞ control has the property of minimizing the closed-loop root-mean-square gain from the disturbance to the output, which can be utilised to reject disturbances for active suspension [92]. Application of H_∞ control for a quarter-car suspension model is demonstrated in [93]. The structured uncertainties are treated as robust LQR design task, and parametric uncertainties problem is solve by direct state feedback H_∞ control. Design of H_∞ control for a full-car model is discussed in [94]. The desired robust performance of the closed-loop system is verified in an actual vehicle. Time-domain constraints of a realistic ASS are considered in [95] using reachable sets and state-space ellipsoids technique. A state

feedback constrained H_∞ control with LMI is proposed to achieve multi-objective control, and ride comfort is improved indicated by simulation results.

1.2.2   Linear switched reluctance actuator

Switched reluctance Actuator (SRA) is an electric double salient actuator. The operating principle of SRA is moving to the aligned position of minimum reluctance [96], [97]. Motion control of SRA is achieved by exciting the windings in a specified sequence. There are two types of SRA: rotary type (RSRA) and linear type (LSRA). Both SRAs have the merits of simple geometric structure, high force/torque density, fault tolerance, low manufacturing cost and free of maintenance. The LSRA runs in a linear motion for horizontal movement [98], [99] and vertical propulsion [100], [101].

  The feasibility of LSRAs for vertical propulsion application has been demonstrated in [102]. Compared to other linear motors such as linear induction motor and linear PM synchronous motor, LSRA is attractive for its high fault and thermal tolerance. Various designs and configurations of LSRA have been investigated for application. A standard design procedure of single-sided longitudinal LSRA is presented in [103]. By utilizing the knowledge and design procedure of RSRA, the author converts the rotary domain design into linear domain design. A prototype LSRA is fabricated, and the inductance and force characteristic is tested for verification of the analysis and design. Double-sided structure of LSRA is proposed to achieve higher force density by Deshpande [98]. A novel double-sided design of LSRA is proposed to generate lifting force for a linear elevator, and the experimental results show the great potential of LSRA in vertical propulsion application [100]. Furthermore, four longitudinal LSRA configurations are proposed in [102] for vertical elevating application. The design of these four LSRAs has similar static force that allows the comparison among them to obtain the optimised design with highest force density.

1.3 Objectives and Structure

Electromagnetic type ASS with electric actuators has been investigated extensively. However, the applicability of LSRA for ASS is a new challenge and there is no previous research work on this topic. The primary objective of this thesis is to design and build an experimental quarter-car ASS with LSRA. The ASS is a nonlinear system due to inherently nonlinearity of LSRA, system parameter uncertainties and external disturbances. Thus, the second objective is to investigate real-time reliable nonlinear control methods to improve riding comfort and handling safety of ASS.

To achieve the above objectives, the thesis is organised as follows.

Chapter 1 provides some background about vehicle suspension system. The control schemes of active suspension are explored. Control methods on ASS and design of LSRA for vertical elevator have been introduced extensively. The objectives and structures of this thesis are summarised in this chapter.

Chapter 2 gives a brief introduction of the development of vehicle suspension. Design of a quarter-car ASS is proposed in this chapter, including the mechanical structure of suspension system and its related electric power amplifiers. A test rig of quarter-car suspension is fabricated for experiment verification. Characteristics of quarter-car and full-car ASS are modelled for control purpose.

Chapter 3 reviews the properties of switched reluctance actuator. Analysis and design procedure of the LSRA is presented, and the dynamic characteristic of the specified LSRA is obtained through FEA methods and experiment test. The design is examined by a prototype. A simple direct force control method is developed to implement active force generation.

A nonlinear proportional-derivative (PD) control scheme is developed for quarter-car ASS in Chapter 4. In this chapter, a tracking differentiator (TD) is introduced to obtain position and velocity tracking and eliminate the sense noise. Nonlinear PD control method is studied them. The analysis of stability and robustness between the linear PD and nonlinear PD is explored. The analysis results illustrate that nonlinear PD achieves better control quality. Simulation and experimental results verified the effectiveness of the proposed nonlinear PD controller.

In Chapter 5, further investigation of nonlinear control theory on ASS is carried out. Nonlinear control methods, such as sliding mode control and adaptive control, are reviewed. Thus, the control strategies of sliding mode scheme and adaptation mechanism are developed. An integral sliding mode controller is studied to guarantee the stability of nominal system at the initial time instant. Adaptation mechanism with Popov hyperstability theorem is applied to the ASS with partially known parameters. Besides, hysteresis update rule of control gains is introduced to reduce the risk of chattering. The stability and robustness of those developed control methods are numerically analysed and examined by simulation and experiment results. The combination of sliding mode technique and adaptation mechanism is developed to improve the dynamic performance of the system.

Control of a full-car ASS is proposed in Chapter 6. For a linear model, linear model following control method is introduced. The uncertainties and nonlinearities of the suspension are compensated by a simple PD control. The control gains of the linear model following control are designed to fulfil the perfect model following conditions. For a nonlinear model, sliding mode control technique is used. It seems as an extension of nonlinear control on quarter-car case. The stability and robustness of these two control methods are analysed. The effectiveness of these two controllers is verified by simulation results.

Chapter 7 summaries the achievement and remarks of this thesis, future plans are suggested for further research.

Chapter 2 Structure and Modelling of the Active Suspension System

This chapter focuses on the design of the active suspension system and its related power amplifier. Besides, the models of the ASS are developed for the purpose of system control.

A brief introduction of conventional passive and semi- active suspension systems is reviewed, as well as three main types of ASSs, e.g. pneumatic type, hydraulic type, and electromagnetic type. Then the structure of the electromagnetic system with LSRA is described, including the specified schematic and hardware instalment. Finally, for the purpose of system optimization and control, the dynamics of mechanical part and electrical part of the device are modelled and utilised for further analyzing and optimizing.

2.1 Brief introduction of suspension system

The purpose of a vehicle is to move the passengers or payload comfortably, safely, and expediently, in despite of the external road terrain. Comfort and safety are controversial issues in vehicle steering. To solve this problem, automotive suspension systems have been developed and optimised continuously.

2.1.1 Passive Suspension System

Passive suspensions are referred to the system composes of passive components, such as springs, dampers and linkages. Along with the development of vehicle technology, the tuning of suspensions is optimised by compromise between driving safety and steering comfort.

In conventional suspensions, passive springs are used to support the load and connect the vehicle with the wheels, and dampers are installed parallel to control spring motions. Based on different motions and connections of the wheel and the chassis, the suspensions can be categorised as dependent type, semi-dependent type and independent type.

During the development of automotive industry, the early leaf springs were replaced by torsion bar suspensions, and now the modern independent suspension is almost invariably based on the coil spring. The main types of independent suspensions are double wishbone and MacPherson strut. MacPherson strut was invented by E.S. MacPherson and patented in 1953 [104]. The modern strut suspension is a combination of strut and wishbone and usually used for small and medium passenger cars.

Although the design of a mechanical passive suspension is tuned continuously, driving comfort and steering safety are two conflicted objectives and needed to be compromised. The worse cases occurred when the suspension system is out of its limited travel, in which the above two objectives were deteriorated dramatically and must be avoided theoretically.

To solve that conflict, based on the experience and test of automotive manufacturers, a good choice is to change the spring stiffness and damping ratio; hence, the passive suspension system is modified to semi-active and fully active suspension systems.

2.1.2   Semi-Active Suspension System

Semi-active suspension systems are the adaptation of the damping ratio and/or the spring stiffness to the actual demands without energy injection. The variation of the damping ratio provides flexibility for suspensions; however, optimization of the damping ratio becomes a design problem in the closed-loop control algorithm. Once the controls of the damping ratio are well tuned, the semi-active suspensions can ensure good filtering performance and guarantee good damping of the body resonance together.

The core of the semi-active suspension systems is the shock absorber, which is capable of changing the damping ratio through electronically control mechanism. The electrical semi-active suspension system was firstly produced by Mitsubishi in 1987. In 2002, General Motors (GM) releases its Cadillac Seville STS with an innovative damper filled with magnetorheological fluid. In modern automotive industry, there are three main types of shock absorbers equipped by vehicles [18]: solenoid-valve Electrohydraulic (EH) damper, Magnetorheological (MR) damper and Electrorheological (ER) damper.

The mainstream of semi-active suspension techniques development is focused on the optimization of damping ratio, as discussed above. In fact, new trends are evolving and not limited to the design of control methods. A new technology namely air-damping AIRMATIC Dual Control is developed by BMW to change the spring stiffness and damping ratio. Compressed air spring is adjusted by electrical system to accommodate various driving comfort requirements.

2.1.3   Active Suspension System

The active suspension system contains "active" electrical components to transfer external energy into the vehicle, in order to achieve excellent ride quality and car handling. The active suspensions sustain each wheel independently and move up and down based on the road surface and driving status through controllable actuators. These active actuators provide flexible control and fast response. These advantages ensure that the on-road /off-road vehicles are isolated from driving situations, such as cornering, accelerating, braking, and passing through uneven road. Although the

performance of ASS is superior to passive and semi-active suspensions, the main drawbacks to popularise this are high cost in manufacturing and maintenance.

Lotus had initialled the use of electro-hydraulic active suspensions with double-acting hydraulic actuators in 1982, and then introduced this technology to F1 with Lotus 99T in 1987. In 1990, Hydractive suspension was introduced on the XM by Citroën based on the oleo pneumatic suspension design. The most advanced commercial ASS was awarded to the Active Body Control (ABC) developed by Mercedes-Benz in 1999. By applying hydraulic servomechanisms, the ABC system can adjust the body movement of the vehicle through hydraulic pressure, to eliminate body roll and even achieve self-levelling in response to various driving situations.

The aforementioned hydraulic/pneumatic active suspensions contain many hydraulic components, which make the commercial products very expensive and complicated. Moreover, the hydraulic systems are marked as a slow response and high energy consumption system. Along with the rapid development of power electronics techniques, the electrical system is more and more reliable and has potential to replace the hydraulic system. By replacing the hydraulic valves with electromagnetic actuators, the electromagnetic suspension systems eliminate mechanical part greatly and simplify the system configuration, also provide extremely fast response and improve energy efficiency through power regeneration.

The concept of electromagnetic ASS has attracted lots of interest from academic research to industry applications. Among those reported prototypes, the Bose electromagnetic ASS mostly approaches a commercial product and is under optimization now [8].

The Bose ASS includes a linear electromagnetic actuator and related power amplifier at each wheel and is controlled by a set of superior control algorithms. The linear electromagnetic actuator is composed of magnets and coils of wire. The linear motion can be accomplished by retracting and extending the motor using electrical power. The Bose suspension module equips a linear electromagnetic actuator as the telescoping suspension strut, and supports the vehicle and load with a torsion bar spring connected to the lower arm. The Bose system installs a suspension module at each corner, and a control unit at the rear of the vehicle. The central unit handles the measurement signals observed by the sensors, and sends commands to the linear

actuators. Roll and pitch oscillation due to road profile can be suppressed rapidly by linear motion of actuators. Moreover, the bi-directional power amplifiers allow regeneration of the system and reduce the power consumption down to one-third of a typical vehicle's air conditioner system.

Moreover, new architectures with more electrical means are proposed to reduce pollution. The conceptual full-corner vehicle is a completely new vehicle architecture where partly or all of the main dynamic elements of the vehicle are packed in the wheel [18]: the main electric motor, the electro-mechanical "by-wire" brake, the suspension, and the electro-mechanical "by-wire" steer. The full-corner vehicle can be seen as "all-in-wheel" vehicle. The recently released Active Wheel of Michelin [5] and VDO e-Corner of Siemens [105] are two representatives of full-corner vehicles.

2.2 Design and fabrication of the electromagnetic active suspension system

The primary objective of the project is to develop an electromagnetic ASS with linear actuator. As mentioned above, the mechanical components of the suspension have been investigated and developed for many years, i.e. the technology of coil springs and bearings is mature now. Therefore, the first task of this research is to investigate and design the linear actuator and the assembly of the ASS. After that, a set of control algorithms is studied to ensure the dynamic performance of the ASS and to achieve driving comfort and handling safety.

2.2.1 Structure of the electromagnetic active suspension module

Similar to the Bose active suspension module, the proposed active suspension module in this project includes an electromagnetic actuator and its controller, a bi-directional power amplifier, a set of batteries and capacitor bank, a mechanical coil spring and related linkages.
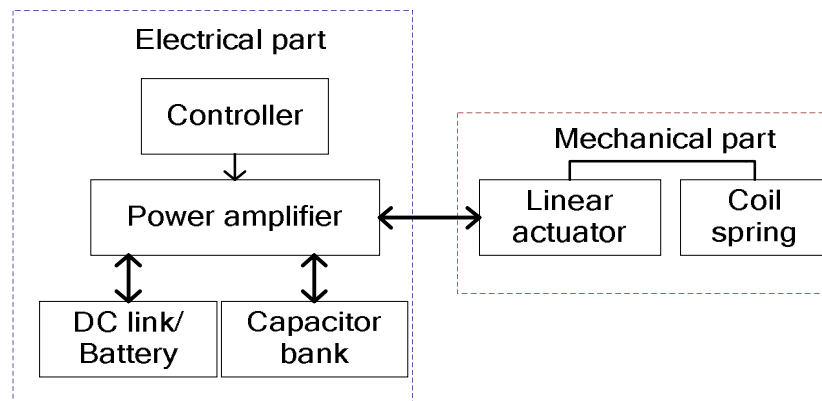
Fig. 2-1 Structure of the proposed electromagnetic active suspension module

As depicted in Fig. 2-1, the module can be roughly divided into electrical part and mechanical part. The mechanical part is composed of linear actuator and coil spring in parallel that is used to sustain the car body and produce active force to eliminate pitch and roll vibration. In this project, the switched reluctance actuator is selected as the linear actuator for its robustness and simplicity. More details of LSRA are described in the next section. The power of the whole module is derived from the battery or DC link. The power amplifier is used to monitor and operate the ASS. Bi-directional

topology provides two modes of power flow: normal mode that injects the energy into the actuator and drive the system; regenerating mode that extracts energy to the capacitor bank and save energy consumption. The capacitor bank is used to store the recursive energy and provide extra power for instantaneous high force. The detailed structure of the module is described below.

2.2.2 Design of mechanical part
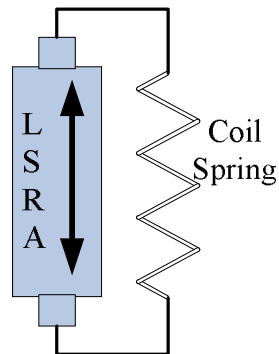
Fig. 2-2 Structure of the mechanical part

The mechanical part of the module includes an LSRA and a coil spring, as shown in Fig. 2-2. These two components are connected in parallel, in which the top side sustains the vehicle body and the bottom side links with the chassis and wheel.

The developed linear actuator is linear SRA. This type of motor is well known for its simple structure, robustness, low cost and free of maintenance. The structure of the proposed LSRA is outlined here, and the detailed design is described in the next chapter. Four identical double-sided actuator modules are arranged in a rotation-symmetrical manner form the LSRA structure shown in Fig. 2-3. To achieve a significant eddy current loss reduction the stator and translator cores are laminated. The longitudinal cross section structure of a double-sided module is shown in Fig. 2-3(a). Each module consists eight pairs of stator poles energized by four phases and eight translator poles. The translator is light in weight due to the absence of excitation windings and back iron. No permanent magnetic materials in translator facilitate the module compatibility with various harsh environments. A double-sided structure achieves a higher force density compared with a single-side one. Four double-sided LSRA modules can be rotation-symmetrically integrated in a more compact configuration depicted in Fig. 2-3(b). Parallel-connected modules can attain a high

propulsion force and eliminate the lateral forces by force balancing. Moreover, this elimination is helpful for reducing the acoustic noise during the operation. Lastly, this configuration is easier for heat dissipation due to the good thermal contact of the coil and the actuator frame, which consequently enhances the overload capability of LSRA. The prototype of the LSRA is shown in Fig. 2-4.
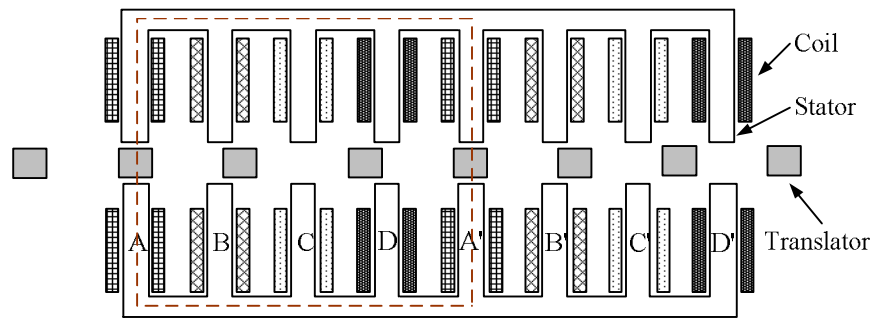
(a) Longitudinal structure (double-sided four-phase module)
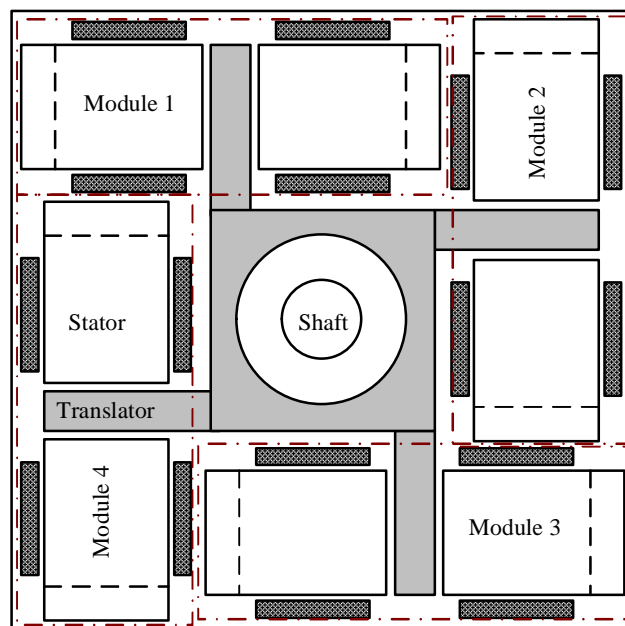
(b) Transverse structure (four modules in parallel)

Fig. 2-3 Structure of the LSRA
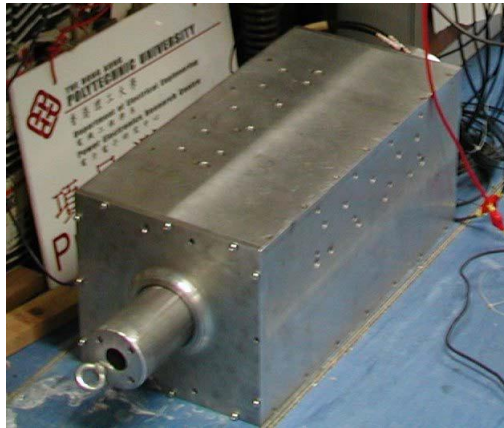
Fig. 2-4 Prototype of the LSRA

The diagram and prototype of coil spring are shown in Fig. 2-5. In this research, the target vehicle is medium class, and its sprung mass is less than 1400kg in general. Therefore, the sprung mass of single wheel is 350kg in maximum. In order to sustain the vehicle body, the diameters of the spring are selected in an appropriate range, as shown in Fig. 2-5. The key coefficient of the spring, stiffness, is determined by the sprung mass and stroke of the suspension system, and by the required dynamic performance: hard coil spring preferred by safety requirement or soft coil spring preferred by comfort concerning. The stiffness of the prototype is fixed to 18.66kN/m by compromising between safety and comfort. The length of the spring is affected by the stroke, maximum available length of the active suspension and the stiffness, the normal length is calculated as 500mm.
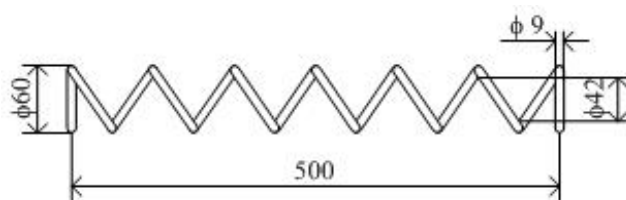
Fig. 2-5 Design of the coil spring

2.2.3 Power amplifier
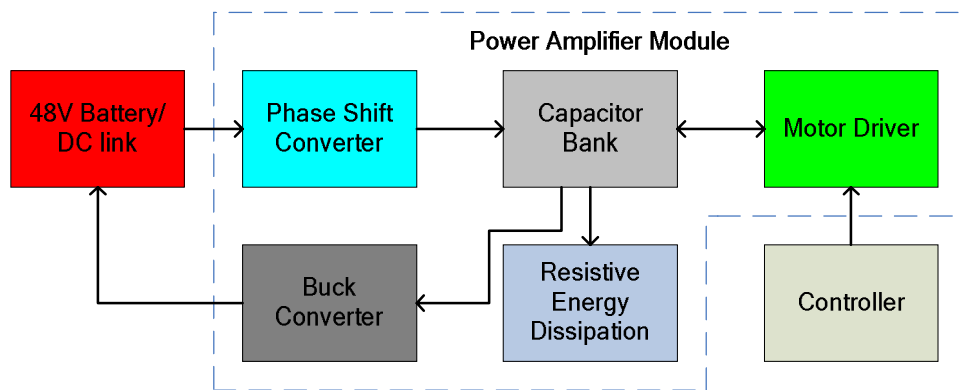
Fig. 2-6 Diagram of power amplifier

The power converter consists of the phase shift converter, buck converter, capacitor bank, resistive dissipation and motor driver. As depicted in Fig. 2-6, the phase shift converter is used to boost low battery voltage of 48V to high SRA input voltage at 150V. Then the capacitor bank is utilised to stabilise the shifted voltage and store regenerated energy through bi-directional motor driver. Regenerated energy is transferred to the battery through the buck converter. Resistive energy dissipation is installed to protect the overcharge of the capacitor bank by releasing excess stored energy.

The phase shift converter is a type of full-bridge zero-voltage-switching (ZVS) converter by applying a phase-shifting approach, which is widely used soft-switching circuit in high-power application. The switching frequency of the phase shift topology is constant, and its control method is similar to that of hard-switched topology [106], [107]. The main drawback of the phase shift converter is the loss of duty cycle. There are several methods to reduce the power loss, such as a hybrid combination of an uncontrolled half-bridge section and a phase-shift controlled full-bridge section [108], or employing a coupled inductor to achieve ZVS of the primary switches [109].
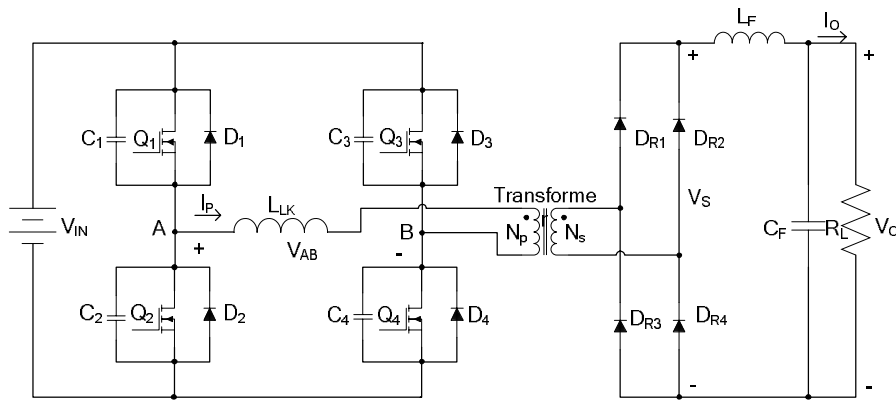
Fig. 2-7 Topology of full-bridge phase shift ZVS converter

The operating principle of basic phase shift converter is described below. The phase shifted function can be achieved by delayed switching of the lagging leg of the bridges, i.e. Q_1-Q_4 branch and Q_2-Q_3 branch. When no phase shift is occurred (0°), the voltage on the primary of the transformer is zero, and then the output voltage is zero; when maximum phase shift is occurred (180°), the voltage on the primary of the transformer is the highest, and then the output voltage is the maximum. The inductance of output filter inductor L_F is selected relatively large to store enough energy and ensure the completely discharging of parasitic capacitances C_1 and C_2, to achieve ZVS of Q_1 and Q_2 even the load is very light. On the other hand, the ZVS of Q_3 and Q_4 is ensured by completely discharging parasitic capacitances C_3 and C_4 through leakage inductance L_{LK} of the transformer. The selection of the leakage inductance highly depends on the load current and the parasitic capacitance. A ZVS range can be obtained by resonant property of the components [110], [111]. In this research, the inductances of the PFC are selected as $L_F = 250$ μH and $L_{LK} = 376$ nH.

The specified power amplifier with ZVS converter is developed in this project. In Fig. 2-8, zone A is the output filter capacitor to filter the ripple voltage from the filter inductor. Zone B is the output filter inductor, zone C is the transformer to transform the voltage, and zone D is the resonant inductor and DC blocking capacitors of the primary of transformer. Zone E is the control board used to generate pulse width modulation (PWM) signal to the phase-shifted converter, to process the signals from different parts of the whole circuit and to perform the housekeeping to the whole circuit. Finally, zone F is the circuit of the buck converter, including the output capacitor and the inductor.

Fig. 2-8 Prototype of the power amplifier

In this research, bi-directional power flow is required based on different operating statuses. The operating modes of the power amplifier alter that depends on different system statuses and environmental variables, such as road ramp and voltage of capacitor bank. When the power amplifier runs on motoring mode, the power flows into the LSRA through phase-shift converter and capacitor bank, as depicted in Fig. 2-9(a) for positive half cycle and Fig. 2-9(b) for negative half cycle of ZVS respectively. When the power amplifier changes to regenerating mode, the power flows back to the battery through capacitor bank and buck converter, as shown in Fig. 2-9(c) when the buck converter switch is on and Fig. 2-9(d) when the buck converter switch is off.
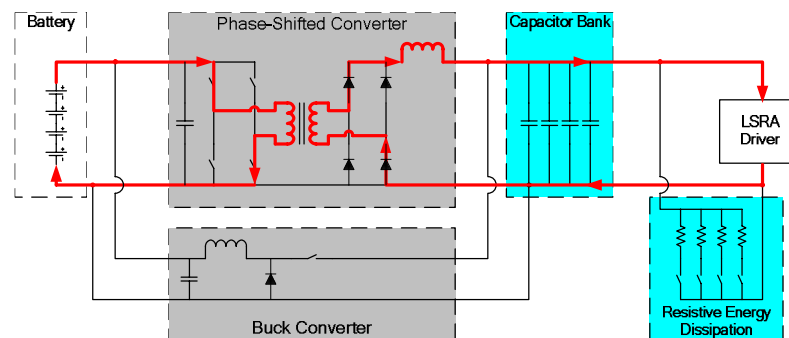
(a) Motoring mode I: positive half cycle
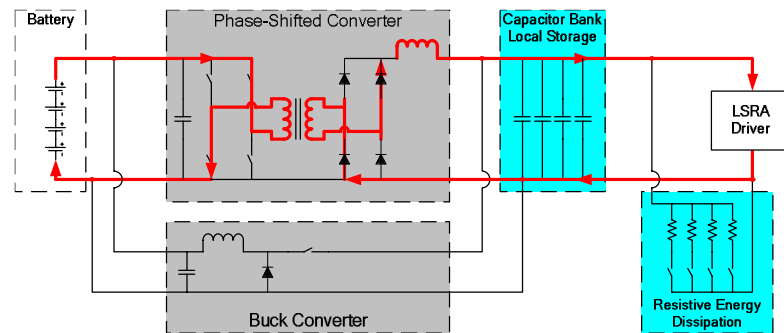
(b) Motoring mode II: negative half cycle
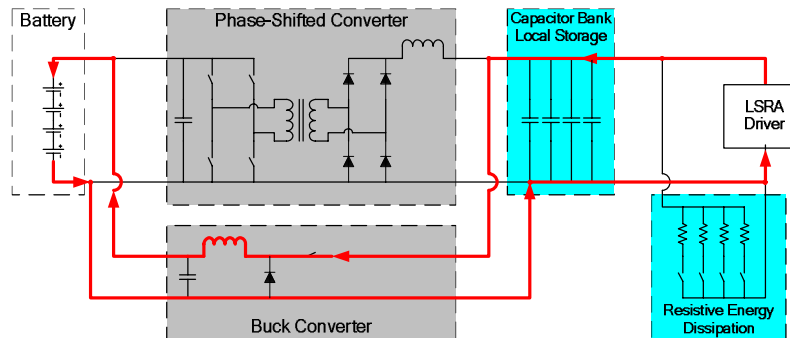
(c) Regenerating mode I: on state of buck converter
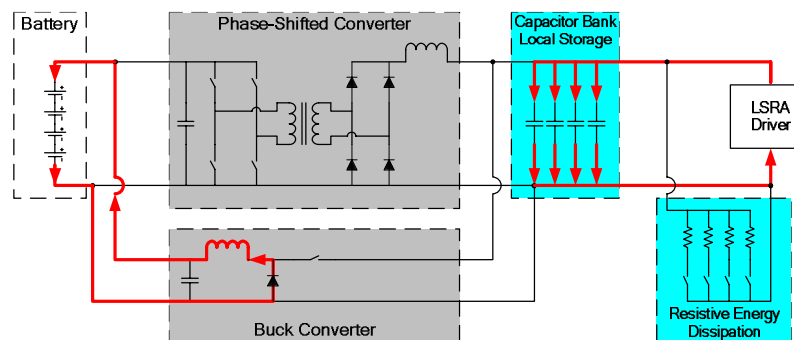
(d) Regenerating mode II: off state of buck converter

Fig. 2-9 Voltage adjusting and power flows of power amplifier

The motor driver includes four independent half-bridge switching modules to conduct the four-phase LSRA, as shown in Fig. 2-10(a). Take phase A as an example, the phase winding is connected with two terminals: A and A', as depicted in Fig. 2-10. During the normal conducting period in Fig. 2-10(b), two IGBTs Q_1 and Q_2 are switched on and the power flows from Q_1 to Q_2 to maintain the phase current in motoring mode. When the phase current is needed to decrease in chopping mode as shown in Fig. 2-10(c), Q_1 is switched off while Q_2 is kept on, the current flows through Q_2 and D_1. Once the translator is moved out of the motoring region of phase

A, the regenerating mode is active and both Q_1 and Q_2 are switched off, and the current decreases to zero and flows through D_1 and D_2, as illustrated in Fig. 2-10(d).
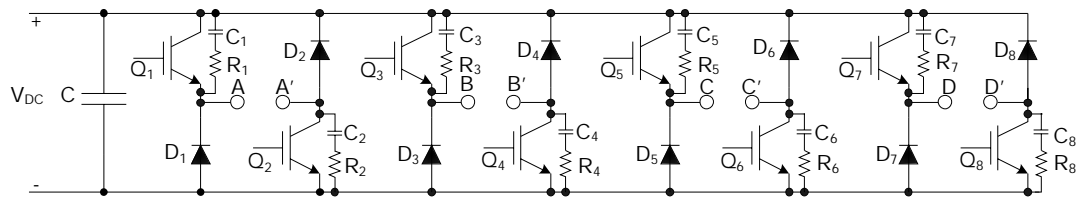
(a) Topology
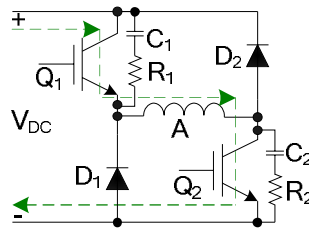
(b) Motoring mode
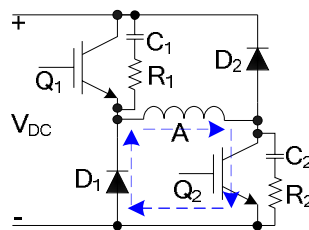
I Chopping mode
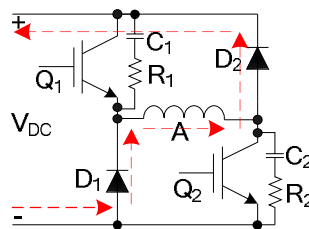
(d) Regenerating mode

Fig. 2-10 Four phase driver for LSRA

The prototype of the motor driver is shown in Fig. 2-11, includes the above discussed main driver module, also the DC-DC converter module to supply multilevel voltage and current transducer modules to measure the real time phase currents. The current transducer is selected as LTS15-NP, and the measured analogue current values are adjusted and converted to the control unit - a DSP of TI TMS320F2808.
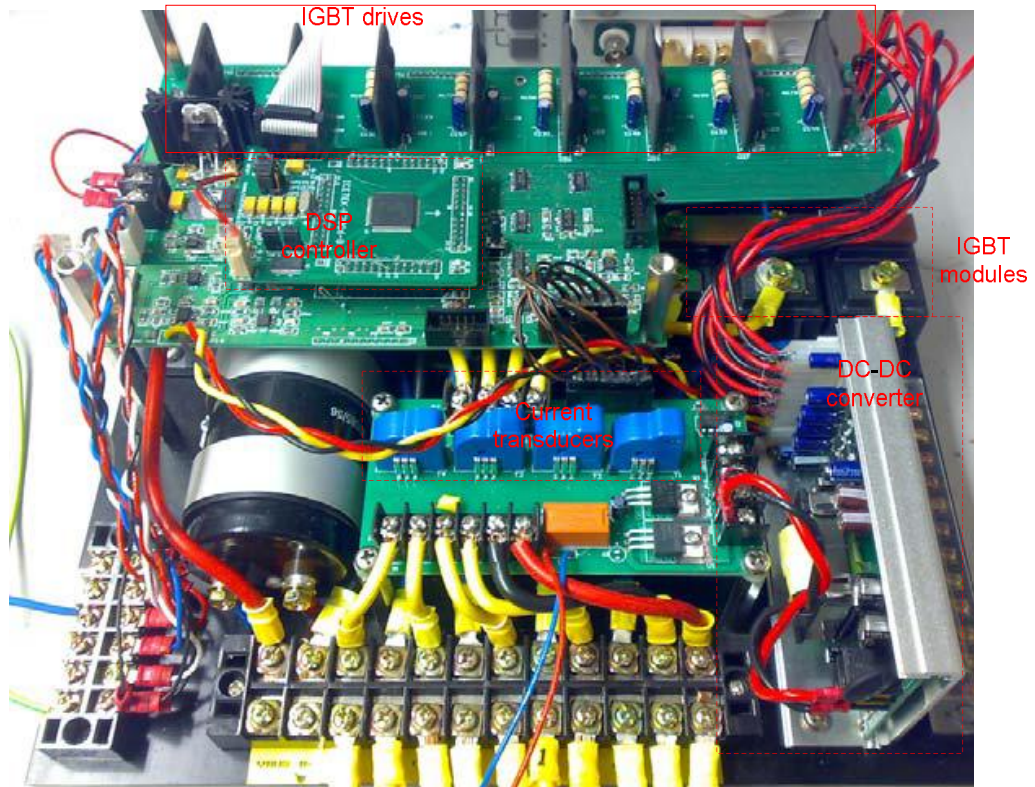
Fig. 2-11 Prototype of the motor driver combined with controller

2.3 Modelling of the active suspension system

Since the modules of electromagnetic ASS have been developed, the next step is to build a test rig for verifying the performance of the proposed ASS and then model it for investigating further control algorithms.

2.3.1 Design and fabrication of the test rig
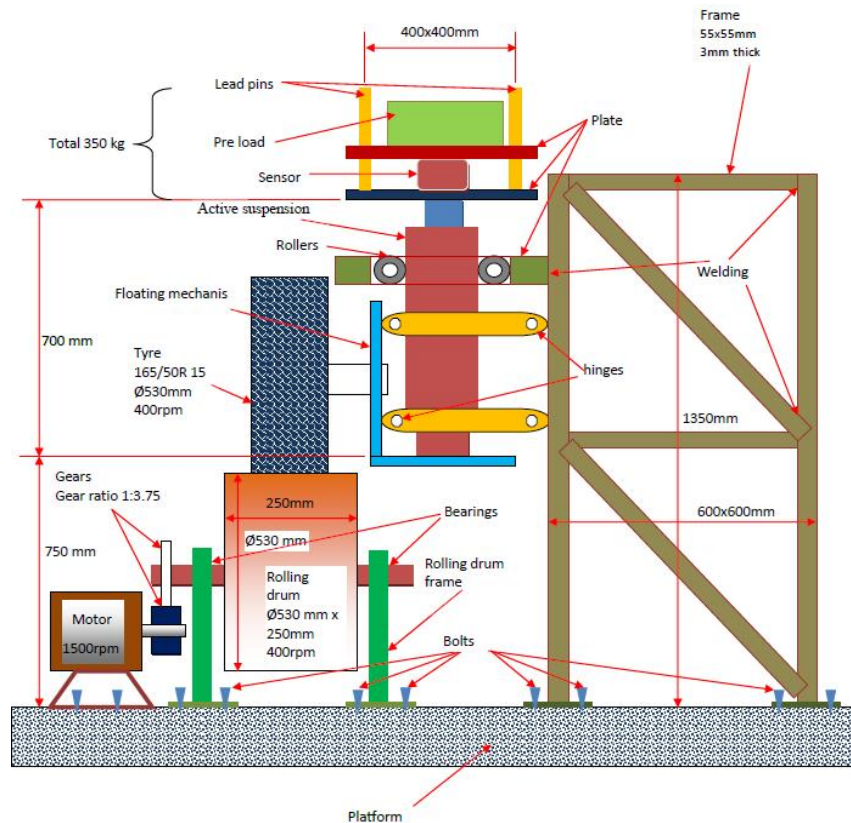
Fig. 2-12 Design of test rig

The design of test rig is sketched in Fig. 2-12, which indicates that the test rig system can be divided into two parts: frame part is used to maintain a rigid structure and mount the ASS; rolling part allows the drum moving to act as road disturbance. As shown in Fig. 2-12, the maximum sprung mass of the test rig is 350kg. Rolling part includes a tyre of 165/50R 15 as the tyre of a medium vehicle, and a rolling drum is made of steel with uneven surfaces to simulate different road conditions. An induction motor and related gearbox are used to drive the rolling drum at different speeds. More details of the parameter are shown in Fig. 2-12. A floating mechanism is mounted on the frame part and rolling part, to support the ASS and the sprung mass. An electrical

transformer, linear variable differential transformer (LVDT) is used to measure linear displacement of the suspension.

The surface of rolling drum is composed of plain plate, concave plate and convex plate to simulate the road disturbance. Each plate is one-sixth of the drum, i.e. an arc with the value of 60°.

The prototype of the test rig has been fabricated and assembled for examining the performance of the ASS and related control algorithms. Fig. 2-13 shows the test rig equipped with active suspension module. The rolling drum is driven by induction motor that is behind the rolling drum and unseen in the photo. Once the drum rolls, the tyre runs on the surface of the drum to simulate longitudinal movement of the vehicle. Uneven road surface induces vibration and oscillation to both the sprung mass subsystem and unsprung mass subsystem of the quarter-car system. Then the ASS is activated to generate force to suppress these movements and keep the sprung mass subsystem stable.
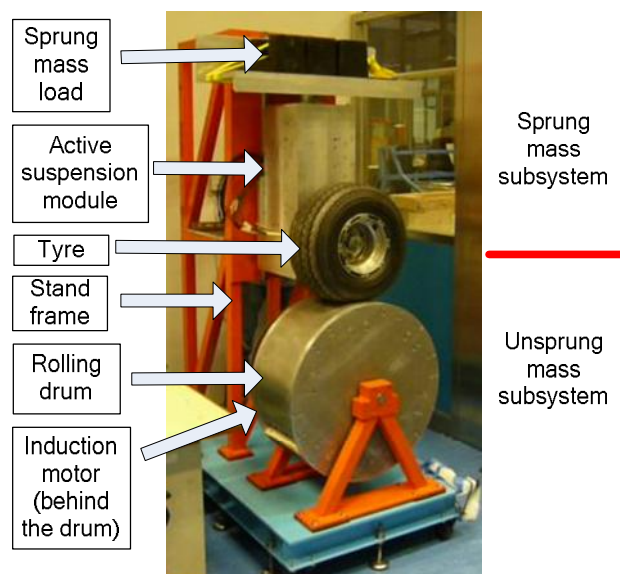
Fig. 2-13 Test rig of the quarter-car ASS

2.3.2 Modelling of the active suspension system

In view of building control algorithms, the dynamic model of the ASS must be obtained. The vehicle suspension links the chassis and the car body, and it allows a relative motion of the car body while the wheels encounter the road irregularities. Developing a model of suspension mechanism requires the knowledge of kinematics and dynamics aspects. As the ASS could be modelled as a rigid body, the principles

of Newton and Euler equations of motion can be employed to describe the dynamics of the ASS with its translational and rotational motion.

With the above hypothesis and stated principles, an ASS is modelled as follows. Vertical motions of the vehicle body can be interpreted as an interaction of road roughness and reacted movement of vehicle suspension. An important function of vehicle suspension is to keep the tyres in contact with the road. Therefore, the geometry of road and tyre should be introduced. The coil spring is a passive component and constrained by skyhook rule. The LSRA is an electrical component and has a faster response than the mechanical components, then it can be treated as a first-order force generator for simplicity.

A   *Road geometry*

Road geometry describes the shape of a road. The road surface is generally defined by a coordinate system. In the ISO 8855 standard of road vehicle dynamics [112], the forward X-axis and left Y-axis construct the Earth-fixed coordinates, and the upward Z axis denotes the ground altitude. The road surface can be presented in a form of Z(X, Y) in principle. However, the quality of the ground road is sometimes separated from the road geometry. Tyre grip and ride quality of vehicle are affected by a small-scaled road surface. To describe this situation, a conditional parameter namely road roughness is defined to measure deviations from the intended longitudinal profile of a road surface, with characteristic dimensions that affect vehicle dynamics, ride quality and dynamic pavement loading [112]-[115].

Conventionally, road profiles could be represented by Gaussian processes. In [115], a power spectral density (PSD) function is used to represent road profile and classifies road roughness. To determine the roughness of road surface, so-called PSD function, it is necessary to measure the vertical road profile with respect to a reference plane. Let n be the spatial frequency, n_0=0.1 cycles/m be the reference value, $\Omega=2\pi n$ be the angular spatial frequency and Ω_0=1 rad/m be its reference value. It is assumed that energy with the spatial frequency below 0.011 cycles/m represents landscape variability and has no effect on vehicle dynamics; when the spatial frequency excesses 2.83 cycles/m the energy is filtered out by the tyres. Therefore, the effective spectrum is constrained as [0.011, 2.83] in frequency or [0.022π, 5.66π] in angular frequency.

The general form of the fitted PSD, i.e. the roughness of the road profile, is

$$R(n) = R(n_0) \cdot (n/n_0)^{-\omega} \ or \ R(\Omega) = R(\Omega_0) \cdot (\Omega/\Omega_0)^{-\omega} \tag{2-1}$$

where ω is the waviness and is recommended to fix $\omega = 2$ by ISO 8608. Degree of roughness $R(n_0)$ or $R(\Omega_0)$ is classified by different road classes in ISO 8608. To avoid negative wavelength, a single-sided PSD is preferred, $R_{single}(\Omega)=2R(\Omega)$, for $\Omega > 0$.

Given a road segment with its length is L, a vehicle runs over it with a constant velocity υ, and then the road irregularities $z_r(t)$ can be expressed by the following series approximately [116]:

$$z_r(t) = \sum_{n=1}^{N} A_n \sin\left(n(2\pi\upsilon/L)t + \phi_n\right) \tag{2-2}$$

where the amplitudes $A_n = \sqrt{2R(n\Delta\Omega) \cdot \Delta\Omega}$ with $\Delta\Omega=2\pi/L$, the phase angles ϕ_n are random variables within $[0, 2\pi]$, wave numbers is ideal as $N \to \infty$ and sufficiently as long as hundreds in practice. Alternatively, the random road profile $z_r(t)$ can be obtained as the output of a linear filter expressed by differential equation [117], or condensed into a sequence of IRI values [114].

Theoretically, any particular Gaussian road profile can be presented in the form of (2-2). In practice, some typical types of road for simulations and physical test can be expressed by a simple way, e.g. isolated ramps, bumps, and sinusoidal roads. The ramp is a disturbance with a residual change of height, which includes simple step, linear ramp, and haversine ramp. The bump is similar to a ramp and returns to its original elevation, and the main types of bump are simple step, triangular, trapezoidal, sine half-wave, and haversine. The heights of ramps and bumps could be positive or negative, and some types of bumps are composed of two ramps. The sinusoidal road can be seems as two sinusoidal-shaped tracks with the same wavelength and arbitrary phase-shift angle. The detailed shapes of the above road profiles are referred to [118].

The road disturbances in the test rig could be categorised as positive haversine bump (convex plate) and negative haversine bump (concave plate). The haversine bump can be expressed as

$$Z = Hhav\left(\frac{2\pi X}{L}\right), 0 \le X \le L, hav(\theta) = \frac{1}{2}\left(1 - \cos(\theta)\right) \qquad (2\text{-}3)$$

In the platform of the test rig, the surface of the rolling drum is composed of plain plates and concave plates. Three isolated bumps located around the drum and formed a periodic surface as shown in Fig. 2-14.
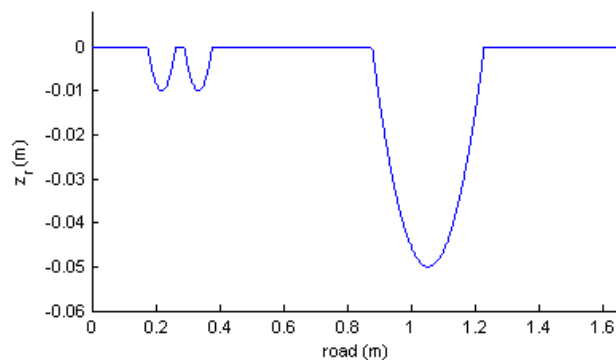
Fig. 2-14 Road profile of test rig per cycle

B   Tyre and wheel

From the viewpoint of supporting the vehicle, the model of the wheel and tyre can be simplified as a linear or nonlinear spring and a damper. The tyre-road interaction and force can be illustrated by a Cartesian coordinate frame at the centre of the tire print [12] [105]. When the tyre contacts with the road, the tyre forces coordinate is a three-dimension frame. The X-axis is along the intersection line of the tyre-plane and the ground, the Y-axis is along the right-hand side of the X-axis, and Z-axis is along the vertical line normal to the ground plane. For a quarter-car ASS, the normal force is considered; for a full-car ASS, the longitudinal forces, lateral forces and normal forces should be taken into effect.

C   Quarter-car model

Fig. 2-15 depicts a quarter-car ASS. The core components of an active suspension unit consists a passive spring and an active linear actuator connected in parallel. This configuration aids the sprung mass subsystem as well as rejects the road irregularities that the unsprung mass subsystem encounters. The elasticity can simply be adjusted by a passive linear spring with large stiffness.

The quarter-car ASS can be modelled as follows by applying force-balancing

principle:

$$\begin{cases} M_s \ddot{z}_s = -K_s\left(z_s - z_u\right) - C_s\left(\dot{z}_s - \dot{z}_u\right) + F \\ M_u \ddot{z}_u = K_s\left(z_s - z_u\right) + C_s\left(\dot{z}_s - \dot{z}_u\right) - F - K_u\left(z_u - z_r\right) \end{cases} \tag{2-4}$$

where C_s is the equivalent damper coefficient due to friction in ASS.

Table 2-1 Symbols of quarter-car ASS

Symbol	Quantity
z_s	displacement of sprung mass subsystem
z_u	displacement of unsprung mass subsystem
z_r	road disturbance
F	linear active force
M_s	mass of sprung mass subsystem
M_u	mass of unsprung mass subsystem
K_s	stiffness of sprung mass subsystem
K_u	stiffness of unsprung mass subsystem
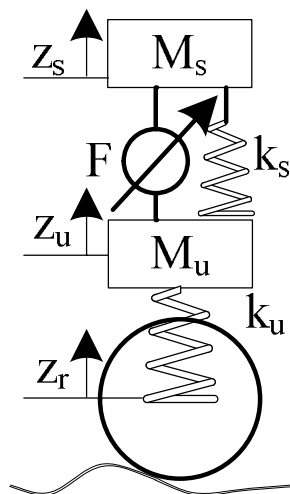
Fig. 2-15 Diagram of the quarter-car ASS

D   Full-car model

The design of the full-car ASS is similar to quarter-car type, as shown in Fig. 2-16. The ASS is divided into two parts: sprung mass part and unsprung mass part. The sprung mass part is mainly the rigid car body, which contains the seat for passengers. The goal of the suspension system is to maintain the passive suspension spring part in

a stable status and ignore the road irregularities. The unsprung mass part is connected to the sprung mass subsystem through four springs and electromagnetic actuators.
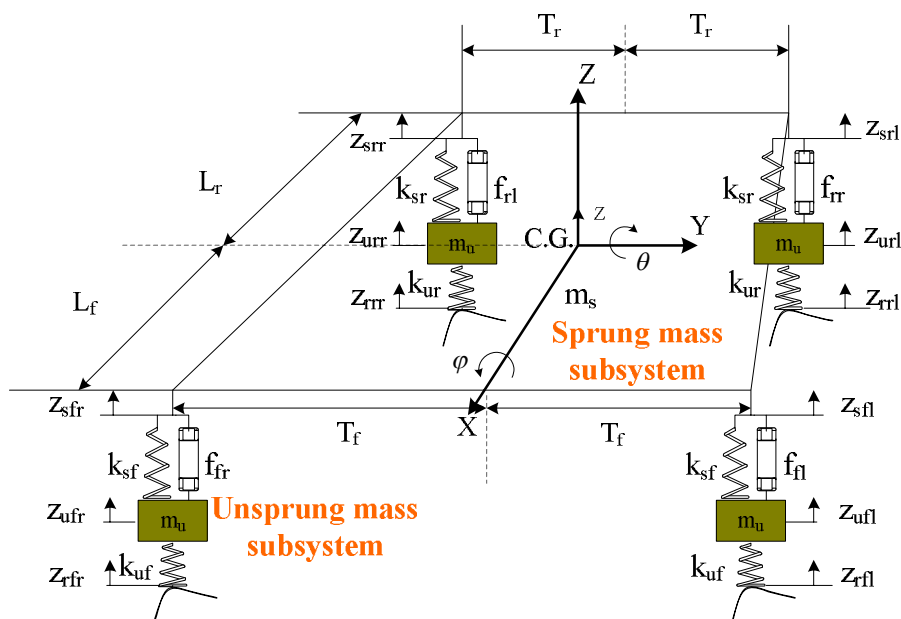
Fig. 2-16 Diagram of the full-car ASS

Table 2-2 Symbols of full-car ASS

Symbol	Quantity
z	heave position
θ	pitch angle
φ	roll angle
z_{ufl}, z_{ufr}, z_{url}, z_{urr}	displacement of four corners of unsprung mass subsystem
z_{rfl}, z_{rfr}, z_{rrl}, z_{rrr}	vertical road disturbances of four wheels
M_s	mass of sprung mass subsystem
M_u	mass of unsprung mass subsystem
K_{sf}, K_{sr}	stiffness of front and rear sprung mass subsystem
K_{uf}, K_{ur}	stiffness of front and rear tires unsprung mass subsystem
I_p, I_r	pitch and roll axis moment of inertia
L_f, L_r	distance from C.G. to the front axle and rear axle
T_f, T_r	half track width of front and rear car body
g	gravitational constant
F_{fl}, F_{fr}, F_{rl}, F_{rr}	active forces generated by electromagnetic actuators

The nonlinear model of the ASS is a 7-DOF system. Applying the principle of force and torque balance, a nonlinear model is evaluated as follows:

$$
\begin{cases}
M_s \ddot{z} = -\left(2K_{sf} + 2K_{sr}\right)z - \left(2K_{sf}L_f - 2K_{sr}L_r\right)\sin\theta + K_{sf}\left(z_{ufl} + z_{ufr}\right) + K_{sr}\left(z_{url} + z_{urr}\right) \\
\qquad - M_s g + \cos\theta\cos\varphi\left(F_{fl} + F_{fr} + F_{rl} + F_{rr}\right) \\[4pt]
I_p \ddot{\theta} = -\left(2K_{sf}L_f - 2K_{sr}L_r\right)\cos\theta \cdot z - \left(2K_{sf}L_f^2 + 2K_{sr}L_r^2\right)\cos\theta\sin\theta + K_{sf}L_f\cos\theta\left(z_{ufl} + z_{ufr}\right) \\
\qquad - K_{sr}L_r\cos\theta\left(z_{url} + z_{urr}\right) + L_f\cos^2\theta\cos\varphi\left(F_{fl} + F_{fr}\right) - L_r\cos^2\theta\cos\varphi\left(F_{rl} + F_{rr}\right) \\[4pt]
I_r \ddot{\varphi} = -\left(2K_{sf}T_f^2 + 2K_{sr}T_r^2\right)\cos\varphi\sin\varphi + K_{sf}T_f\cos\varphi\left(z_{ufl} - z_{ufr}\right) + K_{sr}T_r\cos\varphi\left(z_{url} - z_{urr}\right) \\
\qquad + T_f\cos\theta\cos^2\varphi\left(F_{fl} - F_{fr}\right) + T_r\cos\theta\cos^2\varphi\left(F_{rl} - F_{rr}\right) \\[4pt]
M_u \ddot{z}_{ufl} = K_{sf}z + K_{sf}L_f\sin\theta + K_{sf}T_f\sin\varphi - \left(K_{uf} + K_{sf}\right)z_{ufl} + K_{uf}z_{rfl} - M_u g - F_{fl}\cos\theta\cos\varphi \\[4pt]
M_u \ddot{z}_{ufr} = K_{sf}z + K_{sf}L_f\sin\theta - K_{sf}T_f\sin\varphi - \left(K_{uf} + K_{sf}\right)z_{ufr} + K_{uf}z_{rfr} - M_u g - F_{fr}\cos\theta\cos\varphi \\[4pt]
M_u \ddot{z}_{url} = K_{sr}z - K_{sr}L_r\sin\theta + K_{sr}T_r\sin\varphi - \left(K_{ur} + K_{sr}\right)z_{url} + K_{ur}z_{rrl} - M_u g - F_{rl}\cos\theta\cos\varphi \\[4pt]
M_u \ddot{z}_{urr} = K_{sr}z - K_{sr}L_r\sin\theta - K_{sr}T_r\sin\varphi - \left(K_{ur} + K_{sr}\right)z_{urr} + K_{ur}z_{rrr} - M_u g - F_{rr}\cos\theta\cos\varphi
\end{cases}
$$

(2-5)

The above nonlinear model can be linearised to (2-6), with the assumptions of: a) effective control algorithms, b) the pitch and roll angles are relative small and c) around zero-point.

$$
\left\{
\begin{aligned}
M_s \ddot{z} &= -\left(2K_{sf} + 2K_{sr}\right)z - \left(2K_{sf}L_f - 2K_{sr}L_r\right)\theta + K_{sf}\left(z_{ufl} + z_{ufr}\right) \\
&\quad + K_{sr}\left(z_{url} + z_{urr}\right) - M_s g + \left(F_{fl} + F_{fr} + F_{rl} + F_{rr}\right) \\
I_p \ddot{\theta} &= -\left(2K_{sf}L_f - 2K_{sr}L_r\right)z - \left(2K_{sf}L_f^{\,2} + 2K_{sr}L_r^{\,2}\right)\theta + K_{sf}L_f\left(z_{ufl} + z_{ufr}\right) \\
&\quad - K_{sr}L_r\left(z_{url} + z_{urr}\right) + L_f\left(F_{fl} + F_{fr}\right) - L_r\left(F_{rl} + F_{rr}\right) \\
I_r \ddot{\varphi} &= -2\left(K_{sf}T_f^{\,2} + 2K_{sr}T_r^{\,2}\right)\varphi + K_{sf}T_f\left(z_{ufl} - z_{ufr}\right) + K_{sr}T_r\left(z_{url} - z_{urr}\right) \\
&\quad + T_f\left(F_{fl} - F_{fr}\right) + T_r\left(F_{rl} - F_{rr}\right) \\
M_u \ddot{z}_{ufl} &= K_{sf}z + K_{sf}L_f\theta + K_{sf}T_f\varphi - \left(K_{uf} + K_{sf}\right)z_{ufl} + K_{uf}z_{rfl} - M_u g - F_{fl} \\
M_u \ddot{z}_{ufr} &= K_{sf}z + K_{sf}L_f\theta - K_{sf}T_f\varphi - \left(K_{uf} + K_{sf}\right)z_{ufr} + K_{uf}z_{rfr} - M_u g - F_{fr} \\
M_u \ddot{z}_{url} &= K_{sr}z - K_{sr}L_r\theta + K_{sr}T_r\varphi - \left(K_{ur} + K_{sr}\right)z_{url} + K_{ur}z_{rrl} - M_u g - F_{rl} \\
M_u \ddot{z}_{urr} &= K_{sr}z - K_{sr}L_r\theta - K_{sr}T_r\varphi - \left(K_{ur} + K_{sr}\right)z_{urr} + K_{ur}z_{rrr} - M_u g - F_{rr}
\end{aligned}
\right.
\tag{2-6}
$$

Compared with (2-5) and (2-6), two models are equivalent each other under the situation that θ and φ are varied at the neighbourhoods of zero, i.e. $\cos\theta \approx 1$, $\cos\varphi \approx 1$, $\sin\theta \approx \theta$ and $\sin\varphi \approx \varphi$.

2.4 Summary

Suspension system is used to keep the tyre in contact with the road closely and reduce the vibration of vehicle body, i.e. improve driving comfort and handling safety. The history of vehicle suspension has been outlined briefly. Passive suspension is proposed with dependent design at the beginning, and then independent type is developed to improve the ride quality and handling stability. Varying spring stiffness and damping ratio is a good choice to solve the conflict of driving comfort and steering safety, which is the inherent drawback of passive suspension. Semi-ASS is to change the damping ratio without energy injection. Once the controls of the damping ratio are well tuned, the semi-active suspensions can ensure good filtering performance and guarantee good damping of the body resonance together. In modern automotive industry, there are three main semi-active shock absorbers: solenoid-valve Electrohydraulic damper, Magnetorheological damper and Electrorheological damper. The ASS contains more electrical and magnetic components to transfer external energy into the vehicle and achieve great ride quality and car handling. There are two main types of ASSs: electro-hydraulic type and electromagnetic type. By now, commercial electro-hydraulic ASSs have been equipped in vehicle. They are all power assistive suspensions without elimination of the hydraulic subsystem. The electromagnetic ASS is under study and test for further improving and future application.

The proposed electromagnetic active suspension module includes a LSRA and its controller, a bi-directional power amplifier, a set of batteries and capacitor bank, a mechanical coil spring and related linkages. Bi-directional power flow design allows energy regeneration to improve system efficiency.

A test rig has been built to sustain the design active suspension module and verify the performance of the module. For control purpose, the models of the quarter-car and full-car ASS have been developed, including the road profile and tyre deflection.

Chapter 3 Design and Direct Drive of Linear Switched Reluctance Actuator

This chapter focuses on design and direct drive of the electromagnetic actuator of the ASS. The structure and basis theory of the switched reluctance actuator are reviewed. A prototype of LSRA is developed with specified design, and is optimized by finite element analysis. The performance of the actuator is verified by experimental testing. The direct-drive scheme of LSRA is developed for force regulating, to generate active force rapidly and sustain the sprung mass system regardless of road profile.

3.1 Review of switched reluctance actuator

LSRA is the linear design of rotary switched reluctance motor, in which the electromagnetic force is produced by the tendency of aligning its translator position to minimum reluctance and maximum flux is achieved in the magnetic flux path [96], [97], [119]. The inherent variation of phase inductance versus phase current and translator position causes the variation of force. Hence, a proper phase commutation is mandatory to maintain a constant force output and stabilises the translator position.

3.1.1 Characteristic of phase inductance

Adapting to the dynamic characteristic of phase inductance is the essential design criteria of LSRA. Along with the movement of translator, the phase inductance value varies periodically. As depicted in Fig. 3-1, the phase inductance reaches its minimum value L_{min} in which the translator poles are fully unaligned with the stator poles. When the translator moves to the aligned position, the phase inductance increases and reaches its maximum value L_{max} at the fully aligned position. In this research, the interaction during phase commutation has little contribution to the overall dynamic, and hence the mutual inductance is neglected.

There are four remarkable points per period for phase A. x_{a1} is the point leaves the fully unaligned position; x_{a2} is the point reaches the fully aligned position; x_{a3} is the point leaves the fully aligned position; and x_{a4} is the point reaches the fully unaligned position. These points are related to the actuator geometry, such as the stator and translator pole widths, phase numbers, and pole numbers. The relationship is presented as follows:

$$
\begin{cases}
x_{a2} - x_{a1} = x_{a4} - x_{a3} = \min(w_{sp}, \quad w_{tp}) \\
x_{a3} - x_{a2} = \left| w_{sp} - w_{tp} \right| \\
x_{a1}^{'} - x_{a1} = \tau_t = w_{sp} + w_{tp} \\
x_{b1} - x_{a1} = \sigma = \dfrac{\tau_t}{N_{ph}}
\end{cases}
\tag{3-1}
$$

where w_{sp} and w_{tp} are the stator and translator pole widths, τ_t is the translator pole pitch, σ is the stroke, and N_{ph} is the number of phases. As shown in Fig. 3-1, a positive force is generated with increasing inductance while a negative force is developed with decreasing inductance.
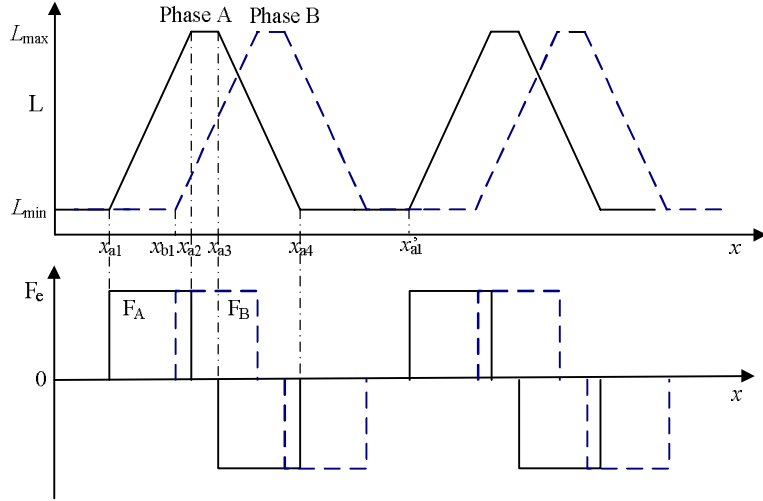
Fig. 3-1 Dynamic of phase inductance of LSRA

3.1.2 Electrical force

Since the mutual inductances of LSRA are neglected, an equivalent circuit for an independent phase can be used to analyse the dynamic performance. As depicted in Fig. 3-2, when DC voltage V is applied to phase winding, the current i flows through the phase resistance R and the phase inductance L to generate flux linkage λ, and the induced back electromagnetic field (EMF) e_a, the voltage equation is

$$V = Ri + \frac{d\lambda}{dt} = Ri + L\frac{di}{dt} + e_a = Ri + L\frac{di}{dt} + v_a i \frac{dL}{dx_a} \qquad (3\text{-}2)$$

where x_a and $v_a = \frac{dx_a}{dt}$ is the position and speed of the translator, respectively.
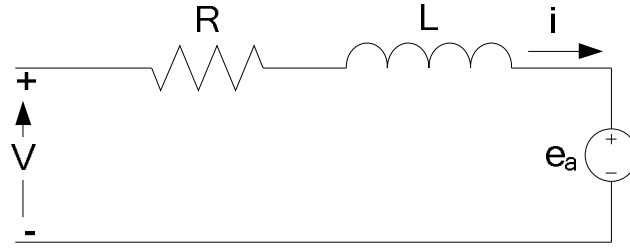
Fig. 3-2 Equivalent circuit for one phase in motoring mode

The input electrical power can be obtained by multiplying phase current i on both side of (3-2)

$$P = Vi = Ri^2 + Li\frac{di}{dt} + vi^2\frac{dL}{dx_a} \tag{3-3}$$

The rate of change of magnetic stored energy can be derived by

$$\frac{d}{dt}\left(\frac{1}{2}Li^2\right) = \frac{1}{2}i^2\frac{dL}{dt} + Li\frac{di}{dt} = \frac{1}{2}vi^2\frac{dL}{dx_a} + Li\frac{di}{dt} \tag{3-4}$$

Therefore, the mechanical power can be obtained by subtracting the power loss of the resistance and the rate of magnetic stored energy from the input power. In another side, the mechanical power is the product of electrical force and speed. Hence, the electromagnetic force can be calculated from (3-3) and (3-4), i.e.

$$F_e = \frac{1}{2}i^2\frac{dL}{dx_a} \tag{3-5}$$

From (3-5), the sign of F_e is determined only by the rate of change of inductance versus position, which is illustrated by Fig. 3-1.

3.1.3 Energy conversion principle

For LSRA, the energy is stored in the air gap and changed to mechanical power output by changing the displacement. The dynamic performance of LSRA is determined by the energy conversion procedure within one stroke, i.e. from unaligned position to aligned position.

The energy conversion of one phase is depicted in Fig. 3-3, using the magnetization curve to illustrate the relationship of flux linkage λ versus current i under a particular position. The zone of magnetization curves is within the area of OUAO, with the boundary of OU for unaligned position and OA for aligned position. From the graph below, the stored energy W_f and co-energy W_c are expressed as

$$W_f = \int i d\lambda \tag{3-6}$$

$$W_c = \int \lambda di = \lambda i - W_f \tag{3-7}$$
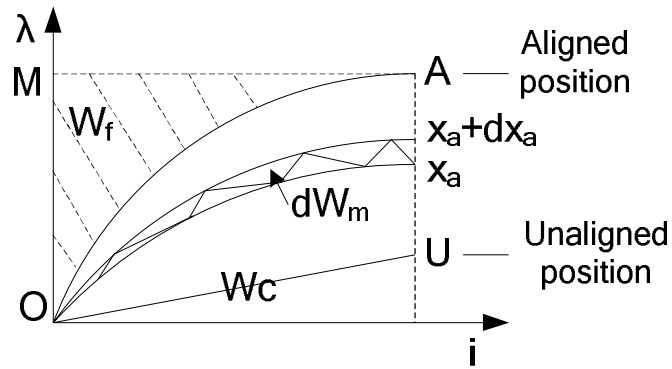
Fig. 3-3 Graphical depiction of energy conversion

By neglecting the transfer power loss, the input electrical energy W_e can be divided into two parts, namely the stored magnetic field energy W_f and the mechanical power W_m,

$$W_e = W_f + W_m \tag{3-8}$$

The total output mechanical power is the area of {OUAO} [96], [97], [119].

To evaluate the electromagnetic force, incremental analysis method is used to calculate the force F_e. Assuming that an electromagnetic force F_e drives the translator moves from x_a to $x_a + dx_a$, the mechanical work is

$$dW_m = F_e dx_a \tag{3-9}$$

From the above equations, we have

$$dW_f = dW_e - dW_m = id\lambda - F_e dx_a \tag{3-10}$$

Substituting (3-10) into (3-7)

$$dW_c(i, x_a) = \lambda di + F_e dx_a = \frac{\partial W_c(i, x_a)}{\partial i} di + \frac{\partial W_c(i, x_a)}{\partial x_a} dx_a \tag{3-11}$$

It can be observed from (3-11) that

$$\lambda = \frac{\partial W_c(i, x_a)}{\partial i} \tag{3-12}$$

$$F_e = \frac{\partial W_c(i, x_a)}{\partial x_a} \tag{3-13}$$

It is reasonable in motoring mode to consider the current i as a constant value during incremental movement, the calculation of electromagnetic force F_e can be simplified from (3-13) to (3-5).

3.2 Design of the LSRA

The performance of the active suspension is mainly determined by the LSRA to achieve riding comfort and handling safety over different road profiles and steering status. The demanded electromagnetic force and stroke of the LSRA depend on the car body weight, affordable load, and external road disturbance. Vehicle's vibration is the most important perception for passengers and is a critical factor of driving safety. Research on the evaluation of human exposure to the vertical vibration has been presented in the report of ISO 2631. It has verified that the acceptable vibration magnitudes for human vary with the duration and type of activities [120].

  Stroke of the LSRA equals the maximum relative travel distance between the sprung mass unit and unsprung mass unit of the vehicle. The stroke value is determined by the requirement to absorb the external disturbances and to smooth the pitch and roll motion. Vertical movement of the vehicle should not exceed the stroke to ensure passengers safety. In light of the high degree of protection, stroke should be long enough to guarantee the function of suspension system. In the following paragraphs, the significance of sufficient stroke in a suspension system is investigated.

  Compromise between actuator size and output electromagnetic force has been considered in the design stage of LSRA. An optimal control method LQR is used to identify the parameters of actuator. In [121], sprung mass acceleration is used to verify the performance of LSRA with different parameters under severe working points, i.e. natural frequencies of suspension system. To constraint the acceleration within $[-10\text{m/s}^2, 10\text{m/s}^2]$, the required peak force is 1000N under external road disturbance with 10rad/s frequency and the required continuous force is 500N under external road disturbance with frequency 100rad/s.

Table 3-1 Optimal Design Requirements of LSRA

Parameters	Value
Peak Force	1000N
Continuous Force	500N
Stroke	±50mm
Maximum Speed	1m/s
Maximum Volume	300mm×300mm×600mm

The optimal result, which is specified in Table 3-3, satisfies the requirement of a medium size vehicle based on "reduced comfort boundary" [9].

3.2.1 Structure

The LSRA design consists of four identical double-sided actuator modules, as shown in Fig. 3-4. Fig. 3-4(a) shows the configuration of double-sided module, which is constructed of four phases with eight pairs of stator poles and eight translator poles. The absence of excitation windings and back iron reduces the translator weight considerably. Double-sided structure enhances the force density [97] compared with single-sided configuration and eliminates the unbalanced lateral forces. Hence, four identical double-sided LSRA modules are rotation-symmetrically arranged in a highly compact way that is depicted in Fig. 3-4(b). In each module, the translators are connected through a hollow shaft where the spring is to be placed to form a single structure. High propulsion force can be achieved with four parallelly energized modules. The lateral forces generated by both sides of the stator are well-eliminated by construction geometry. The lateral force balance assists in reducing the acoustic noise during the operation. Lastly, this configuration offers better heat dissipation with good thermal contact between the coil and the actuator frame, which consequently enhances the overload capability of LSRA.

The number of phases of LSRA is determined at the beginning of the design procedure. Higher number of phases can smooth the output force ripples and obtain higher power density, at the price of higher cost of the LSRA drive due to increase in power switching devices and electrical transducers. In the present design, four-phase LSRA is selected to alleviate the force ripple and maintain the reliability and simplicity.

The number of stator poles is fixed as two times of the number of phases, i.e. eight stator poles. Unlike the rotary case, the number of translator poles in LSRA is unrelated to the number of stator poles, but it is related to the stroke of the system. The effective range of single phase is 12mm (without overlapping) due to the configuration of the stator poles. Hence, at least eight translator poles are equipped to ensure the movement of translator from -50mm to 50mm, which governs the total length of the stroke.

(a) Double-sided module

(b) Cross-section

Fig. 3-4 Configuration of the LSRA

The stator and translator pole width, which are denoted by w_{sp} and w_{tp} respectively. The selection of two parameters values affects the average force and force ripple accordingly that is critical in LSRA design. These parameters follow the constraints derived by [122] and [123]:

$$\begin{cases} \dfrac{l}{N_{ph}N_{tp}} < w_{sp} < \dfrac{\left(N_{ph}-2\right)l}{N_{ph}N_{tp}} \\[3mm] \dfrac{l}{N_{ph}N_{tp}} < w_{tp} < \dfrac{\left(N_{ph}-1\right)l}{N_{ph}N_{tp}} \\[3mm] w_{sp} \le w_{tp} \end{cases} \qquad (3\text{-}14)$$

where l is the stator length, N_{ph} is the number of phases and is greater than 2, and N_{tp} is the number of translator poles. Alternatively, the above constraints can be illustrated by a feasible triangle [122]. Besides, the stator pole pitch is fixed and winding area is related to the magnetic motive force (MMF) which is fixed for required electromagnetic force. Then the stator pole width w_{sp} has the positive relationship with the stator length that is restricted by the suspension volume.

Both the stator and translator pole widths affect the LSRA performance, including average force, force ripple and average force per core volume. These effects are analysed and used for parameter optimization through 2-D FEA. The detailed discussion of these effects is addressed by [121]. The conclusion is summarised as follows: 1) increasing of stator pole width increases the average force and reduces force ripple significantly, while the variation of translator pole width has little effect. 2) the average force per core volume decreases with the increase of stator pole width.

The objective of LSRA design is to achieve high average force, low force ripple, and high force density for the application of active suspension. Based on above analysis, variations of stator and translator pole width have different impacts on these parameters. Thus, multi-objective optimization procedure has been conducted by importing a weighted multi-objective function to minimise the force ripple, maximise the average force, and force density. Furthermore, the volume of LSRA should be reasonable for the space constrain of the active suspension unit due to the installation between the vehicle body and wheel.

The optimal value of stator and translator pole widths with different volume limitations of active suspension unit is listed in Table 3-2. The optimal result illustrates that the suspension volume affects the preliminary design of LSRA. It can be observed that the average forces of three pole width pairs are similar, and the smallest suspension unit achieves the highest force density and is more suitable for industry application. Therefore, the optimal pole widths are selected as $w_{sp} = 13mm$, $w_{tp} = 17mm$. The force ripple issue can be alleviated by force control with force distribution factor.

Table 3-2 Optimal Pole Widths under Different Volume Constrain

Volume Constrain	w_{sp}	w_{tp}	Average Force	Force Ripple	Force Density
300mm×300mm×600mm	16mm	17mm	609N	27.9%	135190N/m^3
270mm×270mm×600mm	15mm	19mm	592.5N	34.3%	148299N/m^3
250mm×250mm×600mm	13mm	17mm	551.6N	43.7%	167927N/m^3

The determination air gap g_a is independent of other parameters, and the inverse $\dfrac{1}{g_a}$ is proportional to the average force and efficiency [124]. Hence, the air gap should be selected as the minimum value available in manufacturing. Moreover, the uniformity of air gap must be guaranteed to eliminate the lateral force.

The parameters of LSRA are ruled by the geometry illustrated in Fig. 3-4:

$$
\begin{cases}
\tau_s = w_{sp} + w_{ss} \\
\tau_t = w_{tp} + w_{ts} \\
l = 7\tau_s + w_{sp} = 8w_{sp} + 7w_{ss} \\
b_s = w_{sp} \\
w = 2\left(b_s + h_s + g_a\right) + h_t \\
D \geq w + l_s + 2w_c \\
A_c = w_c h_c
\end{cases}
\tag{3-15}
$$

where τ_s and τ_t are the stator and translator pitch, w_{ss} and w_{ts} are the slot width of stator and translator, l and l_s are the length of stator and stack, b_s is the thickness of stator back iron, h_s and h_t are the pole height of stator and translator, w and D are the width of double-sided module and whole actuator, w_c, h_c and A_c are the winding width, height and area, respectively.

3.2.2 Magnetic circuit analysis

The flux linkage is the key factor to analyse the characteristics of LSRA from the principle of energy conversion and voltage equation. Thus, the flux linkage is an important tool in the design of proposed LSRA. Since the flux linkage is the product

of inductance and current, the phase inductance is calculated with different current values to predict the characteristics of the LSRA.

There are two methods to analyse the flux linkage behaviour. They are magnetic circuit analysis (MCA) and finite element analysis (FEA). MCA is an analytical calculation method to estimate the flux linkage in a magnetic circuit. By ignoring the nonlinearity and saturation, the actuator characteristics can be expressed analytically by design variables based on the specified geometrical structure. MCA is a faster method to obtain the flux linkage than FEA, and the acquired accuracy is satisfactory in primary design. Furthermore, FEA is applied to optimise the design variables in a more accurate way by considering the magnetic nonlinearity and saturation. Combination of MCA and FEA provides a fast and reliable way for LSRA design.
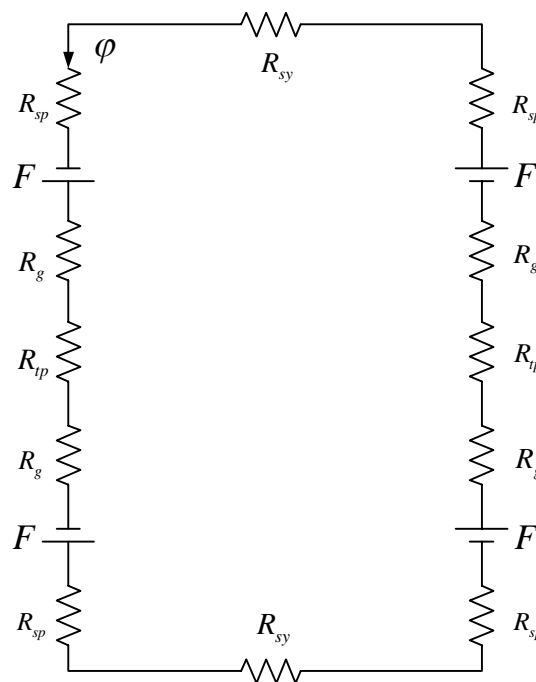
(a) Original circuit
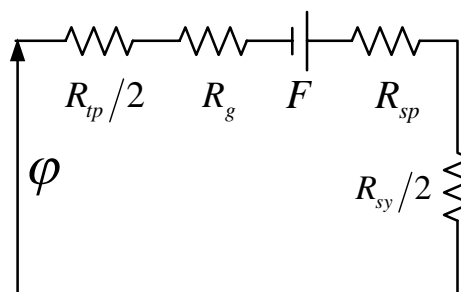
(b) Simplified circuit

Fig. 3-5 Magnetic equivalent circuit for double-sided LSRA

The principle of MCA is to find out the distribution of magnetic flux paths for each translator position, and the total inductance is the sum of each flux path's inductance calculated by Ampere's circuital law. The inductance of each path is calculated based on the magnetic equivalent circuit depicted in Fig. 3-5. In the magnetic equivalent circuit of double-sided actuator, each segment is represented by its corresponding reluctance R and magnetomotive force (MMF) F_m, as shown in Fig. 3-5(a). For the symmetry of the topology, the equivalent circuit can be simplified to Fig. 3-5(b).

The reluctance of each segment can be calculated from the magnetic circuit's permeability μ, effective length l and area A. The reluctances of the stator pole (denoted subscript $_{sp}$), translator pole (denoted subscript $_{tp}$), stator yoke (denoted subscript $_{sy}$) and air gap (denoted subscript $_g$) are given by:

$$\begin{cases} R_{sp} = \dfrac{l_{sp}}{\mu_{sp} A_{sp}} = \dfrac{H_{sp}}{B_{sp}} \dfrac{l_{sp}}{A_{sp}} \\[3mm] R_{tp} = \dfrac{l_{tp}}{\mu_{tp} A_{tp}} = \dfrac{H_{tp}}{B_{tp}} \dfrac{l_{tp}}{A_{tp}} \\[3mm] R_{sy} = \dfrac{l_{sy}}{\mu_{sy} A_{sy}} = \dfrac{H_{sy}}{B_{sy}} \dfrac{l_{sy}}{A_{sy}} \\[3mm] R_g = \dfrac{l_g}{\mu_g A_g} \end{cases} \tag{3-16}$$

where B denotes flux density and H denotes magnetic field intensity.

The flow chart for estimation the inductance through iterative method is described in Fig. 3-6. When the phase current I flows through the N turns winding, an MMF F_{mk} is generated. Assuming an initial stator pole flux ϕ_{sp_k} presents in magnetic flux path k, the corresponding l_{j_k} and A_{j_k} of segment j are calculated. Then, the flux densities B_{j_k} of segment j are

$$B_{B_{j\_k}}(i,x) = \frac{\phi_{sp\_k}}{A_{B_{j\_k}}} \tag{3-17}$$

The corresponding magnetic field intensity H_{j_k} is obtained using the B-H curve. Then, the applied MMF F_{mc_k} can be calculated by summing up the MMF of each segment. The error MMF ΔF_{mk} is obtained to adjust the flux ϕ_{sp_k}. These procedures are carried out iteratively until ΔF_{mk} is less than the predefined value.

$$\Delta F_{mk} = F_{mk} - F_{mc\_k} = F_{mk} - \sum_{j} H_j l_j < \varepsilon \tag{3-18}$$
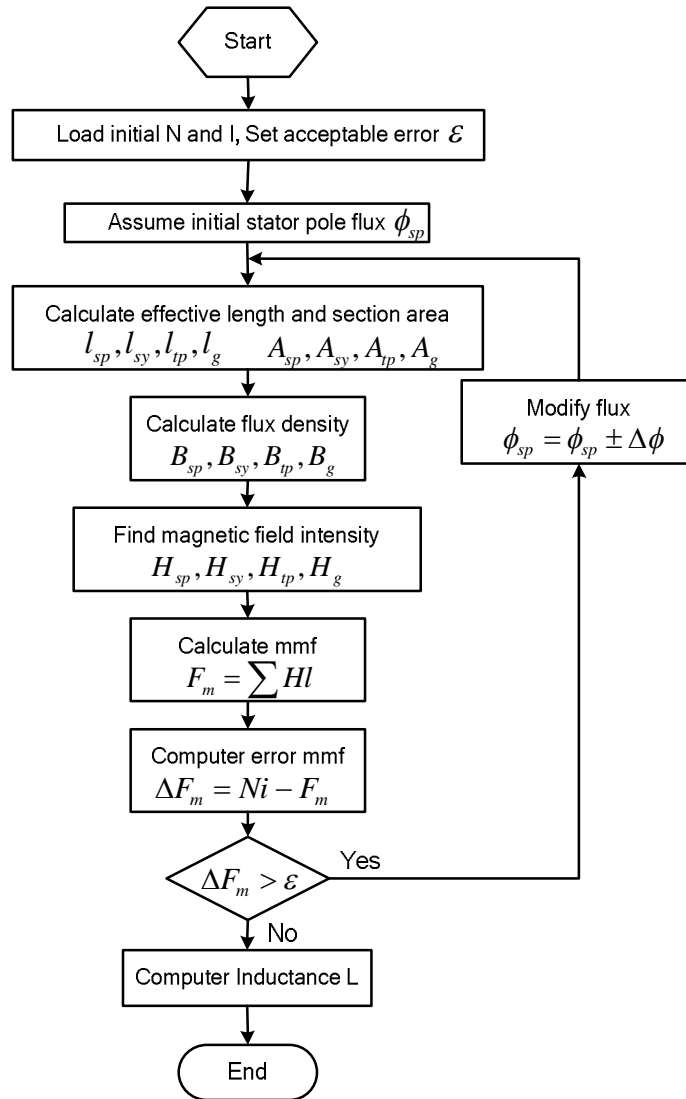
Fig. 3-6 Flow chart of inductance calculation

When the iterative calculation is finished, the flux linkage ϕ_{sp_k} of the path k is obtained, and then the inductance L_k of the path k can be calculated. All the path

inductances can be calculated by repeating the above iterative procedures, and the phase inductance L is the sum of inductance of each path. By exploring each position per period, the inductance characteristics can be obtained.

$$L_k = \frac{N\phi_{sp\_k}}{I} \tag{3-19}$$

$$L = \sum_k L_k \tag{3-20}$$

3.2.3 Design procedure

The objective of this section is to design the proposed LSRA meeting the requirements of force and dimensions listed in Table 3-1. The selection of actuator variables is constrained by (3-14) and (3-15). Fig. 3-7 describes the procedure of LSRA design. The inductances at unaligned position and aligned position can be calculated by the methods illustrated in Fig. 3-6. Once the characteristics of flux linkage are estimated, the force can be calculated by solving (3-12) and (3-13). Similar to the calculation of inductance, the design procedure is an iterative process until the required force is obtained.

Furthermore, the performance of the designed LSRA is verified by FEA with considering the nonlinearity and saturation, such as longitudinal and transversal end effects. The designed variables are well tuned to fulfil the requirements. The optimised values of design variables parameters are listed in Table 3-3. The average force, force ripple and force density of the proposed LSRA are listed in Table 3-2. A prototype of LSRA is fabricated to verify the performance in next section.
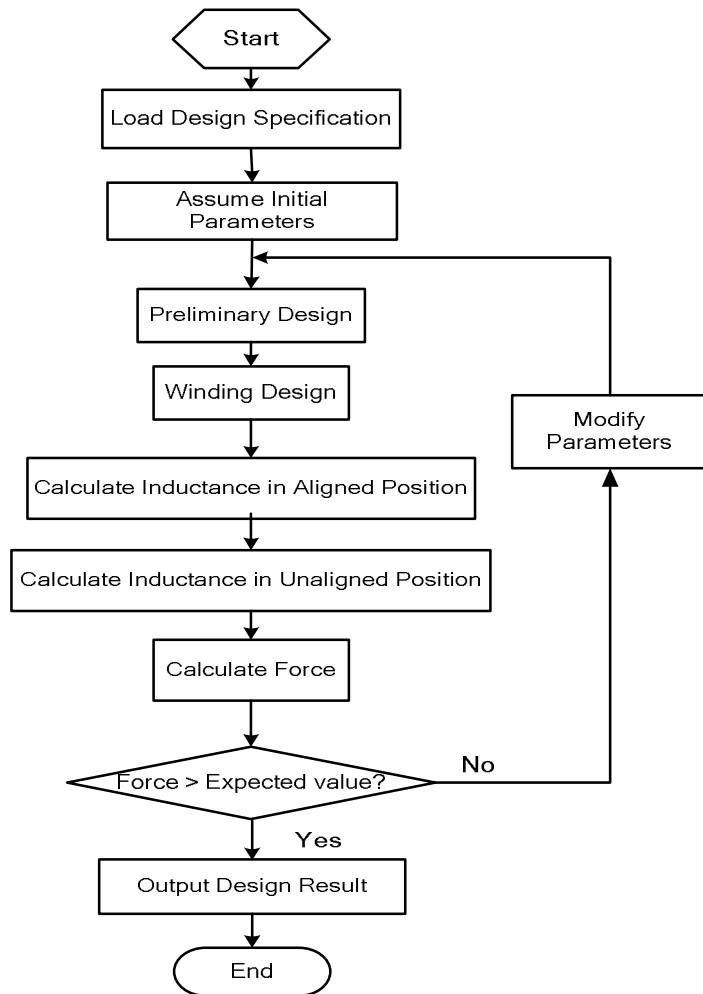
Fig. 3-7 Flowchart of design procedure

Table 3-3 Design Specification of the LSRA

Quantity	Value	Quantity	Value
Number of modules	4	DC-link voltage	200 V
Number of phases per module	4	Nominal current	10 A
Number of stator poles per module	16	Peak transient power	4.8 kW
Number of translator poles per module	8	Stroke	96 mm
Stator pole pitch	36 mm	Nominal force	500 N
Translator pole pitch	48 mm	Peak force	1000 N
Stator pole width	13mm		
Translator pole width	17 mm		
Stator pole height	49 mm		
Stator yoke thickness	13 mm		
Stack length	43 mm		

3.3 Dynamic performance of the LSRA

3.3.1 Prototype of the LSRA

A prototype of LSRA is fabricated to verify the design with the optimised parameters of third combination listed in Table 3-2. As illustrated in Fig. 3-8, the stator of the LSRA unit is composed of four modules, and four translator modules are mounted on the shaft to achieve upward and downward movements. The dimension of the outer rectangle frame is 250mm×250mm×600mm, which is the smallest volume among the optimization results.
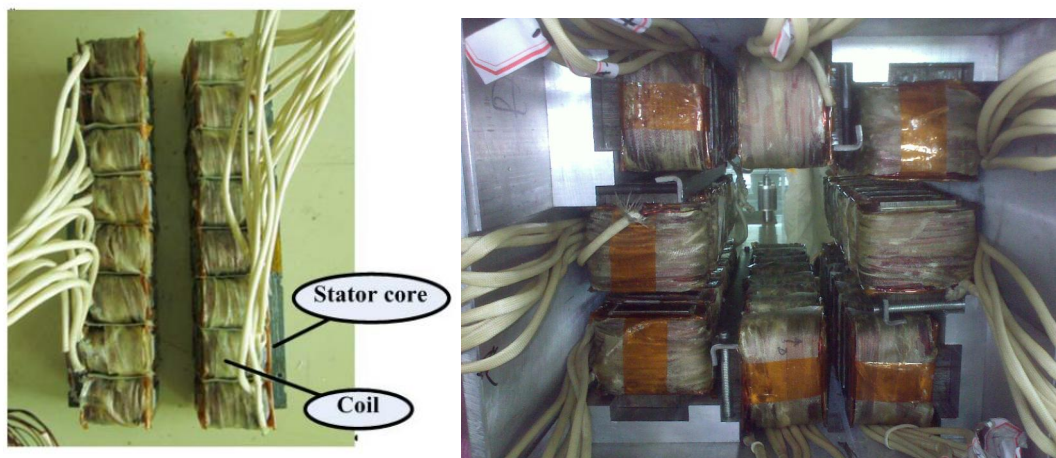
(a) Stator (left: module, right: whole unit)

(b) Translator mounted on shaft
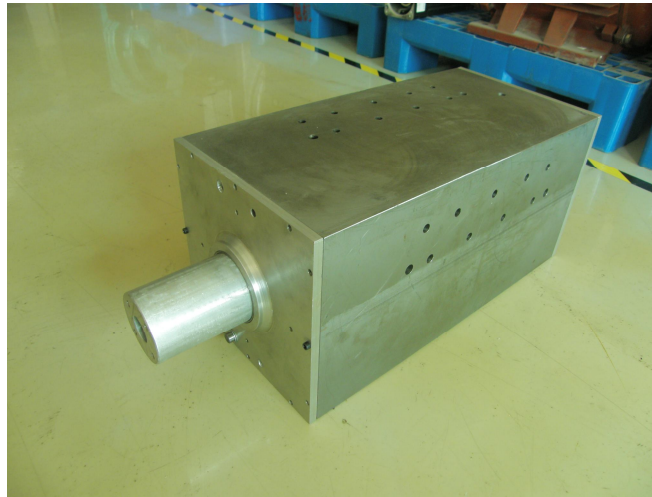
(c) Assembly with frame and covers

Fig. 3-8 Fabrication of the proposed LSRA

3.3.2   Computed characteristics

The characteristics of the proposed LSRA are obtained by FEA to determine the performance of the design optimization. Parts of the flux linkage curve and active force curve are shown in Fig. 3-9 and Fig. 3-10. The minimum flux linkage appears at the unaligned position $x = 0$mm and the maximum flux linkage is obtained at the aligned position $x = 24$mm . From Fig. 3-10, the active force reaches the nominal value 500N while the current is 10A, and the peak force is greater than 1000N when the current is raised by 16A.
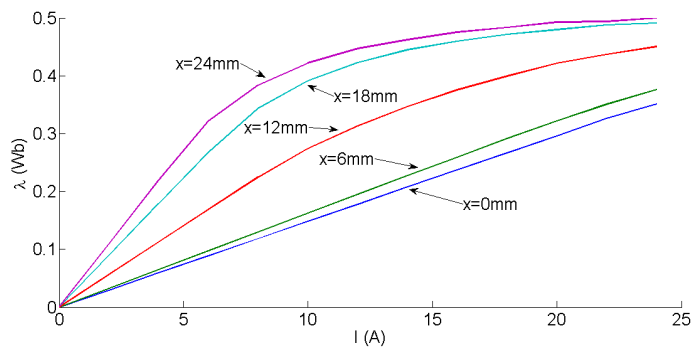
(a) Flux v.s. current
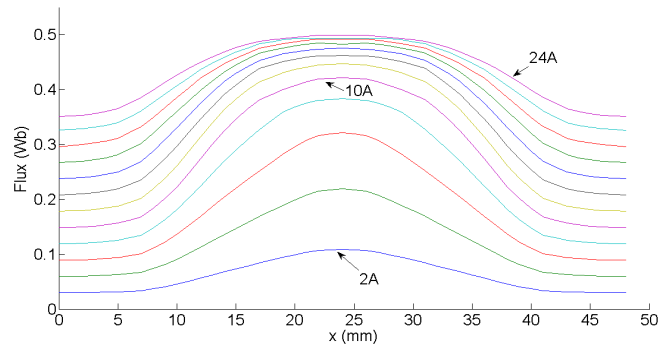
(b) Flux v.s. position

Fig. 3-9 Flux linkage of the LSRA by FEA
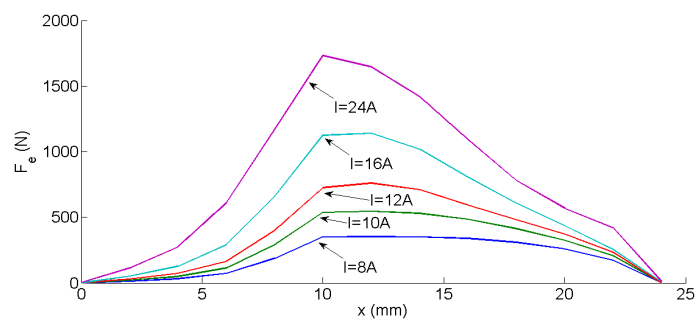
Fig. 3-10 Electromagnetic force of the LSRA by FEA

3.3.3   Experimental characteristics
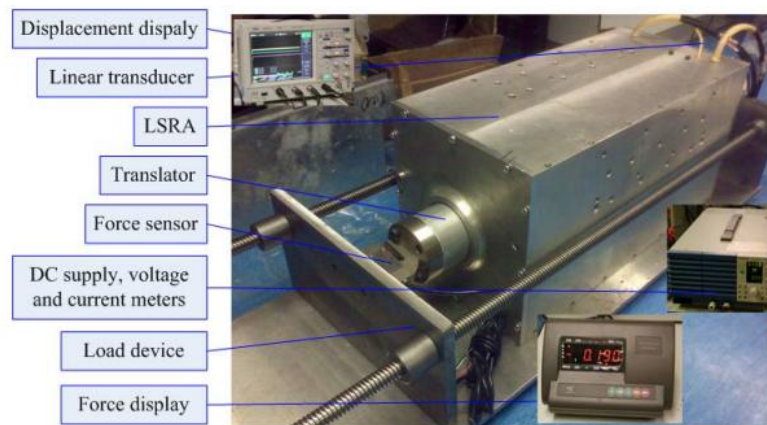
Fig. 3-11 Test platform for force measurement

In order to verify the performance of the LSRA, an experiment system is built up to test the static characteristics of flux linkage and force. The electromagnetic force can be measured by the force sensor directly, as shown in Fig. 3-11. The excitation current is provided by current meters of DC supply, and the translator movement is measured by the LVDT.

The accuracy of the LSRA profiles depends on the accuracy of the transducers, and the precision is determined by the test intervals of the excitation current and translator movement. Smaller interval leads to a more precise profile at the price of more delicate measurement and computation burden. To obtain adequate precision while minimise the measurement workload, the test intervals are selected as 2mm for translator movement and 1A for excitation current.

The experimental results of flux linkage and active force are illustrated in Fig. 3-12 and Fig. 3-13, respectively. The measurement of four-phase force is implemented whilst the excitation current rises up to 24A. By comparing with the computed results and the experimental results, it can be conducted that the force error between two results is almost less than 10%, especially for the design range from 0N to 1000N. The discrepancy is due to manufacturing and measurement error.
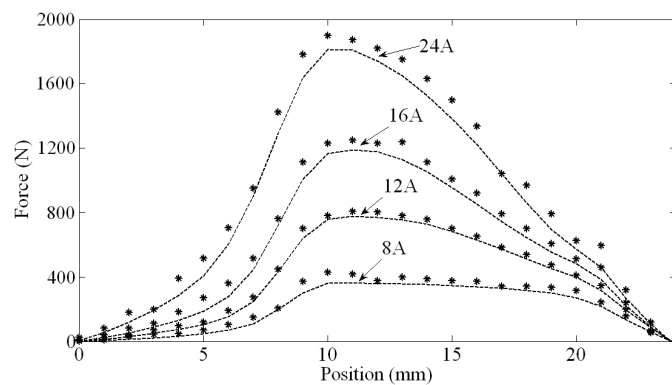
Fig. 3-12 Comparison of FEA and measured force profile
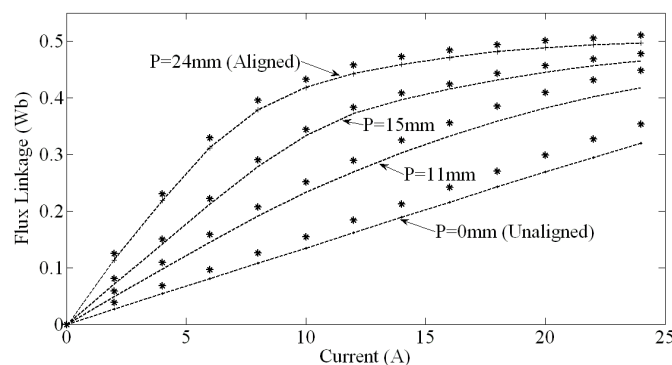
Fig. 3-13 Comparison between computed and actual flux linkage

(Note: dotline denotes measured data and solid line denotes FEA data)

3.4 Direct force control of the LSRA

The dynamic behaviour of the ASS can be regarded as the combination of two dynamics according to different time responses: fast electromagnetic force generation and slow mechanical movement. It is reasonable to suppose that the step response of the electromagnetic behaviour can be achieved during the implementation interval of the mechanical movement [125]. Therefore, a two-time-scale strategy [126], [127] is used for modelling analysis and controller design for the ASS.

The force control of the LSRA is discussed in this section. Recall the voltage equation, the dynamic of the LSRA prototype can be expressed as

$$u_j = R_s i_j + \frac{d\lambda_j}{dt} = R_s i_j + L_j \frac{di_j}{dt} + v_a i_j \frac{dL_j}{dx_a}, \; j = a, b, c, d \qquad (3\text{-}21)$$

where u_j and i_j is phase voltage and phase current, R_s and L_j is phase resistance and inductance, respectively, $\lambda_j = L_j i_j$ is phase flux linkage and j is the phase identifier. In the right hand side of (3-21), the first term is the resistive voltage drop, the second term is the inductive voltage drop and the third term is the induced emf.

The output force of LSRA is the sum of phase forces; the phase force can be evaluated by the following relationship which is a function of the current and the derivative of the inductance according the position:

$$F = \sum_j F_j, \; F_j = \frac{1}{2}\left(\frac{dL_j}{dx_a}\right)i_j^{\,2}, \; j = a, b, c, d \qquad (3\text{-}22)$$

where F_j is phase electrical force, F is total electrical force.

A simple and reliable PI control method is used for the direct force control of the LSRA, as shown in Fig. 3-14. Assuming the rate of change of phase inductance is estimated with the knowledge of position x_a and phase current I, the relationship between the active force and phase currents is obtained as shown in (3-22). For a given force command F^*, the required phase current I^* is calculated by

$$I^* = \sqrt{\frac{2F^*}{dL_{est}(x_a,i)}} \tag{3-23}$$

where $dL_{est}(x_a,i)$ is the estimation of the phase inductance derivative with respect to the excitation current and translator position.

The phase current error e_i between the current command and measured value is used as the input of PI controller. Then the duty ratio d generated by the PI controller is used to drive the switching devices, thus the LSRA can generate the required electromagnetic force F.
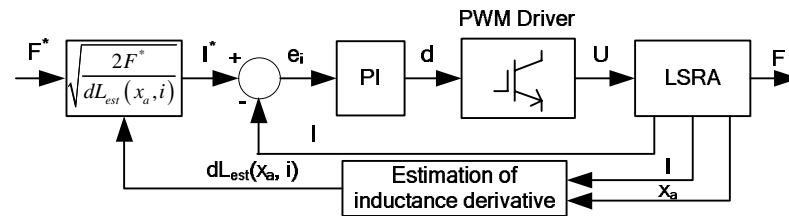
Fig. 3-14 Direct force drive of LSRA

3.4.1 Estimation of inductance and its derivative

For the direct force control, the change rate of the inductance is critical for the generation of current command. As discussed above, the inductance is a highly nonlinear parameter that is related to phase current and translator position. The phase inductance of the LSRA can be calculated by the pre-obtained flux linkage and corresponding excitation current. A series of inductance curves are illustrated in Fig. 3-15. The phase inductance varies with different translator positions and excitation currents. The corresponding derivative versus translator position is obtained in Fig. 3-16. In general, there are two types of method to describe the complicated behaviour of phase inductance variation: look-up table method [99], [125], [128], [129] and approximated analytical function [127], [130], [131]. Both methods require the force profile versus excitation currents and translator position, the command current can be obtained by interpolation of the pre-obtained look-up table method, which is a simple and direct method, but lacks flexibility; otherwise the analytical functions are synthesised to provide more flexibility for real-time implementation, while the accuracy is affected by the accuracy of the approximation.

A simple method with least data is developed in this application to reduce the memory requirement and provide control flexibility while keeping the calculation accuracy of the direct drive system. As shown in Fig. 3-15 and Fig. 3-16, the shapes of phase inductance and its derivative are similar to sinusoid waveform; therefore, Fourier series method is used to conduct the analytical expressions of inductance. Each inductance curve with fixed excitation current is expressed in a Fourier series, and the inductance value vs. arbitrary excitation current and translator position can be obtained by the interpolation of adjacent curves. The related inductance derivative can be deduced from the analytical inductance expression.
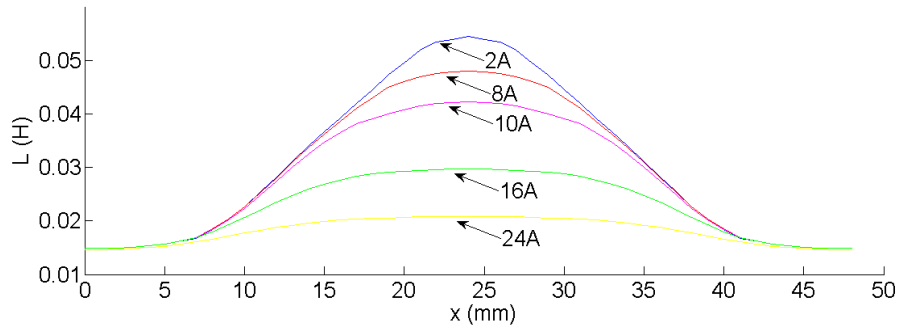
Fig. 3-15 Phase inductance of the LSRA
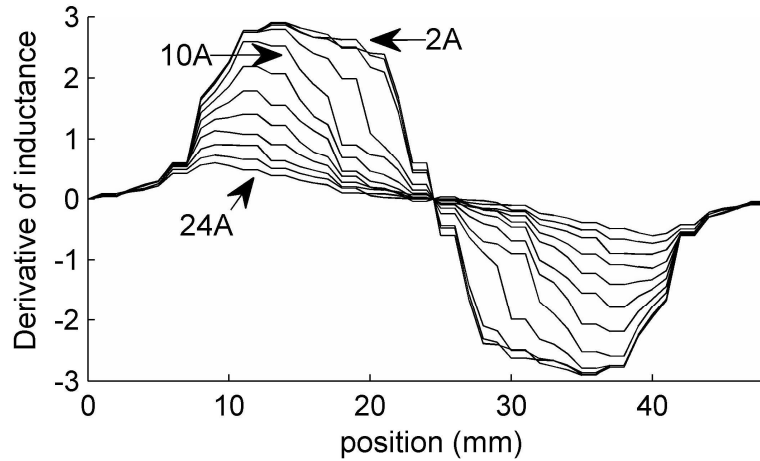
Fig. 3-16 Derivative of phase inductance

Take the inductance curve with nominal current 10A for examplem, the nominal inductance, denoted as L_{nom}, is approximated as follows in the form of Fourier series:

$$
\begin{aligned}
L_{nom} = a_0 &+ a_1 \cos(wx_a) + a_2 \cos(2wx_a) \\
&+ a_3 \cos(3wx_a) + a_4 \cos(4wx_a) + a_5 \cos(5wx_a)
\end{aligned}
\tag{3-24}
$$

where the angular frequency $w = 2\pi / 48$, the coefficients are $a_0 = 0.02782$, $a_1 = -0.01495$, $a_2 = 0.0005895$, $a_3 = 0.001502$, $a_4 = 0.0001508$, $a_5 = -0.0002093$.

The inductance change rate can be deduced by (3-24)

$$\begin{aligned} \frac{dL_{nom}}{dx} = &-wa_1 \sin(wx_a) - 2wa_2 \sin(2wx_a) - 3wa_3 \sin(3wx_a) \\ &- 4wa_4 \sin(4wx_a) - 5wa_5 \sin(5wx_a) \end{aligned} \quad (3\text{-}25)$$

The approximation of the inductance and its derivative is illustrated in Fig. 3-17. The actual data is marked as asterisk to compare with the approximated curves. It can be observed that two inductance curves in the upper plot are coincided through the whole period. The points of actual inductance derivative are located around the curve of analytical inductance derivative with error mostly less than 5%, which verifies the effectiveness of the proposed method. Moreover, a series of inductance formulations are synthesised to estimate the dynamic inductance profile from 2A to 24A, then the approximated inductance derivative $dL_{est}(x_a, i)$ of the LSRA can be obtained. Thus, the current command can be transformed by force directly expressed in (3-23).
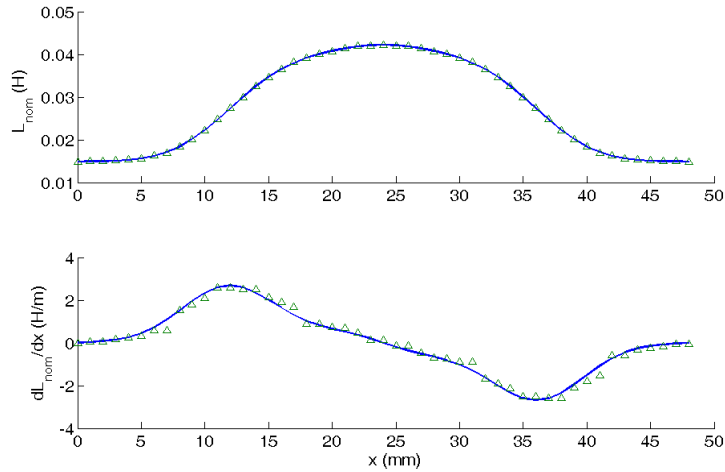
Fig. 3-17 Approximation of nominal inductance and its derivative

(Actual values denoted by asterisk)

A bulk of the approximated inductance derivative expressions has been illustrated in Fig. 3-16, and the nominal inductance derivative dL_{est_nom} lays the middle of the whole curves. Considering in an intuitive way, the approximated inductance derivative

$dL_{est}(x_a, i)$ can be expressed by dL_{est_nom} only, i.e. $dL_{est}(x_a, i) = dL_{est\_nom}(x_a, i)$ to reduce the computation workload and make the handling of storage memory of controller easy. The difference between $dL_{est}(x_a, i)$ and the actual phase inductance derivative can be compensated by the closed-loop current controller [100], [131]. Moreover, the inductance derivative can be approximated in a simple quadratic form, which is based on the maximum value of dL_{est_nom} which appears around the centre of phase conducting interval [131].

3.4.2 Force distribution function

Force distribution function (FDF) is an effective way to deal with the overlapping of two adjacent windings and reduce the force ripple. The relationship between the command force of the phases F_j^* and actuator F^* is represented as

$$F_j^* = f_j \cdot F^*, \quad \sum_{j=a,b,c,d} f_j = 1 \tag{3-26}$$

where f_j is the FDF for each phase.

The FDF can be expressed in many forms, such as linear, sinusoidal and exponential. Recall (3-5), the electrical force of each phase F_j is positive related to the inductance derivative $\dfrac{dL_j}{dx}$ with constant excitation current. Therefore, the FDF can be represented in the form of

$$f_j = g_j^\kappa \Big/ \sum_{j=a,b,c,d} g_j^\kappa, \quad j = a, b, c, d \tag{3-27}$$

where $g_j = \begin{cases} |dL_{jest}/dx|, & if\ \left(F^* \cdot dL_{jest}/dx\right) > 0 \\ 0, & else \end{cases}$, κ is the impact factor of the FDF to provide flexibility of the force control, L_{jest} is the estimation of jth phase inductance.

The value of κ has direct impact on the shape of the FDF and thus affects the force profile of the LSRA. The criterion for selecting κ is to minimum the force ripple.

Here, $\kappa = 2$ is selected. Fig. 3-18 illustrates the shape of the proposed FDF and the commutation sequence.
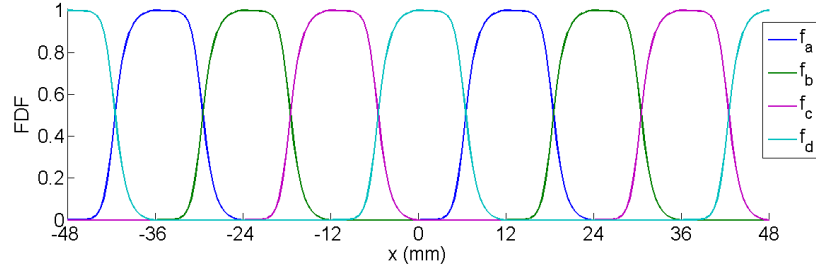
(a) Upward movement
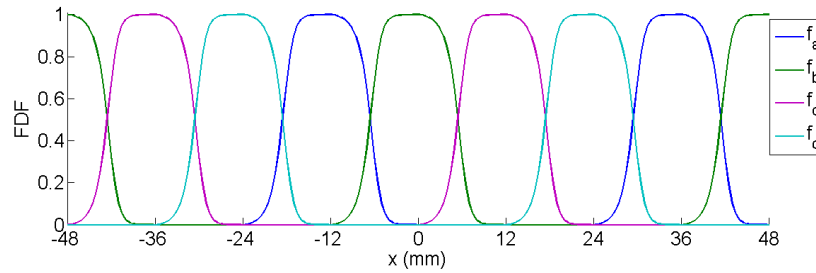
(b) Downward movement

Fig. 3-18 The proposed FDF

3.4.3 PI control method for force control

Since the force command of each phase can be determined by the command force multiplies the force distribution functions, the phase current commands I^* are specified previously. The phase current equation is represented in (3-28) by rearranging (3-21),

$$\frac{di_j}{dt} = -\frac{R_j}{L_j}i_j + \frac{1}{L_j}u_j, \ R_j = R_s + v_a\frac{dL_j}{dx_a}, \ j = a,b,c,d \qquad (3\text{-}28)$$

where R_j is the phase equivalent resistor.

From (3-28), the dynamic behaviours of the LSRA system can be approximated as a first-order differential equation. Thus, the transfer function of the current loop is also first order. Then, PI controller is appropriate to regulate the system and achieve perfect current tracking. The input error e_i can be obtained by $e_i = i^* - i$, the required terminal voltage is calculated as

$$u^* = k_{p\_i}e_i + k_{i\_i}\int e_i dt \qquad (3\text{-}29)$$

where k_{p_i} and k_{i_i} is the proportional and integral gain of inner current PI controller. Additionally, the performance of PI controller can be improved by adding anti-windup scheme to prevent the PI output from saturation [28], [132].

The determination of the controller gains is ruled by the Ziegler–Nichols method in industrial application. However, insufficient use of process information and poor robustness are the main severe drawback of that method [29]. A refining Ziegler–Nichols step response method is developed based on maximization of integral gain according to a constraint on the maximum sensitivity, so called M-constrained integral gain optimization (MIGO) [133], [134]. Alternatively, a tuning rule denoted as approximate MIGO (AMIGO) is developed to explore the simple relationship between process parameters and the control parameters through a large test batch of process. Using AMIGO, the controller gains k_{p_i} and k_{i_i} can be evolved analytically to enhance the robustness of the PI controller. Here, the proportional gain is set to be $k_{p\_i} = 200$, the integral gain can be calculated as $k_{i\_i} = k_{p\_i} \cdot \dfrac{T}{T_s}$, in which T is the sampling period, T_s is the settling time and is set to be $T_s = 0.005s$.

3.4.4   Simulation results

The force control method of the LSRA has been discussed above. In order to verify the effectiveness of proposed PI control method with the FDF, a number of simulations are performed in the Matlab/Simulink environment. The model of LSRA is constructed based on the measured flux linkage and force characteristics.

The effectiveness of the proposed PI control method with the FDF can be examined, as shown in Fig. 3-19. When the LSRA lifts the shaft, the actuator generates positive electrical force. The required force of upward movement is $F^* = 500N$, the commutation sequence and force distribution function are depicted in the upper of Fig. 3-19(a). The generated force is approximately 500N, which indicates that the controller has a good force tracking performance, as shown in the middle of Fig. 3-19(a). The force ripples occur at the turn-off stage of phase currents, and it is relatively small compared with the output force. The excitation currents are depicted

in the bottom part of Fig. 3-19(a). It can be observed that the phase excitation current is around 10A when the FDF of the specified phase is near 1; the results verify the performance of the proposed LSRA, i.e. nominal current of 10A generates the continuous nominal force of 500N. The case of downward movement with negative force is similar to the positive case, as illustrated in Fig. 3-19(b).
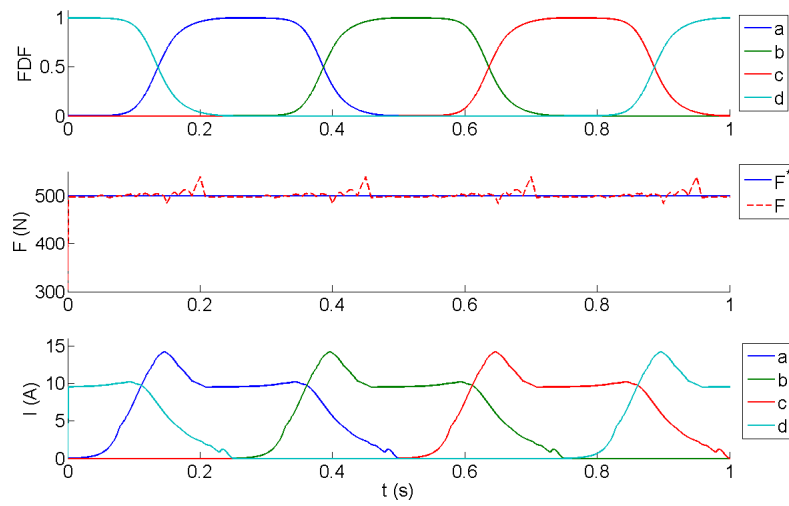
(a) Upward movement
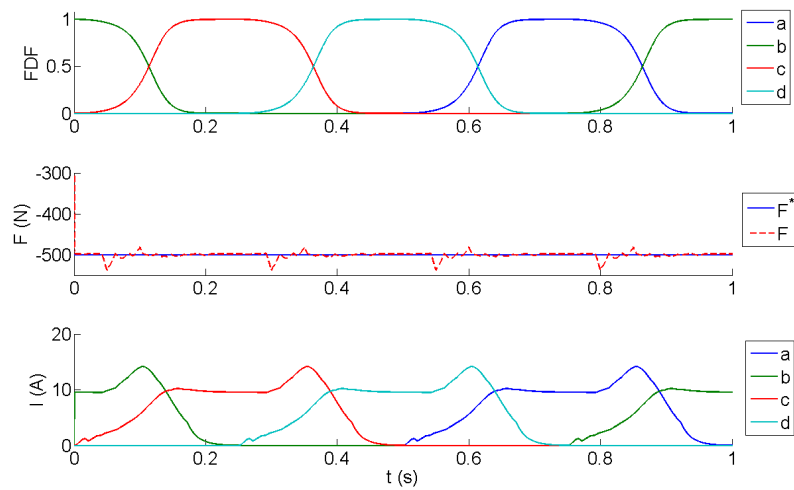
(b) Downward movement

Fig. 3-19 Force control of the LSRA

3.5 Summary

In this chapter, the basic theory and energy conversion principle of the LSRA are reviewed. The force generation is investigated from the viewpoint of electromagnetic energy conversion. The flux linkage and force can be obtained by the partial differentiation of the co-energy, versus excitation current and translator position, respectively.

The structure of the proposed LSRA is investigated, and the volume constraint and force requirement of the ASS unit is then determined. The flux linkage is an important tool in the design of proposed LSRA, and the phase inductance is calculated with different current values to predict the characteristics of the flux linkage. MCA is an analytical calculation method to estimate the flux linkage in a magnetic circuit by ignoring the nonlinearity and saturation, thus the actuator characteristics can be expressed analytically by design variables based on the specified geometrical structure. Furthermore, FEA is applied to optimise the design variables in a more accurate way by considering the magnetic nonlinearity and saturation.

The prototype of the proposed LSRA is built for testing and verifying the performance of the actuator. Force control of the LSRA drive is investigated to fulfil the movement of the ASS. The characteristics of the inductance and its derivative are synthesised to approximate the dynamic behaviour of the actual flux linkage and force profile. To reduce the force ripple, force distribution function is developed and optimised. A simple and effective PI controller is developed and its gains are refined using the approximate M-constrained integral gain optimization. The simulation results show that good force tracking is achieved by using the proposed PI control.

Chapter 4 Nonlinear PD control for the quarter-car active suspension system

High precision position estimation is essential for the control of the quarter-car and full-car active suspension systems to achieve high performance. The road profile is irregular and varies here and there. For the purpose of accurate control, the vertical vibration information of the ASS should be obtained timely for real-time application, i.e. the positions and angles of relative degree-of-freedom (DOF). Measurement and estimation play important roles on high performance control of real time application

In this chapter, the position of the sprung mass is estimated for the control of quarter-car ASS. Then, the transfer function of the quarter-car suspension system is explored for the purpose of control. An effective nonlinear PD control method is developed to improve the robustness of the ASS.

4.1 Tracking Differentiator

A novel tracking differentiator (TD) is introduced to track the feedback displacement signal and calculate its velocity directly through numerical method based on optimal control theory [135], [136]. TD is effective to obtain differential signal without the prior knowledge of the practical acquisition for real-time application [136], [137]. More details of TD are referred to Appendix I.

4.1.1 Forms of TD

TD has the advantages of fast response and high precision. Moreover, the derivative of the signal can be obtained directly and noise rejection is achieved simultaneously. There are many forms of TD, such as nonlinear TD, second-order and higher-order TD. For a given reference signal $r(t)$, TD is used to obtain its tracking signal $r_1(t) \rightarrow r(t)$ and derivative $r_2(t) \rightarrow \dot{r}(t)$. One reliable second-order TD is presented as follows:

$$\begin{cases} \dot{r}_1 = r_2 \\ \dot{r}_2 = -\Omega sat\left(r_1 - r + \dfrac{r_2 |r_2|}{2\Omega}, \delta \right) \end{cases} \tag{4-1}$$

where Ω and δ are two positive design parameters, and the saturation function is

$$sat(z, \quad \delta) = \begin{cases} 1, z > \delta \\ \dfrac{z}{\delta}, |z| \le \delta \\ -1, z < -\delta \end{cases} \tag{4-2}$$

Though perfect reference signal tracking can be achieved by using TD, the chattering phenomenon may appear occasionally. Thus, a discrete time version of TD is encouraged to use in practical implementation to avoid unnecessary oscillations. Additionally, the discrete time form is suitable for real-time application. Suppose the discrete signals r_1 and r_2 of TD are the traces of the input signal r and its derivative [136], it can be obtained that

$$\begin{cases} r_1(k+1) = r_1(k) + hr_2(k) \\ r_2(k+1) = r_2(k) + h\varpi\left(r_1(k) - r(k), r_2(k), \upsilon, ch\right) \end{cases} \tag{4-3}$$

where h is the sampling step, υ is the tracking velocity factor for signal tracking, and c is the filtering factor to reject stochastic noise. The updated function $\varpi(p_1, p_2, \upsilon, H)$ is of the form

$$\varpi(p_1, p_2, \upsilon, H) = -\upsilon sat(a, \quad d) \tag{4-4}$$

with

$$a = \begin{cases} p_2 + \dfrac{b-d}{2} sign(\gamma), |\gamma| > d^2 \\ p_2 + \dfrac{\gamma}{d}, |\gamma| \le d^2 \end{cases}, \quad d = \upsilon H \;, \; \gamma = \upsilon p_1 + dp_2 \;, \; b = \sqrt{d^2 + 8|\gamma|}\;.$$

4.1.2 Implementation of TD

For a quarter-car ASS, the displacement signal z_s of the sprung mass is acquired from LVDT to the controller with white noise. The first step is to smooth the displacement signal and calculate vertical velocity by TD. The smoothed displacement signal z_{s1} and vertical velocity z_{s2} are derived from

$$\begin{cases} z_{s1}(k+1) = z_{s1}(k) + hz_{s2}(k) \\ z_{s2}(k+1) = z_{s2}(k) + h\varpi\left(z_{s1}(k) - z_s(k), z_{s2}(k), \upsilon, ch\right) \end{cases} \tag{4-5}$$

The performance of nonlinear TD is mainly depending on the tracking velocity factor υ and filtering factor c. Large υ is beneficial for fast transition and tracking, and large c is helpful to reject stochastic sensor noise. However, improper choice of parameters will deteriorate the system performance. Too large υ causes chattering of the tracking signals, especially the derivative of reference signal. Too large c will delay the response of system. A trade-off between tracking and filtering must be considered to obtain good tracking and differentiating performance [137].

Determining the filtering factor and velocity factor is necessary in this application. As mentioned above, large filtering factor is required to cancel the sensor noise injected by electronic components and motor driving. Then, large velocity factor is preferred in fast position tracking application. Several combinations of $(\upsilon,\quad c)$ are tested with large factors. Based on the simulation results, $(200,\quad 10)$ is selected as the optimal parameters of TD. The filtering factor is set to be large to improve the filtering capability of TD. The velocity factor is set to be medium in case of unnecessary signals oscillating.

4.1.3 Performance of TD

To demonstrate the effect of nonlinear TD, the tracking of a sinusoidal road with white noise is shown. The maximum amplitude of the isolated bumps in test is 0.05m, and the duration time is 0.3s when the wheel runs over it at a constant speed of approximate 1m/s. To simulate the critical situation encountered by the wheel, the reference input signal is 0.05m with a frequency of 3.33Hz and 0.001m white noise. The parameters of the TD is selected as $\upsilon=200$, $c=10$, as described above. The sampling period of ADC module of DSP is set to be 0.00025s, thus h=0.00025.

The simulation of the reference tracking is shown in Fig. 4-1. The generalised displacement signal z_s tracks the reference input signal z_s^*, indicates that the TD outperforms in position tracking as seen in the top waveforms in Fig. 4-1(a). Using conventional differentiator fails to obtain the velocity of the noisy signals, as described in the middle of waveform in Fig. 4-1(b). In contrast, the differentiator of TD can estimate the velocity of the reference signal and reject the noise. The estimated velocity tracks the variation of the reference signal, as shown in the bottom waveforms of Fig. 4-1(c).

An experiment of the TD is done to verify the simulation results, as show in Fig. 4-2. It can be observed in Fig. 4-2(a) that the tracking displacement signal of the TD is smooth and almost overlaps with the reference displacement signal, which verifies the perfect tracking performance of the TD. In Fig. 4-2(b), the velocity of the

displacement signal is obtained simultaneously which is unavailable in conventional calculation. Furthermore, the acceleration is easy to obtain through tracking the estimated velocity by one more TD [135].
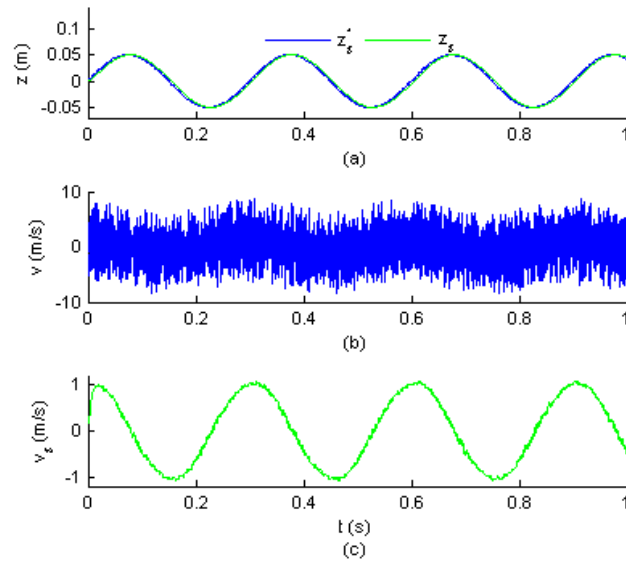
Fig. 4-1 Comparison of the TD and conventional differentiator

(a) Tracking

(b) Differentiating
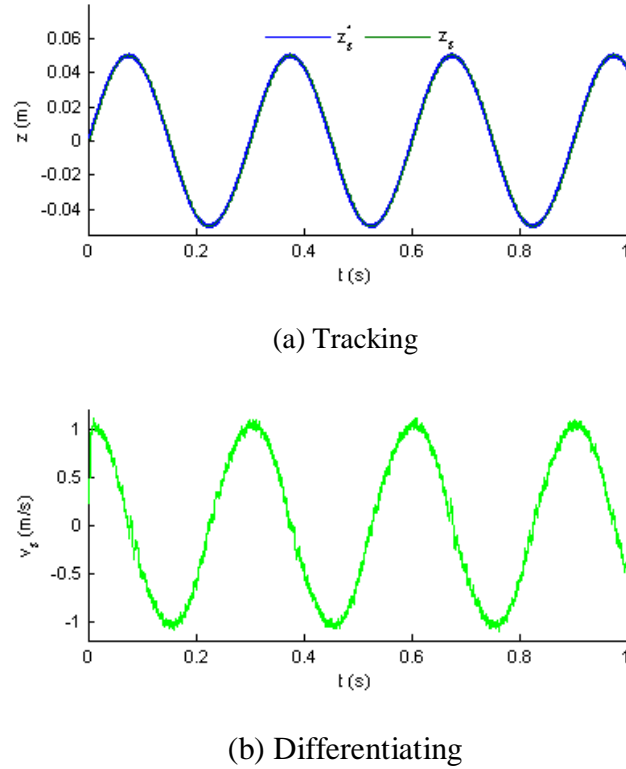
Fig. 4-2 TD of sinusoidal road profile

4.2 Nonlinear PD control strategy

The main purpose of the ASS is to stabilise the sprung mass with fast response. Suppose the reference commands are referred to zero displacement and zero velocity, i.e. $z_s^* = 0$ and $\dot{z}_s^* = 0$. Thus, the objective of the control strategy for the quarter-car ASS is to guarantee the proportional error $e_p = z_s^* - z_s$ and the derivative error $e_d = \dot{z}_s^* - \dot{z}_s$ converge to zero.

From the state equation (2-4) of the quarter-car ASS, the sprung mass subsystem can be obtained. Let $x_1 = z_s$, $x_2 = \dot{z}_s$, $d_u = \begin{bmatrix} z_u & \dot{z}_u \end{bmatrix}^T$, we have

$$\begin{bmatrix} \dot{x}_1 \\ \dot{x}_2 \end{bmatrix} = \begin{bmatrix} 0 & 1 \\ -K_s/M_s & -C_s/M_s \end{bmatrix} \begin{bmatrix} x_1 \\ x_2 \end{bmatrix} + \begin{bmatrix} 0 \\ 1/M_s \end{bmatrix} F + \begin{bmatrix} 0 & 0 \\ K_s/M_s & C_s/M_s \end{bmatrix} d_u \quad (4\text{-}6)$$

Thus, the transfer function of the sprung mass subsystem is

$$G(s) = \frac{\dfrac{1}{M_s}}{s^2 + \dfrac{C_s}{M_s}s + \dfrac{K_s}{M_s}} \quad (4\text{-}7)$$

The system with second-order transfer function can be controlled by a linear Proportional-Derivative (PD) controller expressed in (4-8) for simplicity. Here, k_{lp} and k_{ld} are the constant proportional and derivative gains respectively. The transfer function of the PD controller is given by (4-9)

$$F^* = k_{lp}e_p + k_{ld}e_d \quad (4\text{-}8)$$

$$p_l(s) = k_{lp} + k_{ld}s \quad (4\text{-}9)$$

Therefore, the transfer function of the closed-loop linear PD controller is obtained by

$$W_l(s) = p_l(s) \cdot G(s) = \frac{\dfrac{k_{ld}}{M_s} s + \dfrac{k_{lp}}{M_s}}{s^2 + \dfrac{C_s}{M_s} s + \dfrac{K_s}{M_s}} \tag{4-10}$$

The control scheme is shown in Fig. 4-3. The derivative gain k_{ld} should be determined to suppress the vertical vibration due to road disturbance; the proportional gain k_{lp} is tuned later to smooth the response of the system.
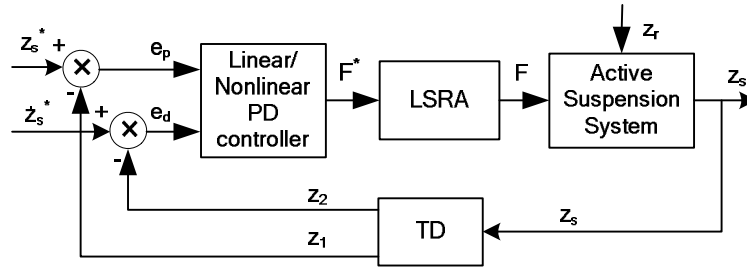
Fig. 4-3 PD control schemes for ASS

The advantages of adopting linear PD controller are its simplicity and satisfactory performance. Meanwhile, some drawbacks exist when linear PD controller is utilized as the control scheme for ASS. The linear fixed gain between outputs and errors is one of the possible flaws. A nonlinear feedback error strategy can be a solution to overcome this drawback [136]-[138]. The form of nonlinear PD control law is similar to linear PD control and can be synthesised as

$$F^* = k_{np}(\cdot) e_p + k_{nd}(\cdot) e_d \tag{4-11}$$

where $k_{np}(\cdot)$ and $k_{nd}(\cdot)$ are error-dependent time-varying nonlinear gains.

The purpose of employing nonlinear PD controller is to reduce the rise time of small error and to enhance robustness of large error. The large error is mainly due to increasing amplitude of road disturbance. The form of the specified nonlinear PD controller is developed as

$$F^* = k_p p(e_p, \ \delta_p, \ \alpha_{p1}, \ \alpha_{p2}) + k_d p(e_d, \ \delta_d, \ \alpha_{d1}, \ \alpha_{d2}) \tag{4-12}$$

where k_p and k_d are proportional gain and derivative gain to be determined, δ_p and δ_d are error set-point, α_{p1}, α_{p2}, α_{d1} and α_{d2} are converging factors. $p(e,\ \delta,\ \alpha_1,\ \alpha_2)$ is nonlinear error function, and one feasible form is presented as

$$p(e,\ \delta,\ \alpha_1,\ \alpha_2)=\begin{cases}\left|e/\delta\right|^{\alpha_1} sign(e), |e|>\delta \\ \left|e/\delta\right|^{\alpha_2} sign(e), |e|\le\delta\end{cases},\delta>0\,.$$

Substituting the nonlinear error function $p(e,\ \delta,\ \alpha_1,\ \alpha_2)$ into (4-12), the nonlinear time-varying gains are represented as

$$k_{np}(\cdot)=\begin{cases}k_p\left|e_p\right|^{\alpha_{p1}-1}\delta^{-\alpha_{p1}}, |e|>\delta_p \\ k_p\left|e_p\right|^{\alpha_{p2}-1}\delta^{-\alpha_{p2}}, |e|\le\delta_p\end{cases},\delta_p>0 \qquad (4\text{-}13)$$

$$k_{nd}(\cdot)=\begin{cases}k_d\left|e_d\right|^{\alpha_{d1}-1}\delta_d{}^{-\alpha_{d1}}, |e|>\delta_d \\ k_d\left|e_d\right|^{\alpha_{d2}-1}\delta_d{}^{-\alpha_{d2}}, |e|\le\delta_d\end{cases},\delta_d>0 \qquad (4\text{-}14)$$

4.2.1 Comparison between the linear and nonlinear PD control

As expressed in (4-13) and (4-14), nonlinear PD controller offers time-varying gains whereas linear PD controller offers pre-defined fixed gains. Such difference prompts flexible choices and better system performance for the closed-loop system in adopting nonlinear PD control scheme [137], [138]. Given that an identical output generated by both PD controllers at error set points, a better response is recorded in nonlinear PD control scheme. Supposed the proportional terms in both controllers output the same force at $|e|=\delta=0.1$, a higher force is generated in nonlinear PD controllers with $\alpha\in(0,\ 1)$ than the linear one when the error located at interval with $|e|\le\delta$ except the set point. The behaviour of nonlinear PD controller regard to different error zones and converging factors are depicted in Fig. 4-4. When large error appears with $|e|>\delta$

in Fig. 4-4(b), selecting $\alpha \in (1, \infty)$ is appropriate to generate higher force that stabilises the ASS. To conclude, the nonlinear PD control schemes is advantageous over the linear PD ones with higher generated force in same error interval, shorter response time to small vibrations and better responses to suppress large oscillations.

Based on the aforementioned arguments, the converging factor is selected as $\alpha \in (0, 1)$ with small error and $\alpha \in (1, \infty)$ with large error. The parameters of nonlinear PD controller are listed in Table 4-1. It can be concluded that the time-varying nonlinear gains are greater than the linear gains in most cases, i.e.

$$k_{np} \geq k_{lp}, k_{nd} \geq k_{ld}. \tag{4-15}$$
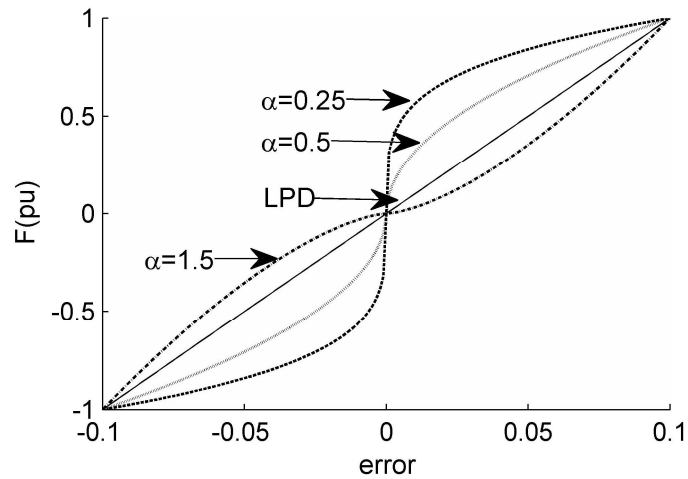
(a) Small error
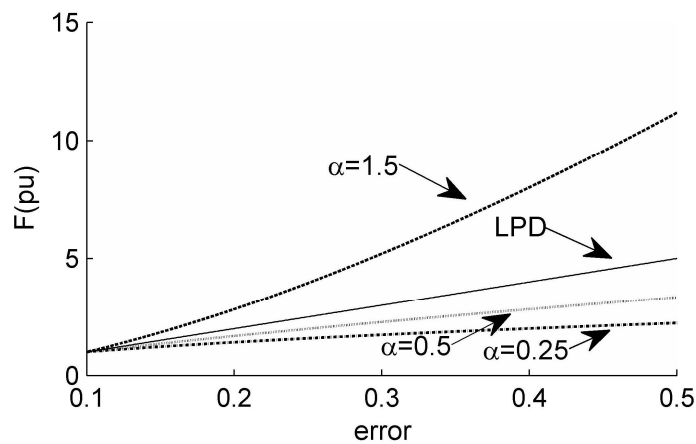
(b) Large error

Fig. 4-4 Comparison between the outputs of linear and nonlinear PD controllers

Table 4-1 Parameters of the nonlinear PD controller

Symbol	Value	Symbol	Value
υ	200	α_{p1}	2
c	10	α_{p2}	0.5
h	0.00025	δ_p	0.01
k_{lp}	30000	α_{d1}	1.5
k_{ld}	3200	α_{d2}	0.75
k_p	250	δ_d	0.1
k_d	200		

4.2.2 Stability analysis

The loop transfer function of the nonlinear PD control system is achieved by substituting (4-11) into (4-7)

$$W_n(s) = G(s)(k_{np} + k_{nd}s) = \frac{\dfrac{k_{nd}}{M_s}s + \dfrac{k_{np}}{M_s}}{s^2 + \dfrac{C_s}{M_s}s + \dfrac{K_s}{M_s}} \tag{4-16}$$

For a class of time-varying nonlinear system, the Popov stability criterion is a useful tool for stability judgment. The time-varying nonlinear gains are selected by Popov criterion, which ensure the Popov plot lies completely to the right hand side of a non-negative slope and intersect the negative real axis [139].

The standard Popov criterion is summarised as follow:

For a closed-loop nonlinear control system with time-varying parameters, the sufficient condition of global stability is that the Popov plot of the controlled system lies entirely to the right hand side of a straight line with slope $q \geq 0$ passing through the point $\left(-\dfrac{1}{k},\ 0\right)$, where k is the maximum control amplitude.

The real part and image part of Popov plot of the closed loop system (4-16) are

$$\begin{cases} \mathrm{Re}\left[W_n(j\omega)\right] = \dfrac{(C_s k_{nd} - M_s k_{np})\omega^2 + K_s k_{np}}{C_s^2\omega^2 + (K_s - M_s\omega^2)^2} \\[4mm] \omega\,\mathrm{Im}\left[W_n(j\omega)\right] = \dfrac{-(M_s k_{nd}\omega^2 + C_s k_{np} - K_s k_{nd})\omega^2}{C_s^2\omega^2 + (K_s - M_s\omega^2)^2} \end{cases} \tag{4-17}$$

Based on (4-17), the Popov plot of the controlled system (4-16) starts at the point of

$\left(\dfrac{k_{np}}{K_s}, \quad 0 \right)$ and ends at the point of $\left(0, \quad -\dfrac{k_{nd}}{M_s} \right)$.

The ranges of controller gains k_{np} and k_{nd} are determined by applying Popov stability criterion. Since k_{np} and k_{nd} are time-varying parameters related to the position error and its derivative, two cases are distinct and switched continuously through the process of global stability: case(a) with $C_s k_{np} \geq K_s k_{nd}$ and case(b) with $C_s k_{np} < K_s k_{nd}$. Table 4-2 shows the system parameters for the case study here.

Case(a). The following relationship exists: $\omega \operatorname{Im} W(j\omega) \leq 0$ for $\omega \in (0, \quad \infty)$. Hence, the Popov plot of controlled system (4-16) remains entirely below the real axis, as shown in Fig. 4-5(a). The range of parameters are unlimited according to Popov criterion, i.e. $k_{np} \in (0, \quad \infty)$, $k_{nd} \in (0, \quad \infty)$.

Case(b). The crossover frequency ω_c of (4-16) to the real axis is $\omega_c^2 = \dfrac{K_s k_{nd} - C_s k_{np}}{M_s k_{nd}}$, and the crossover point is $\left(\dfrac{k_{nd}}{C_s}, \quad 0 \right)$ which lies in the positive real axis. In Fig. 4-5(b), the general shape of the Popov plot is shown that a possible straight line with positive slope passing through the origin exists outside in the left of entire Popov plot. Thus, the range of parameters is unlimited according to Popov criterion.

Based on the discussion of two cases, the stability of the nonlinear PD controlled system can be guaranteed with $k_{np} > 0$ and $k_{nd} > 0$.
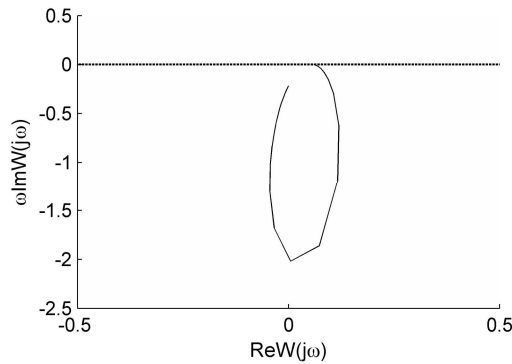
(a) Case a
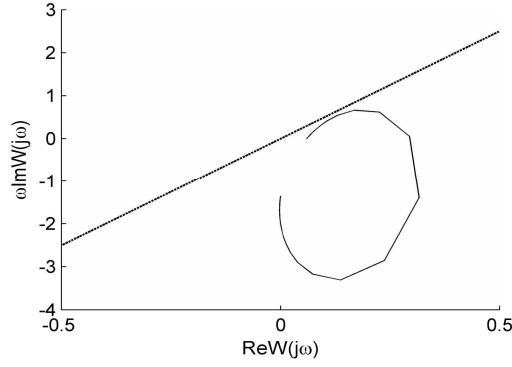
(b) Case b

Fig. 4-5 Popov plot of two cases

4.2.3 Robustness analysis

Two controllers robustness analysis can be categorized as follows: parameters variation and external disturbance. Once the ASS is equipped, the most varied system parameter is sprung mass M_s. From (4-10) and (4-16), the variation of sprung mass changes the poles of the controlled system; the effects of parameter variation are almost the same on both controlled system. It is noticeable that the system parameters are positive all the time. The Popov plots of the controlled systems lie entirely to the right side of the straight line; therefore, both systems are always stable. Besides, the damping ratio C_s may change from time to time due to mechanical fatigue and load variation. The variation of damping ratio has the similar effects on the controlled systems.

  The effect of external disturbances is analysed using Popov stability criterion. Given injected bounded disturbances with non-zero input errors, and some bounded gains exist to represent the disturbance as follow:

$$d_u = \frac{K_s}{M_s} z_u + \frac{C_s}{M_s} \dot{z}_u = g_1(\cdot) z_s + g_2(\cdot) \dot{z}_s = -g_1(\cdot) e_p - g_2(\cdot) e_d \qquad (4\text{-}18)$$

where $g_1(\cdot)$ and $g_2(\cdot)$ are bounded nonlinear time-varying terms related to external bounded disturbances. When the external disturbances occur, the ASS vibrates and then e_p and e_d are not equal to zero. Hence, non-zero $g_1(\cdot)$ and $g_2(\cdot)$ exist in (4-18).

Furthermore, it is reasonable to assume that large $g_1(\cdot)$ and/or $g_2(\cdot)$ appear when large disturbances are injected.

The general transfer function with equivalent external disturbance (4-18) is

$$W_r(s) = \frac{\dfrac{1}{M_s}\left(k_{pr} + k_{dr}s\right)}{s^2 + \dfrac{C_s}{M_s}s + \dfrac{K_s}{M_s}} \tag{4-19}$$

where k_{pr} and k_{dr} are the equivalent proportional and derivative gains of the closed loop controlled systems considering external disturbance. For linear PD controller, $k_{lpr} \equiv k_{pr} = k_{lp} - g_1$ and $k_{ldr} \equiv k_{dr} = k_{ld} - g_2$; for nonlinear PD controller, $k_{npr} \equiv k_{pr} = k_{np} - g_1$ and $k_{ndr} \equiv k_{dr} = k_{nd} - g_2$. From (4-15) and (4-19), the following inequality always exists: $k_{npr} \geq k_{lpr}$ and $k_{ndr} \geq k_{ldr}$.

When the disturbances are small, especially within the set-point errors, controller gains of both controllers are large enough to keep the system stable. The related Popov plot is shown in Fig. 4-6. As the disturbances increase, if g_1 and g_2 increase as well, the control gains k_{npr}, k_{ndr}, k_{lpr} and k_{ldr} decrease eventually. Once the external disturbances excess the tipping point, k_{lpr} and (or) k_{ldr} decrease to negative while k_{npr} and k_{ndr} remain positive. Based on the Popov stability criterion, the nonlinear PD controller lies entirely in the right hand side of the straight line and the controlled system is therefore stable. Meanwhile, the transfer function of linear PD control has positive zeros that the controlled system becomes unstable. Therefore, the nonlinear PD controller is more robust than that of the linear PD controller in reference to the variation of external disturbances.
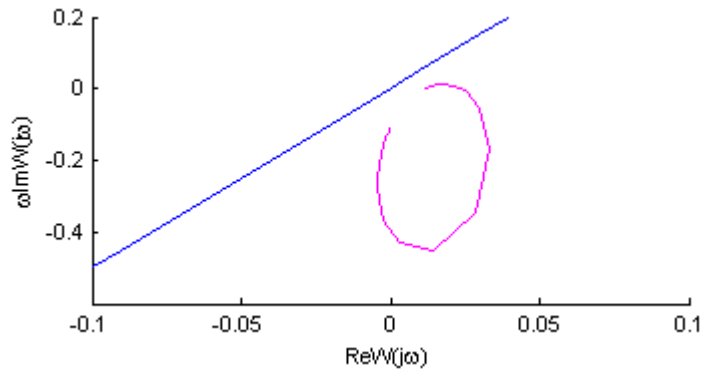
(a) Nonlinear PD
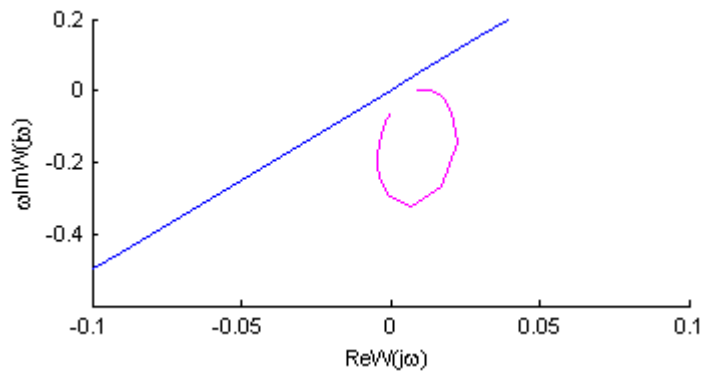
(b) Linear PD

Fig. 4-6 Popov plot of linear and nonlinear PD controlled system

4.3 Simulation and experimental results

A test rig of quarter-car ASS based on TMS320F2808 fixed-point DSP was built at the laboratory, as shown in Fig. 2-13. The road model of the test rig is a rolling wheel with concave plates that have been described in Fig. 2-14. Suppose the car runs over the test rig in a constant speed of 0.9m/s, the road profile is a periodically surface with three isolated bumps described in Fig. 4-7. The load of a vehicle with full passengers denotes as nominal value of the vehicle weight, and only a driver without passengers denotes as reduced value of the vehicle weight. The load difference between two statuses is from 100% to 80% of its nominal value. The test has used scaled parameters as in Table 4-2.

Table 4-2 Parameter of Quarter-Car ASS

Symbol	Value
M_s	110 kg
M_u	90 kg
K_s	18600 N/m
K_u	160000 N/m
C_s	600 N/(m/s)
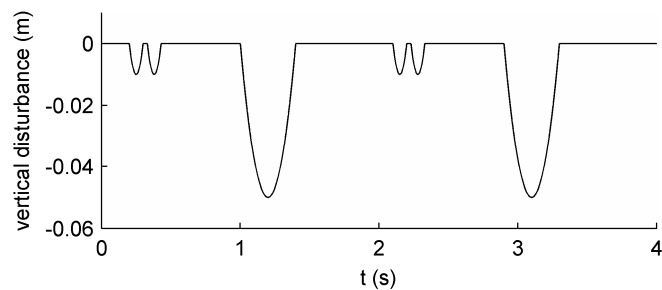
Fig. 4-7 Road profile of test rig

4.3.1 Simulation results

Suppose the car is running on a road similar to the test rig. The output force of LSRA is restricted within [-900N, 900N] due to the mechanical limitation and protection of the whole system. Examinations of robustness are simulated with the variation of sprung mass and external disturbance, as shown in Fig. 4-8 and Fig. 4-9. The responses of the passive and ASS are compared when the sprung mass varies from 80% to 100% of its nominal value. The vertical displacement and acceleration of the sprung mass subsystem are suppressed significantly with PD controllers, which

indicate that the performance of the ASS is better than the passive suspensions system. Moreover, the responses of the linear and nonlinear PD controllers are almost the same on both cases. The results show that the sprung mass variations have the same effects on both controllers as discussed above.
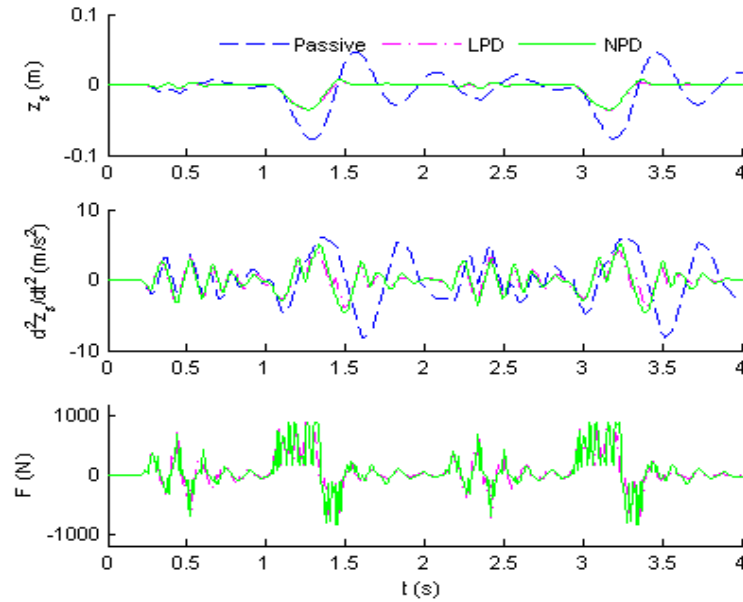
(a) $M_s = M_{s0}$
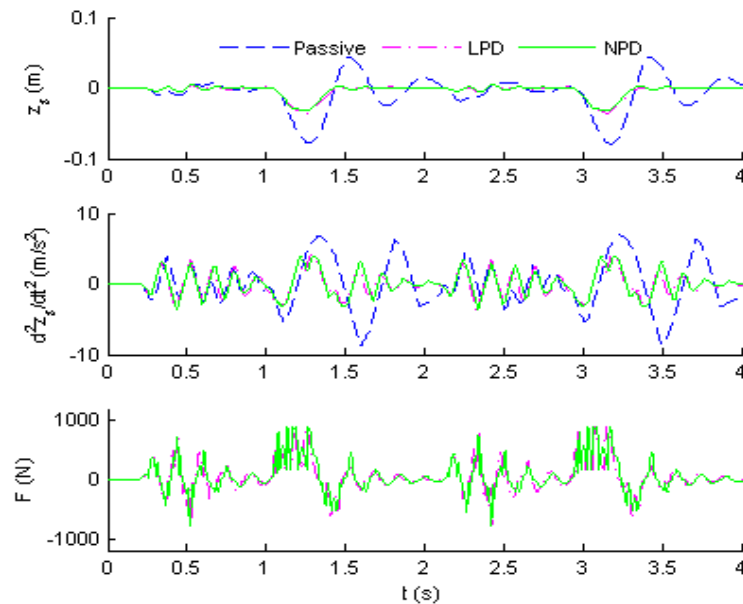
(b) $M_s = 80\% M_{s0}$

Fig. 4-8 Comparison of passive and ASS with different M_s
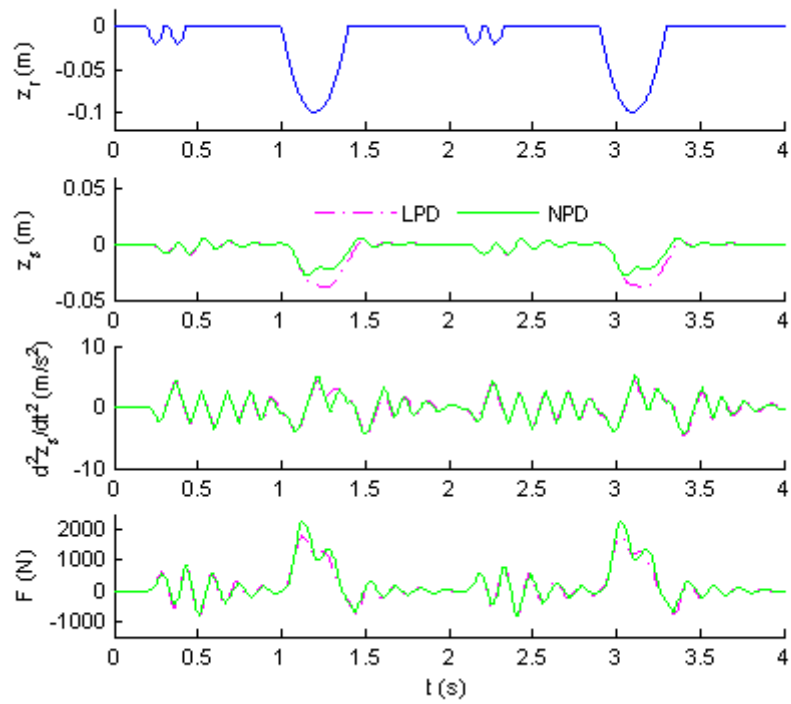
(a) $M_s = 100\%\,M_{s0}$
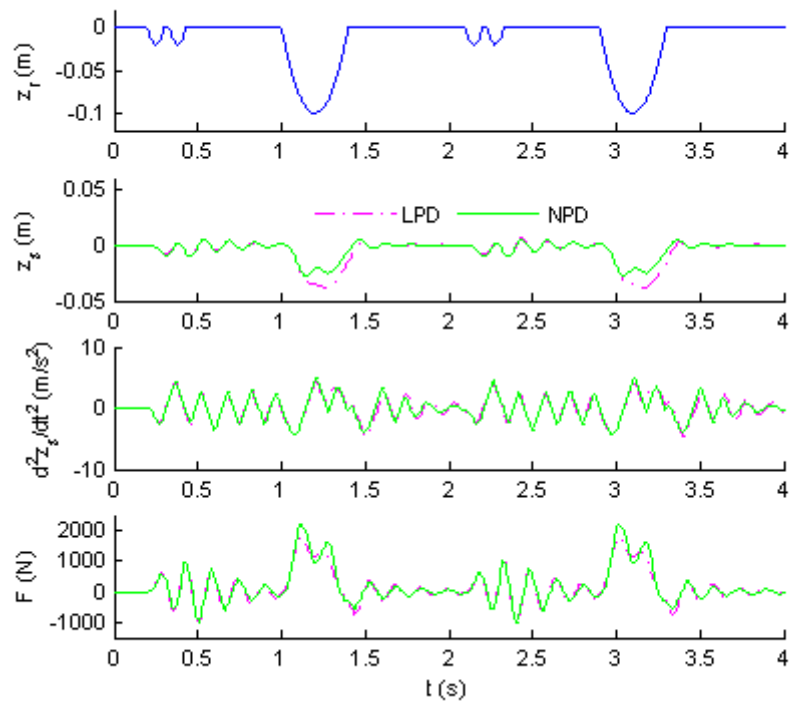
(b) $M_s = 80\%\,M_{s0}$

Fig. 4-9 Robustness of ASS to twice amplitude of bump

The robustness of PD controllers related to road disturbances is verified in Fig. 4-9. The road profile amplitude is deepened to twice of the original road terrain. When the disturbance increases to twice, the equivalent control gains will be decreased as discussed in (4-18) and (4-19). It can be seen that the equivalent control gains of the linear PD in (4-19) are closer to zero than the gains of nonlinear PD controller. Hence, the performance of controlled system with the linear PD will be deteriorated dramatically. Fig. 4-9(a) and (b) shows that the displacement of the system using the nonlinear PD controller is reduced considerably as compared with the linear PD controller, due to the higher generated peak force. It is verified that nonlinear PD controller is more robust than that of the linear PD controller when the external disturbance increases dramatically.

4.3.2 Experimental results

To verify the effectiveness of linear PD controller and proposed nonlinear PD controller, experiments are conducted with two sprung masses. It is obvious that ASSs are more effective than the passive suspension system according to the experiment results shown in Fig. 4-10 because both the displacement and acceleration of sprung mass are reduced significantly. From the experimental results shown in Fig. 4-10, a minor deviation between linear PD controller and proposed nonlinear PD controller is observed, which cannot be observed in the simulation results shown in Fig. 4-8. One of the possible reasons to that incoherence is the limitation and accuracy in computation of DSP. The nonlinear PD controller deals with more floating-point calculations, and hence a compromise has to be made between data accuracy and range, that results in the difference in produced forces between simulation and experiment especially large force output is required. Other possible reasons are the estimation error of parameters, such as the equivalent damper coefficient and the difference of force characteristics of LSRA between FEA data and practical force.

In Fig. 4-10(a), the maximum accelerations of active suspension and passive suspension are almost the same under the deepest hole, which is due to the restriction of peak force provided by the LSRA. In order to reduce the maximum acceleration, the value of the peak output force of the LSRA should be increased to suppress the dynamic oscillation significantly. Similar situation appears when the load varies to 80% of nominal value, as shown in Fig. 4-10(b).
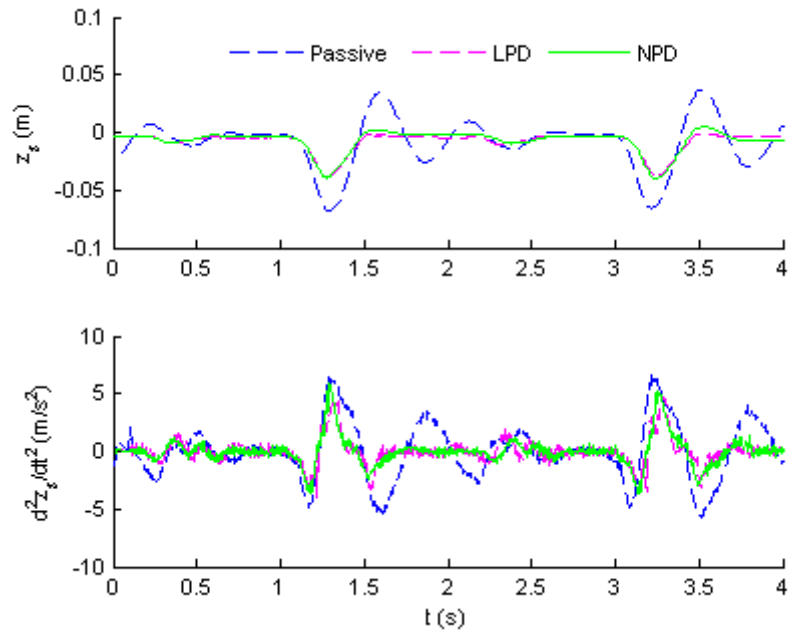
(a) $M_s = M_{s0}$
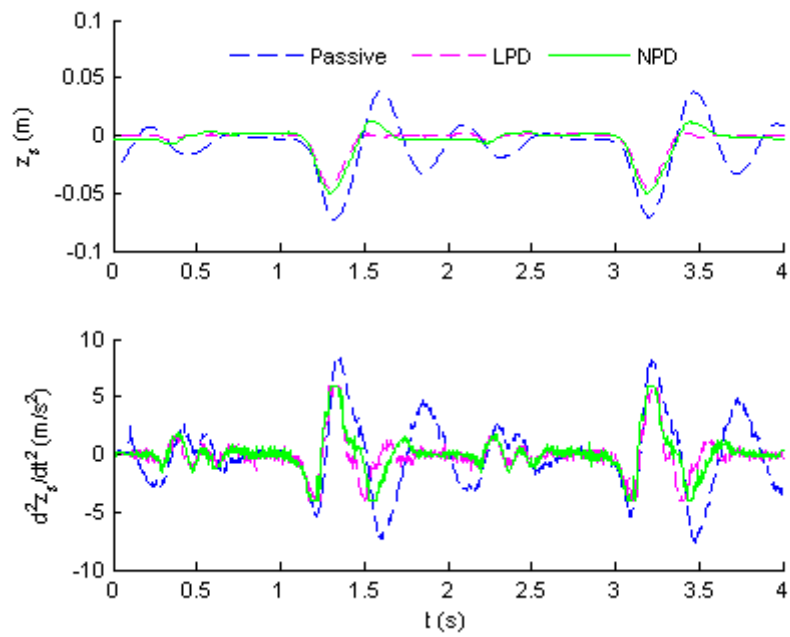
(b) $M_s = 80\% M_{s0}$

Fig. 4-10 Experimental results of ASS with varied sprung mass

4.4 Summary

Tracking differentiator is introduced to calculate the velocity directly from vertical displacement and reject the sensor noise effectively, which is unavailable in conventional calculation. A discrete time TD is applied for position tracking. An experimental result shows the effectiveness of the proposed TD.

PD control methods, both linear and nonlinear cases, are studied and designed to achieve required dynamic performance while maintaining its simplicity and robustness that is suitable for real-time application. A thorough comparison between linear PD control and nonlinear PD control has been made. Simulation and experimental results have demonstrated the effectiveness of the ASS with LSRA when adopting these two control methods. Moreover, the proposed nonlinear PD control method enhances the robustness of the ASS and is more suitable in complicated road terrain than the linear PD controller.

The performance of the proposed nonlinear PD is preferable. However, the nonlinear PD is not capable of adjusting the control gains when the system parameters are varied. Advanced control methods, including sliding mode control and adaptive control, will be introduced in next chapter to achieve self-tuning of control gains.

Chapter 5 Advanced control methods for the quarter-car active suspension system

A number of advanced control methods have emerged and been adopted to wide range of applications for decades. Two advanced control methods are studied and distinguished in this research work: sliding mode control (SMC) method and adaptive control method. With an advantage of high simplicity and reliability as conventional PID control, SMC method is especially suitable for nonlinear system with parameters variations. Meanwhile, adaptive control method is employed to build up a reference model and forces the plant to approach the reference model.

In this chapter, both SMC and adaptive control methods are introduced to deal with the parameters variation and external disturbance. The design of the controllers is based on the nominal values of the quarter-car ASS, and the optimal values are determined by considering the margin of the stability.

5.1 Review of nonlinear control theories

5.1.1 Sliding mode control

Sliding mode control is a type of nonlinear control with high (ideally infinite) frequency switching discontinuous inputs. SMC is originated from the control of variable structure system (VSS) and has been studied for decades since 1950's. Nowadays, the SMC and VSS can further be used to analyse and stabilise the continuous linear and nonlinear systems due to simple structure and robustness. Research interest on SMC has aroused worldwide since the publication of a survey paper in 1977 [59], revealing that the attractive invariance property of SMC with regard to parameters uncertainties and external disturbances [140]. The system motion is switching between two distinctively different structures based on feedback signals, so called sliding mode. Following the high frequency switching action, for instance, two statuses "on" and "off" respectively, the system tracks the desired manifold to achieve the superb performance, renowned for its insensitivity to parameter variations and rejection of disturbances [44], [52]. The major drawback of this control structure is oscillation or chattering phenomenon due to the discontinuous nature of the control strategy and high frequency switching action. The chattering problem can be simply alleviated using saturation function instead of sign function; furthermore, a series of analytical design methods have been developed to reduce its effect, such as frequency shaping method [44], observer based method [42], regular form approach [141] and higher order method [142].

 The design procedure of sliding mode control consists of two stages [140]. First, the geometric manifolds are regarded as the desired dynamic behaviours, which are formulated to equations of sliding modes according to the desired performance criterion. Once the sliding modes are determined, the second task is to find out the discontinuous control law, in which the states of the system would be forced to reach and stay in the small vicinity boundary of the manifolds, thus the sliding modes exist. Following these two stages, decoupling and system order reduction can be achieved which benefits to control design and implementation [140].

 The conventional linear sliding mode is a reduced-order control method, which the system order is reduced by the dimension of the control input. This characteristic

reduces the calculation burden and is favoured in real time control application. However, the robustness of the controlled system is not guaranteed during the reaching phase unless the occurrence of sliding mode. To overcome this drawback, a novel type integral sliding mode control (ISMC) is studied in [140], [143], in which the order of the motion equation in ISMC equals the order of the original system. Thus, the robustness of the feedback system is guaranteed from the initial time instant.

5.1.2 Adaptive model following control

Linear model following control (LMFC) is an efficient control method used for optimal control on multivariable control systems by specifying a referenced model as the design objective [144], [145]. However, large plant parameter variations and external disturbances often deteriorate the performance of the linear method. Adaptive model following control (AMFC) is proposed to overcome this difficulty and is capable of achieving high performance in the presence of system perturbations [146], [147].

The primary objective of AMFC is to guarantee the state errors and output errors to converge to zero [147]. Based on different stability theorems, there are two classes of AMFC design method [148]: Lyapunov stability method based and Popov hyperstability theory based [149]. The first adaptive control law using Lyapunov stability methods is so-called model reference adaptive control method, which is used to identify the parameters and reconstruct the reference model [150], [151]. The major challenge using this method is the selection of positive definite Lyapunov function candidate with negative definite time derivative to assure the asymptotic stability. The second adaptive control law based on Popov hyperstability theory is an alternative to the first method without selecting of Lyapunov function. Design of AMFC based on Popov hyperstability theory allows the reconstruction of the controlled system. The forward path is a linear time-invariant operator with the property of strictly positive reality; the feedback path is a passive operator that satisfies the inequality [147]. This structure provides great flexibility in choosing adaptive rules [148].

5.2 Sliding mode control on quarter-car active suspension system

The control scheme of the proposed SMC for the quarter-car ASS is shown in Fig. 5-1. The control purpose is to generate the active force and track the required sprung mass position. An integral SMC is adopted for the quarter-car ASS, and then the design of the proposed controller is completed based on the knowledge of the plant.
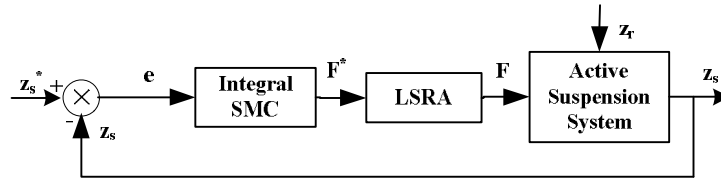
Fig. 5-1 SMC control scheme of the quarter-car ASS

5.2.1 State space equation

The model of the sprung mass subsystem can be obtained by rewriting (4-6)

$$M_s\ddot{z}_s + C_s\dot{z}_s + K_s z_s = F + C_s\dot{z}_u + K_s z_u \tag{5-1}$$

The parameters of the ASS have their nominal value and these values are obtained as a prior parameter. As aforementioned, the value of sprung mass varies from time to time. Supposed the nominal value of sprung mass is M_{so}, and the range of affordable load (weight) is $M_s \in \left[M_{s\,\min}, \quad M_{s\,\max} \right]$, thus the relationship between the nominal sprung mass and actual sprung mass is

$$M_{s\,\min} \le M_s = M_{so} + \Delta M_s \le M_{s\,\max} \tag{5-2}$$

where $M_{s\,\min}$ and $M_{s\,\max}$ are the minimum and maximum values of affordable load respectively, ΔM_s is the offset value from the nominal load. Therefore, the system matrices vary with the variation of sprung mass.

Furthermore, measurement errors due to the unpredictable noise should be considered since the car is exposed to the open field filled with electromagnetic

interference (EMI). There is an error position signal Δz_s between the filtered signals z_s and the real signal z_s^*, which is represented as

$$z_s = z_s^* + \Delta z_s \qquad (5\text{-}3)$$

As illustrated in Fig. 4-2, the filtered position signal has a perfect tracking performance using TD. Thus, it is reasonable to assume that $\Delta z_s = 0$ for a robust control that the time instant of the electromechanical system is relatively large, i.e. sensor and filter noise could be ignored during the procedure of controller design.

By ignoring sensor noise, parameter variation and external disturbance, the nominal model is obtained based on (5-1) and (5-2)

$$\begin{bmatrix} \dot{z}_s \\ \ddot{z}_s \end{bmatrix} = \begin{bmatrix} 0 & 1 \\ -K_s/M_{s0} & -C_s/M_{s0} \end{bmatrix} \begin{bmatrix} z_s \\ \dot{z}_s \end{bmatrix} + \begin{bmatrix} 0 \\ 1/M_{s0} \end{bmatrix} F_0 \qquad (5\text{-}4)$$

where F_0 is the nominal input force.

The nominal sprung mass model of (5-4) is a linear time-invariant system. The dynamic behaviour of the ASS can be determined by regulating the nominal control F_0. Assume that the reference input to be z_s^* and time derivative to be $\dot{z}_s^*$, thus the tracking error is $z_e = z_s - z_s^*$ and its time derivative is $\dot{z}_e = \dot{z}_s - \dot{z}_s^*$. The selection of nominal control F_0 is to guarantee the convergence of tracking error z_e. Assuming that the desired trajectory of the tracking error is given by

$$\ddot{z}_e + k_d \dot{z}_e + k_p z_e = 0 \qquad (5\text{-}5)$$

Using the direct computation method based on the nominal model without perturbations, the required nominal input force is obtained as

$$F_0 = M_{s0} \left(\ddot{z}_s^* - k_d \dot{z}_e - k_p z_e \right) + C_{s0} \dot{z}_s + K_{s0} z_s \qquad (5\text{-}6)$$

where M_{s0} is nominal load, K_{s0} is nominal spring stiffness and C_{s0} is nominal damping ratio.

Under the feedback control F_0 of (5-6), the tracking error z_e tends to zero asymptotically as expressed in (5-5). However, the tracking error is perturbed for a real quarter-car ASS with load variation ΔM_s and road disturbance z_r, the actual tracking error dynamic is ruled by

$$\ddot{z}_e = \frac{1}{M_s}\left(-C_s\dot{z}_s - K_s z_s\right) + \frac{1}{M_s}F - \ddot{z}_s^* + \frac{1}{M_s}\left(C_s\dot{z}_u + K_s z_u\right) \qquad (5\text{-}7)$$

where the control force

$$F = F_0 + F_d$$

is divided into two parts: nominal input F_0 to feedback control of the nominal system and compensation input F_d to the perturbed system,

5.2.2 Sliding surface

The quarter-car ASS is a second-order single input single output (SISO) linear system, the sliding surface is a switching line in the phase space. The hypersurface using conventional SMC rule is represented by a reduced-order equation

$$s_{z0} = \dot{z}_e + c z_e \qquad (5\text{-}8)$$

where $c > 0$ is a positive constant to determine the dynamic of the sliding surface. The time derivative of sliding surface s_{zo} is

$$\dot{s}_{z0} = \ddot{z}_e + c\dot{z}_e = \frac{1}{M_s}F_{smc} + d_{z0} \qquad (5\text{-}9)$$

where

$$d_{z0} = \frac{1}{M_s}\left(-C_s\dot{z}_s - K_s z_s\right) + \frac{1}{M_s}\left(C_s\dot{z}_u + K_s z_u\right) - \ddot{z}_s^* + c\dot{z}_e \qquad (5\text{-}10)$$

The control law F_{smc} is to force the error dynamic to reach the sliding surface $s_{z0} = 0$ and finally moves to the origin point, i.e. $z_e = 0$. Before reaching the sliding surface, the reduced order equation (5-8) is non-zero, i.e. $s_{z0} \neq 0$. The proposed integral SMC, in another way, makes the switching function stay at zero from the initial time instant by adding compensation function.

The sliding surface of the proposed controller is

$$s_z = s_{zo} + s_{zd} \tag{5-11}$$

with

$$\dot{s}_{zd} = \frac{C_s}{M_{s0}} \dot{z}_s + \frac{K_s}{M_{s0}} z_s - \frac{1}{M_{s0}} F_0 + \ddot{z}_s^* - c\dot{z}_e \tag{5-12}$$

and the initial condition of (5-12) is $s_{zd}(0) = -\dot{z}_e(0) - cz_e(0)$ to guarantee reaching of sliding surface at the initial time instant.

The derivative of the sliding mode is extracted from (5-6) to (5-12)

$$\dot{s}_z = \dot{s}_{z0} + \dot{s}_{zd} = \gamma_1 + \gamma_2 F_0 + \frac{1}{M_s} d_z + \frac{1}{M_s} F_d \tag{5-13}$$

where the first two items $\gamma_1 = \left(\frac{1}{M_{s0}} - \frac{1}{M_s} \right)(C_s \dot{z}_s + K_s z_s)$ and $\gamma_2 = \left(\frac{1}{M_s} - \frac{1}{M_{s0}} \right)$ are the mismatches between the nominal sprung load M_{s0} and the real load M_s, the third item is related to the real load and external disturbance $d_z = (C_s \dot{z}_u + K_s z_u)$.

5.2.3   Control law

The discontinuous control law of linear SMC is selected as

$$F_{d\_smc} = -K_z s_{z0} - N_z sat(s_{z0}, \Delta_z) \tag{5-14}$$

where $K_z \geq 0$ is a constant gain, and $N_z > M_{s\max} d_{z0\max}$ is the maximum positive gain, and $d_{z0\max} = \sup_{M_s} |d_{z0}|$ is the upper boundary of the disturbance. The saturation function $sat(s_{z0}, \Delta_z)$ is defined by (4-2) in which Δ_z denotes a small vicinity differs from sliding mode and is defined as the boundary layer within the range of $(0, \ 1)$.

As seen in (5-14), the discontinuous control law has been converted to continuous control by saturation function. The chattering problem can be alleviated. However, the reaching of sliding mode is made after a time interval.

The control law of ISMC is dedicated as

$$F_{ismc} = F_{0\_ismc} + F_{d\_ismc} \tag{5-15}$$

where F_{0_ismc} is the nominal feedback input and is obtained by (5-6)

$$F_{0\_ismc} = M_{s0}\left(\ddot{z}_s^* - k_d \dot{z}_e - k_p z_e\right) + C_{s0}\dot{z}_s + K_{s0}z_s$$

and F_{d_ismc} is the compensation force that is similar to (5-14)

$$F_{d\_ismc} = -K_{zd}s_z - N_{zd}sat\left(s_z, \Delta_z\right) \tag{5-16}$$

where

$$K_{zd} = \eta M_s, \ \ \forall \eta > 0 \tag{5-17}$$

$$N_{zd} = \tau_d M_s, \tau_d > 0 \tag{5-18}$$

here, τ_d is the upper boundary of generalised disturbance due to parameter variations and road profiles, i.e. $\tau_d = \sup\left|\gamma_1 + \gamma_2 F_{0\_ismc} + \dfrac{d_z}{M_s}\right|$. Let $\gamma_{1\max} = \sup_{M_s}|\gamma_1|$, $\gamma_{2\max} = \sup_{M_s}|\gamma_2|$ and $d_{z\max} = \sup_{M_s}|d_z|$ be the upper boundaries of the absolute value of γ_1 , γ_2 and d_z respectively, one possible form of τ_d is represented as

$$\tau_d = \gamma_{1\max} + \gamma_{2\max} \left| F_{0\_ismc} \right| + \frac{d_{z\max}}{M_{s\min}} \tag{5-19}$$

The control scheme of integral sliding mode control is figured out in Fig. 5-2.
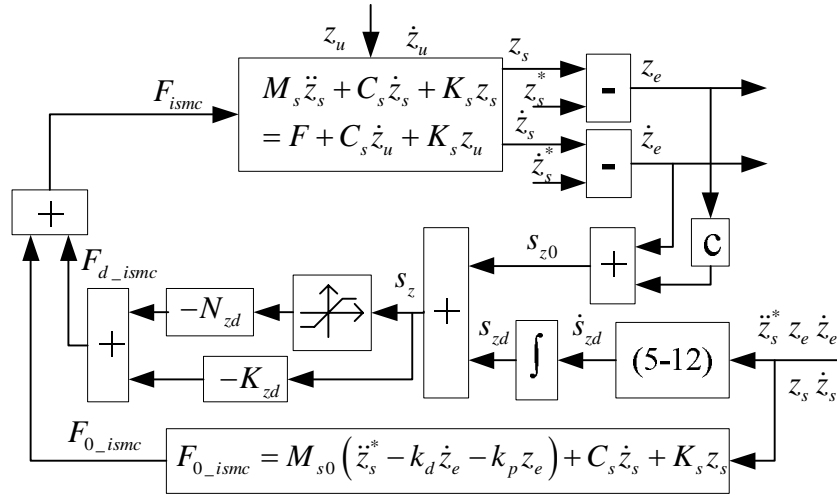
Fig. 5-2 Control law of ISMC

5.2.4 Stability analysis

The stability of the proposed sliding mode control system is analysed employing Lyapunov stability theorem. The positive definite Lyapunov function is selected as

$$V_z = \frac{1}{2} M_s s_z^2 \tag{5-20}$$

The derivative of the sliding mode is extracted by substituting (5-6) and (5-16) to (5-13)

$$\dot{s}_z = \gamma_1 + \gamma_2 F_{0\_ismc} + \frac{1}{M_s} d_z - \frac{K_{zd}}{M_s} s_z - \frac{N_{zd}}{M_s} sat\left(s_z, \Delta_z\right) \tag{5-21}$$

The derivative of the Lyapunov function is then expressed as

$$\dot{V}_z = M_s s_z \dot{s}_z$$

$$= M_s s_z \left(\gamma_1 + \gamma_2 F_{0\_ismc} + \frac{1}{M_s} d_z - \frac{K_{zd}}{M_s} s_z - \frac{N_{zd}}{M_s} sat(s_z, \Delta_z) \right) \tag{5-22}$$

$$\leq -K_{zd} s_z^2 + M_s \left(|s_z| \left| \gamma_1 + \gamma_2 F_{0\_ismc} + \frac{1}{M_s} d_z \right| - \frac{N_{zd}}{M_s} s_z sat(s_z, \Delta_z) \right)$$

The system is recognised as stable if the phase trajectory stays within the boundary layer. The system behaviour beyond the boundary layer is now considered by replacing the saturation function with the sign function. The derivative of Lyapunov function $\dot{V}_z$ is

$$\dot{V}_z \leq -K_{zd} s_z^2 + M_s |s_z| \left(\left| \gamma_1 + \gamma_2 F_{0\_ismc} + \frac{1}{M_s} d_z \right| - \frac{N_{zd}}{M_s} \right) \tag{5-23}$$

Substituting (5-17) and (5-18) into (5-23), we have

$$\dot{V}_z \leq -\eta M_s s_z^2 + M_s |s_z| \left(\left| \gamma_1 + \gamma_2 F_{0\_ismc} + \frac{1}{M_s} d_z \right| - \tau_d \right) \tag{5-24}$$

Based on (5-19), (5-24) can be simplified as

$$\dot{V}_z \leq -2\eta V_z < 0 \tag{5-25}$$

It has been proved that the positive define Lyapunov function V_z of (5-20) has negative time derivative function $\dot{V}_z$ of (5-25). Based on the Lyapunov stability theorem, the phase trajectory converges to zero exponentially and sliding mode occurs. The stability of the proposed quarter-car sprung mass subsystem is verified.

5.2.5 Robustness analysis

The robustness of the proposed ISMC can be guaranteed through regulating the compensation force F_{d_ismc}. The vertical vibration z_r during vehicle running is bounded, thus the displacement z_u and velocity $\dot{z}_u$ of unsprung mass subsystem due

to z_r are bounded. Thus, the upper bound of external disturbance $d_{z\max}$ exists. Meanwhile, the load of the sprung mass subsystem is bounded within the lightest value $M_{s\min}$ (only the driver) and heaviest value $M_{s\max}$ (loading capacity of the vehicle). Thus, the upper boundary τ_d exists. Theoretically, large τ_d enhances the robustness of the ISMC, at the risk of chattering issue due to high system gain. Hence, a reasonable τ_d should be moderately large to reject the system uncertainties and external disturbance and avoid being too high to cause system chattering.

To guarantee the robustness of the controller within the whole load variation and road distribution, the controller gains can be selected as follows

$$
\begin{cases}
K_{zd} = \eta M_{s\max} \\
N_{zd} = \tau_d M_{s\max} \\
\tau_d = \gamma_{1\max} + \gamma_{2\max}\left|F_{0\_ismc}\right| + \dfrac{d_{z\max}}{M_{s\min}}
\end{cases}
\tag{5-26}
$$

5.2.6 System characteristics analysis

The hypersurface of the sliding mode can be calculated from the integral function (5-21) that

$$
\begin{cases}
s_z = c_1 e^{-\frac{K_{zd}}{M_s}t} + \dfrac{M_s}{K_{zd}}\left(\gamma_1 + \gamma_2 F_{0\_ismc} + \dfrac{1}{M_s}d_z - \dfrac{N_{zd}}{M_s}sign(s_z)\right), \forall \left|s_z\right| > \Delta_z \\
s_z = c_2 e^{-\frac{K_{zd}\Delta_z + N_{zd}}{M_s\Delta_z}t} + \dfrac{M_s\Delta_z}{K_{zd}\Delta_z + N_{zd}}\left(\gamma_1 + \gamma_2 F_{0\_ismc} + \dfrac{1}{M_s}d_z\right), \forall \left|s_z\right| \leq \Delta_z
\end{cases}
\tag{5-27}
$$

If the system parameters C_s and K_s are accurate, i.e. $C_s = C_{s0}$ and $K_s = K_{s0}$. The equation (5-27) can be simplified as

$$
\begin{cases}
s_z = c_1 e^{-\frac{K_{zd}}{M_s}t} + \frac{M_s}{K_{zd}}\left(\left(\frac{M_{s0}}{M_s}-1\right)\left(\ddot{z}_s^* - k_d\dot{z}_e - k_p z_e\right) + \frac{1}{M_s}d_z - \frac{N_{zd}}{M_s}sign\left(s_z\right)\right), \forall \left|s_z\right| > \Delta_z \\
s_z = c_2 e^{-\frac{K_{zd}\Delta_z + N_{zd}}{M_s\Delta_z}t} + \frac{M_s\Delta_z}{K_{zd}\Delta_z + N_{zd}}\left(\left(\frac{M_{s0}}{M_s}-1\right)\left(\ddot{z}_s^* - k_d\dot{z}_e - k_p z_e\right) + \frac{1}{M_s}d_z\right), \forall \left|s_z\right| \leq \Delta_z
\end{cases}
$$

(5-28)

where c_1 and c_2 are constant parameters to fulfil the initial conditions and boundary conditions.

The error dynamic can be obtained by the combination of (5-7) and (5-28)

$$
\begin{cases}
\ddot{z}_e + k_d\dot{z}_e + k_p z_e = -\frac{K_{zd}}{M_s}c_1 e^{-\frac{K_{zd}}{M_s}t}, \forall \left|s_z\right| > \Delta_z \\
\ddot{z}_e + k_d\dot{z}_e + k_p z_e = -\frac{K_{zd}\Delta_z + N_{zd}}{M_s\Delta_z}c_2 e^{-\frac{K_{zd}\Delta_z + N_{zd}}{M_s\Delta_z}t}, \forall \left|s_z\right| \leq \Delta_z
\end{cases}
$$

(5-29)

The solution to the second-order linear differential equation (5-29) is

$$
\begin{cases}
z_e = c_3 e^{\lambda_1 t} + c_4 e^{\lambda_2 t} + c_5 e^{-\frac{K_{zd}}{M_s}t}, \forall \left|s_z\right| > \Delta_z \\
z_e = c_6 e^{\lambda_1 t} + c_7 e^{\lambda_2 t} + c_8 e^{-\frac{K_{zd}\Delta_z + N_{zd}}{M_s\Delta_z}t}, \forall \left|s_z\right| \leq \Delta_z
\end{cases}
$$

(5-30)

where $c_i, i = 3,...,8$ are the coefficients of the solution, λ_1 and λ_2 are the characteristic roots of the characteristic equations of (5-29), i.e.

$$
\lambda_{1,2} = -\frac{k_d}{2} \pm \sqrt{\frac{k_d^2}{4} - k_p}
$$

(5-31)

The selection of positive k_p and k_d ensures that the characteristic roots are negative real numbers or a pair of complex numbers whose real part are negative.

From equations (5-28), (5-29) and (5-30), it can be concluded that:

i) The error dynamic is determined by k_p and k_d. The error characteristics are affected by K_{zd} or η before reaching the sliding mode and is constrained by N_{zd} and Δ_z after reaching the sliding mode, as represented in (5-29).

ii) The ideal characteristics of steady error state system can be achieved theoretically:

$$
\begin{cases}
\lim_{t \to \infty} s_z = \dfrac{M_s \Delta_z}{K_{zd}\Delta_z + N_{zd}}\left(\left(\dfrac{M_{s0}}{M_s} - 1\right)\ddot{z}_s^* + \dfrac{1}{M_s}d_z\right) \\
\lim_{t \to \infty}\left(\ddot{z}_e + k_d \dot{z}_e + k_p z_e\right) = 0 \\
\lim_{t \to \infty} z_e = 0
\end{cases}
\tag{5-32}
$$

The sliding mode is affected by the parameter mismatching and external road oscillation. High gain τ_d can reduce the sliding error; however, the only issue to be noticed is that too high value of τ_d may cause the chattering problem.

5.2.7 Simulation results

Table 5-1 Parameters of ISMC controller

Symbol	Value
k_p	8
k_d	50
c	10
Δ_z	0.001
η	10
$\tau_d\,(SMC)$	5
$\tau_d\,(ISMC)$	1

The system parameters are specified in Table 4-2. The linear sliding surface determines the dynamics of the ASS, and the value of c is set to be 10 to achieve fast convergence. Besides, the selection of k_p and k_d depicts the dynamic behaviour of the tracking error and guarantees the global stability of the suspension system with positive values. The boundary layer Δ_z is selected as 0.001 to constrain the sliding surface in small vicinity. τ_d is selected to compensate the external disturbance and system nonlinearities. η is used to determine the exponential convergence speed. The

controller gains are listed in Table 5-1. The road profile is a periodically surface with three isolated bumps as described in Fig. 4-7.

Suppose the car is running on a road similar to the test rig. The output force of LSRA is restricted within [-900 N, 900 N] due to the mechanical limitation and protection of the whole system. To illustrate the effectiveness and improvement of the proposed control method, both linear SMC and developed ISMC are used to control the ASS with specified controller gains listed in Table 5-1. The integral sliding surface is composed of the linear sliding surface determined by c_0 and an integral item determined by k_p and k_d .

The responses of passive and ASS under the road profile of test rig have been shown in Fig. 5-3. It can be seen that both the displacements and accelerations of the car body converge to zero in a finite time with the presence of ASS, in which the load varies from 80% (reduced load) to 100% (nominal load) of its nominal value. Moreover, the performances of ISMC in two cases are consistently smooth when the vehicle encounters large hole. The displacement of linear SMC is similar to ISMC and converges to zero quickly under nominal load, as illustrated in Fig. 5-3(a); however, the performance deteriorates when the load varies to 80% of the nominal value, as depicted in Fig. 5-3(b). It can be proved that better dynamic performance is achieved by using ISMC. The cause of the response differences is due to the selection of sliding surface. In view of (5-8) and (5-11), the integral sliding surface and its derivative converges to zero immediately when the external disturbance is removed; while the conventional sliding surface may take a finite time to approach zero. The force is constrained at the maximum output of 900 N as shown in Fig. 5-3.
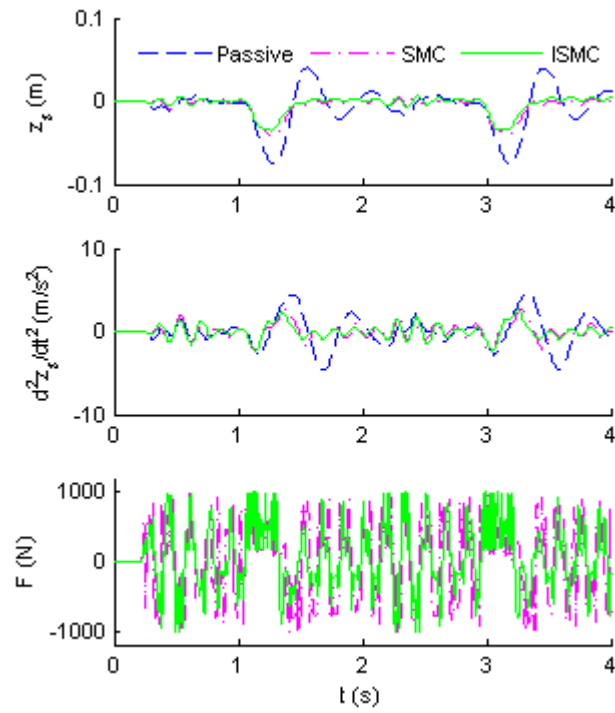
(a) $M_s = 100\% M_{s0}$
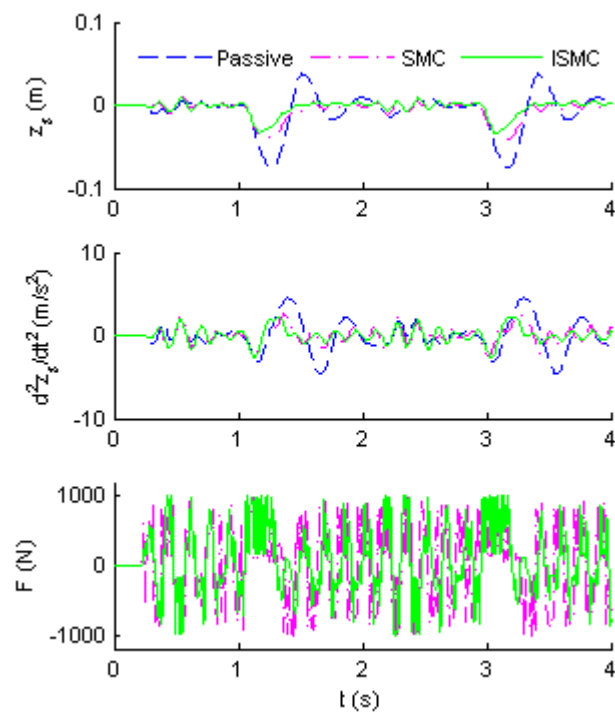
(b) $M_s = 80\% M_{s0}$

Fig. 5-3 Performance of SMC based ASS with different M_s
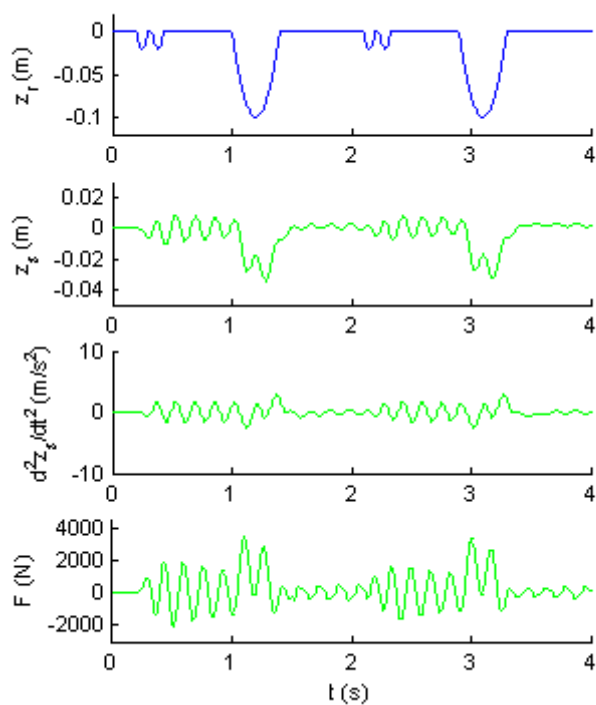
(a) $M_s = M_{s0}$
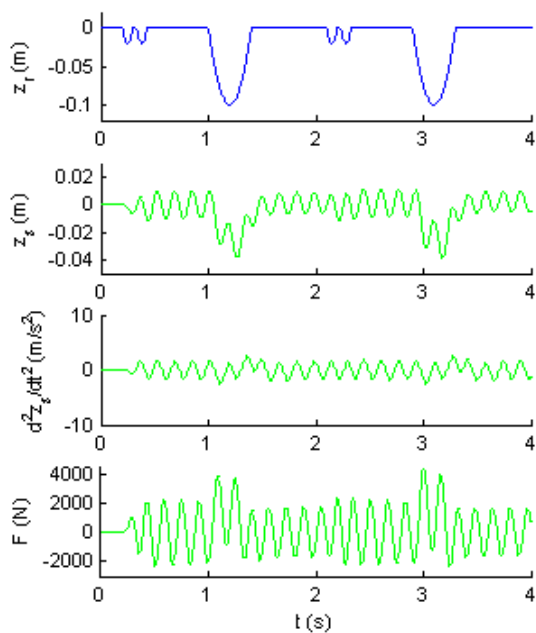
(b) $M_s = 80\% M_{s0}$

Fig. 5-4 Robustness of ISMC to twice amplitude of bump

The robustness of ISMC to road profile is demonstrated in Fig. 5-4. The road profile is now twice the amplitude of test rig. The mechanical and force output limitation are ignored in this situation. The displacement of the car body offset from reference point

when the vehicle falls into a large hole; then a large demand force is generated by ISMC to sustain the car body in its reference position. When the wheel passes the large hole, the car body returns to its reference position quickly. The largest displacement of car body is about 30% (nominal load, in Fig. 5-4(a)) or 40% (reduced load, in Fig. 5-4(b)) of the amplitude of the hole. The simulation results indicate the effectiveness of ISMC over a wide range of road profile.

5.2.8 Experimental results

Robustness of the proposed ISMC controller and linear SMC controller over variation of sprung masses has been carried out in the test platform. The experiment results indicate that ASSs are more effective than the passive suspension system as shown in Fig. 5-5. The displacements and accelerations of ASSs stay tightly at their reference lines all the time over smooth road surface. Once isolated bumps occur, the vertical vibration is suppressed significantly in active suspensions system whereas the passive suspension oscillates seriously for more than 1s which is around 4 times of the bump duration. The amplitudes of displacement of both linear SMC and ISMC are 0.03m in nominal load (in Fig. 5-5(a)) and 0.04m in reduced load (in Fig. 5-5(b)). The displacement difference between two ASSs is due to the load variation. Furthermore, the displacement dynamic of ISMC is better than that of linear SMC. When the car passes the large hole, the displacements of ISMC return to reference line quickly, and additional 0.1s is needed for SMC controller to retain the reference line. The system reaches the integral sliding mode immediately when the external disturbance is removed. On the other hand, linear SMC takes a finite time to approach its sliding mode. The experimental results reinforced that the performance of ISMC is better than SMC.
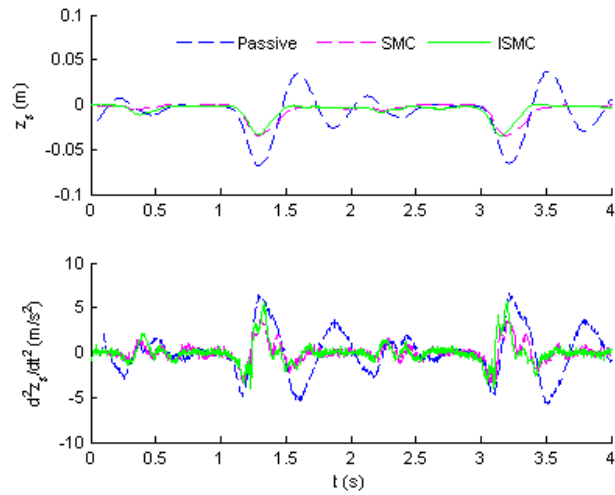
(a) $M_s = M_{s0}$
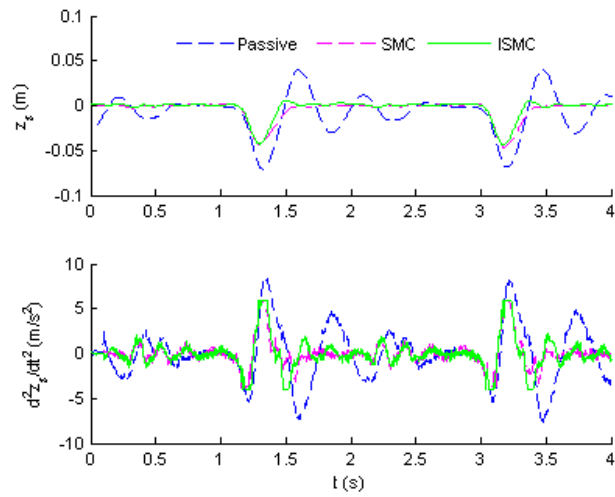
(b) $M_s = 80\%M_{s0}$

Fig. 5-5 Experimental results of SMC based ASS with reference to load variation

5.3 Adaptive model following control on quarter-car active suspension system

The control scheme of the proposed AMFC for the quarter-car ASS is shown in Fig. 5-6. z_s^* is the reference input, and the desired dynamic Z_m of the suspension system is determined by the reference model. Adaptive mechanism is used to regulate the input force to make the tracking error Z_e approach zero.
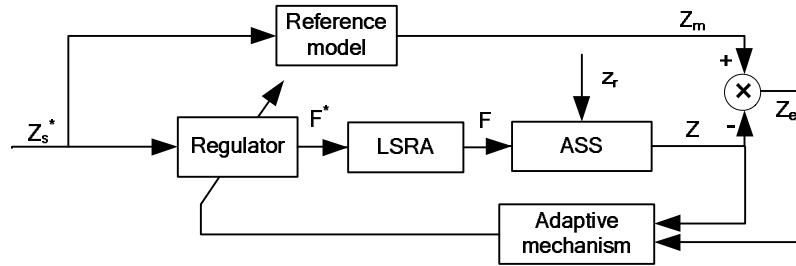
Fig. 5-6 AMFC control scheme of the quarter-car ASS

5.3.1 State space equation

The state space equation of the quarter-car ASS can be obtained by rewriting (5-1) as follows

$$\dot{Z} = AZ + BF + E \tag{5-33}$$

where $Z = \begin{bmatrix} z_s & \dot{z}_s \end{bmatrix}^T$ is the input vector and $E = \begin{bmatrix} 0 & \dfrac{K_s}{M_s} z_u + \dfrac{C_s}{M_s} \dot{z}_u \end{bmatrix}^T$ is the disturbance vector. The state matrix is $A = \begin{bmatrix} 0 & 1 \\ -K_s/M_s & -C_s/M_s \end{bmatrix}$, the input matrix is $B = \begin{bmatrix} 0 \\ 1/M_s \end{bmatrix}$.

The desired trajectory of the reference model is represented as

$$\dot{Z}_m = A_m Z_m + B_m z_s^* \tag{5-34}$$

where $Z_m = \begin{bmatrix} z_m & \dot{z}_m \end{bmatrix}^T$, $A_m = \begin{bmatrix} 0 & 1 \\ -a_0 & -a_1 \end{bmatrix}$, $B_m = \begin{bmatrix} 0 \\ 1 \end{bmatrix}$. Here, a_0 and a_1 are positive

constant which ensures the reference model stable. The system matrix A_m determines the dynamic characteristics of the reference model.

The motivation of adaptive control is to make the plant approach the reference model. Let $Z_e = Z_m - Z = \begin{bmatrix} z_m - z_s & \dot{z}_m - \dot{z}_s \end{bmatrix}^T$ be the error vector, the error dynamic system can be presented based on (5-33) and (5-34)

$$\dot{Z}_e = A_m Z_e + B_e \varsigma \qquad (5\text{-}35)$$

where $B_e = \begin{bmatrix} 0 & 1 \end{bmatrix}^T$, $\varsigma = -a_0 z_s - a_1 \dot{z}_s + z_s^* + \dfrac{K_s}{M_s} z_s + \dfrac{C_s}{M_s} \dot{z}_s - \dfrac{K_s}{M_s} z_u - \dfrac{C_s}{M_s} \dot{z}_u - \dfrac{1}{M_s} F$.

5.3.2 Adaptive control law

The error dynamic quarter-car system (5-35) can be rewritten to a standard form of Popov hyperstable system as follows

$$\dot{Z}_e = A_m Z_e + I_2 w_1 \qquad (5\text{-}36)$$

where I_2 is an identity matrix of order 2, $w = -w_1 = -B_e \varsigma$.

The output equation can be defined as

$$v_e = R_e Z_e \qquad (5\text{-}37)$$

where the output vector is $v_e = \begin{bmatrix} v_{e1} & v_{e2} \end{bmatrix}^T$, the positive definite symmetric output

matrix $R_e = \begin{bmatrix} R_{e1} & R_{e2} \\ R_{e2} & R_{e4} \end{bmatrix}$ is constrained by

$$R_e A_m + A_m^T R_e = -S_e \qquad (5\text{-}38)$$

here, $S_e = \begin{bmatrix} S_{e1} & S_{e2} \\ S_{e2} & S_{e4} \end{bmatrix}$ is a positive definite symmetric matrix. Thus, the constructed

system $\left(A_m, \quad I_2, \quad R_e \right)$ has a property of forward strictly positive reality.

The control law of the adaptive mechanism is divided into two parts: nominal feedback force F_0 and auto-regulating force F_r, i.e.

$$F = F_0 + F_r \qquad (5\text{-}39)$$

in which the nominal feedback force is based on parameters of the reference model and nominal variable of the plant M_{s0}

$$F_0 = M_{s0}\left(-a_0 z_s - a_1 \dot{z}_s + z_s^* \right) + K_s z_s + C_s \dot{z}_s \qquad (5\text{-}40)$$

The auto-regulating force is a form of unit vector control

$$F_r = M_{s\max}\left(\hat{\alpha}_1 \left| v_{e2} \right| + \hat{\alpha}_2 \left| \dot{z}_s \right| + \hat{\alpha}_3 \right) sign\left(v_{e2} \right) \qquad (5\text{-}41)$$

where $\hat{\alpha}_i \geq 0, i = 1, 2, 3$ are the estimated upper bound of α_i. The update law of the adaptive parameters $\hat{\alpha}_i$ is summarised as follows

$$\dot{\hat{\alpha}}_1 = k_1 \left| v_{e2} \right|^2, \dot{\hat{\alpha}}_2 = k_2 \left| v_{e2} \right| \left| \dot{z}_s \right|, \dot{\hat{\alpha}}_3 = k_3 \left| v_{e2} \right| \qquad (5\text{-}42)$$

where $k_{1,2,3} \geq 0$ are appropriate gains and $K = diag\left(k_1 \quad k_2 \quad k_3 \right)$ is a positive definite diagonal matrix. Let $\alpha = \begin{bmatrix} \alpha_1 & \alpha_2 & \alpha_3 \end{bmatrix}^T$, $\hat{\alpha} = \begin{bmatrix} \hat{\alpha}_1 & \hat{\alpha}_2 & \hat{\alpha}_3 \end{bmatrix}^T$, $\rho = \begin{bmatrix} \left| v_{e2} \right| & \left| \dot{z}_s \right| & 1 \end{bmatrix}^T$ and $\gamma = \alpha^T \rho$, then the update law of (5-42) can be rewritten as

$$\dot{\hat{\alpha}}_i = k_i \left| v_{e2} \right| \frac{\partial \gamma}{\partial \alpha_i} \ or \ \dot{\hat{\alpha}} = \left| v_{e2} \right| K \rho \qquad (5\text{-}43)$$

The synthesised adaptive control scheme is illustrated in Fig. 5-7. It is worthy to point out that the selection of known variable vector ρ is flexible, i.e. ρ with two elements is available to simplify the calculation burden.
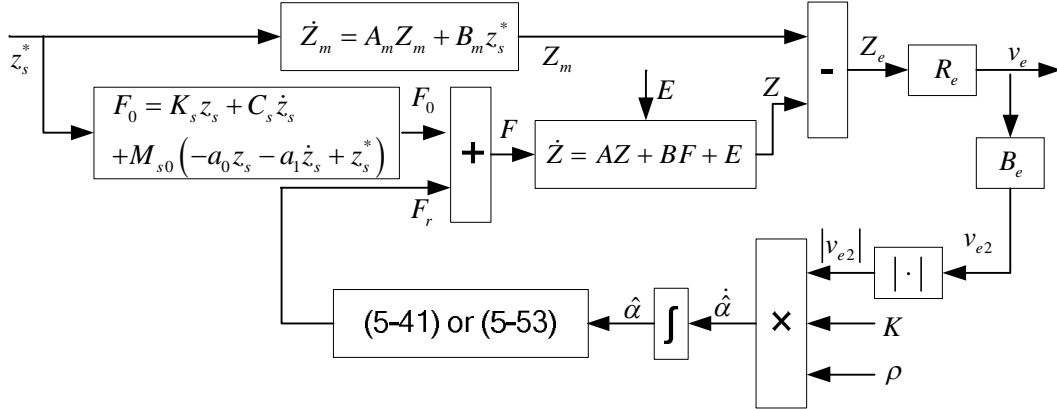
Fig. 5-7 Adaptive control mechanism

5.3.3 Stability analysis

The Popov stability theorem is presented here for the analysis of stability. First the following inequality is given

$$\int_0^t w^T(\tau) v_e(\tau) d\tau \geq -\gamma_0^2, \forall t \tag{5-44}$$

where γ_0^2 depends on the initial state of the system but does not depend on time t.

Popov stability theorem [149], [152]**.** For a given controllable and observable system $\left(A_m, \ I_2, \ R_e\right)$ described by (5-36), (5-37) and (5-38), and the control $w_1 = -w$ satisfies the inequality (5-44). The necessary and sufficient conditions of $\left(A_m, \ I_2, \ R_e\right)$ to be an asymptotically hyperstable system are that

1) the transfer matrix from w_1 to v_e: $G_e(s) = R_e\left(sI - A_m\right)^{-1} I_2$ be strictly positive real (in the sense that $G_e(s)$ is positive real for all s);

2) all the poles of $G_e(s)$ lie in the left half plane $\mathrm{Re}(s) < 0$;

3) $G_e(j\omega) + G_e^*(j\omega)$ should be positive definite Hermitian for all real ω.

The proof of the above theorem is referred to [149]. As mentioned before, the construction of the control system guarantees the strictly forward positive reality. Thus, the condition of ensuring hyperstability is to satisfy the inequality (5-44). The above inequality can be rewritten as

$$\int_0^t w^T(\tau) v_e(\tau) d\tau = -\int_0^t v_{e2}(\tau) \varsigma d\tau \geq -\gamma_0^2, \forall t \tag{5-45}$$

or

$$v_{e2}\varsigma \leq 0, \forall t > 0 \tag{5-46}$$

Substituting the expression of v_{e2} and ς into (5-46)

$$
\begin{aligned}
v_{e2}\varsigma = v_{e2}&\left(-a_0 z_s - a_1 \dot{z}_s + z_s^* + \frac{K_s}{M_s} z_s + \frac{C_s}{M_s}\dot{z}_s - \frac{K_s}{M_s} z_u - \frac{C_s}{M_s}\dot{z}_u - \frac{1}{M_s}F\right) \\
&\leq -\frac{1}{M_s}v_{e2}F_r + |v_{e2}|\left(\left|-\frac{K_s}{M_s}z_u - \frac{C_s}{M_s}\dot{z}_u\right| + \left|\left(1 - \frac{M_{s0}}{M_s}\right)\left(-a_0 z_s - a_1 \dot{z}_s + b_0 z_s^*\right)\right|\right)
\end{aligned}
$$

$$\tag{5-47}$$

There exist the boundaries (Caratheodory conditions) of system parameters and variables, also the external disturbance, as discussed in **Section 5.2**. Assume that the upper bounds are $\alpha_i \geq 0, i = 1, 2, 3$, therefore

$$v_{e2}\varsigma \leq -\frac{1}{M_s}v_{e2}F_r + |v_{e2}|\left(\alpha_1 |v_{e2}| + \alpha_2 |\dot{z}_s| + \alpha_3\right) \tag{5-48}$$

Substituting (5-41) into (5-48)

$$
\begin{aligned}
v_{e2}\varsigma &\leq -\frac{1}{M_s}v_{e2}F_r + |v_{e2}|\left(\alpha_1 |v_{e2}| + \alpha_2 |\dot{z}_s| + \alpha_3\right) \\
&\leq |v_{e2}|\left(\left(\alpha_1 - \hat{\alpha}_1\right)|v_{e2}| + \left(\alpha_2 - \hat{\alpha}_2\right)|\dot{z}_s| + \left(\alpha_3 - \hat{\alpha}_3\right)\right) \\
&= |v_{e2}|\Delta\alpha^T \rho
\end{aligned}
\tag{5-49}
$$

where $\Delta\alpha = \begin{bmatrix} \alpha_1 - \hat{\alpha}_1 & \alpha_2 - \hat{\alpha}_2 & \alpha_3 - \hat{\alpha}_3 \end{bmatrix}^T$ is the parameter error vector.

Select the Lyapunov function as

$$V\left(Z_e, \alpha, \rho\right) = Z_e^T R_e Z_e + \Delta\alpha^T \overline{K} \Delta\alpha \geq 0 \qquad (5\text{-}50)$$

where $\overline{K} = diag\left(\dfrac{1}{k_1} \quad \dfrac{1}{k_2} \quad \dfrac{1}{k_3} \right)$ is a positive definite diagonal matrix.

Assume that α is constant while updating, the derivative of $V\left(Z_e, \alpha, \rho\right)$ is

$$
\begin{aligned}
\dot{V}\left(Z_e, \alpha, \rho\right) &= \dot{Z}_e^T R_e Z_e + Z_e^T R_e \dot{Z}_e - 2\Delta\alpha^T \overline{K} \dot{\hat{\alpha}} \\
&= -Z_e^T S_e Z_e + 2v_{e2}\varsigma - 2\Delta\alpha^T \overline{K} \dot{\hat{\alpha}} \\
&\leq -Z_e^T S_e Z_e + 2|v_{e2}|\Delta\alpha^T \rho - 2\Delta\alpha^T \overline{K} \dot{\hat{\alpha}}
\end{aligned} \qquad (5\text{-}51)
$$

Substituting (5-43) into (5-51), we have

$$\dot{V}\left(Z_e, \alpha, \rho\right) \leq -Z_e^T S_e Z_e < 0 \qquad (5\text{-}52)$$

Therefore, the Lyapunov function (5-50) converges to zero point and stays there after a finite time, i.e. $z_e \to 0$, $\hat{\alpha} \to \alpha$.

5.3.4   Robustness analysis

The robustness of the proposed AMFC can be guaranteed through regulating the nominal force F_0 and compensation force F_r. As represented in (5-40) and (5-41), the output forces are unrelated to the actual mass; the only knowledge is the variation range and nominal value of the load. The displacements and velocities of the quarter-car system are bounded. Thus, the upper bound of parameters uncertainty and external disturbance exists. Without the prior knowledge of the ASS, the estimated upper bound can be evaluated quickly online.

The adaptation mechanism applied before is so-called unit vector control. The drawback of this mechanism is the risk of chattering problem due to the sign function. To eliminate the chattering problem and enhance the robustness of adaptive controller,

a modified update law using the saturation function is presented here [153]. The modified adaptive law is

$$
F_r = M_{s\max} \begin{cases} \dfrac{v_{e2}}{|v_{e2}|} \hat{\alpha}^T \rho, & if \ |v_{e2}| \hat{\alpha}^T \rho > \varepsilon \\[4mm] \dfrac{v_{e2}}{\varepsilon} \left(\hat{\alpha}^T \rho\right)^2, & if \ |v_{e2}| \hat{\alpha}^T \rho \leq \varepsilon \end{cases}
$$

(5-53)

where positive constant $\varepsilon > 0$ is the boundary of the adaptive controller. The stability analysis of the adaptive law with saturation function is similar to the unit vector control as discussed above.

5.3.5 Improvement of adaptation mechanism

The updated law of $\hat{\alpha}$ increases continuously as shown in (5-43). This behaviour will cause the chattering problem due to high gain. The estimated parameter vector is updated as

$$
\dot{\hat{\alpha}} = \beta \left(\|Z_e\|\right) |v_{e2}| \rho, \hat{\alpha}(0) \geq 0
$$

(5-54)

where $\|Z_e\| = \sqrt{z_e^2 + \dot{z}_e^2}$, $\beta\left(\|Z_e\|\right)$ is a hysteresis loop expressed as

$$
\beta\left(\|z_e\|\right) = \begin{cases} 1 & if \ \|z_e\| \geq \delta_2 \\ 0 & if \ \|z_e\| \leq \delta_1 \\ \beta\left(\|z_e\|\right) & else \end{cases}
$$

(5-55)

with

$$
\delta_1 = \sqrt{\dfrac{(3\varepsilon + h)}{\lambda_{S\min}}}, \ \delta_2 = \sqrt{\dfrac{\lambda_{R\max}}{\lambda_{R\min}}} \sqrt{\dfrac{(3\varepsilon + h)}{\lambda_{S\min}}}, \ \forall h > 0
$$

(5-56)

Here, $\lambda_{R\min}$ and $\lambda_{R\max}$ are the minimum and maximum eigenvalues of R_e, $\lambda_{S\min}$ is the minimum eigenvalue of S_e. Proof of the modified adaptation law is referred to Appendix II.

5.3.6   Simulation results

Assume the cut-off frequency of the reference model is $\omega_n = 30$ rad/s, then the reference parameters are $a_0 = \omega_n^2 = 30^2$ and $a_1 = \sqrt{2}\omega_n = 30\sqrt{2}$. Suppose $S_{e2} = 0$ and $R_{e2}/R_{e4} = \lambda = 10 < a_1$, and let $R_{e4} = 1$, therefore we have $R_{e2} = 10$. The minimum eigenvalue of S_e can be calculated from (5-38) as $\lambda_{S\min} = 2a_1 R_{e4} - 2R_{e2}$. The ratio $\lambda_{R\max}/\lambda_{R\min}$ is calculated from R_e, it may be selected with a relatively large value in case of the calculated value is too large. The parameters of the proposed AMFC controllers are listed in Table 5-2.

Table 5-2 Parameters of AMFC controller

Symbol	Value
a_0	900
a_1	42.4264
R_{e2}	10
R_{e4}	1
$\lambda_{R\max}/\lambda_{R\min}$	9
$\lambda_{S\min}$	64.8528
ε	0.05
k_1	80
k_2	20
k_3	0.05
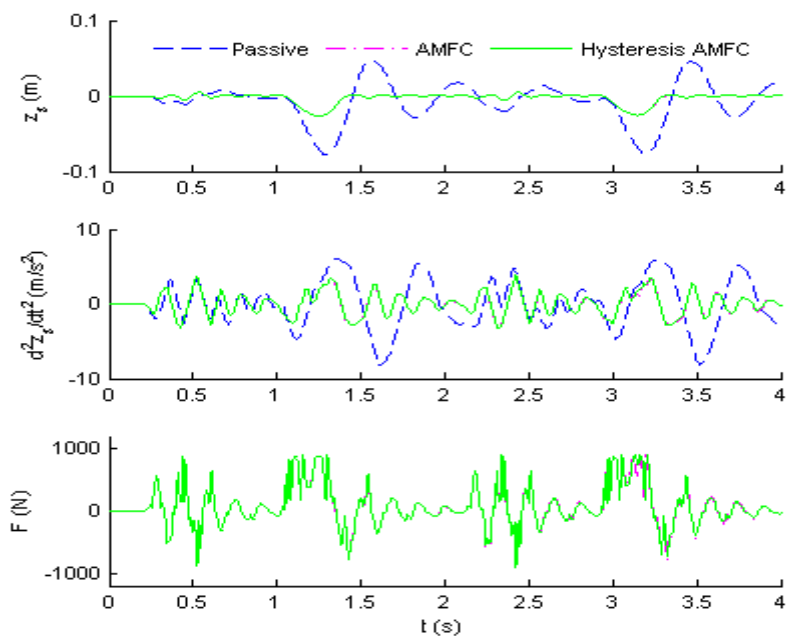
(a) $M_s = 100\% M_{s0}$
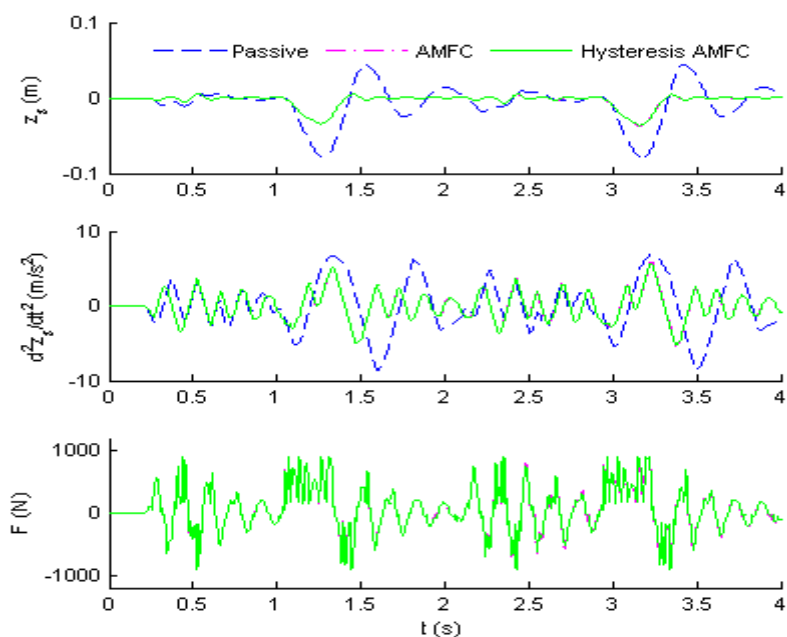
(b) $M_s = 80\% M_{s0}$

Fig. 5-8 Performance of AMFC based ASS with different M_s

When the car passes through the nominal bump, the output force F of LSRA is restricted within [-900N, 900N]. The adaptation mechanism, AMFC, is used to generate active force based on the errors between the system outputs and reference

signals. The effectiveness of the proposed AMFC is illustrated in Fig. 5-8. In Fig. 5-8(a), the nominal load lays at the sprung mass subsystem. The displacement of the car body tracks the reference line closely, even the appearances of small bumps. When the vehicle encounters with large bump, the car body falls into the hole about 0.03m depth and then returns to the reference line in 0.35s. The amplitude of acceleration is suppressed significantly by AMFC controller as compared to the passive mode. Similar responses are achieved when the load varies to 80% of its nominal value. The displacement amplitude increases with the reduction of load as shown in Fig. 5-8(b). The reason is that the inertia of the suspension system is reduced, and thus the system becomes sensitive to the external disturbance. The responses of displacement and acceleration of active suspension based on hysteresis AMFC are almost the same with AMFC based system with reference to load variation, as depicted in Fig. 5-8. The effectiveness of both AMFC and hysteresis AMFC are verified through simulation results.

To illustrate the improvement of the proposed hysteresis AMFC method, the estimated values of $\hat{\alpha}$ are shown in Fig. 5-9. Under AMFC scheme, the estimated values of $\hat{\alpha}$ increase continuously. Meanwhile, the value of $\hat{\alpha}$ in hysteresis mechanism freezes when the system is within the boundary layer. In a long run, the estimated values will increase to excessive values, especially when the system is exposed to harsh road and light load. As shown in Fig. 5-9(b), $\hat{\alpha}$ increases rapidly with time, and large $\hat{\alpha}$ causes the risk of system oscillation based on AMFC. The hysteresis scheme can prevent the rapid increasing of $\hat{\alpha}$ which in turn reduces the risk of system crashing.
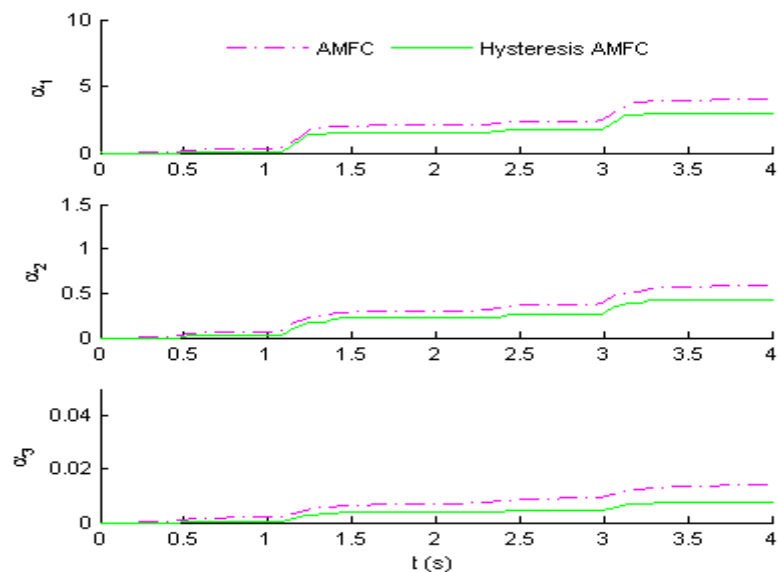
(a) $M_s = 100\% M_{s0}$
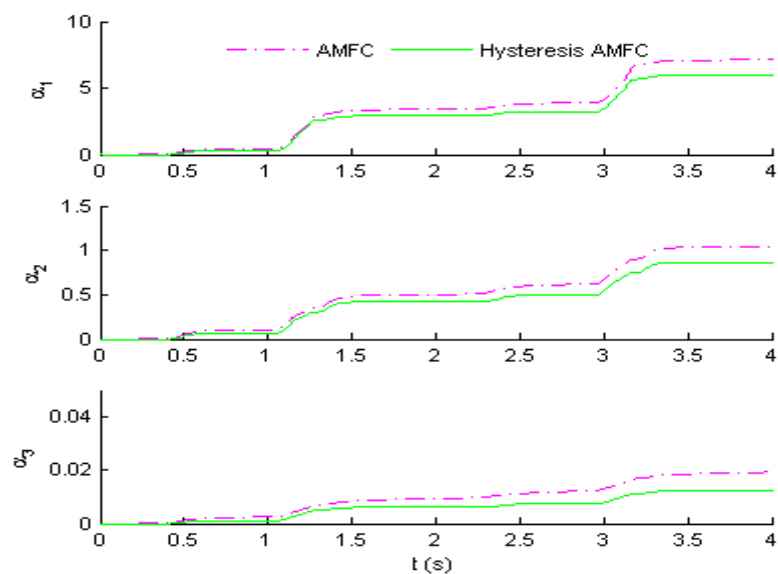
(b) $M_s = 80\% M_{s0}$

Fig. 5-9 Estimated values of α

The robustness of AMFC to road profile is illustrated in Fig. 5-10, by increasing the road amplitude twice of the test rig. The mechanical and force output limitation are ignored. The vertical responses of sprung mass system are similar under different road profiles. The displacement of the car body returns to the reference line quickly when the wheel passes the large hole. The largest displacement of car body is about 0.02m,

i.e. 20% of the amplitude of the hole regardless of load variation. The simulation results depicted in Fig. 5-10 indicate the displacement of car body is suppressed significantly under AMFC control over a wide range of road profile.
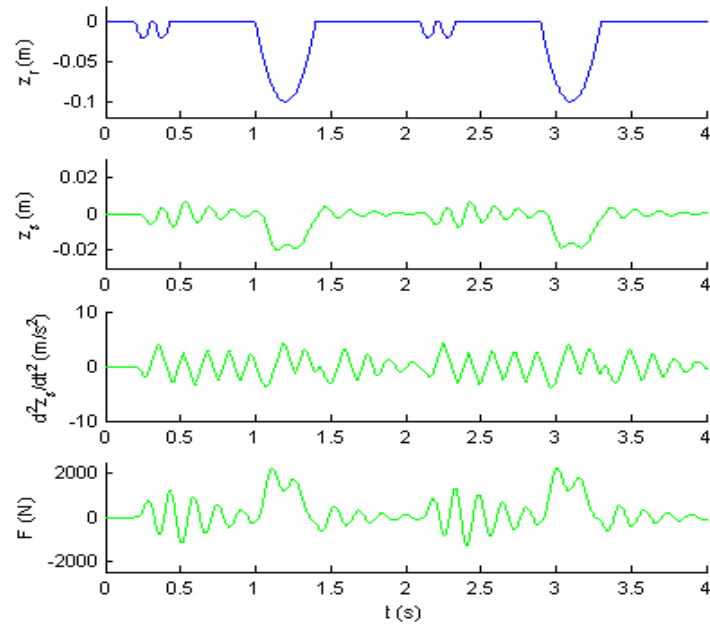
(a) $M_s = 100\% M_{s0}$
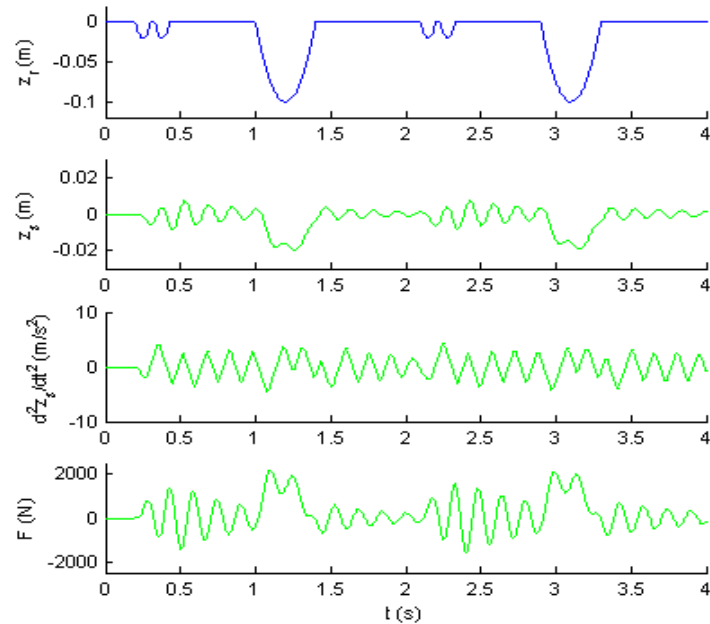
(b) $M_s = 80\% M_{s0}$

Fig. 5-10 Robustness of AMFC to twice amplitude of bump

5.3.7 Experimental results

Robustness of the proposed AMFC controller and hysteresis AMFC controller with regard to load variation has been carried out in the test platform. The experiment results indicate that ASSs are more effective than the passive suspension system, even though the prior knowledge of the system is unknown. As shown in Fig. 5-11, the displacements and accelerations of ASSs stay tightly at their reference lines all the time over smooth road surface. Once isolated bumps occur, the vertical vibration is suppressed significantly in active suspensions system whereas the passive suspension oscillates seriously for more than 1s which is around 4 times of the bump duration. The amplitudes of displacement of both AMFC and hysteresis AMFC are 0.03m in nominal load (in Fig. 5-11(a)) and 0.04m in reduced load (in Fig. 5-11(b)). The minor mismatch of curves of displacements for AMFC and hysteresis AMFC is caused by different update rule of control gains. The suspension system based on AMFC is more sensitive to variations of load and disturbance than that of hysteresis AMFC. The difference, however, is relatively minor. In other words, hysteresis loop has no additional disadvantage to suppress the vertical oscillation. In fact, the introduction of hysteresis can prevent the controller gains from increasing too large that is shown in Fig. 5-9.
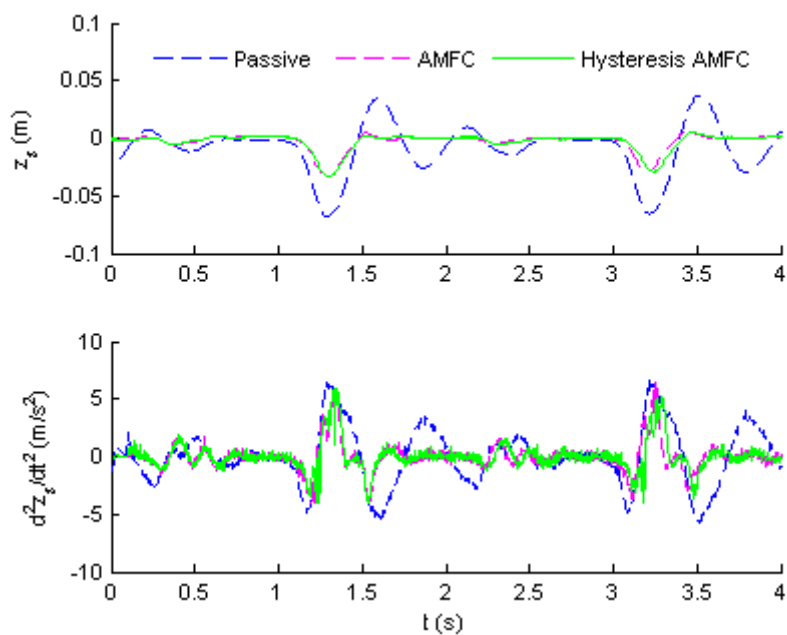
(a) $M_s = 100\% M_{s0}$
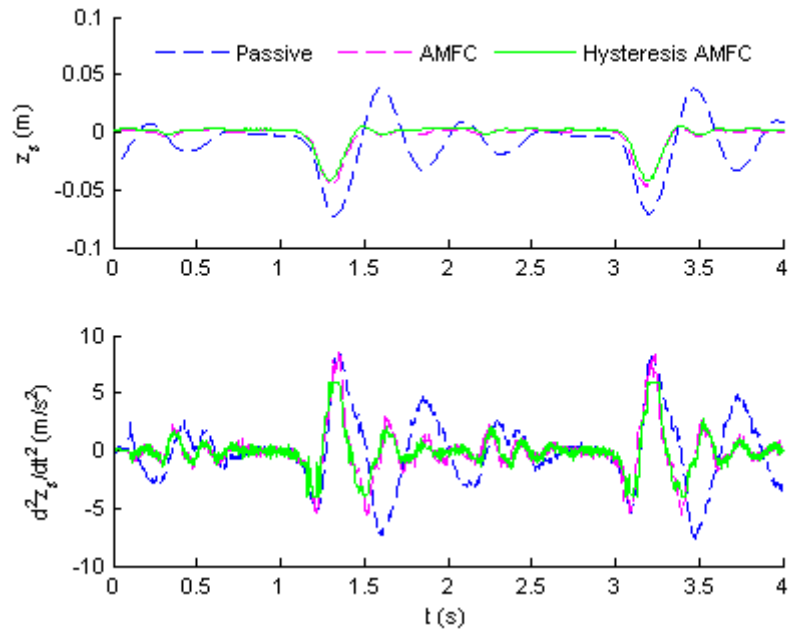
(b) $M_s = 80\% M_{s0}$

Fig. 5-11 Experimental results of AMFC based ASS with reference to load variation

5.4 Adaptive ISMC on quarter-car active suspension system

Two nonlinear control methods, ISMC and AMFC, have been studied. The ISMC enhances the robustness of the controlled system in a simple way. However, its control law requires constant discontinuous controlled parameters, which may be too large for some situations, such as a bump below horizontal surface or negative half part of sinusoidal road. The AMFC provides an online parameters estimation scheme without fully knowledge of the system. However, it has to construct a refined forward model to persist the strict positive reality and feedback inequality. One intuitive way is trying to combine two methods and to develop a robust online estimation mechanism, so-called Adaptive ISMC. Parameter identification is used here to ensure that the system follow the desired trajectory without the knowledge of the ASS. The elements of coefficient matrix are time slowly varying.

The model dynamic and sliding surface is similar to the ISMC as expressed above. The gain of the controller is tuned continuously by adaptive mechanism, and the Lyapunov function is modified to fit the proposed method.

5.4.1 Adaptive sliding mode control law

Let $\gamma_s = \alpha_s^{T}\rho$ be the upper bound of the external disturbance and system parameters, $\alpha_s = \begin{bmatrix} \alpha_{s1} & \alpha_{s2} & \alpha_{s3} \end{bmatrix}^{T}$, $\alpha_{si} > 0$ is the slow time-varying coefficients, then we have the following inequality

$$\gamma_1 + \gamma_2 F_0 + \frac{1}{M_s}d_z \leq \gamma_s \qquad (5\text{-}57)$$

The compensation force can be modified by rewriting (5-16) using adaptive mechanism. One of the available forms is

$$F_r = -\eta M_s s_z - M_s \begin{cases} \dfrac{s_z}{|s_z|}\hat{\alpha}_s^{T}\rho & |s_z|\hat{\alpha}_s^{T}\rho > \Delta \\[3mm] \dfrac{s_z}{\Delta}\left(\hat{\alpha}_s^{T}\rho\right)^2 & |s_z|\hat{\alpha}_s^{T}\rho \leq \Delta \end{cases} \qquad (5\text{-}58)$$

where $\hat{\alpha}_s$ is the estimation of α_s and is updated as

$$\dot{\hat{\alpha}}_s = \begin{cases} |s_z|\rho & |s_z|\hat{\alpha}_s^T \rho > \Delta \\ 0 & |s_z|\hat{\alpha}_s^T \rho \le \Delta \end{cases} \tag{5-59}$$

The adaptive ISMC control scheme is synthesised in Fig. 5-12.
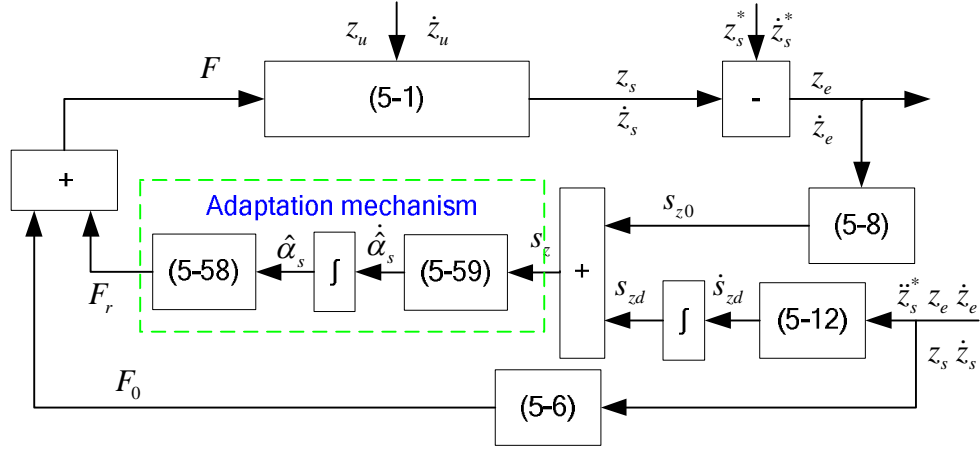
Fig. 5-12 Control scheme of adaptive ISMC

5.4.2 Stability analysis

The Lyapunov function is refined as

$$V_z = \frac{1}{2}M_s s_z^2 + \frac{1}{2}M_s \Delta\alpha_s^T \Delta\alpha_s \tag{5-60}$$

where $\Delta\alpha_s = \hat{\alpha}_s - \alpha_s$ is the coefficients error vector.

The time derivative of the Lyapunov function is

$$\begin{cases} \dot{V}_z \le -\eta M_s s_z^2 < 0 & if \ |s_z|\hat{\alpha}_s^T \rho > \Delta \\ \dot{V}_z \le -\eta M_s s_z^2 + M_s |s_z|\hat{\alpha}_s^T \rho \left(1 - \dfrac{|s_z|\hat{\alpha}_s^T \rho}{\Delta}\right) & if \ |s_z|\hat{\alpha}_s^T \rho \le \Delta \end{cases} \tag{5-61}$$

Suppose that $\hat{\alpha}_s$ starts at a small value, and s_z offsets from the origin point, then $|s_z|$ will increase. If $|s_z|\hat{\alpha}_s^T \rho \le \Delta$ occurs, $\hat{\alpha}_s$ is frozen; once $|s_z|\hat{\alpha}_s^T \rho > \Delta$ appears, $\hat{\alpha}_s$ increases and forces $\dot{V}_z < 0$, s_z will converge to zero and $\hat{\alpha}_s$ will approach to α_s.

This situation may repeat during a finite time T_0 depends on the maximum value of α_s divided by slope of $\dot{\hat{\alpha}}_s$, i.e. $T_0 = \max\limits_{j=1,\cdots,3}\left(\dfrac{\alpha_{sj}}{\dot{\hat{\alpha}}_{sj}}\right)$.

After T_0, $\hat{\alpha}_s$ is greater than α_s, i.e. $\hat{\alpha}_s^{\ T}(T_0) > \alpha_s$. The time derivative $\dot{V}_z$ is constraint in case II with $|s_z|\hat{\alpha}_s^{\ T}\rho \leq \Delta$. In that case, there is no guarantee that $\dot{V}_z$ is positive or negative.

$$\dot{V}_z \leq -\eta M_s s_z^{\ 2} + M_s |s_z|\hat{\alpha}_s^{\ T}\rho\left(1 - \frac{|s_z|\hat{\alpha}_s^{\ T}\rho}{\Delta}\right), \quad \forall \ |s_z|\hat{\alpha}_s^{\ T}\rho \leq \Delta \qquad (5\text{-}62)$$

The time derivative of Lyapunov function can be classified into two cases

$$\begin{cases} \dot{V}_z \leq 0 & |s_z| \geq \dfrac{\hat{\alpha}_s^{\ T}(T_0)\rho}{\dfrac{\left(\hat{\alpha}_s^{\ T}(T_0)\rho\right)^2}{\Delta} + \eta} \\[4em] \dot{V}_z > 0 & |s_z| < \dfrac{\hat{\alpha}_s^{\ T}(T_0)\rho}{\dfrac{\left(\hat{\alpha}_s^{\ T}(T_0)\rho\right)^2}{\Delta} + \eta} \end{cases} \qquad (5\text{-}63)$$

It can be seen from (5-63) that large η and small Δ is beneficial to keep the sliding mode staying near the vicinity of zero point. The sliding mode may oscillate within $\dfrac{\hat{\alpha}_s^{\ T}(T_0)\rho}{\dfrac{\left(\hat{\alpha}_s^{\ T}(T_0)\rho\right)^2}{\Delta} + \eta}$. It is worthy to note that an appropriate initial value of $\hat{\alpha}_s(0)$ is helpful to decrease the converging time and reduce the oscillation procedure, which improve the dynamic performance of the ASS.

5.4.3　Simulation results

The parameters of the proposed adaptive ISMC controllers are listed in Table 5-3.

Table 5-3 Parameters of adaptive IMSC controller

Symbol	Value
λ	10
η	8
Δ	0.05
k_1	5
k_2	1
k_3	0.01
$\hat{\alpha}_1(0)$	1
$\hat{\alpha}_2(0)$	1
$\hat{\alpha}_3(0)$	005

When the car passes through the nominal bump, the output force F of LSRA is restricted within [-900N, 900N]. By selecting appropriate initial value of $\hat{\alpha}(0)$, the adaptive scheme will estimate the disturbance and converge the system to zero point quickly. The effectiveness of the proposed adaptive ISMC scheme is illustrated in Fig. 5-13. The performance of adaptive ISMC is similar to ISMC by comparing Fig. 5-3 and Fig. 5-13, with regard to load variation. The displacement amplitudes are 0.03m (nominal load, in Fig. 5-13(a)) and 0.035m (nominal load, in Fig. 5-13(b)), respectively. The amplitudes of acceleration are suppressed by adaptive ISMC controller as compared to the passive mode in both cases. The achieved performance of adaptive ISMC indicates that the proposed controller is effective in a class of systems with unknown or partially known system knowledge is available.
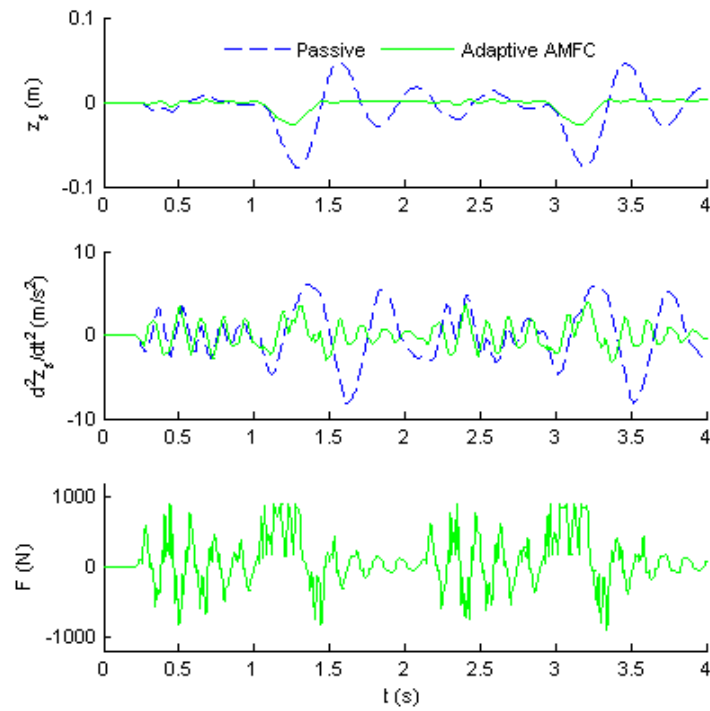
(a) $M_s = 100\% M_{s0}$
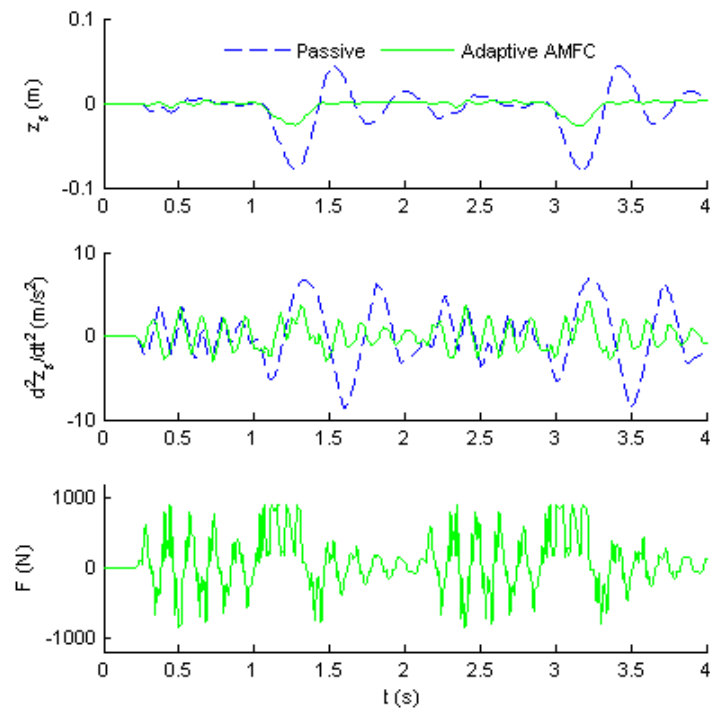
(b) $M_s = 80\% M_{s0}$

Fig. 5-13 Performance of adaptive ISMC based ASS with different M_s

The robustness of the proposed controller is guaranteed by sliding mode technique, as illustrated in Fig. 5-14. The amplitude of road increases to twice of nominal value. The mechanical and force output limitation are ignored in this situation. The vertical responses of sprung mass system are similar under different road profiles. In both Fig. 5-14(a) and (b), the maximum displacements of the car body during the first period are 0.025m whereas the maximum displacements are 0.02m in the second period. The difference is due to the controller gains increase with output errors through adaptation mechanism and the force output is higher in second period than that of the first period. The simulation results depicted in Fig. 5-14 indicate the effectiveness of adaptive ISMC over a wide range of road profile.
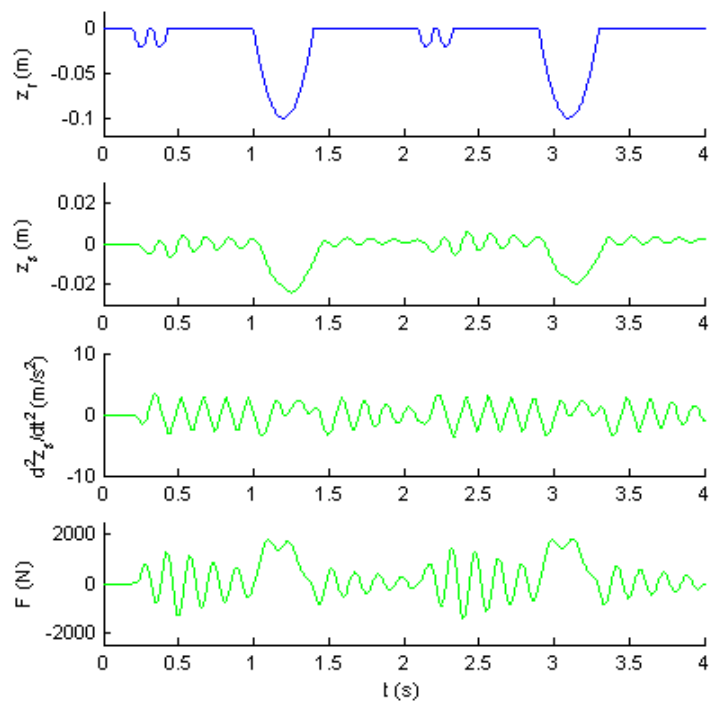
(a) $M_s = 100\% M_{s0}$
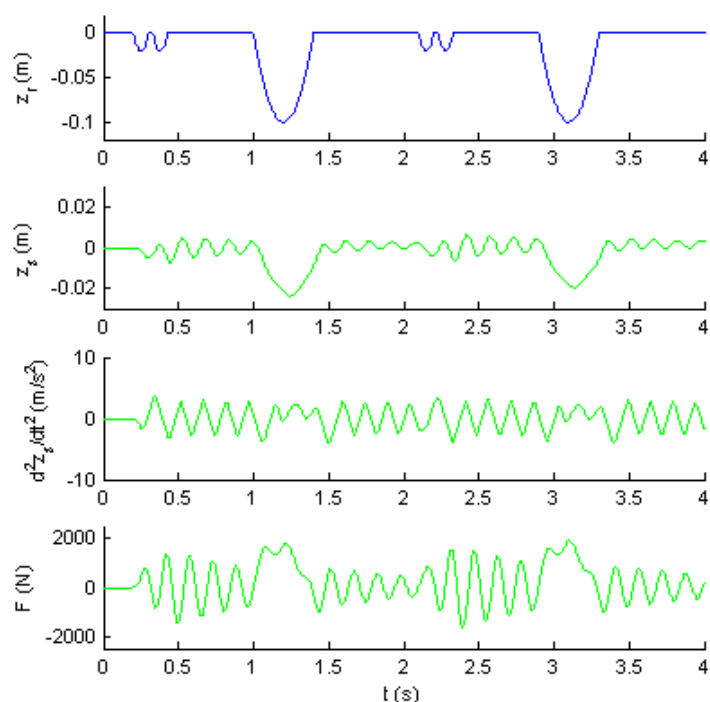
(b) $M_s = 80\% M_{s0}$

Fig. 5-14 Robustness of adaptive ISMC to twice amplitude of bump

5.4.4 Experimental result

Robustness of the proposed adaptive ISMC with regard to load variations has been carried out in the test platform. The experiment results indicate that ASSs are more effective than the passive suspension system, even though the prior knowledge of the system is unknown. The dynamic performance of adaptive ISMC is similar to that of ISMC, as shown in Fig. 5-5 and Fig. 5-15. The amplitudes of displacement of adaptive ISMC are 0.03m in nominal load (in Fig. 5-15(a)) and 0.045m in reduced load (in Fig. 5-15(b)). The experimental results verify the remarkable advantages of the proposed adaptive ISMC scheme, which combines the simplicity and robustness. Besides, the control gains vary with the output error that is more flexible than that of ISMC control scheme.
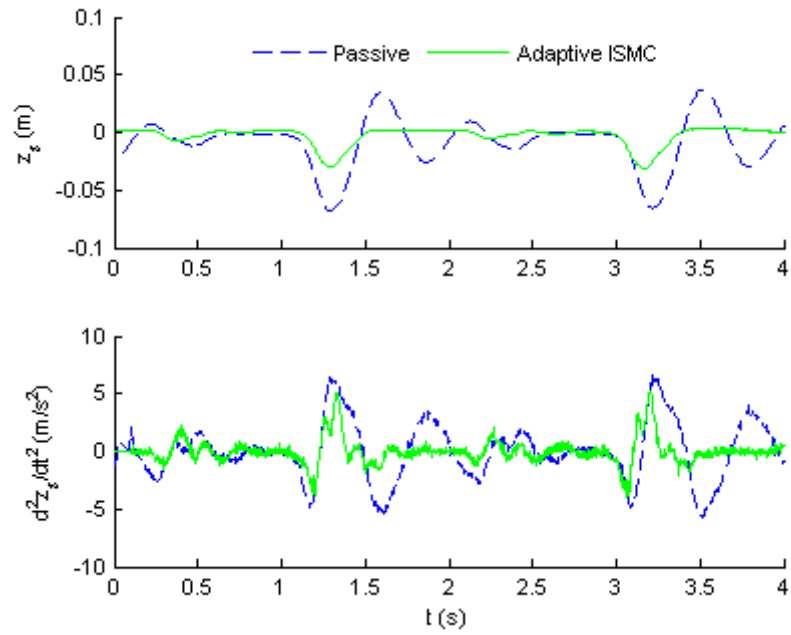
(a) $M_s = 100\% M_{s0}$
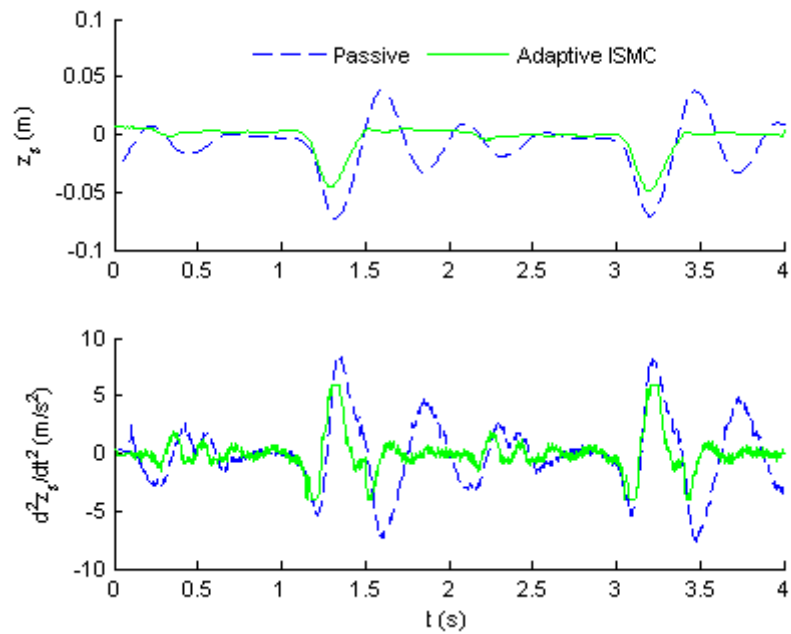
(b) $M_s = 80\% M_{s0}$

Fig. 5-15 Experimental results of adaptive ISMC based ASS with reference to load

variation

5.5 Comparison among different control methods

Various nonlinear control methods have been demonstrated in this research. The first proposed control method is nonlinear proportional-derivative control with time-varying control gains based on feedback errors. It maintains the characteristics of classical PD control with simple structure and control law. The second control method is integral sliding mode control renowned for its simplicity and robustness. An integral part is incorporated into the linear sliding surface to guarantee the reaching of sliding surface at the initial time instant. The knowledge of upper boundary of the ASS is needed for the control of ISMC. The third developed control method is adaptive model following control. To converge the output error to zero, model reconstruction method is employed to guarantee the control law fulfil the required conditions of Popov hyperstability theorem. The adaptive law can estimate the parameter variations and external disturbance, thus prior knowledge is not required. The fourth control method is a combination of sliding mode technique and adaptation mechanism. It can obtain the advantages of both control methods: simplicity, robust, and without prior knowledge. Their performances are examined with regard to load variation by both simulation and experiment results.

For further study, comparisons among those aforementioned control algorithms are explored here. Suspension load is the most likely varied parameter of the suspension system, responses against load variation are needed to be studied. Besides, stiffness of the coil spring will be decreased after long-time utilization, thus the responses against stiffness variation are also needed to be studied. In this section, responses with regard to load and stiffness variations are simulated to demonstrate the performances of different control algorithms. As shown in Fig. 5-16, both load and stiffness vary from 80% to 100% of their nominal values. A combination of simulation results with regard to different system parameters are illustrated below, including 100% load and 100% stiffness (Fig. 5-16(a)), 80% load and 100% stiffness (Fig. 5-16(b)), 100% load and 80% stiffness (Fig. 5-16(c)), and 80% load and 80% stiffness (Fig. 5-16(d)).

It can be observed that all control methods are effective and can converge the displacement and acceleration to zero when the external disturbance returned to zero. Moreover, the impacts of load variation and stiffness change on the ASS are different

as shown at Table 5-4. Suppose the stiffness is constant, the load range from 80% to 100% of its nominal value, as shown in pairs of Fig. 5-16(a) and (b) or (c) and (d), the maximum values of displacement are similar, about 0.03m with 100% stiffness and 0.02m with 80% stiffness. While the stiffness changes, the response of the displacement changes significantly, about 33% of the original amplitude. The main reason is that the passive force generated by coil spring is reduced and the active force can compensate the force gap. With regard to the total output force of the system that is composed of passive force and active force, the proportion of active force has been increased, hence the suspension system is more active and the vertical vibration can be suppressed fast. The accelerations of different control methods against parameter variations are similar to the responses of displacement.

From Fig. 5-16 , quarter-car ASS under different control methods performs well against parameter variations. The simulation results verify the effectiveness of the developed controllers. Furthermore, the AISMC can obtain good performance with the characteristics of simple and robust, it is suitable for the application of suspension systems equipped at different vehicle models since it can estimate the system parameters without prior system knowledge.

Table 5-4 Maximum values of sprung mass variables under different control methods

		NPD	ISMC	AMFC	AISMC
Nominal load Nominal stiffness	z (m)	0.035	0.029	0.027	0.028
	$\ddot{z}$ (m/s^2)	5.04	3.71	3.79	3.93
Reduced load Nominal stiffness	z (m)	0.031	0.028	0.036	0.027
	$\ddot{z}$ (m/s^2)	3.9	4.1	5.67	4.24
Nominal load Reduced stiffness	z (m)	0.018	0.016	0.014	0.023
	$\ddot{z}$ (m/s^2)	3.66	3.52	3.82	3.71
Reduced load Reduced stiffness	z (m)	0.02	0.018	0.015	0.017
	$\ddot{z}$ (m/s^2)	3.77	3.72	3.8	3.57

(Note: Reduced load equals 80% of nominal load, reduced stiffness equals 80% of nominal stiffness)
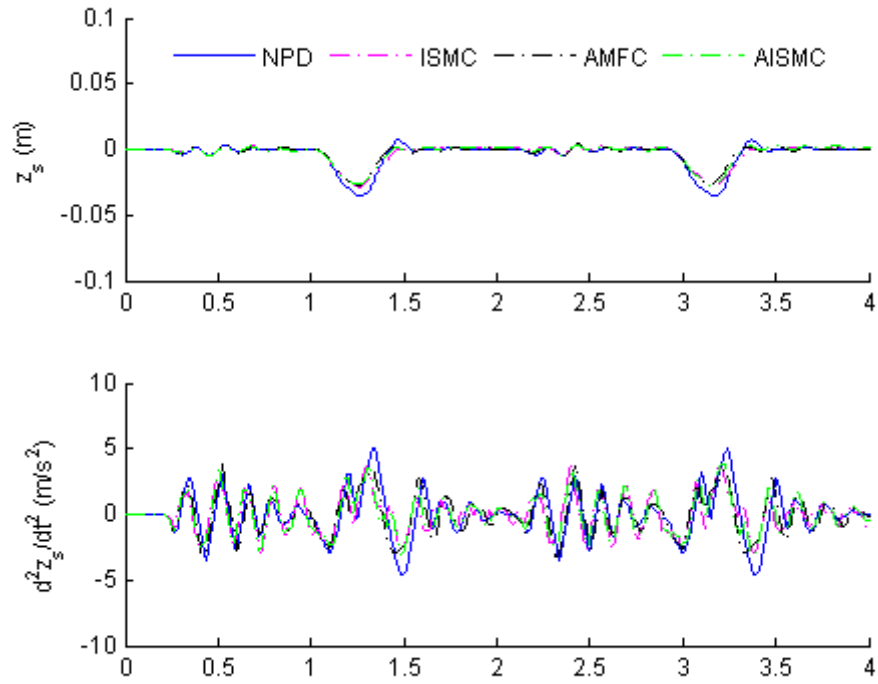
(a) $M_s = 100\% M_{s0}$, $K_s = 100\% K_{s0}$
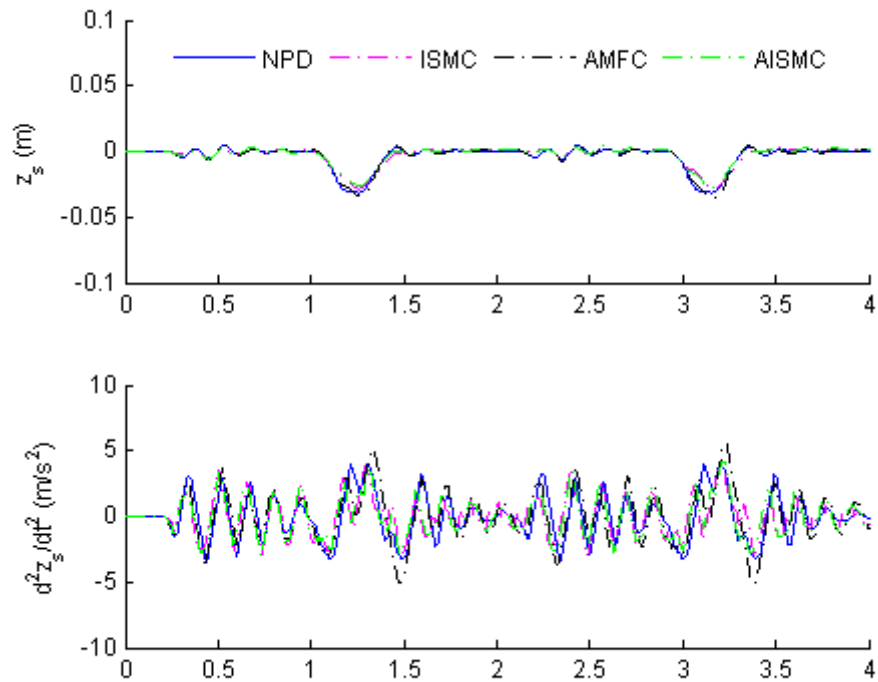
(b) $M_s = 80\% M_{s0}$, $K_s = 100\% K_{s0}$
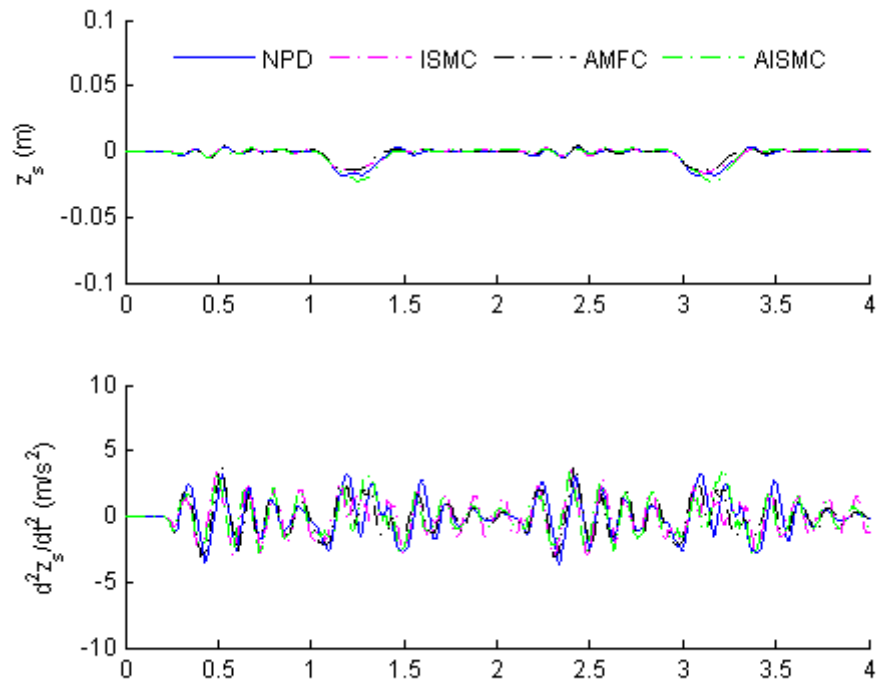
(c) $M_s = 100\% M_{s0}$, $K_s = 80\% K_{s0}$
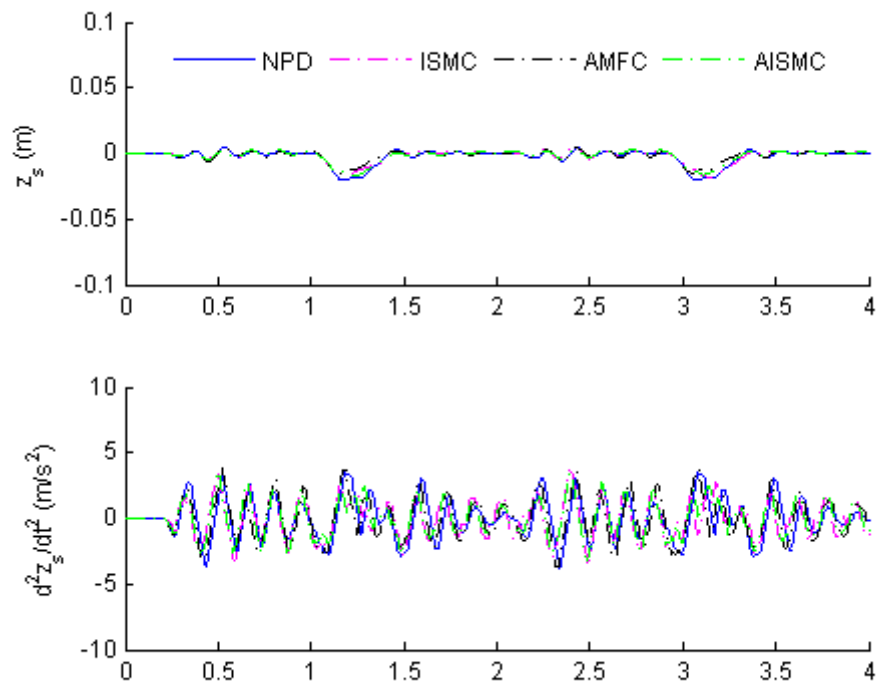
(d) $M_s = 80\% M_{s0}$, $K_s = 80\% K_{s0}$

Fig. 5-16 Comparisons among different control methods

5.6 Summary

Two nonlinear controllers have been studied and developed for quarter-car ASS. The first method is sliding mode control, which is renowned for its simplicity and robustness. Without a prior knowledge of the plant structure and system parameters, the sliding mode controller can force the system performance to trace the required sliding mode dynamic. By considering the upper bound of the parameters uncertainty and external disturbance, the sliding mode controller is effective to stabilise the error dynamic at zero point after a finite time.

The second method is adaptive model following control with partially known parameters. The adaptive mechanism is effective to deal with slow time-varying problems. A reference model is built to describe the required performance of the quarter-car ASS. The system input with adaptive gains can be regulated based on the system output errors through the adaptive mechanism. The hysteresis loop is applied in the updating rule to avoid rapid change of controller gains and reduce the risk of system crashing; meanwhile the system performances are maintained.

A combination of sliding mode and adaptive mechanism is proposed to obtain the advantages of both controllers, i.e. robustness and adaptive. The knowledge of upper bound required by SMC is unnecessary, only some parameters are required for the updating of adaptive gains. Among these methods, a saturation function is used to alleviate the chattering problem of the sliding modes, and a hysteresis loop is employed to limit the increase of adaptive gains. The simulation results illustrate the effectiveness of the proposed nonlinear control methods. The largest displacement amplitudes of car body are suppressed to within 0.03m (normal load) and 0.045m (light load) when the vehicle runs over isolated bump (0.05m depth), whereas the displacement amplitude of passive suspension system is over 0.07m. Furthermore, the upward movement of the car body is rejected due to the action of ASS while the oscillation continuous for three periods under passive suspension and the peak-peak amplitude is over 0.1m.

Chapter 6 Control methods for the full-car active suspension system

In this chapter, a literature review on the objectives and research work of linear model following control is first presented, followed by linearisation work within small vicinity of zero points of system parameters from a full-car system that is inherently nonlinear.

Two controllers have been built to achieve the desired response from both linear and non-linear system. A linear model following controller is designed to deal with the linear suspension system. The developed controller aims to force the sprung mass subsystem to trace the reference model so that required performance can be obtained. In case of nonlinear one, SMC control scheme is studied and implemented to deal with the system nonlinearities. The design of the controllers is based on the nominal values of the full-car ASS, and the optimal values are determined by considering the margin of the stability.

6.1 Review of linear model following control

Model following control (MFC) is a reconfiguration control method on the basic of matching the output responses of the plant with a pre-defined reference model. The purpose of LMFC is to design a compensating control law for a linear multivariable system such that the closed loop system output follows the response of linear referenced model. The MFC can be classified into two types: implicit case and explicit case. The implicit model following uses only a feedback control structure while explicit model following has a combination of feed forward and feedback structures. Explicit model following scheme is suitable for a class of system in the presence of external disturbance because the errors between the model and plant outputs are used [154].

The investigation of MFC has started since 1950s. An early research based on optimal control theory was conducted by Tyler [155] and Winsor [156]. The concept of perfect model following (PMF) was proposed by Erzberger [157] in which the outputs of the plant follow the outputs of the referenced model exactly. The solvability and structure of the model following problem is synthesised in [158]. The necessary and sufficient conditions for the existence of a solution to the problem are clarified by Morse. Recently, a modified LMFC is proposed using only the available information of the reference model output and the plant output. A reduced order referenced model is used to simplify the controller design and the stability can be guaranteed in [159].

6.2 Modelling of full-car active suspension system

6.2.1 Modelling

The linear and nonlinear model of full-car ASS have been represented in (2-5) and (2-6). For applying modern control theory, the models should be rewritten in state space equations. Let the sprung and unsprung mass variable vector be $q_s = \begin{bmatrix} z & \theta & \varphi \end{bmatrix}^T$ and $q_u = \begin{bmatrix} z_{ufl} & z_{ufr} & z_{url} & z_{urr} \end{bmatrix}^T$ respectively, the mass and inertia matrix be $H = diag\left(M_s \quad I_p \quad I_r \right)$. The initial position is set to be zero by coordination shifting to compensate the movement due to gravity effect of loading, and then the state space equation of linear model (2-6) is

$$\begin{cases} \ddot{q}_s = H^{-1}A_{s1}q_s + H^{-1}A_{s2}q_u + H^{-1}F_{eq1} \\ \ddot{q}_u = -M_u^{-1}A_{u1}q_u + M_u^{-1}A_{u2}q_s + M_u^{-1}E_u q_r - M_u^{-1}F_{c1} \end{cases} \tag{6-1}$$

where the system matrices and disturbance matrices are

$$A_{s1} = \begin{bmatrix} -\left(2K_{sf} + 2K_{sr} \right) & -\left(2K_{sf}L_f - 2K_{sr}L_r \right) & 0 \\ -\left(2K_{sf}L_f - 2K_{sr}L_r \right) & -\left(2K_{sf}L_f^2 + 2K_{sr}L_r^2 \right) & 0 \\ 0 & 0 & -\left(2K_{sf}T_f^2 + 2K_{sr}T_r^2 \right) \end{bmatrix},$$

$$A_{s2} = \begin{bmatrix} K_{sf} & K_{sf} & K_{sr} & K_{sr} \\ K_{sf}L_f & K_{sf}L_f & -K_{sr}L_r & -K_{sr}L_r \\ K_{sf}T_f & -K_{sf}T_f & K_{sr}T_r & -K_{sr}T_r \end{bmatrix},$$

$$A_{u1} = diag\left(-K_{uf} - K_{sf} \quad -K_{uf} - K_{sf} \quad -K_{ur} - K_{sr} \quad -K_{ur} - K_{sr} \right),$$

$$A_{u2} = \begin{bmatrix} K_{sf} & K_{sf}L_f & K_{sf}T_f \\ K_{sf} & K_{sf}L_f & -K_{sf}T_f \\ K_{sr} & -K_{sr}L_r & K_{sr}T_r \\ K_{sr} & -K_{sr}L_r & -K_{sr}T_r \end{bmatrix},$$

$E_u = diag\left(K_{uf} \quad K_{uf} \quad K_{ur} \quad K_{ur} \right)$. $q_r = \begin{bmatrix} z_{rfl} & z_{rfr} & z_{rrl} & z_{rrr} \end{bmatrix}^T$ is the road profile vector. The four corner force vector is $F_{c1} = \begin{bmatrix} F_{fl} & F_{fr} & F_{rl} & F_{rr} \end{bmatrix}^T$, the equivalent

force vector is $F_{eq1} = \begin{bmatrix} F_z & F_\theta & F_\varphi \end{bmatrix}^T$. The relationship between the corner force

vector and equivalent force vector is $F_{eq1} = B_l F_{c1}$ with $B_l = \begin{bmatrix} 1 & 1 & 1 & 1 \\ L_f & L_f & -L_r & -L_r \\ T_f & -T_f & T_r & -T_r \end{bmatrix}$.

Similarly, the state space equation of nonlinear model (2-5) is

$$\begin{cases} \ddot{q}_s = H^{-1} f_{s1}(q_s) + H^{-1} f_{s2}(q_u) + H^{-1} F_{eq2} \\ \ddot{q}_u = M_u^{-1} f_{u1}(q_s) + M_u^{-1} f_{u2}(q_u) + M_u^{-1} d(q_r) + M_u^{-1} F_{c2} \end{cases}$$

(6-2)

where

$$f_{s1}(q_s) = \begin{bmatrix} -(2K_{sf} + 2K_{sr})z - (2K_{sf}L_f - 2K_{sr}L_r)\sin\theta \\ -(2K_{sf}L_f - 2K_{sr}L_r)\cos\theta \cdot z - (2K_{sf}L_f^2 + 2K_{sr}L_r^2)\cos\theta\sin\theta \\ -(2K_{sf}T_f^2 + 2K_{sr}T_r^2)\cos\varphi\sin\varphi \end{bmatrix},$$

$$f_{s2}(q_u) = \begin{bmatrix} K_{sf}(z_{ufl} + z_{ufr}) + K_{sr}(z_{url} + z_{urr}) \\ K_{sf}L_f\cos\theta(z_{ufl} + z_{ufr}) - K_{sr}L_r\cos\theta(z_{url} + z_{urr}) \\ K_{sf}T_f\cos\varphi(z_{ufl} - z_{ufr}) + K_{sr}T_r\cos\varphi(z_{url} - z_{urr}) \end{bmatrix},$$

$$f_{u1}(q_u) = \begin{bmatrix} -(K_{uf} + K_{sf})z_{ufl} \\ -(K_{uf} + K_{sf})z_{ufr} \\ -(K_{ur} + K_{sr})z_{url} \\ -(K_{ur} + K_{sr})z_{urr} \end{bmatrix}, \qquad f_{u2}(q_s) = \begin{bmatrix} K_{sf}z + K_{sf}L_f\sin\theta + K_{sf}T_f\sin\varphi \\ K_{sf}z + K_{sf}L_f\sin\theta - K_{sf}T_f\sin\varphi \\ K_{sr}z - K_{sr}L_r\sin\theta + K_{sr}T_r\sin\varphi \\ K_{sr}z - K_{sr}L_r\sin\theta - K_{sr}T_r\sin\varphi \end{bmatrix},$$

$d(q_r) = \begin{bmatrix} K_{uf}z_{rfl} \\ K_{uf}z_{rfr} \\ K_{ur}z_{rrl} \\ K_{ur}z_{rrr} \end{bmatrix}$. The four-corner force vector is $F_{c2} = \cos\theta\cos\varphi F_{c1}$ and the

equivalent force vector is $F_{eq2} = B_n F_{c2}$ with

$$B_n = \begin{bmatrix} 1 & 1 & 1 & 1 \\ L_f\cos\theta & L_f\cos\theta & -L_r\cos\theta & -L_r\cos\theta \\ T_f\cos\varphi & -T_f\cos\varphi & T_r\cos\varphi & -T_r\cos\varphi \end{bmatrix}.$$

6.2.2 Decoupling transformation matrix

The transformation from the controlled equivalent force vector to the actual four-corner force vector is important in the implementation of the ASS. Since there are three variables in sprung mass subsystem, thus only three controlled forces are generated through the controller. A force-decoupling matrix is used to translate three controlled forces into four commands for the four actuators installed in each corner. Generalised inverse or pseudo inverse technology is used here to obtain the decoupling matrix. Assume that a full rank matrix G has dimensions $m \times n$, it exists as left pseudo inverse G_l^+ if $m > n$ or right pseudo inverse G_r^+ if $m < n$. The calculation of generalised inverse is as follows:

$$
\begin{aligned}
G_l^+ &= \left(G^T G\right)^{-1} G^T, \ G_l^+ G = I_n \\
G_r^+ &= G^T \left(GG^T\right)^{-1}, \ \ GG_r^+ = I_m
\end{aligned}
\tag{6-3}
$$

For the full-car ASS, right pseudo inverse is selected. The generalised inverses for linear and nonlinear case are

$$
B_l^+ = B_l^T \left(B_l B_l^T\right)^{-1} =
\begin{bmatrix}
\dfrac{L_r}{2\left(L_f + L_r\right)} & \dfrac{1}{2\left(L_f + L_r\right)} & \dfrac{T_f}{2(T_f^2 + T_r^2)} \\[4mm]
\dfrac{L_r}{2\left(L_f + L_r\right)} & \dfrac{1}{2\left(L_f + L_r\right)} & \dfrac{-T_f}{2(T_f^2 + T_r^2)} \\[4mm]
\dfrac{L_f}{2\left(L_f + L_r\right)} & \dfrac{-1}{2\left(L_f + L_r\right)} & \dfrac{T_r}{2(T_f^2 + T_r^2)} \\[4mm]
\dfrac{L_f}{2\left(L_f + L_r\right)} & \dfrac{-1}{2\left(L_f + L_r\right)} & \dfrac{-T_r}{2(T_f^2 + T_r^2)}
\end{bmatrix}
\tag{6-4}
$$

and

$$B_n^+ = B_n^T \left(B_n B_n^T \right)^{-1} = \begin{bmatrix} \dfrac{L_r}{2\left(L_f+L_r\right)} & \dfrac{1}{2\left(L_f+L_r\right)\cos\theta} & \dfrac{T_f}{2(T_f^2+T_r^2)\cos\varphi} \\[4mm] \dfrac{L_r}{2\left(L_f+L_r\right)} & \dfrac{1}{2\left(L_f+L_r\right)\cos\theta} & \dfrac{-T_f}{2(T_f^2+T_r^2)\cos\varphi} \\[4mm] \dfrac{L_f}{2\left(L_f+L_r\right)} & \dfrac{-1}{2\left(L_f+L_r\right)\cos\theta} & \dfrac{T_r}{2(T_f^2+T_r^2)\cos\varphi} \\[4mm] \dfrac{L_f}{2\left(L_f+L_r\right)} & \dfrac{-1}{2\left(L_f+L_r\right)\cos\theta} & \dfrac{-T_r}{2(T_f^2+T_r^2)\cos\varphi} \end{bmatrix} \quad (6\text{-}5)$$

Thus, we have $B_l B_l^+ = I_3$ and $B_n B_n^+ = I_3$.

Through the modeling of the quarter-car and full-car ASS, there are serveral differences between two types ASS: 1) full-car ASS is composed of four qurater-car ASS modules; 2) quarter-car ASS is relatively simple while full-car ASS has more mechanical components and linkages, and sustains the car body to achieve drive safety and ride comfort; 3) quarter-car ASS focous on the motion control of the active actuator, full-car ASS concerns the co-ordination control and system stability; 4) decoupling control is empolyed to divide the high-order complex MIMO system (7-DOF) into three independant second-order SISO systems to obtain better performance.

6.3 LMFC for linear model

6.3.1 Basic theory of LMFC

The purpose of LMFC is to develop a compensation control for a controllable system and trace the outputs of reference model. For a given controllable and observable linear plant $\Sigma\left(A_p \quad B_p \quad C_p\right)$, the state space equation is represented as

$$\dot{x}_p = A_p x_p + B_p u_p \tag{6-6}$$

$$y_p = C_p x_p \tag{6-7}$$

where $x_p \in R^n$, $u_p \in R^m$ and $y_p \in R^l$; A_p, B_p and C_p are constant matrices of appropriate dimensions.

The controllable and observable reference model $\Sigma_m\left(A_m \quad B_m \quad C_m\right)$ has the following form:

$$\dot{x}_m = A_m x_m + B_m r \tag{6-8}$$

$$y_m = C_m x_m \tag{6-9}$$

where $x_m \in R^n$, $r \in R^m$ and $y_m \in R^l$; A_m, B_m and C_m are constant matrices with the same dimensions of A_p, B_p and C_p.

The objective of the reconfigured control method is to minimise the output errors between the plant and reference model. Without loss of generality, the output matrices of plant and model are set to be identical, i.e. $C_m = C_p$, then the compensation control law is designed to minimise the state error vector $e = x_m - x_p$ and output error vector $\varepsilon = C_m e = y_m - y_p$. The control scheme is illustrated in Fig. 6-1. The feed forward input, the feedback states and the reference states are used to generate the plant input, and the related gains satisfy the perfect model following conditions.
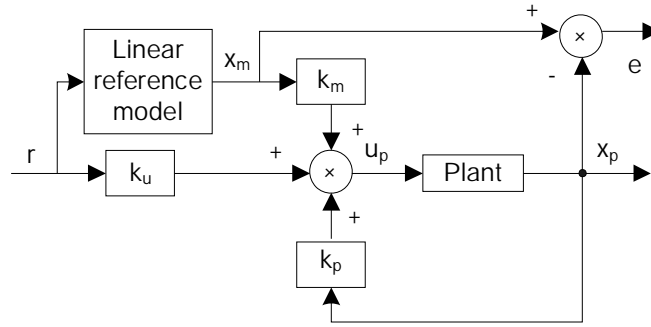
Fig. 6-1 Scheme of explicit linear model following control

The compensating control law is related to the reference inputs, the plant states, and model states. The form is synthesised as

$$u_p = K_u r + K_m x_m + K_p x_p \qquad (6\text{-}10)$$

where K_u, K_m and K_p are constant gain matrices with appropriate dimensions.

The state error equation is calculated by (6-6), (6-8) and (6-10)

$$\dot{e} = \left(A_m - B_p K_m\right)e + \left(A_m - A_p - B_p(K_m + K_p)\right)x_p + \left(B_m - B_p K_u\right)r \qquad (6\text{-}11)$$

If the error equation (6-11) is stabilised, then the output error vector ε or the state error vector e will decay to zero. To fulfil the asymptotically convergence requirement of output error, the constant matrices should satisfy the following:

i) $\left(A_m - B_p K_m\right)$ be a Hurwitz matrix;

ii) $A_m - A_p - B_p(K_m + K_p) = 0$;

iii) $B_m - B_p K_u = 0$.

Once the above conditions are satisfied, the output error vector will converge to zero asymptotically, thus the output response matches the reference response perfectly. Hence, the PMF conditions are:

$$\text{Re}\left[\lambda_i\left(A_m - B_p K_m\right)\right] < 0 \qquad (6\text{-}12)$$

$$K_m + K_p = B_p^+ \left(A_m - A_p \right) \qquad (6\text{-}13)$$

$$K_u = B_p^+ B_m \qquad (6\text{-}14)$$

where B_p^+ is the generalised inverse of B_p. The constant matrices K_u, K_m and K_p can be solved from PMF conditions (6-12), (6-13) and (6-14).

6.3.2 Decoupled SISO models

Using equivalent force vector F_{eq1}, the linear MIMO model of sprung mass subsystem can be decoupled into three second-order SISO models, as illustrated in (6-1). Three reduced-order SISO models are represented as follows

$$\begin{aligned} \dot{q}_{s1} &= q_{s4} \\ \dot{q}_{s4} &= a_{s1}q_{s1} + b_{s1}F_z + d_{s1}\left(q_s \quad \dot{q}_s \quad q_u \right) \end{aligned} \qquad (6\text{-}15)$$

$$\begin{aligned} \dot{q}_{s2} &= q_{s5} \\ \dot{q}_{s5} &= a_{s2}q_{s2} + b_{s2}F_\theta + d_{s2}\left(q_s \quad \dot{q}_s \quad q_u \right) \end{aligned} \qquad (6\text{-}16)$$

$$\begin{aligned} \dot{q}_{s3} &= q_{s6} \\ \dot{q}_{s6} &= a_{s3}q_{s3} + b_{s3}F_\varphi + d_{s3}\left(q_s \quad \dot{q}_s \quad q_u \right) \end{aligned} \qquad (6\text{-}17)$$

where $\dot{q}_s = \begin{bmatrix} \dot{z} & \dot{\theta} & \dot{\varphi} \end{bmatrix}^T = \begin{bmatrix} q_{s4} & q_{s5} & q_{s6} \end{bmatrix}^T$, the plant gains are $a_{s1} = -\dfrac{2K_{sf} + 2K_{sr}}{M_s}$,

$a_{s2} = -\dfrac{2K_{sf}L_f^{\,2} + 2K_{sr}L_r^{\,2}}{I_p}$ and $a_{s3} = -\dfrac{2K_{sf}T_f^{\,2} + 2K_{sr}T_r^{\,2}}{I_r}$, the input gains are

$b_{s1} = \dfrac{1}{M_s}$, $b_{s2} = \dfrac{1}{I_p}$ and $b_{s3} = \dfrac{1}{I_r}$, the disturbances are

$d_{s1} = -\dfrac{\left(2K_{sf}L_f - 2K_{sr}L_r \right)}{M_s}\theta + \dfrac{K_{sf}\left(z_{ufl} + z_{ufr} \right) + K_{sr}\left(z_{url} + z_{urr} \right)}{M_s}$,

$d_{s2} = -\dfrac{\left(2K_{sf}L_f - 2K_{sr}L_r \right)}{I_p}z + \dfrac{K_{sf}L_f\left(z_{ufl} + z_{ufr} \right) - K_{sr}L_r\left(z_{url} + z_{urr} \right)}{I_p}$,

$$d_{s3} = \frac{K_{sf}T_f\left(z_{ufl} - z_{ufr}\right) + K_{sr}T_r\left(z_{url} - z_{urr}\right)}{I_r}.$$

The model (6-1) or reduced-order models (6-15), (6-16) and (6-17) contains the disturbance items, in which a robust scheme is needed to compensate these disturbances. There are many methods proposed to solve that problem, such as high controller gains [160], variable structure theory [144], min-max control [161] and adaptive scheme [153]. Here, a simple PD controller is used to compensate the external disturbances and parameter uncertainties, thus the sprung mass system are decoupled into three first-order SISO systems.

Assuming the input reference heave position, pitch angle and roll angle to the inner loop PD controller are z_u, θ_u and φ_u respectively. The output errors and their derivatives are $e_z = z_u - z$, $\dot{e}_z = \dot{z}_u - \dot{z}$, $e_\theta = \theta_u - \theta$, $\dot{e}_\theta = \dot{\theta}_u - \dot{\theta}$, $e_\varphi = \varphi_u - \varphi$ and $\dot{e}_\varphi = \dot{\varphi}_u - \dot{\varphi}$. The control laws of the PD controllers are

$$\begin{cases} F_z = M_s\left(k_{pz}e_z + k_{dz}\dot{e}_z\right) \\ F_\theta = I_p\left(k_{p\theta}e_\theta + k_{d\theta}\dot{e}_\theta\right) \\ F_z = I_r\left(k_{p\varphi}e_\varphi + k_{d\varphi}\dot{e}_\varphi\right) \end{cases} \tag{6-18}$$

where k_{pz}, k_{dz}, $k_{p\theta}$, $k_{d\theta}$, $k_{p\varphi}$ and $k_{d\varphi}$ are appropriate PD controller gains.

As discussed in **Chapter 4**, the external disturbance and parameters variation of the plant can be compensated by the PD controller. The transfer function from the reference inputs to output sprung variables are

$$\begin{cases} G_z = \dfrac{k_{dz}s + k_{pz}}{s^2 + k_{dz}s + k_{pz} - a_{s1}} \\[3mm] G_\theta = \dfrac{k_{d\theta}s + k_{p\theta}}{s^2 + k_{d\theta}s + k_{p\theta} - a_{s2}} \\[3mm] G_\varphi = \dfrac{k_{d\varphi}s + k_{p\varphi}}{s^2 + k_{d\varphi}s + k_{p\varphi} - a_{s3}} \end{cases} \tag{6-19}$$

To ensure the stability of the PD controlled systems, the transfer functions of (6-19)

should have negative roots, i.e. $k_{dz,\theta,\varphi} > 0$, $k_{pz,\theta,\varphi} > 0$, $k_{pz} > a_{s1}$, $k_{p\theta} > a_{s2}$ and

$k_{p\varphi} > a_{s3}$.

The corresponding space state equations of controlled SISO systems are

$$
\begin{cases}
\begin{bmatrix} \dot{z} \\ \ddot{z} \end{bmatrix} = \begin{bmatrix} 0 & 1 \\ a_{s1} - k_{pz} & -k_{dz} \end{bmatrix} \begin{bmatrix} z \\ \dot{z} \end{bmatrix} + \begin{bmatrix} 0 \\ 1 \end{bmatrix} z_u \\
\quad y_z = \begin{bmatrix} k_{pz} & k_{dz} \end{bmatrix} \begin{bmatrix} z \\ \dot{z} \end{bmatrix}
\end{cases}
\tag{6-20}
$$

$$
\begin{cases}
\begin{bmatrix} \dot{\theta} \\ \ddot{\theta} \end{bmatrix} = \begin{bmatrix} 0 & 1 \\ a_{s2} - k_{p\theta} & -k_{d\theta} \end{bmatrix} \begin{bmatrix} \theta \\ \dot{\theta} \end{bmatrix} + \begin{bmatrix} 0 \\ 1 \end{bmatrix} \theta_u \\
\quad y_\theta = \begin{bmatrix} k_{p\theta} & k_{d\theta} \end{bmatrix} \begin{bmatrix} \theta \\ \dot{\theta} \end{bmatrix}
\end{cases}
\tag{6-21}
$$

$$
\begin{cases}
\begin{bmatrix} \dot{\varphi} \\ \ddot{\varphi} \end{bmatrix} = \begin{bmatrix} 0 & 1 \\ a_{s3} - k_{p\varphi} & -k_{d\varphi} \end{bmatrix} \begin{bmatrix} \varphi \\ \dot{\varphi} \end{bmatrix} + \begin{bmatrix} 0 \\ 1 \end{bmatrix} \varphi_u \\
\quad y_\varphi = \begin{bmatrix} k_{p\varphi} & k_{d\varphi} \end{bmatrix} \begin{bmatrix} \varphi \\ \dot{\varphi} \end{bmatrix}
\end{cases}
\tag{6-22}
$$

Through the inner PD controller, each SISO system has become a linear model without disturbance, the aforementioned standard LMFC method can be used. Let the required heave position be z^*, pitch angle be θ^* and roll angle be φ^*. The second-order reference models of the SISO systems are

$$
\begin{cases}
\begin{bmatrix} \dot{z}_m \\ \ddot{z}_m \end{bmatrix} = \begin{bmatrix} 0 & 1 \\ -a_{z1} & -a_{z2} \end{bmatrix} \begin{bmatrix} z_m \\ \dot{z}_m \end{bmatrix} + \begin{bmatrix} 0 \\ 1 \end{bmatrix} z^* \\
\quad y_{zm} = \begin{bmatrix} k_{pz} & k_{dz} \end{bmatrix} \begin{bmatrix} z_m \\ \dot{z}_m \end{bmatrix}
\end{cases}
\tag{6-23}
$$

$$\begin{cases} \begin{bmatrix} \dot{\theta}_m \\ \ddot{\theta}_m \end{bmatrix} = \begin{bmatrix} 0 & 1 \\ -a_{\theta 1} & -a_{\theta 2} \end{bmatrix} \begin{bmatrix} \theta_m \\ \dot{\theta}_m \end{bmatrix} + \begin{bmatrix} 0 \\ 1 \end{bmatrix} \theta^* \\ \\ y_{\theta m} = \begin{bmatrix} k_{p\theta} & k_{d\theta} \end{bmatrix} \begin{bmatrix} \theta_m \\ \dot{\theta}_m \end{bmatrix} \end{cases} \tag{6-24}$$

$$\begin{cases} \begin{bmatrix} \dot{\varphi}_m \\ \ddot{\varphi}_m \end{bmatrix} = \begin{bmatrix} 0 & 1 \\ -a_{\varphi 1} & -a_{\varphi 2} \end{bmatrix} \begin{bmatrix} \varphi_m \\ \dot{\varphi}_m \end{bmatrix} + \begin{bmatrix} 0 \\ 1 \end{bmatrix} \varphi^* \\ \\ y_{\varphi m} = \begin{bmatrix} k_{p\varphi} & k_{d\varphi} \end{bmatrix} \begin{bmatrix} \varphi_m \\ \dot{\varphi}_m \end{bmatrix} \end{cases} \tag{6-25}$$

where z_m, θ_m and φ_m are the states of the reference models, a_{z1}, a_{z2}, $a_{\theta 1}$, $a_{\theta 2}$, $a_{\varphi 1}$ and $a_{\varphi 2}$ are positive system parameters, y_{zm}, $y_{\theta m}$ and $y_{\varphi m}$ are the system outputs respectively.

  The control scheme of LMFC-PD based ASS is illustrated in Fig. 6-2. PD control is used to compensate the disturbance and system nonlinearities, and LMFC is used to make the system output track the reference output determined by linear models.
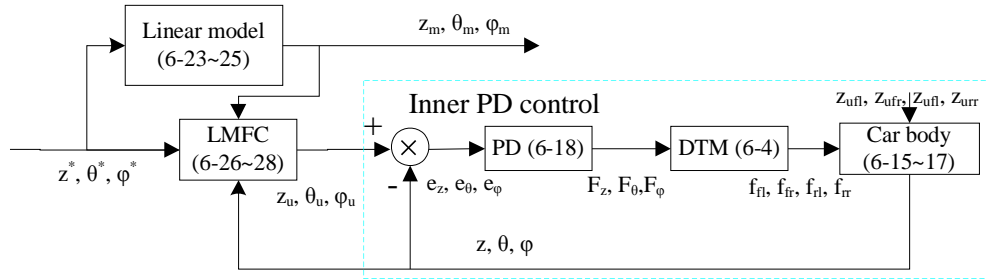
Fig. 6-2 LMFC-PD control of the full-car ASS

6.3.3 Control laws of LMFC

As shown from (6-20) to (6-25), the output matrices of the plant and model are identical. Convergence of system output errors is guaranteed by the converging of state errors. Let $e_z = z_m - z$, $\dot{e}_z = \dot{z}_m - \dot{z}$, $e_\theta = \theta_m - \theta$, $\dot{e}_\theta = \dot{\theta}_m - \dot{\theta}$, $e_\varphi = \varphi_m - \varphi$ and $\dot{e}_\varphi = \dot{\varphi}_m - \dot{\varphi}$, the goal of the developed control law is to compensate the plant outputs and achieve the required values. Based on the control principle of MFC, the control laws are determined to fulfil the PMF conditions (6-12), (6-13) and (6-14) as follows:

$$z_u = z^* + \begin{bmatrix} g_{z1} & g_{z2} \end{bmatrix} \begin{bmatrix} z_m \\ \dot{z}_m \end{bmatrix} + \begin{bmatrix} h_{z1} & h_{z2} \end{bmatrix} \begin{bmatrix} z \\ \dot{z} \end{bmatrix} \tag{6-26}$$

$$\theta_u = \theta^* + \begin{bmatrix} g_{\theta1} & g_{\theta2} \end{bmatrix} \begin{bmatrix} \theta_m \\ \dot{\theta}_m \end{bmatrix} + \begin{bmatrix} h_{\theta1} & h_{\theta2} \end{bmatrix} \begin{bmatrix} \theta \\ \dot{\theta} \end{bmatrix} \tag{6-27}$$

$$\varphi_u = \varphi^* + \begin{bmatrix} g_{\varphi1} & g_{\varphi2} \end{bmatrix} \begin{bmatrix} \varphi_m \\ \dot{\varphi}_m \end{bmatrix} + \begin{bmatrix} h_{\varphi1} & h_{\varphi2} \end{bmatrix} \begin{bmatrix} \varphi \\ \dot{\varphi} \end{bmatrix} \tag{6-28}$$

where $g_{z1} > -a_{z1}$, $g_{z2} > -a_{z2}$, $g_{\theta1} > -a_{\theta1}$, $g_{\theta2} > -a_{\theta2}$, $g_{\varphi1} > -a_{\varphi1}$ and, $h_{z1} = -a_{z1} - a_{s1} + k_{pz} - g_{z1}$, $h_{z2} = -a_{z2} + k_{dz} - g_{z2}$, $h_{\theta1} = -a_{\theta1} - a_{s2} + k_{p\theta} - g_{\theta1}$, $h_{\theta2} = -a_{\theta2} + k_{d\theta} - g_{\theta2}$, $h_{\varphi1} = -a_{\varphi1} - a_{s3} + k_{p\varphi} - g_{\varphi1}$, $h_{\varphi2} = -a_{\varphi2} + k_{d\varphi} - g_{\varphi2}$.

The stability of the developed control laws can be analysed as follows. For the SISO heave position system, the plant model is (6-20) and the reference model is (6-23). The output matrices of both model are identical, thus the analysis of output error is the same to the analysis of state error. Denote the system error of heave position as $e_z = \begin{bmatrix} z_m - z & \dot{z}_m - \dot{z} \end{bmatrix}^T$, its derivative is obtained by using (6-26)

$$\begin{aligned} \dot{e}_z &= \begin{bmatrix} 0 & 1 \\ -a_{z1} - g_{z1} & -a_{z2} - g_{z2} \end{bmatrix} \begin{bmatrix} z_m \\ \dot{z}_m \end{bmatrix} - \begin{bmatrix} 0 & 1 \\ a_{s1} - k_{pz} + h_{z1} & h_{z2} - k_{dz} \end{bmatrix} \begin{bmatrix} z \\ \dot{z} \end{bmatrix} \\ &= \begin{bmatrix} 0 & 1 \\ -a_{z1} - g_{z1} & -a_{z2} - g_{z2} \end{bmatrix} \begin{bmatrix} z_m \\ \dot{z}_m \end{bmatrix} - \begin{bmatrix} 0 & 1 \\ -a_{z1} - g_{z1} & -a_{z2} - g_{z2} \end{bmatrix} \begin{bmatrix} z \\ \dot{z} \end{bmatrix} \\ &= \begin{bmatrix} 0 & 1 \\ -a_{z1} - g_{z1} & -a_{z2} - g_{z2} \end{bmatrix} e_z \\ &= A_z e_z \end{aligned} \tag{6-29}$$

Here, $A_z = \begin{bmatrix} 0 & 1 \\ -a_{z1} - g_{z1} & -a_{z2} - g_{z2} \end{bmatrix}$ is Hurwitz stable since $-a_{z1} - g_{z1}$ and $-a_{z2} - g_{z2}$ are both negative constants. The dynamic of state error e_z illustrated by (6-29) indicates the output error converges to zero, thus the plant output z traces the reference output z_m. The stability analysis of pitch angle and roll angle is similar to

the heave position. It is easy to calculate the dynamic equations of state error vector e_θ and e_φ which are Hurwitz stable:

$$\dot{e}_\varphi = \begin{bmatrix} 0 & 1 \\ -a_{\varphi 1} - g_{\varphi 1} & -a_{\varphi 2} - g_{\varphi 2} \end{bmatrix} e_\varphi \tag{6-30}$$

$$\dot{e}_\theta = \begin{bmatrix} 0 & 1 \\ -a_{\theta 1} - g_{\theta 1} & -a_{\theta 2} - g_{\theta 2} \end{bmatrix} e_\theta \tag{6-31}$$

6.3.4 Modified control law of LMFC

The complete solution to LMFC control method has been described above. In practice, the order of SISO systems can be reduced using model reduction technique [159]. Such that, the control structure is simplified significantly meanwhile the desired dynamic performance is maintained [162].

 Using PD control laws (6-18), the decoupled SISO systems are simplified as

$$\begin{cases} \dot{z} = a_1 z + b_1 z_u \\ \dot{\theta} = a_2 \theta + b_2 \theta_u \\ \dot{\varphi} = a_3 \varphi + b_3 \varphi_u \end{cases} \tag{6-32}$$

where $-a_1 = b_1 > 0$, $-a_2 = b_2 > 0$ and $-a_3 = b_3 > 0$.

 The reference models are specified as

$$\begin{cases} \dot{z}_m = a_{1m} z_m + b_{1m} z^* \\ \dot{\theta}_m = a_{2m} \theta_m + b_{2m} \theta^* \\ \dot{\varphi}_m = a_{3m} \varphi_m + b_{3m} \varphi^* \end{cases} \tag{6-33}$$

where $-a_{1m} = b_{1m} > 0$, $-a_{2m} = b_{2m} > 0$ and $-a_{3m} = b_{3m} > 0$.

 The control laws are designed as

$$\begin{cases} u_z = k_{uz} z^* + k_{mz} z_m + k_z z \\ u_\theta = k_{u\theta} \theta^* + k_{m\theta} \theta_m + k_\theta \theta \\ u_\varphi = k_{u\varphi} \varphi^* + k_{m\varphi} \varphi_m + k_\varphi \varphi \end{cases} \qquad (6\text{-}34)$$

where $k_{uz} = b_{1m}/b_1$, $k_z = (a_{1m} - a_1)/b_1 - k_{mz}$, $k_{mz} > a_{1m}/b_1$; $k_{u\theta} = b_{2m}/b_2$, $k_\theta = (a_{2m} - a_2)/b_2 - k_{m\theta}$, $k_{m\theta} > a_{2m}/b_2$; $k_{u\varphi} = b_{3m}/b_3$, $k_\varphi = (a_{3m} - a_3)/b_3 - k_{m\varphi}$, $k_{m\varphi} > a_{3m}/b_3$.

6.3.5 Robustness analysis

Based on the principle of linear model following method, an explicit plant model is needed to meet the perfect model following condition. Variation of system parameters or induced external disturbance changes the explicit model and the PMF may not be guaranteed. Therefore, lack of robustness is the main disadvantage of the original LMFC. To improve the robustness, a simple linear PD controller is applied to compensate the parameters variation and external disturbance. The detailed robustness analysis of the linear PD controller can be referred to **Section 4.2.3**. By applying the linear PD scheme, the plant model can be determined by the gains of PD controller and the nominal plant model.

6.3.6 Simulation results

Table 6-1 Parameters of full-car ASS

Symbol	Value	Symbol	Value
M_s	1500 kg	I_p	2160 kgm^2
M_u	59 kg	I_r	460 kgm^2
K_{sf}	16000 N/m	L_f	1.4 m
K_{sr}	17000 N/m	L_r	1.7 m
K_{uf}	190000 N/m	T_f	0.76 m
K_{ur}	190000 N/m	T_r	0.84 m

This section illustrates a series of simulation results of control responses when road irregularities exist. Variation of sprung variables is within the range of $H = \begin{bmatrix} 80\% & 120\% \end{bmatrix} H_0$. General road profiles are evaluated and control responses are

recorded with the adoption of i) PD control & ii) LMFC control scheme. Simulation results are justified in terms of sprung variables and their accelerations.

The parameters of the full-car ASS are shown in Table 6-1. The controller is verified by comparison between PD control and LMFC control; the simulation results against road irregularity are shown as follows. For simplicity, the control laws of (6-34) are used. Without loss of generality, the gains of the subsystems are selected to be identical for simplicity, i.e. $k_p = k_{pz} = k_{p\theta} = k_{p\varphi}$, $k_d = k_{dz} = k_{d\theta} = k_{d\varphi}$, $a_m = a_{1m} = a_{2m} = a_{3m}$, $b_m = b_{1m} = b_{2m} = b_{3m}$, $k_u = k_{uz} = k_{u\theta} = k_{u\varphi}$, $k_m = k_{mz} = k_{m\theta} = k_{m\varphi}$ and $k = k_z = k_\theta = k_\varphi$.

Table 6-2 Control parameters of LMFC

Parameter	Value
k_p	20
k_d	5
a_m	-80
b_m	80
k_u	20
k_m	-17.1
k	-1.9

The track length between the front and rear axles is $L = L_f + L_r = 3.1m$. Suppose the longitudinal velocity of the vehicle is assumed to be $v = 20m/s$, the time delay can be calculated as $\tau = L/v = 0.155s$.

The road irregularity is sinusoidal two-track roads, as illustrated in Fig. 6-3. Sinusoidal two-track roads are general form of the practical road profiles. By changing the wavelength and phase shift, generic road profiles can be obtained. When the phase shift equals zero, two tracks are symmetrical and the response is similar to the continuous bump. When the phase shift equals 180°, two tracks are anti-symmetrical, and the roll angle is the main issue to compensate. Fig. 6-3 shows the anti-symmetrical sinusoidal road profile. The wavelength of the sinusoidal road is 20m, and the amplitude of the sinusoidal road is 0.1m. Two sides of road profile are identical and the delay distance is 5m.
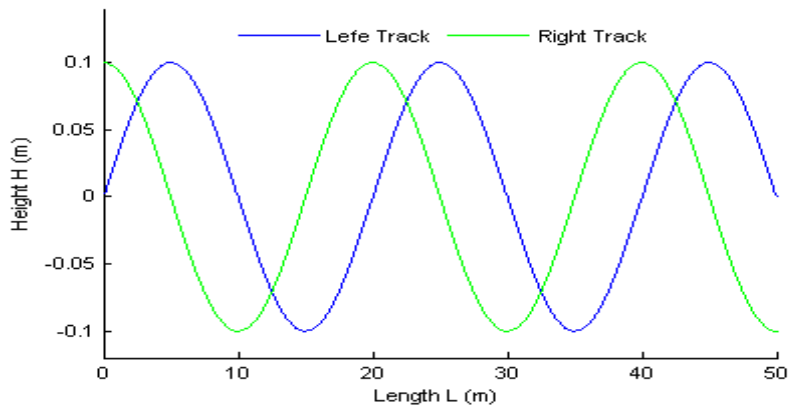
Fig. 6-3 Anti-symmetric sinusoidal road

The response outputs of car body with PD and LMFC under anti-symmetric sinusoidal road are shown from Fig. 6-4 to Fig. 6-6 with regard to load variation. In Fig. 6-4, the responses of car body under nominal load are described. The responses of suspension variables including heave position, pitch angle and roll angle are depicted in Fig. 6-4(a). The vehicle runs over an anti-symmetric sinusoidal road at time 1s. The corresponding dynamics of car body are three sinusoidal waveforms with the frequency of 1.25Hz, which is typical in road profile. As illustrated in Fig. 6-4(a), the amplitudes of sprung variables under PD control are 0.08m of heave position (top waveform), 0.055rad of pitch angle (middle waveform), and 0.067rad of roll angle (bottom waveform). On the other hand, the amplitudes of sprung variables under LMFC control are 0.025m of heave position (top waveform), 0.0221rad of pitch angle (middle waveform), and 0.028rad of roll angle (bottom waveform). The performance of LMFC based system has been improved significantly comparing to the PD based suspension.

Acceleration responses of the sprung mass variables are illustrated in Fig. 6-4(b), with the same frequency of 1.25Hz. Similar to the difference in Fig. 6-4(a), the amplitudes of corresponding accelerations under LMFC control are half of those under PD control. The acceleration amplitudes of heave position are about 5.17m/s^2 under PD control and about 1.78m/s^2 under LMFC control. The acceleration amplitudes of pitch angle are about 3.66rad/s^2 under PD control and about 1.47rad/s^2 under LMFC control. The acceleration amplitudes of roll angle are about 4.81rad/s^2 under PD control and about 2.15rad/s^2 under LMFC control.

Table 6-3 Maximum values of sprung mass variables under sinusoidal road

		z (m)	$\ddot{z}$ (m/s^2)	θ (rad)	$\ddot{\theta}$ (rad/s^2)	φ (rad)	$\ddot{\varphi}$ (rad/s^2)
Light Load	PD	0.07	4.75	0.045	3.22	0.053	4.41
	LMFC	0.024	1.73	0.021	1.45	0.025	2.19
Normal Load	PD	0.08	5.17	0.055	3.66	0.067	4.81
	LMFC	0.025	1.78	0.022	1.47	0.028	2.15
Heavy Load	PD	0.071	4.19	0.071	4.5	0.095	6.08
	LMFC	0.026	1.75	0.024	1.52	0.031	2.16

The output sinusoidal forces of four linear actuators are described in Fig. 6-4(c). The force frequency is 1.25Hz that is identical to the road profile. The force amplitude is about 2000N.

The responses of ASS under PD control and LMFC control are illustrated in Fig. 6-5 and Fig. 6-6 that are summarised in Table 6-3. The performances of ASS based on LMFC are better than those of under PD control. Furthermore, the peak values of responses under PD control vary with the change of load whereas the peak values of responses are consistent and almost constant under LMFC control. It is convinced that the robustness to load variation and external disturbance is improved significantly by LMFC control.
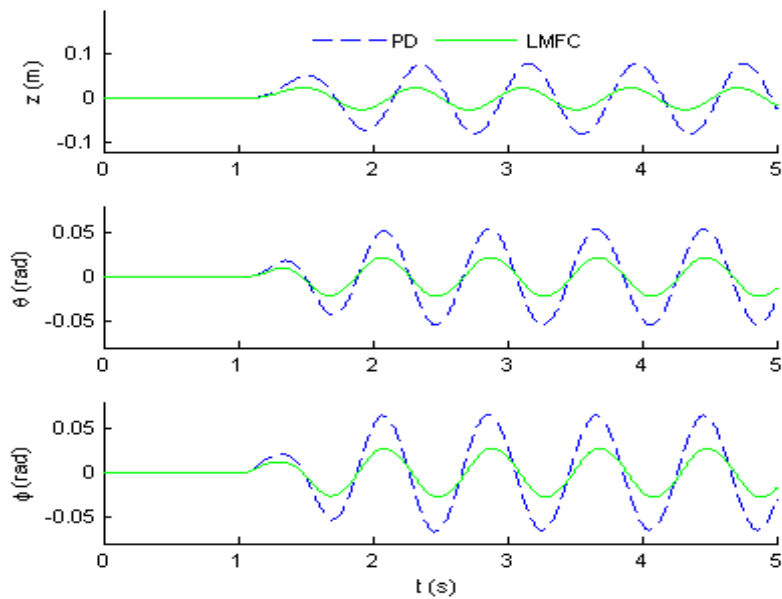
(a) Sprung mass variables
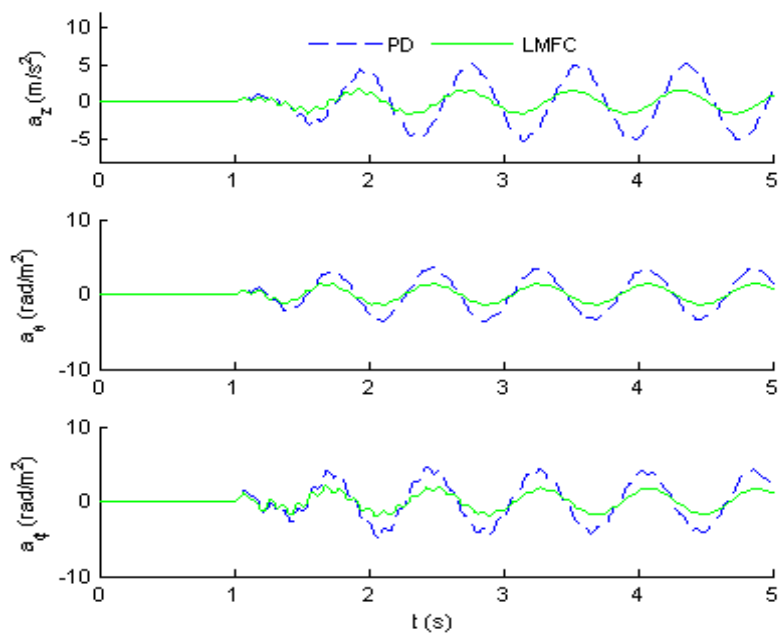
(b) Accelerations of sprung mass variables
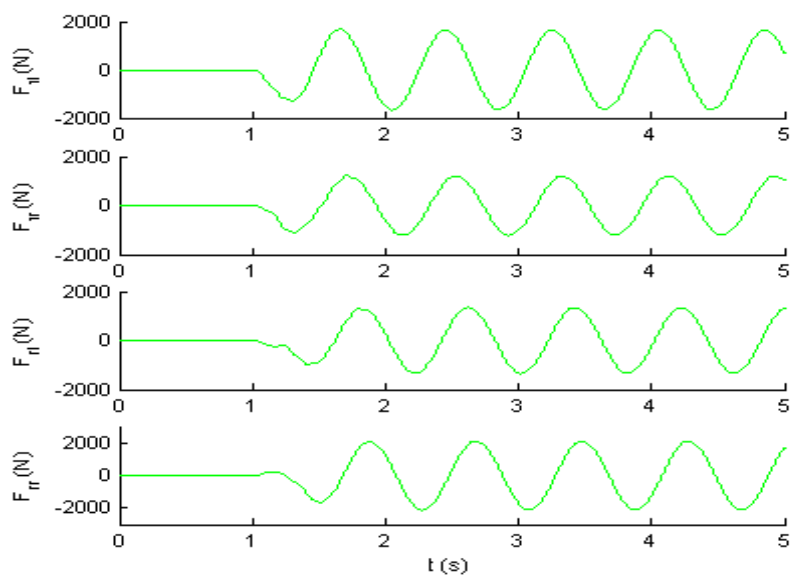
(c) Relative active forces

Fig. 6-4 Response between LMFC and PD control under anti-phase sinusoidal road at

normal load (M_s=100% M_{s0}, I_p=100% I_{p0}, I_r= 100% I_{r0})
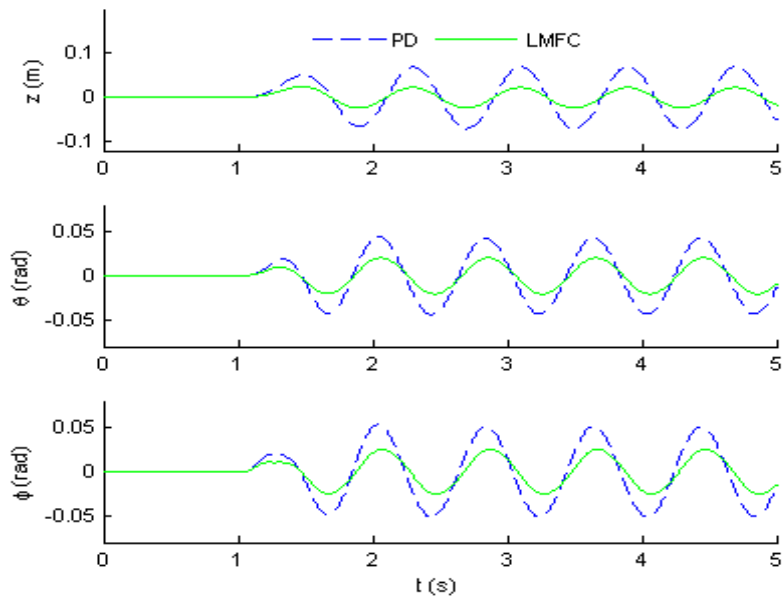
(a) Sprung mass variables
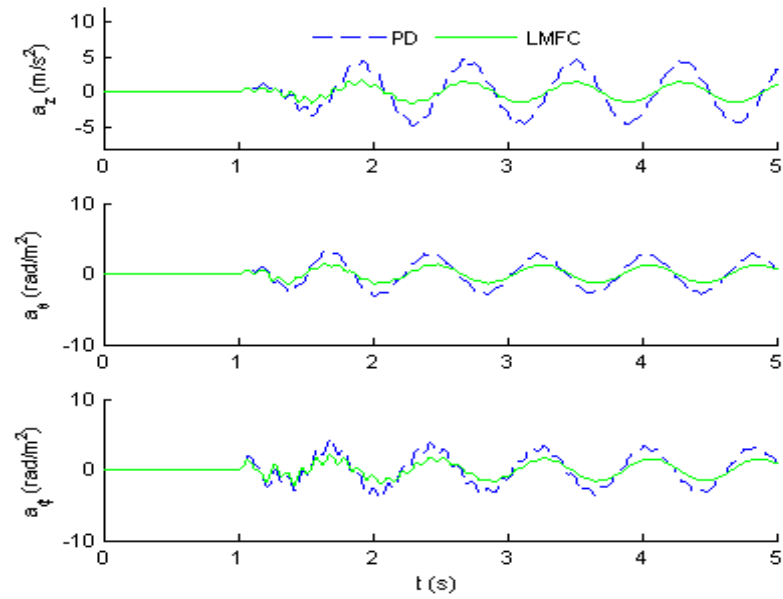
(b) Accelerations of sprung mass variables

Fig. 6-5 Response between LMFC and PD control under anti-phase sinusoidal road at

light load (M_s=80% M_{s0}, I_p=80% I_{p0}, I_r= 80% I_{r0})
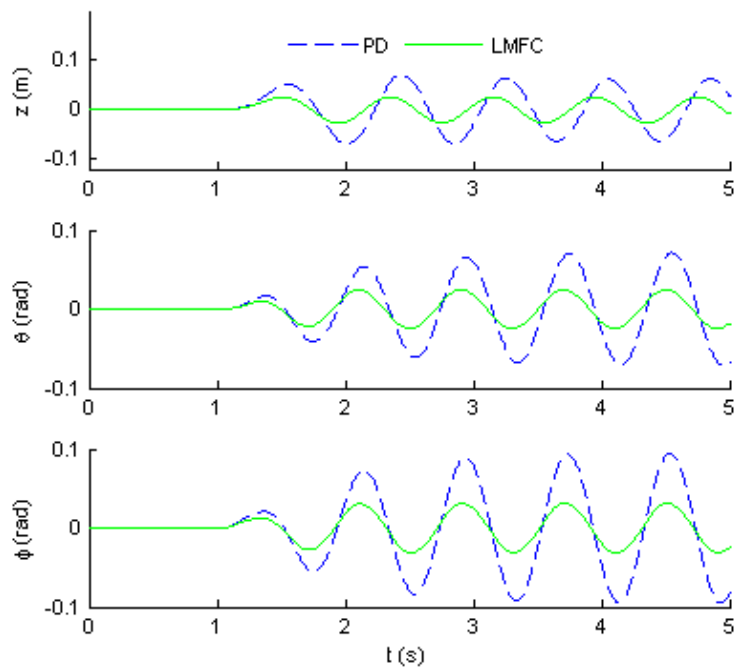
(a) Sprung mass variables
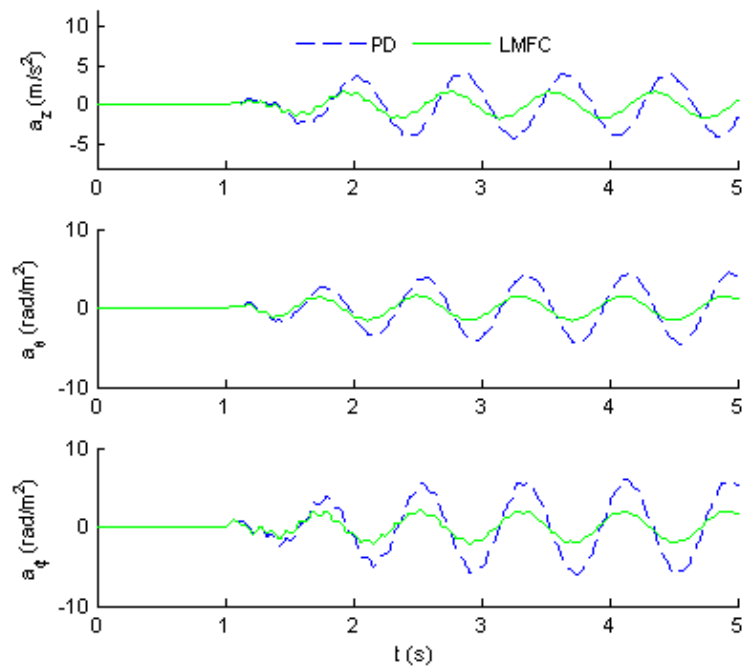
(b) Accelerations of sprung mass variables

Fig. 6-6 Response between LMFC and PD control under anti-phase sinusoidal road at

heavy load (M_s=120% M_{s0}, I_p=120% I_{p0}, I_r= 120% I_{r0})

6.4 ISMC for nonlinear model

The aforementioned LMFC controller with PD mechanism is simple and effective for the linear suspension model. However, the suspension system is nonlinear naturally. Furthermore, the pitch angle and roll angle are relatively large under some situations such as sharp ramp. In those cases, the linear model is difficult to explain the real system. The performance of the ASS is affected and the passenger comfort may not be guaranteed, even the driving safety may be deteriorated. To improve the performance of the ASS, the robust nonlinear SMC controller is proposed for the nonlinear vehicle model.

6.4.1 Nominal feedback control

Using the feedback compensation force and equivalent force vector F_{eq2}, the nonlinear MIMO model of sprung mass subsystem can be decoupled into three second-order SISO models, as illustrated in (6-2). Similar to the quarter-car case, the nominal values of the sprung mass variables are M_{s0}, I_{p0} and I_{r0}. The variation range of these variables is

$$\begin{cases} M_{s\min} \leq M_s = M_{s0} + \Delta M_s \leq M_{s\max} \\ I_{p\min} \leq I_p = I_{p0} + \Delta I_p \leq I_{p\max} \\ I_{r\min} \leq I_r = I_{r0} + \Delta I_r \leq I_{r\max} \end{cases} \tag{6-35}$$

The nominal model without the consideration of parameters variation and external disturbance is

$$\ddot{q}_s = H_0^{-1} f_{s1}(q_s) + H_0^{-1} F_{eq0} \tag{6-36}$$

where $H_0 = diag\begin{pmatrix} M_{s0} & I_{p0} & I_{r0} \end{pmatrix}$.

Assume that the required variable vector is $q_s^* = \begin{bmatrix} z^* & \theta^* & \varphi^* \end{bmatrix}^T$. The tracking error vector is $q_e = \begin{bmatrix} z_e & \theta_e & \varphi_e \end{bmatrix}^T = \begin{bmatrix} z - z^* & \theta - q^* & \varphi - \varphi^* \end{bmatrix}^T$. The desired trajectory of the tracking error is given by

$$\begin{cases} \ddot{z}_e + k_{dz}\dot{z}_e + k_{pz}z_e = 0 \\ \ddot{\theta}_e + k_{d\theta}\dot{\theta}_e + k_{p\theta}\theta_e = 0 \\ \ddot{\varphi}_e + k_{d\varphi}\dot{\varphi}_e + k_{p\varphi}\varphi_e = 0 \end{cases} \tag{6-37}$$

or

$$\ddot{q}_e + K_{df}\dot{q}_e + K_{pf}q_e = 0 \tag{6-38}$$

with $K_{pf} = diag\begin{pmatrix} k_{pz} & k_{p\theta} & k_{p\varphi} \end{pmatrix}$ and $K_{df} = diag\begin{pmatrix} k_{dz} & k_{d\theta} & k_{d\varphi} \end{pmatrix}$.

The required nominal force can be calculated through the direct computation method by combining (6-36) and (6-37)

$$F_0 = \begin{bmatrix} F_{z0} \\ F_{\theta 0} \\ F_{\varphi 0} \end{bmatrix} = -f_{s1}(q_s) + H_0 \begin{bmatrix} \ddot{z}^* - k_{dz}\dot{z}_e - k_{pz}z_e \\ \ddot{\theta}^* - k_{d\theta}\dot{\theta}_e - k_{p\theta}\theta_e \\ \ddot{\varphi}^* - k_{d\varphi}\dot{\varphi}_e - k_{p\varphi}\varphi_e \end{bmatrix} \tag{6-39}$$

Without the consideration of parameter variations and external disturbance, the dynamic of tracking error is identical to (6-37) by inputting the nominal force (6-39).

In real world, the tracking error is perturbed by the parameter variations $\begin{bmatrix} \Delta M_s & \Delta I_p & \Delta I_r \end{bmatrix}^T$ and road disturbance $\begin{bmatrix} z_{rfl} & z_{rfr} & z_{rrl} & z_{rrr} \end{bmatrix}^T$, therefore the tracking error dynamic of the full-car ASS is

$$\ddot{q}_e = H^{-1}f_{s1}(q_s) + H^{-1}f_{s2}(q_u) + H^{-1}F_{eq2} - \ddot{q}_s^* \tag{6-40}$$

where the control force vector is $F_{eq2} = F_0 + F_d = \begin{bmatrix} F_{z0} + F_{zd} & F_{\theta 0} + F_{\theta d} & F_{\varphi 0} + F_{\varphi d} \end{bmatrix}^T$, the compensation input vector $F_d = \begin{bmatrix} F_{zd} & F_{\theta d} & F_{\varphi d} \end{bmatrix}^T$ is used to settle the perturbation of the full-car suspension system.

6.4.2 Structure of sliding modes

The integral sliding surfaces of the tracking error vector for the full-car model are

$$s_q = \begin{bmatrix} s_z & s_\theta & s_\varphi \end{bmatrix}^T = s_{q0} + s_{qd} \qquad (6\text{-}41)$$

where

$$s_{q0} = \begin{bmatrix} s_{z0} & s_{\theta 0} & s_{\varphi 0} \end{bmatrix}^T = \dot{q}_e + c q_e \qquad (6\text{-}42)$$

Substituting (6-40) into (6-42)

$$\dot{s}_{q0} = \begin{bmatrix} \dot{s}_{z0} & \dot{s}_{\theta 0} & \dot{s}_{\varphi 0} \end{bmatrix}^T = H^{-1} F_{eq2} + d_{q0} \qquad (6\text{-}43)$$

$$\dot{s}_{qd} = \begin{bmatrix} \dot{s}_{zd} & \dot{s}_{\theta d} & \dot{s}_{\varphi d} \end{bmatrix}^T = -H_0^{-1} f_{s1}(q_s) - H_0^{-1} F_0 + \ddot{q}_s^* - c\dot{q}_e \qquad (6\text{-}44)$$

with $d_{q0} = H^{-1} f_{s1}(q_s) + H^{-1} f_{s2}(q_u) - \ddot{q}_s^* + c\dot{q}_e$, $s_{qd}(0) = -s_{q0}(0)$ to ensure the sliding surfaces at the initial time instant.

The derivative of the sliding surfaces is obtained from (6-41) to (6-44)

$$\dot{s}_q = \dot{s}_{q0} + \dot{s}_{qd} = \Upsilon_1 + \Upsilon_2 F_0 + H^{-1} d_q + H^{-1} F_d \qquad (6\text{-}45)$$

where

$$\Upsilon_1 = \begin{bmatrix} \gamma_{z1} & \gamma_{\theta 1} & \gamma_{\varphi 1} \end{bmatrix}^T = \left(H^{-1} - H_0^{-1} \right) f_{s1}(q_s),$$

$$\Upsilon_2 = \begin{bmatrix} \gamma_{z2} & \gamma_{\theta 2} & \gamma_{\varphi 2} \end{bmatrix}^T = \left(H^{-1} - H_0^{-1} \right),$$

$$d_q = \begin{bmatrix} d_z & d_\theta & d_\varphi \end{bmatrix}^T = f_{s2}(q_u)$$

It could be seen that Υ_2 is the mismatch between the nominal matrix H_0 and actual matrix H, Υ_1 is related to Υ_2 and the feedback variables. d_q is the external disturbance originated from the corner vibration q_r.

6.4.3 Control law of ISMC

The control law of the ISMC on full-car ASS is composed of two parts:

$$F_{eq2} = F_0 + F_d \tag{6-46}$$

where the nominal feedback force is calculated by (6-39), the compensation law is

$$F_d = -K_{qd}s_q - N_{qd}sat\left(s_q, \Delta_q\right) \tag{6-47}$$

where $K_{qd} = \begin{bmatrix} K_{zd} & K_{\theta d} & K_{\varphi d} \end{bmatrix}^T = \eta H$, $N_{qd} = \begin{bmatrix} N_{zd} & N_{\theta d} & N_{\varphi d} \end{bmatrix}^T = \tau_d H$, $\eta > 0$, τ_d

is a positive definite diagonal matrix. The diagonal elements of τ_d represent the upper boundary of generalised disturbance due to parameter variations and road profile for heave position, pitch angle and roll angle, i.e.

$$\tau_d = diag\left(\sup_i \left| \Upsilon_1 + \Upsilon_2 F_0 + H^{-1}d_q \right|_i \right)_{3\times 3} = diag\left(\tau_{dz} \quad \tau_{d\theta} \quad \tau_{d\varphi} \right) \tag{6-48}$$

The control scheme of ISMC on full-car ASS is illustrated in Fig. 6-7.
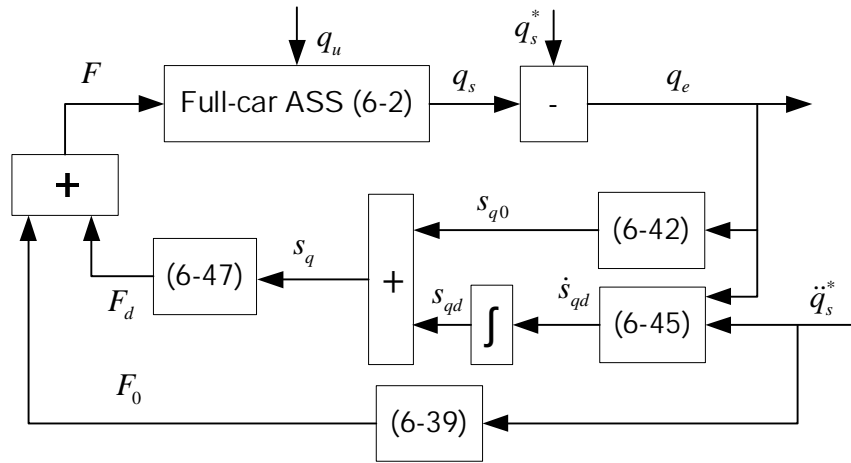
Fig. 6-7 Control scheme of ISMC on full-car ASS

6.4.4 Stability analysis

Similar to the quarter-car case, the stability of the full-car suspension with proposed sliding mode control is analysed by employing Lyapunov stability theorem. The positive definite Lyapunov function is selected as

$$V_q = \frac{1}{2} s_q{}^T H s_q \tag{6-49}$$

The derivative of the Lyapunov function is then

$$\dot{V}_q = s_q{}^T H \dot{s}_q \tag{6-50}$$

Substituting (6-46), (6-39) and (6-47), the related derivative of the sliding modes is obtained

$$\dot{s}_q = \Upsilon_1 + \Upsilon_2 F_0 + H^{-1} d_q - H^{-1} K_{qd} s_q - H^{-1} N_{qd} sat\left(s_q, \Delta_q\right) \tag{6-51}$$

Thus, the derivative of the Lyapunov function is

$$\begin{aligned}
\dot{V}_q &= s_q{}^T H \dot{s}_q \\
&= s_q{}^T H \left(\Upsilon_1 + \Upsilon_2 F_0 + H^{-1} d_q - H^{-1} K_{qd} s_q - H^{-1} N_{qd} sat\left(s_q, \Delta_q\right) \right) \\
&= -s_q{}^T K_{qd} s_q + s_q{}^T H \left(\Upsilon_1 + \Upsilon_2 F_0 + H^{-1} d_q \right) - s_q{}^T \tau_d H sat\left(s_q, \Delta_q\right) \\
&\leq -\eta s_q{}^T H_0 s_q + \left\| s_q{}^T H \left(\Upsilon_1 + \Upsilon_2 F_0 + H^{-1} d_q \right) \right\|_p - s_q{}^T \tau_d H sat\left(s_q, \Delta_q\right)
\end{aligned} \tag{6-52}$$

here, $\|A\|_p$ denotes the p-norm of the matrix A with $p > 0$, $\|A\|_p = \left(\sum_{i=1}^{n} |a_i|^p \right)^{\frac{1}{p}}$ for a vector $A_{n\times 1}$ and $\|A\|_p = \left(\sum_{i=1}^{m} \sum_{j=1}^{n} |a_{ij}|^p \right)^{\frac{1}{p}}$ for a matrix $A_{m\times n}$.

When the sliding modes stay within the boundary layer, the system is recognised as stable. The system behaviour beyond the boundary layer is studied. The saturation function should be replaced by sign function, the derivative of Lyapunov function $\dot{V}_z$ can be rewritten (6-52) as

$$\dot{V}_q = s_q{}^T H \dot{s}_q$$

$$\leq -\eta s_q{}^T H_0 s_q + \left\| s_q \right\|_p \left\| H \left(\Upsilon_1 + \Upsilon_2 F_0 + H^{-1} d_q \right) \right\|_p - s_q{}^T sign\left(s_q \right) H \tau_d$$

$$= -\eta s_q{}^T H_0 s_q + \left\| s_q \right\|_p \left\| H \left(\Upsilon_1 + \Upsilon_2 F_0 + H^{-1} d_q \right) \right\|_p - \left| s_q \right|^T H \tau_d$$

$$= -\eta s_q{}^T H_0 s_q - \left\| s_q \right\|_p \left(\left\| H \tau_d \right\|_p - \left\| H \left(\Upsilon_1 + \Upsilon_2 F_0 + H^{-1} d_q \right) \right\|_p \right)$$

(6-53)

Substituting (6-48) into (6-53), the derivative of Lyapunov function is negative,

$$\dot{V}_q \leq -\eta s_q{}^T H_0 s_q < 0 \qquad (6\text{-}54)$$

On a basic of the Lyapunov stability theorem, the dynamic error trajectories converge to zero exponentially and sliding modes occur. The stability of the proposed full-car sprung mass subsystem is guaranteed.

6.4.5 Robustness analysis

The robustness of the controlled full-car ASS can be guaranteed through adjusting the compensation force vector F_d or F_{c2}. The bounded vertical vibration q_r is limited, thus the displacement q_u and velocity $\dot{q}_u$ of unsprung mass subsystem due to q_r are bounded. Thus, the upper bound of external disturbance exists. Meanwhile, the load of the sprung mass subsystem is bounded within the smallest value $M_{s\min}$ (only the driver) and largest value $M_{s\max}$ (loading capacity of the vehicle); also the inertias are bounded in a rigid structure. The mass and inertia matrix H has its minimum $H_{\min}$ and maximum $H_{\max}$. Thus, the upper boundary τ_d exists. Theoretically, large τ_d enhances the robustness of the ISMC, at the risk of chattering issue due to excessive system gain. Hence, a reasonable τ_d should be large enough meanwhile it can reduce the possibility of chattering problem.

To guarantee the robustness of the controller within the whole load variation and road distribution, the controller gains can be selected as follows

$$\begin{cases} K_{zd} = \eta H_{max} \\ N_{zd} = \tau_d H_{max} \\ \tau_d = diag\left(\left(|\Upsilon_1|_{max} + |\Upsilon_2|_{max}|F_0| + H_{min}^{-1}|d_q|_{max}\right)_i\right) \end{cases}$$

6.4.6 System characteristics analysis of full-car ASS

The hypersurface of the sliding mode can be calculated from the integral function (6-51) that

$$\begin{cases} s_z = c_{z1}e^{-\frac{K_{zd}}{M_s}t} + \frac{M_s}{K_{zd}}\left(\gamma_{z1} + \gamma_{z2}F_{z0} + \frac{1}{M_s}d_z - \frac{N_{zd}}{M_s}sign(s_z)\right), \forall |s_z| > \Delta_z \\ s_z = c_{z2}e^{-\frac{K_{zd}\Delta_z + N_{zd}}{M_s\Delta_z}t} + \frac{M_s\Delta_z}{K_{zd}\Delta_z + N_{zd}}\left(\gamma_{z1} + \gamma_{z2}F_{z0} + \frac{1}{M_s}d_z\right), \forall |s_z| \le \Delta_z \end{cases} \tag{6-55}$$

$$\begin{cases} s_\theta = c_{\theta 1}e^{-\frac{K_{\theta d}}{I_p}t} + \frac{I_p}{K_{\theta d}}\left(\gamma_{\theta 1} + \gamma_{\theta 2}F_{\theta 0} + \frac{1}{I_p}d_\theta - \frac{N_{\theta d}}{I_p}sign(s_\theta)\right), \forall |s_\theta| > \Delta_\theta \\ s_\theta = c_{\theta 2}e^{-\frac{K_{\theta d}\Delta_\theta + N_{\theta d}}{I_p\Delta_\theta}t} + \frac{I_p\Delta_\theta}{K_{\theta d}\Delta_\theta + N_{\theta d}}\left(\gamma_{\theta 1} + \gamma_{\theta 2}F_{\theta 0} + \frac{1}{I_p}d_\theta\right), \forall |s_\theta| \le \Delta_\theta \end{cases} \tag{6-56}$$

$$\begin{cases} s_\varphi = c_{\varphi 1}e^{-\frac{K_{\varphi d}}{I_r}t} + \frac{I_r}{K_{\varphi d}}\left(\gamma_{\varphi 1} + \gamma_{\varphi 2}F_{\varphi 0} + \frac{1}{I_r}d_\varphi - \frac{N_{\varphi d}}{I_r}sign(s_\varphi)\right), \forall |s_\varphi| > \Delta_\varphi \\ s_\varphi = c_{\varphi 2}e^{-\frac{K_{\varphi d}\Delta_\varphi + N_{\varphi d}}{I_r\Delta_\varphi}t} + \frac{I_r\Delta_\varphi}{K_{\varphi d}\Delta_\varphi + N_{\varphi d}}\left(\gamma_{\varphi 1} + \gamma_{\varphi 2}F_{\varphi 0} + \frac{1}{I_r}d_\varphi\right), \forall |s_\varphi| \le \Delta_\varphi \end{cases} \tag{6-57}$$

If the system parameters are accurate, the above equations can be simplified as

$$\begin{cases} s_z = c_{z1}e^{-\frac{K_{zd}}{M_s}t} + \frac{M_s}{K_{zd}}\left(\left(\frac{M_{s0}}{M_s}-1\right)\left(\ddot{z}^* - k_{dz}\dot{z}_e - k_{pz}z_e\right) + \frac{1}{M_s}d_z - \frac{N_{zd}}{M_s}sign(s_z)\right), \forall |s_z| > \Delta_z \\ s_z = c_{z2}e^{-\frac{K_{zd}\Delta_z + N_{zd}}{M_s\Delta_z}t} + \frac{M_s\Delta_z}{K_{zd}\Delta_z + N_{zd}}\left(\left(\frac{M_{s0}}{M_s}-1\right)\left(\ddot{z}^* - k_{dz}\dot{z}_e - k_{pz}z_e\right) + \frac{1}{M_s}d_z\right), \forall |s_z| \le \Delta_z \end{cases}$$

$$\tag{6-58}$$

$$\begin{cases} s_\theta = c_{\theta 1}e^{-\frac{K_{\theta d}}{I_p}t} + \frac{I_p}{K_{\theta d}}\left(\left(\frac{I_{p0}}{I_p} - 1 \right)\left(\ddot{\theta}^* - k_{d\theta}\dot{\theta}_e - k_{p\theta}\theta_e \right) + \frac{1}{I_p}d_\theta - \frac{N_{\theta d}}{I_p}sign\left(s_\theta \right) \right), \forall \left| s_\theta \right| > \Delta_\theta \\ s_\theta = c_{\theta 2}e^{-\frac{K_{\theta d}\Delta_\theta + N_{\theta d}}{I_p\Delta_\theta}t} + \frac{I_p\Delta_\theta}{K_{\theta d}\Delta_\theta + N_{\theta d}}\left(\left(\frac{I_{p0}}{I_p} - 1 \right)\left(\ddot{\theta}^* - k_{d\theta}\dot{\theta}_e - k_{p\theta}\theta_e \right) + \frac{1}{I_p}d_\theta \right), \forall \left| s_\theta \right| \leq \Delta_\theta \end{cases}$$

$$(6\text{-}59)$$

$$\begin{cases} s_\varphi = c_{\varphi 1}e^{-\frac{K_{\varphi d}}{I_r}t} + \frac{I_r}{K_{\varphi d}}\left(\left(\frac{I_{r0}}{I_r} - 1 \right)\left(\ddot{\varphi}^* - k_{d\varphi}\dot{\varphi}_e - k_{p\varphi}\varphi_e \right) + \frac{1}{I_r}d_\varphi - \frac{N_{\varphi d}}{I_r}sign\left(s_\varphi \right) \right), \forall \left| s_\varphi \right| > \Delta_\varphi \\ s_\varphi = c_{\varphi 2}e^{-\frac{K_{\varphi d}\Delta_\varphi + N_{\varphi d}}{I_r\Delta_\varphi}t} + \frac{I_r\Delta_\varphi}{K_{\varphi d}\Delta_\varphi + N_{\varphi d}}\left(\left(\frac{I_{r0}}{I_r} - 1 \right)\left(\ddot{\varphi}^* - k_{d\varphi}\dot{\varphi}_e - k_{p\varphi}\varphi_e \right) + \frac{1}{I_r}d_\varphi \right), \forall \left| s_\varphi \right| \leq \Delta_\varphi \end{cases}$$

$$(6\text{-}60)$$

where c_{z1}, $c_{\theta 1}$, $c_{\varphi 1}$, c_{z2}, $c_{\theta 2}$ and $c_{\varphi 2}$ are constant parameters to fulfil the initial conditions and boundary conditions.

The error dynamic can be obtained by combination of (6-40), (6-58), (6-59) and (6-60)

$$\begin{cases} \ddot{z}_e + k_d\dot{z}_e + k_p z_e = -\frac{K_{zd}}{M_s}c_{z1}e^{-\frac{K_{zd}}{M_s}t}, \forall \left| s_z \right| > \Delta_z \\ \ddot{z}_e + k_d\dot{z}_e + k_p z_e = -\frac{K_{zd}\Delta_z + N_{zd}}{M_s\Delta_z}c_{z2}e^{-\frac{K_{zd}\Delta_z + N_{zd}}{M_s\Delta_z}t}, \forall \left| s_z \right| \leq \Delta_z \end{cases}$$

$$(6\text{-}61)$$

$$\begin{cases} \ddot{\theta}_e + k_{d\theta}\dot{\theta}_e + k_{p\theta}\theta_e = -\frac{K_{\theta d}}{I_p}c_{\theta 1}e^{-\frac{K_{\theta d}}{I_p}t}, \forall \left| s_\theta \right| > \Delta_\theta \\ \ddot{\theta}_e + k_{d\theta}\dot{\theta}_e + k_{p\theta}\theta_e = -\frac{K_{\theta d}\Delta_\theta + N_{\theta d}}{I_p\Delta_\theta}c_{\theta 2}e^{-\frac{K_{\theta d}\Delta_\theta + N_{\theta d}}{I_p\Delta_\theta}t}, \forall \left| s_\theta \right| \leq \Delta_\theta \end{cases}$$

$$(6\text{-}62)$$

$$\begin{cases} \ddot{\varphi}_e + k_{d\varphi}\dot{\varphi}_e + k_{p\varphi}\varphi_e = -\frac{K_{\varphi d}}{I_r}c_{\varphi 1}e^{-\frac{K_{\varphi d}}{I_r}t}, \forall \left| s_\varphi \right| > \Delta_\varphi \\ \ddot{\varphi}_e + k_{d\varphi}\dot{\varphi}_e + k_{p\varphi}\varphi_e = -\frac{K_{\varphi d}\Delta_\varphi + N_{\varphi d}}{I_r\Delta_\varphi}c_{\varphi 2}e^{-\frac{K_{\varphi d}\Delta_\varphi + N_{\varphi d}}{I_r\Delta_\varphi}t}, \forall \left| s_\varphi \right| \leq \Delta_\varphi \end{cases}$$

$$(6\text{-}63)$$

The solutions to the second-order linear differential equations (6-61), (6-62) and (6-63) are

$$
\begin{cases}
z_e = c_{z3}e^{\lambda_{z1}t} + c_{z4}e^{\lambda_{z2}t} + c_{z5}e^{-\frac{K_{zd}}{M_s}t}, \ \forall \left| s_z \right| > \Delta_z \\[2mm]
z_e = c_{z6}e^{\lambda_{z1}t} + c_{z7}e^{\lambda_{z2}t} + c_{z8}e^{-\frac{K_{zd}\Delta_z + N_{zd}}{M_s\Delta_z}t}, \ \forall \left| s_z \right| \le \Delta_z
\end{cases}
\tag{6-64}
$$

$$
\begin{cases}
\theta_e = c_{\theta3}e^{\lambda_{\theta1}t} + c_{\theta4}e^{\lambda_{\theta2}t} + c_{\theta5}e^{-\frac{K_{\theta d}}{I_p}t}, \ \forall \left| s_\theta \right| > \Delta_\theta \\[2mm]
\theta_e = c_{\theta6}e^{\lambda_{\theta1}t} + c_{\theta7}e^{\lambda_{\theta2}t} + c_{\theta8}e^{-\frac{K_{\theta d}\Delta_\theta + N_{\theta d}}{I_p\Delta_\theta}t}, \ \forall \left| s_\theta \right| \le \Delta_\theta
\end{cases}
\tag{6-65}
$$

$$
\begin{cases}
\varphi_e = c_{\varphi3}e^{\lambda_{\varphi1}t} + c_{\varphi4}e^{\lambda_{\varphi2}t} + c_{\varphi5}e^{-\frac{K_{\varphi d}}{I_r}t}, \ \forall \left| s_\varphi \right| > \Delta_\varphi \\[2mm]
\varphi_e = c_{\varphi6}e^{\lambda_{\varphi1}t} + c_{\varphi7}e^{\lambda_{\varphi2}t} + c_{\varphi8}e^{-\frac{K_{\varphi d}\Delta_\varphi + N_{\varphi d}}{I_r\Delta_\varphi}t}, \ \forall \left| s_\varphi \right| \le \Delta_\varphi
\end{cases}
\tag{6-66}
$$

where c_{zi}, $c_{\theta i}$ and $c_{\varphi i}$, $i = 3,...,8$ are the coefficients of the solutions, λ_{zj}, $\lambda_{\theta j}$ and $\lambda_{\varphi j}$, $j = 1,2$ are the characteristic roots of the characteristic equation of (6-64) to (6-66), respectively. The roots can be calculated as

$$
\lambda_{z1,z2} = -\frac{k_{dz}}{2} \pm \sqrt{\frac{k_{dz}^2}{4} - k_{pz}}
\tag{6-67}
$$

$$
\lambda_{\theta1,\theta2} = -\frac{k_{d\theta}}{2} \pm \sqrt{\frac{k_{d\theta}^2}{4} - k_{p\theta}}
\tag{6-68}
$$

$$
\lambda_{\varphi1,\varphi2} = -\frac{k_{d\varphi}}{2} \pm \sqrt{\frac{k_{d\varphi}^2}{4} - k_{p\varphi}}
\tag{6-69}
$$

The selection of positive k_{pz}, $k_{p\theta}$, $k_{p\varphi}$, k_{dz}, $k_{d\theta}$ and $k_{d\varphi}$ ensures characteristic roots are negative real numbers or a pair of complex numbers whose real parts are negative.

The ISMC controller for the full-car ASS can be seen as the extension of the quarter-car ASS. From equations (6-58) to (6-69), it can be concluded similarly to **Section 5.2.6**:

i) The selection of k_{pz}, $k_{p\theta}$, $k_{p\varphi}$, k_{dz}, $k_{d\theta}$ and $k_{d\varphi}$ determines the error dynamic of each SISO, respectively. K_{qd} or η affects the system characteristics before reaching the sliding mode, and N_{qd} and Δ_q affects the system characteristics after reaching the sliding mode, as represented in (6-61), (6-62) and (6-63).

ii) The ideal characteristics of steady error state system can be achieved theoretically:

$$
\begin{cases}
\lim_{t\to\infty} s_q = \dfrac{H\Delta_q}{K_{qd}\Delta_q + N_{qd}}\left(\left(H^{-1}H_0 - I_3\right)\ddot{q}^* + H^{-1}d_q\right) \\
\qquad \lim_{t\to\infty}\left(\ddot{q}_e + K_{df}\dot{q}_e + K_{pf}q_e\right) = 0 \qquad (6\text{-}70) \\
\qquad\qquad \lim_{t\to\infty} q_e = 0
\end{cases}
$$

Similar to the quarter-car case, high gain matrix τ_d can reduce the sliding error; however, the only issue to be noticed is that too high τ_d may cause the chattering problem.

6.4.7 Simulation results

The control gains of the proposed ISMC for full-car ASS are listed in Table 6-4. Without loss of generality, the gains of the subsystems are selected to be identical for simplicity, i.e. $k_p = k_{pz} = k_{p\theta} = k_{p\varphi}$, $k_d = k_{dz} = k_{d\theta} = k_{d\varphi}$. Here, τ_d is selected to be relative small to avoid chattering problem. Variation of sprung variables is around the nominal values and within the range of $H = \begin{bmatrix} 80\% & 120\% \end{bmatrix} H_0$.

Table 6-4 Control parameters of full-car ISMC

Parameter	Value
k_p	25
k_d	7.07
c	10
η	5
τ_d	1

The road irregularity is sinusoidal two-track roads, as illustrated Fig. 6-3. The response outputs of car body with ISMC control under anti-symmetric sinusoidal road are shown from Fig. 6-8 to Fig. 6-10 with regard to load variation. In Fig. 6-8, the responses of car body under nominal load are described. The responses of suspension variables including heave position, pitch angle and roll angle are depicted in Fig. 6-8(a). The vehicle runs over an anti-symmetric sinusoidal road at 1s. The corresponding dynamics of car body are three sinusoidal waveforms when the vehicle runs over the anti-symmetric sinusoidal road with the frequency of 1.25Hz. As illustrated in Fig. 6-8(a), the amplitudes of sprung variables under ISMC control are 0.029m of heave position (top waveform), 0.03rad of pitch angle (middle waveform), and 0.043rad of roll angle (bottom waveform).

Acceleration responses of the sprung mass variables are illustrated in Fig. 6-8(b), with the same frequency of 1.25Hz. The acceleration amplitudes are 2.02m/s^2 of heave position, 2.12rad/s^2 of pitch angle, and 3.01rad/s^2 of roll angle.

The output sinusoidal forces of four linear actuators are described in Fig. 6-8(c). The force frequency is 1.25Hz that is identical to the road profile. The force amplitude is about 2000N.

The responses of ASS under PD control and LMFC control are illustrated in Fig. 6-9 and Fig. 6-10 that are summarised in Table 6-5. It can be observed that the performances of ISMC based ASS are similar with regard to load variation. It is convinced that the robustness to load variation and external disturbance are guaranteed by ISMC control.

Table 6-5 Maximum values of sprung mass variables with ISMC control under

sinusoidal road

	z (m)	$\ddot{z}$ (m/s^2)	θ (rad)	$\ddot{\theta}$ (rad/s^2)	φ (rad)	$\ddot{\varphi}$ (rad/s^2)
Light Load	0.022	2.2	0.028	2.18	0.041	3.05
Nominal Load	0.029	2.02	0.03	2.12	0.043	3.01
Heavy Load	0.03	1.9	0.031	2.02	0.045	2.86
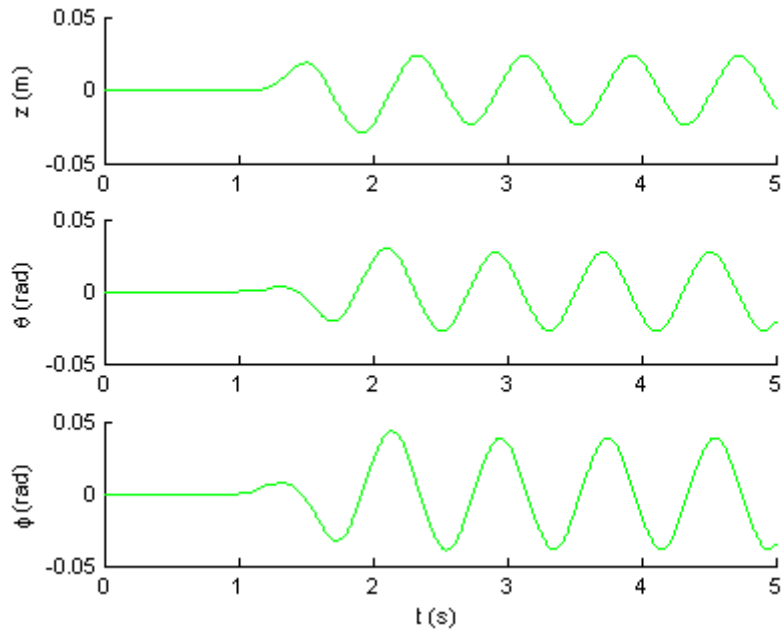
(a) Sprung mass variables
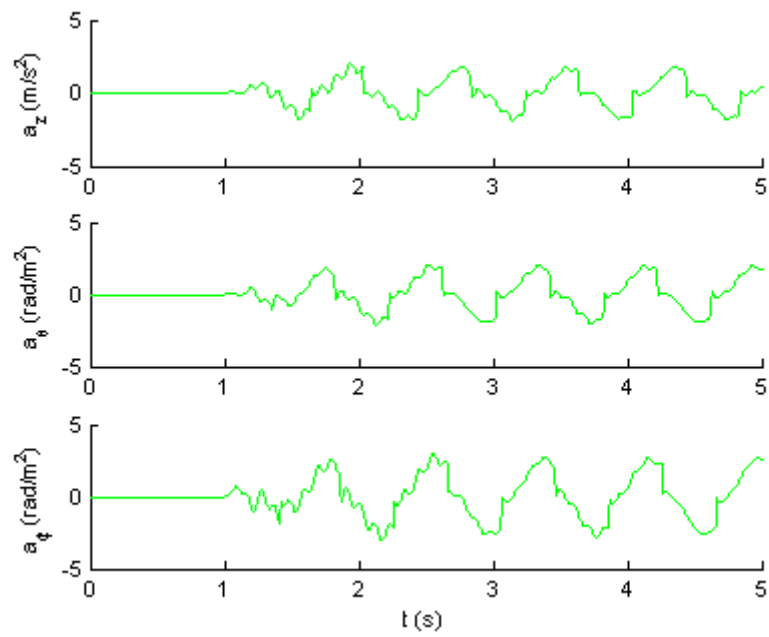
(b) Accelerations of sprung mass variables
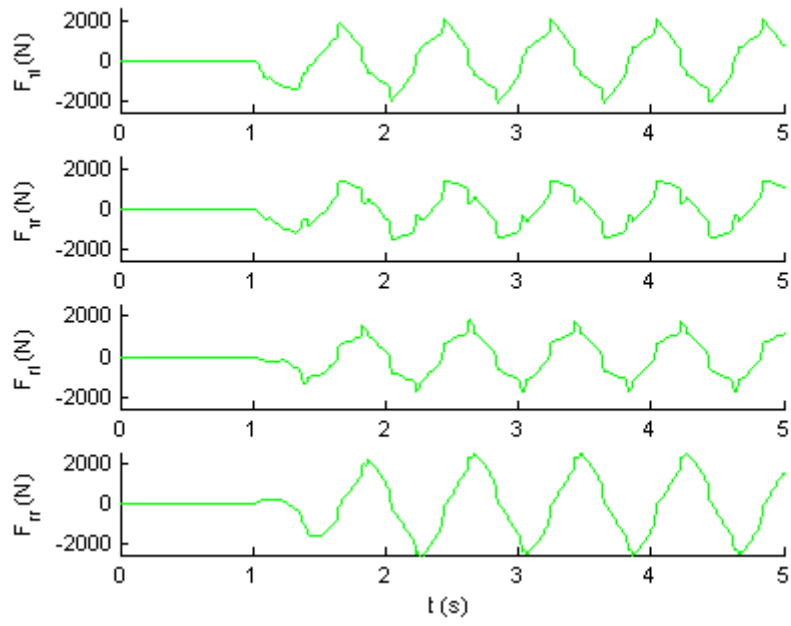
(c) Relative active forces

Fig. 6-8 Response of ISMC under anti-phase sinusoidal road at normal load

(M_s=100% M_{s0}, I_p=100% I_{p0}, I_r= 100% I_{r0})
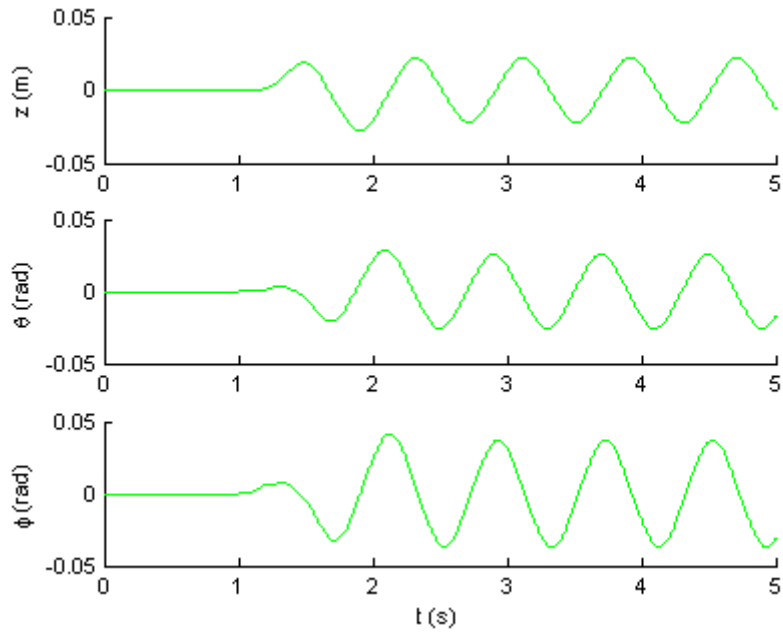
(a) Sprung mass variables
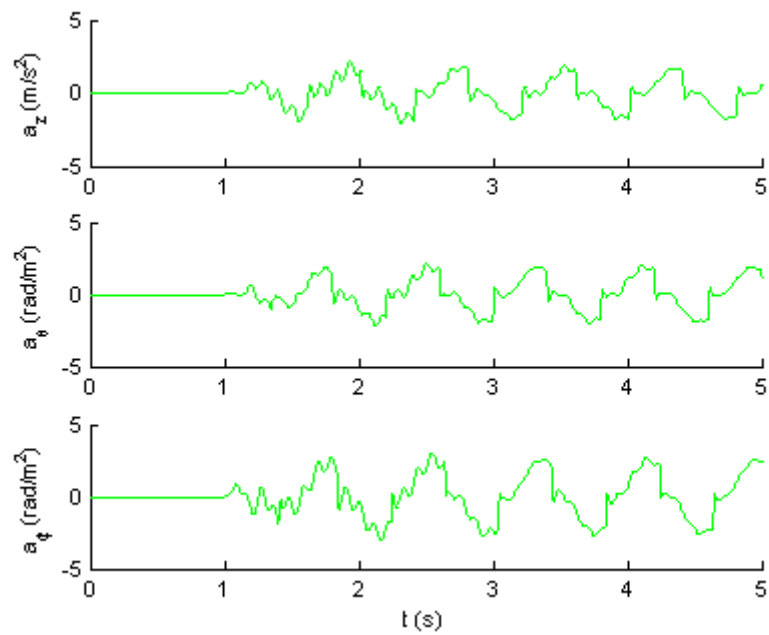
(b) Accelerations of sprung mass variables

Fig. 6-9 Response of ISMC under anti-phase sinusoidal road at light load

(M_s=80% M_{s0}, I_p=80% I_{p0}, I_r= 80% I_{r0})
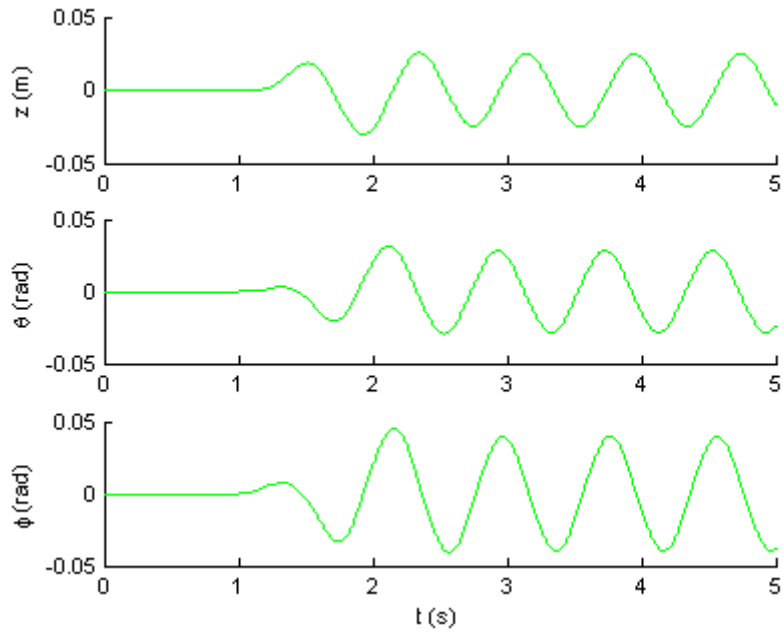
(a) Sprung mass variables
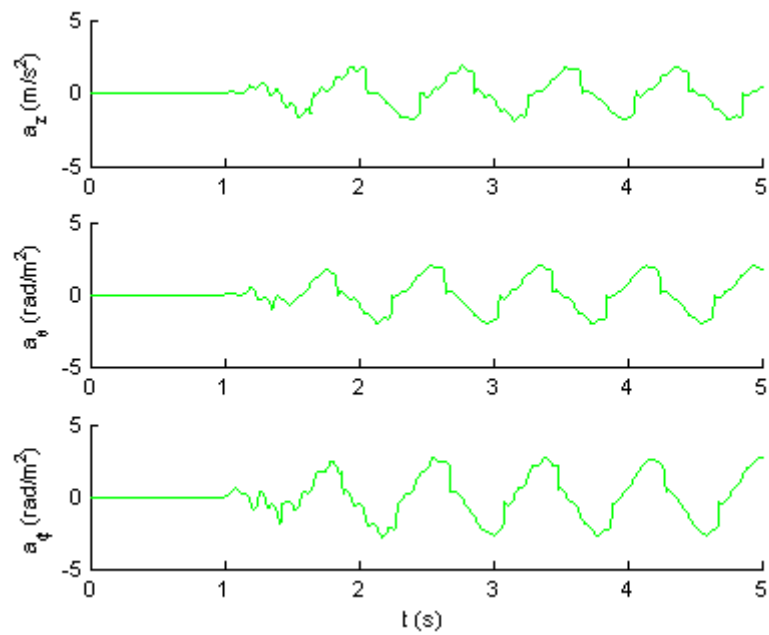
(b) Accelerations of sprung mass variables

Fig. 6-10 Response of ISMC under anti-phase sinusoidal road at heavy load

$(M_s=120\% \ M_{s0}, \ I_p=120\% \ I_{p0}, \ I_r= 120\% \ I_{r0})$

6.5 Summary

In this chapter, two control methods have been studied and further evaluated to cope with a 7-DOF full-car ASS. Effort has been put on stabilising three sprung mass variables with four actuator forces. It is found that mismatch between control inputs and outputs can be solved by decoupling matrix transformation. In other words, the MIMO system can be decoupled into three SISO systems.

For the linearised model, LMFC is used to force the plant output to match with the model output. A PD controller in the inner loop is used to compensate the parameter uncertainties and unknown disturbances. A second-order linear plant model is obtained without a prior knowledge of the plant structure and system parameters. The reference model is outlined to determine the dynamic performance of the suspension system. Once the perfect matching following conditions are fulfilled, the system output can trace the model output. Therefore, the required system variables are obtained through regulating the input controls.

For the nonlinear model, ISMC is selected for its simplicity and robustness. By considering the upper bound of the parameters uncertainty and external disturbance, the sliding mode controller is capable of approaching the sliding mode in a finite time effectively. The required dynamic performance is obtained.

Chapter 7 Conclusions and suggestions for further research

This thesis is dedicated to the design and control of electromagnetic ASS with LSRA. The main objective of the project is to analyse, design and build an experimental quarter-car LSRA ASS with real-time reliable nonlinear control methods to improve riding comfort and handling safety of ASS.

The quarter-car ASS and LSRA have been designed and fabricated for examination of the proposed ASS. Riding comfort, safety handling and various control methods have been investigated to enhance the dynamic performance of ASS by theoretical analyzing and experimental verifying.

This chapter highlights the major achievements and contributions of this thesis, and then brings forward some suggestions for further improvement on riding quality of ASS.

7.1 Achievements and contributions

The major achievements and contributions of this thesis can be summarised in details as follows.

7.1.1 Design of electromagnetic ASS and related power amplifier

In Chapter 2, a novel electromagnetic ASS with LSRA is proposed. The design of quarter-car ASS is divided into two parts: mechanical geometric constructer and electric power amplifier. The linear actuator and coil spring are assembled in parallel as the active suspension unit. A phase-shift DC-DC converter is applied to transfer the low voltage battery source into high voltage DC source for operation of LSRA. The converter design of bi-directional four-phase full-bridge topology allows driving of LSRA to generate active force and energy regenerating to improve system efficiency. A central control unit based on DSP deals with the sensed signals provides desired phase current commands in an appropriate sequence. A test rig has been built in the laboratory, in which a moving drum forces the wheel to run while the uneven plates act as road disturbances. The characteristics of quarter-car and full-car ASS have been modelled for control purpose.

7.1.2 Modelling and control of LSRA

In Chapter 3, design and control of LSRA have been studied for electromagnetic ASS. Following the study of characteristics and operating principle of LSRA, a specified compact arrangement of four double-sided longitudinal LSRA modules are proposed by considering the volume limitation with respect to a commercial vehicle mechanical structure. The parameters are analysed and calculated through magnetic circuit field theory and optimised by iterative design procedure to achieve high force density, and then FEA method is used to verify the design effectiveness. A prototype of LSRA is then fabricated to verify the design model. The force and flux linkage characteristics are examined by experimental test for real time control purpose. The experimental results indicate that the designed LSRA can achieve high force density for vertical propulsion application. Direct force control scheme of LSRA is developed. Nonlinearities of force and flux are the main challenge of motion control. In this thesis, the nominal values of inductance and its derivative are estimated to depict the nominal force and flux characteristics. The error between the nominal value and real

value is compensated by PI control scheme. Thus, the model of LSRA can be simplified drastically and direct force control is guaranteed and illustrated by simulation results.

7.1.3 Nonlinear PD control method on quarter-car ASS

In Chapter 4, a novel nonlinear PD control method on quarter-car ASS is developed with tracking differentiator. A novel TD based on optimal theory is introduced for position tracking. The main advantage of the proposed TD is to obtain the velocity directly, which is less possible for conventional differentiator. Discrete time TD is developed for digital control purpose and the effectiveness of TD is verified by experimental results. Next, a novel nonlinear PD control method is developed for quarter-car ASS. Compared with conventional linear PD control scheme, nonlinear PD control can generate higher force over a wide range of position perturbation, which is required for fast response and eliminating oscillation. The stability analysis of nonlinear PD is based on Popov stability criterion. It is found that the nonlinear PD control is more robust than linear PD while the vehicle encounters complicated and harsh road terrain. The simulation and experimental results verify the stability and robustness of the nonlinear PD controller.

7.1.4 Nonlinear control methods on quarter-car ASS

In Chapter 5, nonlinear control methods, including sliding mode control and adaptive control, are investigated and developed for quarter-car active suspension. Integral SMC mechanism is applied on ASS to deal with bounded parameters uncertainties and road disturbances. Consistent with conventional SMC, integral SMC is a simple and robust controller. Furthermore, integral structure of the proposed controller guarantees the achievement of sliding surface at the initial time instant, i.e. to keep the position sprung mass subsystem stable at the original point. Analysis of system dynamic characteristics illustrates that the stability and robustness of integral ISMC can be improved by reducing boundary layer and increasing controller gains within a reasonable range as discussed above. Next, an adaptive following controller is developed for ASS based on Popov hyperstability theorem. The forward strict reality is guaranteed by the stable reference model to describe the required performance of dynamic system. Parameter uncertainties and road disturbance can be regarded as system perturbation and represented by partially known parameters. Adaptive

regulation mechanism is used to estimate the perturbation vector based on system errors. Improving of riding comfort can be achieved by Adaptive Model Following Controller without the exact knowledge of system parameters. Furthermore, combination of these two control methods is investigated to obtain the advantages of simplicity, robustness, and adaptation. Once the upper boundary of road profile is known, the suspension system can stabilise the vertical oscillation in a short finite time by updating the adaptive gains.

7.1.5 Decoupled control of full-car ASS

In Chapter 6, two decoupled control methods for linear and nonlinear full-car ASS are studied. Based on the modelling of MIMO 7-DOF ASS built in Chapter 2, the full-car suspension system is decoupled into three individual SISO controllable systems. Pseudo inverse matrix technique is used to transfer four actuator forces into three inputs of SISOs. Linear Model Following Control is used to force the sprung mass subsystem to approach the reference dynamics. For each SISO system, the system perturbation is eliminated by PD control. Thus, a second-order linear plant model is obtained. The reference models determine the dynamic performance of ASS. The controller gains are optimised to fulfil the perfect matching following conditions, therefore the system outputs trace the model outputs and the ASS achieves required behaviour. Next, Integral Sliding Mode Control for full-car ASS is proposed. Analysis of stability and robustness of the proposed controller is presented. Finally, the system dynamic analysis indicates that the system dynamic follows the demanded dynamic in a finite time.

 The LSRA has been successfully applied to the ASS through various control methods and each has been analysed by simulation or experiment. The overall performance of the proposed system shows significant advancement as compared to passive unit and it represents a next generation of key component of mobility.

7.2 Suggestions for future work

For further research of electromagnetic ASS with LSRA, some suggestions for future work are listed below.

7.2.1 Optimization of LSRA

The proposed LSRA in this thesis is one of the possible designs to meet the requirements of ASS. The configuration could be improved with higher force density and lower cost. New cooling system can be considered to increase the nominal current and force density of LSRA.

7.2.2 Force control of LSRA

Nonlinearity is the inherent nature of LSRA, which causes some severe problems such as force ripple and fault tolerance. To reduce the force ripple and generate the required force, some predictive force control methods are needed to estimate the force characteristics and switches the conducting phase in advance, in case of current lagging due to large phase inductance near aligned position.

7.2.3 Nonlinear observers to estimate road disturbance

The parameter uncertainties and road disturbance deteriorate the performance of active suspensions that lead to system becomes unstable at adverse situation. It is highly recommended to observe these system perturbations and reconstruct the system model. After then, the controller structure can be simplified and the performance can be improved.

7.2.4 Robust Kalman filter for ASS

The proposed ASS is designed for ground vehicle. The complicated road profile and noisy electrical signals make the suspension system be a nonlinear system with unknown status. It is widely accepted the Kalman filter has a superior performance over filtering noise and estimating status. Therefore, Kalman filter is a good tool for filtering the injected noises of electromagnetic ASS. Furthermore, robust Kalman filter can estimate the input force which maybe different with the referenced force of LSRA due to the nonlinearities. The precise model of ASS can be estimated by robust Kalman filter, thus the control gains of the proposed controller can be appropriately decided and the riding quality can be improved significantly.

Appendices

Appendix I Tracking Differentiator

For a given reference signal $r(t)$, TD is used to obtain its tracking signal $r_1(t) \to r(t)$ and derivative $r_2(t) \to \dot{r}(t)$. Two Lemmas and one Theorem are presented here. The proofs can be referred to [135]-[137] and is presented briefly as follow.

Lemma 1. Given a continuous function $z(t)$, $\forall t \geq 0$ that satisfies

$$\lim_{t \to \infty} z(t) = 0.$$

If

$$w(t) = z(\Omega t), \forall \Omega > 0,$$

then there exists

$$\lim_{\Omega \to \infty} \int_0^T |w(t)| dt = 0, \forall T > 0 \tag{A-1}$$

Proof. Based on the mean value theorem, there is a $\tau \in [0, \quad T]$ such that

$$\int_0^T |w(t)| dt = T |w(\tau)| = T |z(\Omega \tau)| \tag{A-2}$$

Since $\lim_{t \to \infty} z(t) = 0$, it is straightforward that

$$\lim_{\Omega \to \infty} \int_0^T |w(t)| dt = \lim_{\Omega \to \infty} \left(T |z(\Omega \tau)| \right) = 0 \tag{A-3}$$

Thus, Lemma 1 is just established.

Lemma 2. If the solutions to the system

$$\begin{cases} \dot{z}_1 = z_2 \\ \dot{z}_2 = f(z_1, \quad z_2) \end{cases} \tag{A-4}$$

satisfies that $z_1(t) \to 0$ and $z_2(t) \to 0$ when $t \to \infty$, then for an arbitrarily constant c and $T > 0$, the solution $w_1(t)$ to the following system

$$\begin{cases} \dot{w}_1 = w_2 \\ \dot{w}_2 = \Omega^2 f\left(w_1 - c, \quad w_2 / \Omega\right) \end{cases} \tag{A-5}$$

holds

$$\lim_{\Omega \to \infty} \int_0^T \left| w_1(t) - c \right| dt = 0, \ T > 0 \, .$$

Proof. Assume a transformation that

$$\begin{cases} \tau = t / \Omega, \\ w_1(\tau) = z_1(t) + c, \\ w_2(\tau) = \Omega z_2(t). \end{cases}$$

Based on the mean value theorem, there is a $\tau \in [0, \quad T]$ such that

$$\int_0^T \left| w_1(t) - c \right| dt = T \left| w_1(\tau) - c \right| = T \left| z_1(t) \right| \tag{A-6}$$

Applying Lemma 1, it follows that

$$\lim_{\Omega \to \infty} \int_0^T \left| w_1(t) - c \right| dt = \lim_{\Omega \to \infty} \left(T \left| w_1(\tau) - c \right| \right) = T \lim_{\Omega \to \infty} \left| z_1(\Omega \tau) \right| = 0 \tag{A-7}$$

Thus, Lemma 2 is just established.

The Lemma 1 and Lemma 2 are associated with the Theorem 1 below. Theorem 1 is applied to track the given reference signal $r_1(t) \to r(t)$ and its derivative $r_2(t) \to \dot{r}(t)$.

Theorem 1. If the solutions to the system

$$\begin{cases} \dot{z}_1 = z_2 \\ \dot{z}_2 = f\left(z_1, \quad z_2\right) \end{cases} \tag{A-8}$$

satisfy that $z_1(t) \to 0$ and $z_2(t) \to 0$ when $t \to \infty$, then for an arbitrarily bounded integrable function $r(t)$ and given constant $T > 0$, the solution $r_1(t)$ to the system

174

$$\begin{cases} \dot{r}_1 = r_2 \\ \dot{r}_2 = \Omega^2 f\left(r_1 - r, \quad r_2 / \Omega\right) \end{cases} \tag{A-9}$$

satisfies

$$\lim_{\Omega \to \infty} \int_0^T \left| r_1(t) - r(t) \right| dt = 0 \tag{A-10}$$

Proof. The proof can be justified by dividing into two cases:

Case 1: If $r(t)$ is a constant function, then Theorem 1 is Lemma 2.

Case 2: If $r(t), t \in [0, \quad T]$ is a bounded integrable function, then it is an element of $L_1[0, \quad T]$, where $L_1[0, \quad T]$ denotes the set of all first-integrable functions within the range of $[0, \quad T]$. For an arbitrarily given $\varepsilon > 0$, there exists a simple series $g_n(t)(n = 1, 2, \ldots)$ that uniformly converges to a continuous function $g(t) \in C[0, \quad T]$ such that

$$\int_0^T \left| r(t) - g(t) \right| dt < \frac{\varepsilon}{2} \tag{A-11}$$

Thus, there exists an integer N such that $\left| g(t) - g_m(t) \right| < \frac{\varepsilon}{4T}$, $\forall m > N$. Consequently, the following inequality holds

$$\int_0^T \left| r(t) - g_m(t) \right| dt \leq \int_0^T \left| r(t) - g(t) \right| dt + \int_0^T \left| g(t) - g_m(t) \right| dt < \frac{\varepsilon}{2} \tag{A-12}$$

Since $g(t)$ is a continuous function, the simple series $g_m(t)$ that partitions the range $[0, \quad T]$ into some bounded intervals denoted by $T_i (i = 1, 2, \ldots, M)$. Selecting $g_m(t)$ to be a deterministic constant in each bounded interval, and based on Lemma 2, there exists $\Omega_0 > 0$ such that

$$\int_{T_i} \left| r(t) - g_m(t) \right| dt < \frac{\varepsilon}{2M}, \quad i = 1, 2, \ldots, M \tag{A-13}$$

for all $\Omega > \Omega_0$. Then,

$$\int_0^T \left| r(t) - g_m(t) \right| dt < \frac{\varepsilon}{2} \tag{A-14}$$

Thereby, the following inequality holds

$$\int_0^T \left| r_1(t) - r(t) \right| dt < \int_0^T \left| r_1(t) - g_m(t) \right| dt + \int_0^T \left| g_m(t) - r(t) \right| dt < \varepsilon \tag{A-15}$$

for all $\Omega > \Omega_0$. Thus, Theorem 1 is right justified.

Theorem 1 illustrates that for a bounded integrable function $r(t)$ that is viewed as a generalised function. By applying TD $r_1(t)$ converges to $r(t)$ averagely, and $r_2(t)$ converges to the generalised derivative of $r(t)$ weakly. Therefore, the system (A-9) can be used as a nonlinear tracking differentiator to provide a smooth approach to the original generalised function and its generalised derivative in the sense of average convergence and weak convergence, respectively. For higher order systems, similar procedure is demonstrated in [135].

Appendix II Stability Analysis of Hysteresis AMFC

Substituting (5-53) into the derivative of $V(z_e, \alpha, \rho)$, the following inequalities are obtained:

$$\dot{V}(z_e, \alpha, \rho) \leq \begin{cases} -z_e^T S_e z_e + 2|v_{e2}|\Delta\alpha^T \rho - 2\Delta\alpha^T \overline{K}\dot{\hat{\alpha}}, \ if \ |v_{e2}|\hat{\alpha}^T \rho > \varepsilon \\ -z_e^T S_e z_e + 2|v_{e2}|\alpha^T \rho - 2\dfrac{\left(|v_{e2}|\hat{\alpha}^T \rho\right)^2}{\varepsilon} - 2\Delta\alpha^T \overline{K}\dot{\hat{\alpha}}, \ if \ |v_{e2}|\hat{\alpha}^T \rho \leq \varepsilon \end{cases}$$

(A-16)

Combining the conditions of (i) $|v_{e2}|\hat{\alpha}^T \rho$ and ε and (ii) $\|Z_e\|$ and $\delta_{1,2}$, thus we have the following cases:

Case I with $|v_{e2}|\hat{\alpha}^T \rho > \varepsilon$ and $\beta(\|Z_e\|) = 1$. The time derivative of Lyapunov function is

$$\dot{V}(Z_e, \alpha, \rho) \leq -Z_e^T S_e Z_e + 2|v_{e2}|\Delta\alpha^T \rho - 2\Delta\alpha^T \overline{K}\dot{\hat{\alpha}} = -Z_e^T S_e Z_e \leq -\lambda_{S\min}\|z_e\|^2 \leq -3\varepsilon < 0.$$

Therefore, $\dot{V}(Z_e, \alpha, \rho)$ is strictly negative for all $\varepsilon > 0$ and $\hat{\alpha}$ is strictly increasing.

Case II with $|v_{e2}|\hat{\alpha}^T \rho > \varepsilon$ and $\beta(\|Z_e\|) = 0$. The time derivative of Lyapunov function is

$$\dot{V}(Z_e, \alpha, \rho) \leq -Z_e^T S_e Z_e + 2|v_{e2}|\Delta\alpha^T \rho$$

where $\hat{\alpha}$ is frozen. If $\Delta\alpha^T \rho < 0$, then $\dot{V}(z_e, \alpha, \rho) \leq -3\varepsilon$; otherwise $\dot{V}(z_e, \alpha, \rho)$ may be a positive value. If $\dot{V}(z_e, \alpha, \rho) > 0$, then $\|Z_e\|$ increases and turns back to Case I.

Case III with $|v_{e2}|\hat{\alpha}^T \rho \leq \varepsilon$ and $\beta(\|Z_e\|) = 1$. The time derivative of Lyapunov function is

$$\dot{V}(z_e, \alpha, \rho) \leq -z_e^T S_e z_e + 2|v_{e2}|\hat{\alpha}^T \rho - 2\dfrac{\left(|v_{e2}|\hat{\alpha}^T \rho\right)^2}{\varepsilon} \leq -3\varepsilon + 2\varepsilon = -\varepsilon < 0$$

Therefore $\dot{V}(Z_e, \alpha, \rho)$ is strictly negative for all $\varepsilon > 0$ and $\hat{\alpha}$ is strictly increasing.

Case IV with $|v_{e2}|\hat{\alpha}^T\rho \leq \varepsilon$ and $\beta(\|Z_e\|) = 0$. The time derivative of Lyapunov function is

$$\dot{V}(z_e, \alpha, \rho) \leq -z_e^T S_e z_e + 2|v_{e2}|\alpha^T\rho$$

where $\hat{\alpha}$ is frozen. If $\alpha^T\rho < 0$, then $\dot{V}(z_e, \alpha, \rho) \leq -3\varepsilon$; otherwise $\dot{V}(z_e, \alpha, \rho)$ may be a positive value. If $\hat{\alpha}^T\rho \geq \alpha^T\rho$, then the same inequality in the Case III is regained.

As discussed above, $\hat{\alpha}$ increases continuously in Cases I and III, and freezes in Cases II and IV. Once $\hat{\alpha}^T\rho \geq \alpha^T\rho$ or $\hat{\alpha} \geq \alpha$, the system error will converge to zero gradually and stay at Case IV such that

$$\dot{V}(z_e, \alpha, \rho) \leq -z_e^T S_e z_e + 2|v_{e2}|\alpha^T\rho \leq -\varepsilon$$

The remained problem is to prove that $\hat{\alpha} \to \alpha$ in a finite time. A brief description of one of the situations will be explored here, the detailed proof can be referred to [163], [164]. When the system lies in Case I, $\hat{\alpha}$ is strictly increasing with the ratio of $\dot{\hat{\alpha}} = |v_{e2}|\rho \geq \kappa_1 > 0$. After a finite time period $\tau_{11} = \max\limits_{i=1,\cdots,3} \dfrac{\alpha_i}{\kappa_1}$, we have $\hat{\alpha}(\tau_{11}) \geq \alpha$. Along with the increasing of $\hat{\alpha}$, $\|z_e\|$ will decrease gradually and obtain $\|z_e\| \leq \delta_2$ in a finite time τ_{12}. Furthermore, $\hat{\alpha}$ keeps increasing and $\|z_e\|$ remains decreasing until $\|z_e\| = \delta_1$ at τ_{13}. Then, Case II is active and $\hat{\alpha}$ is frozen, thus $\|z_e\|$ can no longer exceed δ_1. According to the above analysis, the consumed time to constraint $\|z_e\| \in \begin{bmatrix} 0 & \delta_1 \end{bmatrix}$ is finite and depends on the initial value $z_e(0)$ but not on initial time, i.e. the system is Globally Uniformly Ultimately Bounded (GUUB) [165].

References

[1]   J. Hedrick and T. Butsuen, "Invariant properties of automotive suspensions", *Proc.Inst.Mech.Eng.Pt.D: J.Automobile Eng.*, vol. 204, no. 1, pp. 21-27, 1990.

[2]   D. Karnopp, "Active damping in road vehicle suspension systems", *Veh.Syst.Dyn.*, vol. 12, no. 6, pp. 291-311, 1983.

[3]   D. Karnopp, "Active and semi-active vibration isolation", *Journal of Mechanical Design*, vol. 117, no. , pp. 177, 1995.

[4]   Citroën. *Hydractive Suspension*. http://www.citroen.com.au/about-citroen/technology/comfort/hydractive-iii-plus-suspension.

[5]   MICHELIN. *MICHELIN Active Wheel*. http://en.wikipedia.org/wiki/Active_Wheel.

[6]   M. Strassberger and J. Guldner, "BMW's dynamic drive: An active stabilizer bar system", *IEEE Control Systems*, vol. 24, no. 4, pp. 28-29, 107, 2004.

[7]   M. Becker, K. Jaker, F. Fruhauf and R. Rutz, "Development of an active suspension system for a Mercedes-Benz Coach (O404)", in, *IEEE International Symposium on Computer-Aided Control System Design*, pp. 146-151, 1996.

[8]   Bose. *Bose Active Suspension System*. http://www.bose.com/controller?url=/automotive/bose_suspension/index.jsp.

[9]   I. Martins, J. Esteves, G.D. Marques and F. Pina da Silva, "Permanent-magnets linear actuators applicability in automobile active suspensions", *IEEE Transactions on Vehicular Technology*, vol. 55, no. 1, pp. 86-94, 2006.

[10] L.R. Miller, "Tuning passive, semi-active, and fully active suspension systems", in *Proceedings of the 27th IEEE Conference on Decision and Control*, pp. 2047-2053, 1988.

[11] D. Hrovat, "Survey of advanced suspension developments and related optimal control applications", *Automatica*, vol. 33, no. 10, pp. 1781-1817, 1997.

[12] R.N. Jazar, *Vehicle Dynamics: Theory and Application*, Springer, 2008.

[13] R. Rajamani, "Vehicle dynamics and control", 2006.

[14] D. Hrovat, "Applications of optimal control to advanced automotive suspension design", *Journal of Dynamic Systems, Measurement, and Control*, vol. 115, no. 2B, pp. 328-342, June 1 1993.

[15]   R. Sharp and D. Crolla, "Road vehicle suspension system design-a review", *Veh.Syst.Dyn.*, vol. 16, no. 3, pp. 167-192, 1987.

[16]   F. Wang, "Design and synthesis of active and passive vehicle suspensions", *Design and synthesis of active and passive vehicle suspensions*, 2001.

[17]   M.C. Smith and G.W. Walker, "Performance limitations and constraints for active and passive suspensions: A mechanical multi-port approach", *Veh.Syst.Dyn.*, vol. 33, no. 3, pp. 137-168, 2000.

[18]   Sergio Savaresi, Charles Poussot-Vassal, Cristiano Spelta, Olivier Sename and Luc Dugard, *Semi-Active Suspension Control Design for Vehicles*, Oxford, UK, Butterworth Heinemann, 2010.

[19]   D. Karnopp and G. Heess, "Electronically controllable vehicle suspensions", *Veh.Syst.Dyn.*, vol. 20, no. 3-4, pp. 207-217, 1991.

[20]   M. Yokoyama, J.K. Hedrick and S. Toyama, "A model following sliding mode controller for semi-active suspension systems with MR dampers", in *American Control Conference, Proceedings of the 2001*, pp. 2652-2657, 2001.

[21]   N.K. Petek, D.J. Romstadt, M.B. Lizell and T.R. Weyenberg, "Demonstration of an automotive semi-active suspension using electrorheological fluid", *SAE publication sp 1074.new developments in vehicle dynamics, simulation, and suspension systems (SAE technical paper 950586)*, 1995.

[22]   B. Spencer, S. Dyke, M. Sain and J. Carlson, "Phenomenological model for magnetorheological dampers", *J.Eng.Mech.*, vol. 123, no. 3, pp. 230-238, 1997.

[23]   R. Stanway, J. Sproston and N. Stevens, "Non-linear modelling of an electro-rheological vibration damper", *J.Electrostatics*, vol. 20, no. 2, pp. 167-184, 1987.

[24]   R. Stanway, J. Sproston and A. El-Wahed, "Applications of electro-rheological fluids in vibration control: A survey", *Smart Mater.Struct.*, vol. 5, no. 4, pp. 464, 1996.

[25]   D. Karnopp, "Force generation in semi-active suspensions using modulated dissipative elements", *Veh.Syst.Dyn.*, vol. 16, no. 5-6, pp. 333-343, 1987.

[26]   D. Bastow, G. Howard and J.P. Whitehead, *Car suspension and handling*, Pentech Press London, 1993.

[27]   M. Appleyard and P.E. Wellstead, "Active suspensions: Some background", *IEE Proc Control Theory Appl*, vol. 142, no. 2, pp. 123-128, 1995.

[28]   K.J. Astrom, "PID controllers: Theory, design and tuning", *Instrument Society of America*, 1995.

[29]   K.J. Åström and T. Hägglund, "The future of PID control", *Control Eng.Pract.*, vol. 9, no. 11, pp. 1163-1175, 2001.

[30]   M.S. Kumar, "Development of active suspension system for automobiles using PID controller", *Proceedings of the World Congress on Engineering 2008 Vol II WCE 2008, July 2 - 4, London, U.K* , 2008.

[31]   S. Ravi Teja and Y. Srinivasa, "Investigations on the stochastically optimized PID controller for a linear quarter-car road vehicle model", *Veh.Syst.Dyn.*, vol. 26, no. 2, pp. 103-116, 1996.

[32]   F. Yu, "GA-based PID and fuzzy logic control for active vehicle suspension system", *International journal of automotive technology*, vol. 4, no. 4, pp. 181-191, 2003.

[33]   Y. Kuo and T. Li, "GA-based fuzzy PI/PD controller for automotive active suspension system", *IEEE Transactions on Industrial Electronics*, vol. 46, no. 6, pp. 1051-1056, 1999.

[34]   P.O. Scokaert and J.B. Rawlings, "Constrained linear quadratic regulation", *IEEE Transactions on Automatic Control*, vol. 43, no. 8, pp. 1163-1169, 1998.

[35]   A. Bemporad, M. Morari, V. Dua and E.N. Pistikopoulos, "The explicit linear quadratic regulator for constrained systems", *Automatica*, vol. 38, no. 1, pp. 3-20, 2002.

[36]   A. Hać, "Optimal linear preview control of active vehicle suspension", *Veh.Syst.Dyn.*, vol. 21, no. 1, pp. 167-195, 1992.

[37]   D. Hrovat, "Optimal active suspension structures for quarter-car vehicle models", *Automatica*, vol. 26, no. 5, pp. 845-860, 1990.

[38]   M. Nagai, "Recent researches on active suspensions for ground vehicles", *JSME international journal.Ser.C, Dynamics, control, robotics, design and manufacturing*, vol. 36, no. 2, pp. 161-170, 1993.

[39]   M. Nagai and S. Tanaka, "Study on the dynamic stability of Repu1sive magnetic levitation systems: Optimal control of active secondary suspension", *JSME international journal.Ser.3, Vibration, control engineering, engineering for industry*, vol. 35, no. 1, pp. 102-108, 1992.

[40]   J.E. Slotine and W. Li, *Applied nonlinear control*, Prentice hall New Jersey, 1991.

[41]   A. Isidori, *Nonlinear control systems. 2 (1999)*, Springer, 1999.

[42]   V.I. Utkin, *Sliding modes in control and optimization*, Springer-Verlag Berlin, 1992.

[43]   K.D. Young, Ü. Özgüner, *Variable structure systems, sliding mode and nonlinear control*, London ; Hong Kong, Springer-Verlag, 1999.

[44]   K.D. Young, V.I. Utkin and U. Ozguner, "A control engineer's guide to sliding mode control", *IEEE Transactions on Control Systems Technology*, vol. 7, no. 3, pp. 328-342, 1999.

[45]   M. Zhihong, A. Paplinski and H. Wu, "A robust MIMO terminal sliding mode control scheme for rigid robotic manipulators", *IEEE Transactions on Automatic Control*, vol. 39, no. 12, pp. 2464-2469, 1994.

[46]   Y. Feng, X. Yu and Z. Man, "Non-singular terminal sliding mode control of rigid manipulators", *Automatica*, vol. 38, no. 12, pp. 2159-2167, 2002.

[47]   J. Slotine and S.S. Sastry, "Tracking control of non-linear systems using sliding surfaces, with application to robot manipulators", *Int J Control*, vol. 38, no. 2, pp. 465-492, 1983.

[48]   A.J. Healey and D. Lienard, "Multivariable sliding mode control for autonomous diving and steering of unmanned underwater vehicles", *IEEE Journal of Oceanic Engineering*, vol. 18, no. 3, pp. 327-339, 1993.

[49]   A. Benallegue, A. Mokhtari and L. Fridman, "High‑order sliding‑mode observer for a quadrotor UAV", *International Journal of Robust and Nonlinear Control*, vol. 18, no. 4‑5, pp. 427-440, 2008.

[50]   Y. Shtessel, J. Buffington and S. Banda, "Tailless aircraft flight control using multiple time scale reconfigurable sliding modes", *IEEE Transactions on Control Systems Technology*, vol. 10, no. 2, pp. 288-296, 2002.

[51]   H. Xu, M.D. Mirmirani and P.A. Ioannou, "Adaptive sliding mode control design for a hypersonic flight vehicle", *Journal of Guidance, Control, and Dynamics*, vol. 27, no. 5, pp. 829-838, 2004.

[52]   V.I. Utkin, "Sliding mode control design principles and applications to electric drives", *IEEE Transactions on Industrial Electronics*, vol. 40, no. 1, pp. 23-36, 1993.

[53]   V.I. Utkin, J. Guldner and J. Shi, *Sliding mode control in electro-mechanical systems*, ed. 2, Boca Raton, FL, CRC Press, 2009.

[54]   T. Yoshimura, A. Kume, M. Kurimoto and J. Hino, "Construction of an active suspension system of a quarter car model using the concept of sliding mode control", *J.Sound Vibrat.*, vol. 239, no. 2, pp. 187-199, 2001.

[55]   N. Yagiz and I. Yuksek, "Sliding mode control of active suspensions for a full vehicle model", *Int.J.Veh.Des.*, vol. 26, no. 2, pp. 264-276, 2001.

[56] Y.M. Sam, J.H.S. Osman and M.R.A. Ghani, "A class of proportional-integral sliding mode control with application to active suspension system", *Systems & Control Letters*, vol. 51, no. 3–4, pp. 217-223, 3 2004.

[57] C. Kim and P. Ro, "A sliding mode controller for vehicle active suspension systems with non-linearities", *J.Automobile Eng., Proc.Inst.Mech.Eng.Pt.D*, vol. 212, no. 2, pp. 79-92, 1998.

[58] R.A. DeCarlo, S.H. Zak and G.P. Matthews, "Variable structure control of nonlinear multivariable systems: A tutorial", *IEEE Proc*, vol. 76, no. 3, pp. 212-232, 1988.

[59] V. Utkin, "Variable structure systems with sliding modes", *IEEE Transactions on Automatic Control*, vol. 22, no. 2, pp. 212-222, 1977.

[60] N. Yagiz, I. Yuksek and S. Sivrioglu, "Robust control of active suspensions for a full vehicle model using sliding mode control", *JSME international journal.Series C, Mechanical systems, machine elements and manufacturing*, vol. 43, no. 2, pp. 253-258, 2000.

[61] J. Xiao and B.T. Kulakowski, "Sliding mode control of active suspension for transit buses based on a novel air-spring model", in *IEEE Proceedings of the American Control Conference*, pp. 3768-3773, 2003.

[62] K.J. Åström and B. Wittenmark, *Adaptive control*, Dover Publications, 2008.

[63] A. Alleyne and J.K. Hedrick, "Nonlinear adaptive control of active suspensions", *IEEE Transactions on Control Systems Technology*, vol. 3, no. 1, pp. 94-101, 1995.

[64] R. Rajamani and J.K. Hedrick, "Adaptive observers for active automotive suspensions: Theory and experiment", *IEEE Transactions on Control Systems Technology*, vol. 3, no. 1, pp. 86-93, 1995.

[65] I. Fialho and G.J. Balas, "Road adaptive active suspension design using linear parameter-varying gain-scheduling", *IEEE Transactions on Control Systems Technology*, vol. 10, no. 1, pp. 43-54, 2002.

[66] I.D. Landau, A. Constantinescu and D. Rey, "Adaptive narrow band disturbance rejection applied to an active suspension—an internal model principle approach", *Automatica*, vol. 41, no. 4, pp. 563-574, 2005.

[67] P. Chen and A. Huang, "Adaptive sliding control of non-autonomous active suspension systems with time-varying loadings", *J.Sound Vibrat.*, vol. 282, no. 3, pp. 1119-1135, 2005.

[68] Jiangtao Cao, Honghai Liu, Ping Li and D.J. Brown, "State of the art in vehicle active suspension adaptive control systems based on intelligent

methodologies", *IEEE Transactions on Intelligent Transportation Systems*, vol. 9, no. 3, pp. 392-405, 2008.

[69] F.J. D'Amato and D.E. Viassolo, "Fuzzy control for active suspensions", *Mechatronics*, vol. 10, no. 8, pp. 897-920, 12/1 2000.

[70] M. Rao and V. Prahlad, "A tunable fuzzy logic controller for vehicle-active suspension systems", *Fuzzy Sets Syst.*, vol. 85, no. 1, pp. 11-21, 1997.

[71] S. Huang and W. Lin, "Adaptive fuzzy controller with sliding surface for vehicle suspension control", *IEEE Transactions on Fuzzy Systems*, vol. 11, no. 4, pp. 550-559, 2003.

[72] N. Al-Holou, T. Lahdhiri, D.S. Joo, J. Weaver and F. Al-Abbas, "Sliding mode neural network inference fuzzy logic control for active suspension systems", *IEEE Transactions on Fuzzy Systems*, vol. 10, no. 2, pp. 234-246, 2002.

[73] N. Yagiz, Y. Hacioglu and Y. Taskin, "Fuzzy sliding-mode control of active suspensions", *IEEE Transactions on Industrial Electronics*, vol. 55, no. 11, pp. 3883-3890, 2008.

[74] S. Huang and H. Chen, "Adaptive sliding controller with self-tuning fuzzy compensation for vehicle suspension control", *Mechatronics*, vol. 16, no. 10, pp. 607-622, 2006.

[75] H. Chen and S. Huang, "A new model-free adaptive sliding controller for active suspension system", *Int.J.Syst.Sci.*, vol. 39, no. 1, pp. 57-69, 2008.

[76] L.A. Zadeh, "Fuzzy sets", *Information and control*, vol. 8, no. 3, pp. 338-353, 1965.

[77] L.A. Zadeh, "Fuzzy logic", *Computer*, vol. 21, no. 4, pp. 83-93, 1988.

[78] L.A. Zadeh, "Fuzzy logic= computing with words", *IEEE Transactions on Fuzzy Systems*, vol. 4, no. 2, pp. 103-111, 1996.

[79] A. Sharkawy, "Fuzzy and adaptive fuzzy control for the automobiles' active suspension system", *Veh.Syst.Dyn.*, vol. 43, no. 11, pp. 795-806, 2005.

[80] H. Kwakernaak, "Robust control and H_∞ optimization—Tutorial paper", *Automatica*, vol. 29, no. 2, pp. 255-273, 1993.

[81] P. Gahinet, A. Nemirovskii, A.J. Laub and M. Chilali, "The LMI control toolbox", *Proceedings of the 33rd IEEE Conference on Decision and Control*, pp. 2038-2041, 1994.

[82]   P. Gahinet and P. Apkarian, "A linear matrix inequality approach to H_∞ control", *International journal of robust and nonlinear control*, vol. 4, no. 4, pp. 421-448, 1994.

[83]   P. Gahinet, "Explicit controller formulas for LMI-based H_∞ synthesis", *Automatica*, vol. 32, no. 7, pp. 1007-1014, 1996.

[84]   E. Fridman and U. Shaked, "Delay-dependent stability and H_∞ control: Constant and time-varying delays", *Int J Control*, vol. 76, no. 1, pp. 48-60, 2003.

[85]   Z. Wang, D.W. Ho, Y. Liu and X. Liu, "Robust H_∞ control for a class of nonlinear discrete time-delay stochastic systems with missing measurements", *Automatica*, vol. 45, no. 3, pp. 684-691, 2009.

[86]   P.P. Khargonekar, I.R. Petersen and K. Zhou, "Robust stabilization of uncertain linear systems: Quadratic stabilizability and H_∞ control theory", *IEEE Transactions on Automatic Control*, vol. 35, no. 3, pp. 356-361, 1990.

[87]   F. Liao, J.L. Wang and G. Yang, "Reliable robust flight tracking control: An LMI approach", *IEEE Transactions on Control Systems Technology*, vol. 10, no. 1, pp. 76-89, 2002.

[88]   C.E. De Souza and X. Li, "Delay-dependent robust H_∞ control of uncertain linear state-delayed systems", *Automatica*, vol. 35, no. 7, pp. 1313-1321, 1999.

[89]   L. Xie, "Output feedback H_∞ control of systems with parameter uncertainty", *Int J Control*, vol. 63, no. 4, pp. 741-750, 1996.

[90]   D. Yue, Q. Han and J. Lam, "Network-based robust H_∞ control of systems with uncertainty", *Automatica*, vol. 41, no. 6, pp. 999-1007, 2005.

[91]   Z. Wang, F. Yang, D.W. Ho and X. Liu, "Robust H_∞ control for networked systems with random packet losses", *IEEE Transactions on Systems, Man, and Cybernetics, Part B*, vol. 37, no. 4, pp. 916-924, 2007.

[92]   H. Li, "Robust control design for vehicle active suspension systems with uncertainty", *PhD thesis, University of Portsmouth*, 2012.

[93]   P. Michelberger, L. Palkovics and J. Bokor, "Robust design of active suspension system", *Int.J.Veh.Des.*, vol. 14, no. 2/3, pp. 145-165 , 1993 .

[94]   M. Yamashita, K. Fujimori, K. Hayakawa and H. Kimura, "Application of H_∞ control to active suspension systems", *Automatica*, vol. 30, no. 11, pp. 1717-1729, 11 1994.

[95]   H. Chen and K. Guo, "Constrained H_∞ control of active suspensions: An LMI approach", *IEEE Transactions on Control Systems Technology*, vol. 13, no. 3, pp. 412-421, 2005.

[96]   T.J.E. Miller, *Switched Reluctance Motors and Their Control*, Magna Physics Publishing, Hillsboro, OH, and Oxford, 1993.

[97]   R. Krishnan, *Switched Reluctance Motor Drives: Modeling, Simulation, Analysis, Design, and Applications*, Taylor & Francis, 2010.

[98]   U.S. Deshpande, J.J. Cathey and E. Richter, "High-force density linear switched reluctance machine", *IEEE Transactions on Industry Applications*, vol. 31, no. 2, pp. 345-352, 1995.

[99]   Han-Kyung Bae, Byeong-Seok Lee, P. Vijayraghavan and R. Krishnan, "A linear switched reluctance motor: Converter and control", *IEEE Transactions on Industry Applications*, vol. 36, no. 5, pp. 1351-1359, 2000.

[100]   Hong Sun Lim, R. Krishnan and N.S. Lobo, "Design and control of a linear propulsion system for an elevator using linear switched reluctance motor drives", *IEEE Transactions on Industrial Electronics*, vol. 55, no. 2, pp. 534-542, 2008.

[101]   Zhen Gang Sun, N.C. Cheung, Shi-Wei Zhao and Wai-Chuen Gan, "Magnetic analysis of switched reluctance actuators in levitated linear transporters", *IEEE Transactions on Vehicular Technology*, vol. 59, no. 9, pp. 4280-4288, 2010.

[102]   N. Lobo, H.S. Lim and R. Krishnan, "Comparison of linear switched reluctance machines for vertical propulsion application: Analysis, design, and experimental correlation", *IEEE Transactions on Industry Applications*, vol. 44, no. 4, pp. 1134-1142, 2008.

[103]   B. Lee, H. Bae, P. Vijayraghavan and R. Krishnan, "Design of a linear switched reluctance machine", *IEEE Transactions on Industry Applications*, vol. 36, no. 6, pp. 1571-1580, 2000.

[104]   E.S. MacPherson, "Wheel Suspension System for Motor Vehicles", US Patent 2,660,449, 24 Nov, 1953.

[105]   Siemens. *Siemens VDO e-Corner*. http://www.siemens.com/innovation/en/publikationen/publications_pof/pof_spring_2007/technology_for_the_environment/green_transportation.htm

[106]   J.A. Sabate, V. Vlatkovic, R.B. Ridley, F.C. Lee and B.H. Cho, "Design considerations for high-voltage high-power full-bridge zero-voltage-switched PWM converter", in *Fifth Annual Conference Proceedings of Applied Power Electronics Conference and Exposition*, pp. 275-284, 1990.

[107]   W. Chen, F.C. Lee, M.M. Jovanovic and J.A. Sabate, "A comparative study of a class of full bridge zero-voltage-switched PWM converters", in *Tenth Annual Conference Proceedings of Applied Power Electronics Conference and Exposition*, vol.2, pp. 893-899, 1995.

[108] R. Ayyanar and N. Mohan, "Novel soft-switching DC-DC converter with full ZVS-range and reduced filter requirement. I. regulated-output applications", *IEEE Transactions on Power Electronics*, vol. 16, no. 2, pp. 184-192, 2001.

[109] Yungtack Jang, M.M. Jovanovic and Yu-Ming Chang, "A new ZVS-PWM full-bridge converter", *IEEE Transactions on Power Electronics*, vol. 18, no. 5, pp. 1122-1129, 2003.

[110] J.A. Sabate, V. Vlatkovic, R.B. Ridley and F.C. Lee, "High-voltage, high-power, ZVS, full-bridge PWM converter employing an active snubber", in *Sixth Annual Conference Proceedings of Applied Power Electronics Conference and Exposition*, pp. 158-163, 1991.

[111] R. Redl, L. Balogh and D.W. Edwards, "Optimum ZVS full-bridge DC/DC converter with PWM phase-shift control: analysis, design considerations, and experimental results", in *Ninth Annual Conference Proceedings of Applied Power Electronics Conference and Exposition*, pp. 159-165, 1994.

[112] ISO 8855, "Road vehicles -- Vehicle dynamics and road-holding ability -- Vocabulary", International Organization for Standardization, ISO, 2011.

[113] M.W. Sayers, T.D. Gillespie and W.D.O. Paterson, "Guidelines for Conducting and Calibrating Road Roughness Measurements", The World Bank, Washington D.C., USA, Technical Report No. 46, 1986.

[114] M.W. Sayers, T.D. Gillespie and C.A.V. Queiroz, "The international road roughness experiment: Establishing correlation and calibration standard for measurement", The World Bank, Washington D.C., USA, Technical Report No. 45, 1986.

[115] ISO 8608, "Mechanical vibration - road surface profiles - reporting of measured data", International Organization for Standardization, ISO, 1995.

[116] G. Verros, S. Natsiavas and C. Papadimitriou, "Design optimization of quarter-car models with passive and semi-active suspensions under random road excitation", *Journal of Vibration and Control*, vol. 11, no. 5, pp. 581-606, 2005.

[117] A. Hać, "Suspension optimization of a 2-DOF vehicle model using a stochastic optimal control technique", *J.Sound Vibrat.*, vol. 100, no. 3, pp. 343-357, 6/8 1985.

[118] J. Dixon, *Suspension Geometry and Computation*, UK, Wiley, 2009.

[119] T. Miller, *Electronic Control of Switched Reluctance Machines*, Elsevier Science, 2001.

[120]   ISO 2631, "Mechanical vibration and shock -- Evaluation of human exposure to whole-body vibration-- Part 2: Vibration in buildings", TC 108/SC 4, Rep. TC 108/SC 4, 2003.

[121]   Z. Zhu, "Application of linear switched reluctance actuator in active suspension systems", *Hong Kong: Dept. of Electrical Engineering, The Hong Kong Polytechnic University*, 2012.

[122]   P.J. Lawrenson, J.M. Stephenson, N.N. Fulton, P.T. Blenkinsop and J. Corda, "Variable-speed switched reluctance motors", *IEE Proceedings B Electric Power Applications*, vol. 127, no. 4, pp. 253-265, 1980.

[123]   M.N. Anwar, I. Husain and A.V. Radun, "A comprehensive design methodology for switched reluctance machines", *IEEE Transactions on Industry Applications*, vol. 37, no. 6, pp. 1684-1692, 2001.

[124]   J.G. Amoros and P. Andrada, "Sensitivity analysis of geometrical parameters on a double-sided linear switched reluctance motor", *IEEE Transactions on Industrial Electronics*, vol. 57, no. 1, pp. 311-319, 2010.

[125]   Wai-Chuen Gan, N.C. Cheung and L. Qiu, "Position control of linear switched reluctance motors for high-precision applications", *IEEE Transactions on Industry Applications*, vol. 39, no. 5, pp. 1350-1362, 2003.

[126]   D.G. Taylor, "An experimental study on composite control of switched reluctance motors", *IEEE Control Systems*, vol. 11, no. 2, pp. 31-36, 1991.

[127]   Shi-Wei Zhao, N.C. Cheung, Wai-Chuen Gan, Jin Ming Yang and Jian Fei Pan, "A self-tuning regulator for the high-precision position control of a linear switched reluctance motor", *IEEE Transactions on Industrial Electronics*, vol. 54, no. 5, pp. 2425-2434, 2007.

[128]   X. Xue, K. Cheng and S. Ho, "A self-training numerical method to calculate the magnetic characteristics for switched reluctance motor drives", *IEEE Transactions on Magnetics*, vol. 40, no. 2, pp. 734-737, 2004.

[129]   X. Xue, K. Cheng, S. Ho and K. Kwok, "Trigonometry-based numerical method to compute nonlinear magnetic characteristics in switched reluctance motors", *IEEE Transactions on Magnetics*, vol. 43, no. 4, pp. 1845-1848, 2007.

[130]   F. Khorrami, P. Krishnamurthy and H. Melkote, *Modeling and adaptive nonlinear control of electric motors*, Springer, 2003.

[131]   J.K. Lin, K.W.E. Cheng, Z. Zhang, N. Cheung, X.D. Xue and T.W. Ng, "Active suspension system based on linear switched reluctance actuator and control schemes", *IEEE Transactions on Vehicular Technology*, vol. 62, no. 2, pp. 562-572, 2013.

[132] K.J. Åström and T. Hägglund, *Advanced PID control*, ed. , The Instrumentation, Systems, and Automation Society, 2006.

[133] K.J. Åström, H. Panagopoulos and T. Hägglund, "Design of PI controllers based on non-convex optimization", *Automatica*, vol. 34, no. 5, pp. 585-601, 1998.

[134] T. Hägglund and K.J. Åström, "Revisiting the Ziegler‐Nichols tuning rules for pi control", *Asian Journal of Control*, vol. 4, no. 4, pp. 364-380, 2002.

[135] J. Han and W. Wang, "Nonlinear tracking-differentiator", *J.Syst.Sci.Math.Sci*, vol. 14, no. 2, pp. 177-183, 1994.

[136] Jingqing Han, "From PID to active disturbance rejection control", *IEEE Transactions on Industrial Electronics*, vol. 56, no. 3, pp. 900-906, 2009.

[137] Y. Su, D. Sun and B. Duan, "Design of an enhanced nonlinear PID controller", *Mechatronics*, vol. 15, no. 8, pp. 1005-1024, 2005.

[138] H. Seraji, "A new class of nonlinear PID controllers for robotic applications", *Journal of Robotic Systems*, vol. 15, no. 3, pp. 161-181, 1998.

[139] P.C. Parks and V. Hahn, *Stability theory*, Prentice Hall New York, 1993.

[140] V.I. Utkin, J. Guldner and J. Shi, *Sliding mode control in electromechanical systems*, CRC press, 1999.

[141] Miroslav Krstic, Ioannis Kanellakopoulos and Petar Kokotovic, *Nonlinear and adaptive control design*, John Wiley and Sons, 1995.

[142] G. Bartolini, A. Ferrara, E. Usai and V.I. Utkin, "On multi-input chattering-free second-order sliding mode control", *IEEE Transactions on Automatic Control*, vol. 45, no. 9, pp. 1711-1717, 2000.

[143] V. Utkin and J. Shi, "Integral sliding mode in systems operating under uncertainty conditions", in *Decision and Control, Proceedings of the 35th IEEE*, pp. 4591-4596, 1996.

[144] K. Young, "Design of variable structure model-following control systems", *IEEE Transactions on Automatic Control*, vol. 23, no. 6, pp. 1079-1085, 1978.

[145] A. Zinober, O. Ei-Ghezawi and S. Billings, "Multivariable variable-structure adaptive model-following control systems", in *IEE Proceedings D: Control Theory and Applications*, pp. 6, 1982.

[146] I. Landau, "A generalization of the hyperstability conditions for model reference adaptive systems", *IEEE Transactions on Automatic Control*, vol. 17, no. 2, pp. 246-247, 1972.

[147]   I.D. Landau and B. Courtiol, "Design of multivariable adaptive model following control systems", *Automatica*, vol. 10, no. 5, pp. 483-494, 9 1974.

[148]   K.S. Narendra and L.S. Valavani, "A comparison of lyapunov and hyperstability approaches to adaptive control of continuous systems", *IEEE Transactions on Automatic Control*, vol. 25, no. 2, pp. 243-247, 1980.

[149]   V. Popov, "The solution of a new stability problem for controlled systems", *Automation and remote control*, vol. 24, no. 1, pp. 1-23, 1963.

[150]   S. Sastry and M. Bodson, *Adaptive control: stability, convergence and robustness*, Dover Publications, 2011.

[151]   P.A. Ioannou and J. Sun, *Robust adaptive control*, ed. , Courier Dover Publications, 2012.

[152]   I. Landau, "A hyperstability criterion for model reference adaptive control systems", *IEEE Transactions on Automatic Control*, vol. 14, no. 5, pp. 552-555, 1969.

[153]   S. Singh, "Adaptive model following control of nonlinear robotic systems", *IEEE Transactions on Automatic Control*, vol. 30, no. 11, pp. 1099-1100, 1985.

[154]   S. Srinathkumar, *Eigenstructure control algorithms: applications to aircraft/rotorcraft handling qualities design*, Institution of Engineering and Technology, 2011.

[155]   J. Tyler Jr, "The characteristics of model-following systems as synthesized by optimal control", *IEEE Transactions on Automatic Control*, vol. 9, no. 4, pp. 485-498, 1964.

[156]   C. Winsor and R. Roy, "The application of specific optimal control to the design of desensitized model following control systems", *IEEE Transactions on Automatic Control*, vol. 15, no. 3, pp. 326-333, 1970.

[157]   H. Erzberger, "Analysis and design of model following control systems by state space techniques", NASA, 1967.

[158]   A. Morse, "Structure and design of linear model following systems", *IEEE Transactions on Automatic Control*, vol. 18, no. 4, pp. 346-354, 1973.

[159]   C. Liaw, "Modified linear model-following controller for current-source inverter-fed induction motor drives", in *Control Theory and Applications, IEE Proceedings D*, pp. 49-56, 1990.

[160]   S. Skoczowski, "Robust model following control with use of a plant model", *Int.J.Syst.Sci.*, vol. 32, no. 12, pp. 1413-1427, 2001.

[161] G. Ambrosino, G. Celentano and F. Garofalo, "Robust model tracking control for a class of nonlinear plants", *IEEE Transactions on Automatic Control*, vol. 30, no. 3, pp. 275-279, 1985.

[162] J. K. Lin, K.W.E. Cheng, N.C. Cheung, Z. Zhang, X. Xue and S.W. Zhao, "Active damper control system based on LMFC", *World Electric Vehicle Journal*, vol. 4, pp.517-524, 2010.

[163] B. Peterson and K. Narendra, "Bounded error adaptive control", *IEEE Transactions on Automatic Control*, vol. 27, no. 6, pp. 1161-1168, 1982.

[164] B. Brogliato and A.T. Neto, "Practical stabilization of a class of nonlinear systems with partially known uncertainties", *Automatica*, vol. 31, no. 1, pp. 145-150, 1995.

[165] B.R. Barmish, I.R. Petersen and A. Feuer, "Linear ultimate boundedness control of uncertain dynamical systems", *Automatica*, vol. 19, no. 5, pp. 523-532, 1983.